IMPERIAL COLLEGE OF SCIENCE, TECHNOLOGY AND MEDICINE

UNIVERSITY OF LONDON

GUIDED WAVE INSPECTION OF EMBEDDED CYLINDRICAL STRUCTURES

by

Malcolm David Beard

A thesis submitted to the University of London for the degree of

Doctor of Philosophy

January 2002

Department of Mechanical Engineering
Imperial College of Science, Technology and Medicine
London
SW7 2BX

ABSTRACT

This thesis investigates the use of ultrasound for two specific non-destructive testing applications, made possible by recent developments in the understanding of guided wave propagation in embedded cylindrical structures. Guided waves offer an opportunity to inspect the rock bolts used to support coal mine roadways, where there is a need for an effective non-destructive test. Rock bolts are secured into pre-drilled holes in the mine roof with an epoxy resin, and provide roof support by resisting the movement and expansion of rock strata. As a result they are prone to failure from tensile overload, and a test is proposed that would identify defects and the residual length of the bolt using a pulse-echo technique. The use of rock bolts in the mining industry is increasing throughout the world, and the industrial use of such a test would have significant safety and economic benefits. In addition, this thesis continues the work of previous authors on the use of guided waves to inspect concrete post-tensioning tendons, and identifies the limitations of such a technique.

The behaviour of guided waves in the two systems is predicted through modelling, and the effect of material and geometry changes on modes that have the potential for long range inspection is investigated. These predictions are compared with experimental results from laboratory and site specimens. Further experimental work investigates the optimum excitation signal and the reflection of waves from selected features and defects, contributing to the general understanding of guided waves. The effect of specimen curvature has been found to be highly significant, and has been explained by comparing mode shapes in flat and curved plates. The previously unreported dispersion curves for a curved bar have also been calculated using a finite element technique, thus laying the foundations for further analytical work on guided wave propagation in curved bars.

ACKNOWLEDGEMENTS

This thesis would not have been possible without the support of many people and organisations. Many thanks to Mike Lowe and Peter Cawley at Imperial, for all their supervision and guidance throughout the research project. Also, to all the members of the NDT lab, now too numerous to mention individually, for their friendship, discussion, and practical help with experiments in the laboratory and on site.

This work was funded by the EPSRC, and supported by the Transport Research Laboratory and Rock Mechanics Technology Ltd. Thanks to Richard Woodward at TRL, and to Brian Clifford at RMT for their provision of industrial knowledge, specimens and access to test sites.

Finally, for all their continuing personal support, thanks to all my family and friends, and especially, to Anne.

CONTENTS

LIST OF FIGURES

LIST OF TABLES

CHAPTER 1

INTRODUCTION

1.1 Motivation and Objectives

Safer working environments in coal mines offer clear benefits to employees and the industry as a whole. Recent developments in the industry include the use of rock bolts to reinforce mine roadways, a faster and more economical method of roof support than traditional methods. Rock bolts consist of a long steel bolt fixed into the mine roof with an epoxy resin. The bolt confines the movement and expansion of the rock strata, both across and into the mine roadway. As a result the rock bolts are prone to failure through tensile overload along their length. A plate attached to exposed end of the rock bolt is designed to buckle under high load, giving a possible warning of potential failure loading. However, this plate does not buckle if localised overloading results from the shearing action of the rock strata, and there is currently no effective non-destructive test for the integrity of these bolts. The development of a suitable rapid underground inspection test for residual length and for the identification of corrosion patches would be a valuable industrial inspection technique [1].

A related problem is the need to inspect the steel tendons used for the post-tensioning of concrete structures. Recent bridge collapses such as the bridge at Ynys-y-Gwas in Wales [2] and in Palau [3, 4] have highlighted corrosion problems caused by inferior grouting, particularly in older bridges. There is a therefore a need to inspect new and existing bridge tendons for breaks and corrosion. Recent work [5] has concentrated on the use of high frequency, low-leakage guided waves for this task. Inspection techniques for such tendons already exist and are summarised in chapter 2, although the only effective techniques are generally invasive, and their use carries a risk of damaging the structure.

1.2 Guided Waves - A Potential Solution

In both of the applications discussed, the need is for a reliable inspection method that can interrogate a length steel, of circular cross section, that is embedded in a material. In the case of the bridge tendons, the embedding material is grout, in the case of the rock bolt, the embedding material is a layer of epoxy resin surrounded by rock of varying type. In both cases the only access is from the free end of steel. The test must therefore be carried from the exposed end of a rock bolt in a mine, and the tendon anchorage points in a post-tensioned bridge. Guided waves can easily be excited from these exposed ends, and because they travel in the structure as a whole, they can be used to interrogate the whole structure. Conventional ultrasonic tests are only capable of examining a single line, either between two transducers or by using a single transducer in a pulse-echo configuration. In both conventional and guided ultrasound tests, defects and breaks will act as reflectors that will reflect some of the energy travelling in the system, which can then be detected and analysed. The two main limitations are the decay of the signal due to leakage into the embedding material and the reflection coefficient for defects such as breaks and corrosion patches. The recent discovery of high frequency, low-leakage guided modes [6] has the potential to reduce the attenuation due to leakage, although the reflection coefficients from defects need to be determined. In addition, for structures embedded in an infinite expanse of material such as a rock bolt, lower frequency modes may offer an alternative to the high frequency modes.

1.3 Outline of Thesis Contents

This thesis presents an outline of the current NDT technology in use for rock bolts and concrete bridges, and explores the development that has taken place in the understanding of guided wave propagation, concentrating particularly on cylindrical structures.

The dispersion curves are then presented in detail for the case of an embedded rock bolt using the modelling tool Disperse [7]. High and low frequency modes with the potential for the long range inspection of rock bolts are identified, and the effect of different parameters such as bond quality and material properties is discussed. This knowledge is then used to explain the observed behaviour of guided waves in site and laboratory specimens. The reflection of the guided waves from angled defects is investigated experimentally, and explained using results from the modelling work. The optimum excitation signal is also researched and identified. Curvature has been found to adversely affect the high frequency test, but a suitable test for straight rock bolts is defined in addition to a lower frequency test that is unaffected by curvature.

The dispersion curves and modelling predictions are also presented for the case of an embedded steel tendon. The predicted attenuation has been compared with attenuation measurements made on short lengths of embedded tendon. This information is used to predict the maximum inspection range for tendons with perfectly reflecting breaks. Many of the findings of the rock bolt research also have implications for the inspection of tendons, and the maximum likely inspection range for tendons is discussed. Conclusions are drawn on the viability of the test for post-tensioning tendons, taking into account these and other significant factors.

Finally, the effect of curvature on the high frequency low-leakage guided waves is investigated. The mode shapes of free curved plates are calculated analytically and compared to those that exist in free straight plates - something that has not been done before. The comparison of mode shapes is used to explain the poor propagation and high attenuation observed for the low-leakage modes in curved bars. This work prepares the ground for the incorporation of leaky curved plate systems in the guided wave modelling software ‘Disperse’ [7]. In addition, the dispersion curves for a curved free bar are calculated using a Finite Element method, and compared to those for a straight bar.

CHAPTER 2

BACKGROUND INFORMATION AND EXISTING INSPECTION TECHNIQUES

2.1 Introduction

This chapter investigates two industrial inspection problems, for which the current non-destructive testing technology is inadequate. The methods of rock bolting for the support of mine roofs, and post-tensioning for the reinforcement of concrete, are discussed. The limitations of the current inspection methods are identified, and proposals are put forward for a pulse-echo inspection technique using guided waves. Much of the work in this thesis requires knowledge of the dispersion curves that describe sound wave propagation in structures. The basis quantities of phase velocity, group velocity, energy velocity and attenuation are introduced in this chapter, although they are also discussed in more detail in later chapters. The convention for numbering guided wave modes is also included, together with a summary of the developments in the field of guided waves that have made this research possible.

2.2 Post-Tensioning Tendon Background Information

This section gives information on the use of post-tensioned concrete in the construction of bridges. Typical problems that occur over the lifetime of such a bridge are examined along with the existing inspection methods. Significant effort has already been put into the tendon inspection problem by the industry and universities, although the problem of how to inspect individual tendons remains. The method of post-tensioning was invented in France, and the rapid growth of the road networks in France and the UK in the second half of the twentieth century led to the construction method becoming quickly established. A full history of the development of the method is given in a book published as a result of an Anglo-French working party looking into the problems, inspection and repair of post-tensioned structures [8].

2.2.1 Reinforcement of Concrete using Post-Tensioning

The post-tensioning of concrete allows material-efficient structures to be built by increasing the load bearing capacity of concrete beams. This is achieved by tensioning steel tendons inside a concrete structure after the concrete has hardened. The tendons are stressed almost to their yield point, which applies a significant compressive load to the structure, hence increasing the tensile load that it can carry. The tendons are located in ducts within the concrete and are secured

between strengthened anchorage regions at each end of the structure. The tendons are tensioned by machines, and are then held in place by a three-jaw collet assembly at the free end, leaving the end exposed. After tensioning, the ducts are pumped full of an alkaline grout, which protects the tendons from water ingress and corrosion. Figure 2.1 shows a schematic diagram of a typical post-tensioning arrangement that may be found in a bridge deck.

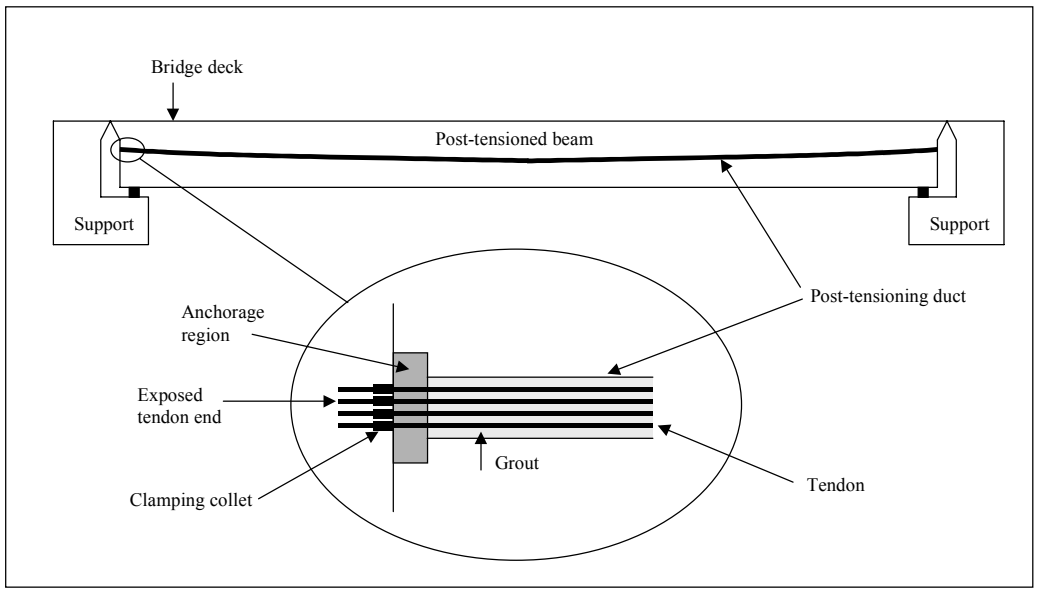

Figure 2.1: Typical post-tensioning construction arrangement in a bridge deck.

The tendons are critical for the strength of the structure, and corrosion has led to the unexpected failure of some older bridges [2-4]. Failures and corrosion are normally associated with incomplete, or loss of, grout material which allows water, often with a high salt content from road treatments, to come into contact with the tendons. Following the collapse of the Ynys-y-Gwas bridge deck [2], there was considerable concern about possible bad grouting in many older bridge decks, where grout voids at duct high points could cause water to collect around the tendons. Over time, the tendons can corrode to such a level that they can no longer support the required tensile load. Failure of one tendon means that load will be transferred to other tendons, which can lead to a chain reaction of failures that ultimately causes the bridge to collapse. The problem has also been recognised in the USA where the need for more sophisticated testing techniques has been identified [9, 10]. It is essential that breaks in individual tendons can be detected, and it is also desirable for corrosion and poor grouting to be detectable with the same method. Ideally, the condition of the tendon needs to be assessed with non-invasive techniques, as drilling the duct and grouting puts the integrity of the grout at risk.

Bridge failures, and other events, led to the Department of Transport placing a moratorium on the design and construction of new post-tensioned bridges in 1992. This moratorium was only

lifted in 1996 [11], following the implementation of new procedures that would eliminate the possibility of tendon corrosion. However, the safeguards, which include NDT, only apply to the design and construction of new bridges [12], and regular inspection of older bridges is still required. In 1993 the Highways Agency started a programme of inspections on 1000 vulnerable bridges, using the limited techniques available. By 1997, over 100 reports on the condition of bridges had been made, with the post-tensioning being satisfactory in most bridges, although with some voiding and light tendon corrosion [13].

Two main types of reinforcing tendon are used in bridge construction, single wire and strand, with single wires typically being 5mm or 7mm in diameter. Strand tendons usually consist of seven wires, with six wires being spirally wrapped around a central wire with a slightly larger diameter. One of the most common strand sizes has a total diameter of 15.9mm, with outer wires of 5.2mm diameter wrapped around a 5.5mm diameter core wire. A 12.5mm diameter strand is also common on older bridges. Several tendons are usually enclosed within a single grouted duct, which makes the resolution of defects on individual tendons difficult.

2.2.2 Existing Inspection Techniques

There are many different techniques in use for assessing the condition of concrete structures, both with and without post-tensioning. These techniques are well documented, and are covered by a number of publications, such as [14]. This section provides a brief summary of the more common methods that are in use, and concentrates on those that can be applied to post-tensioned structures.

Visual Inspection Techniques

Visual inspection is the simplest form of NDT that can give early warning of concrete or structure problems, and is often the only inspection method available to bridge engineers [15]. In post-tensioned bridge inspection the type and detail of visual inspections varies from a simple search for tendon corrosion products on the underside of the bridge, to visual examination using endoscopes inserted through bore holes. There are numerous problems associated with the drilling of bore holes, including the risk of damage to the structure and the difficulty in locating and obtaining access to the ducts. Inspections must be highly detailed, as moisture can penetrate through very small cracks [16], although in practice the general bridge condition is estimated from the condition of several carefully chosen areas. A test that could completely scan sections of a bridge from one point would be a significant improvement, even if access still had to be made through bore holes.

The use of an endoscope requires drilling of the concrete, ducting and grout material, with risk of damage to tendons and subsequent water ingress through poor re-sealing [16]. Since grout

voids and subsequent tendon corrosion are most likely to occur at high points on the bridge, the tendon anchorage points are a crucial area to inspect. This area is often beyond the capabilities of drilled bore holes, because of the large mass of concrete around the bridge piers. Often, inspection is only possible if some of the concrete in the anchorage region is removed, allowing access to drill into the reinforcing duct. The concrete is then re-poured after the inspection has taken place. A technique that could interrogate the tendon from the exposed end would be very beneficial.

Radiography

Radiographic methods are widely used for the inspection of metal structures, but in general, the high level of scattering that occurs in concrete limits their use in civil engineering. The use of radioactive sources can require exclusion zones of several hundred metres, as inspections are made using mainly gamma and X-rays. A further disadvantage of radiographic methods is that access to both sides of the structure is usually required.

The basic radiographic test (Direct Radiography) uses the principle that short wavelength electromagnetic radiation will pass through any solid, but will be absorbed depending on the thickness and density of the material, allowing voids and small defects to be detected. The image of the radiation passing through the structure can be recorded on film. Fluoroscopy is a similar technique that records the image on a florescent screen, removing the need for film developing. The detection of voids in post-tensioning tendon grouting has been achieved using radiographic methods [17]. However, the resolution is poor, and the method is not suitable for detecting defects in individual tendons. Radiographic methods are also unsuitable for older bridges that have metal tendon ducts, as the radiation cannot penetrate through to the grout/tendons. These problems have limited the use of radiographic methods to locating the position of ducts [15]. A commercial system called SCORPION has been developed and is in regular use in France [18], although the inspection can be inconvenient, as the use of high power radioactive sources requires the area to be evacuated. Data can be analysed live or on film, and the equipment is mounted on a lorry that is used to scan the bridge via a gantry system.

Ultrasonic Methods

The use of ultrasound in civil engineering is widespread, although non-destructive techniques are mostly limited to the use of bulk waves, rather than guided waves. Sound travels as a bulk wave in any elastic material where the sound does not interact with the edges of the material, therefore acting as if the material was infinite in extent. The velocity of sound in materials such as concrete varies with its elastic properties, which can be easily calculated by measuring the time of flight between two known points, using equipment such as the PUNDIT probe and

meter [19]. The velocity can be related to a variety of different material properties and conditions, and is often used as a test of concrete uniformity, where velocity is usually displayed on a contour map. Large cracks and voids can be detected by an increase in travel time as the sound travels around the defect. Low frequencies of 20-150kHz are used for testing concrete, primarily because the shorter wavelengths of higher frequencies would quickly be scattered in the concrete material. The high attenuation experienced by sound waves in concrete also means that most tests use a through transmission, rather than a pulse-echo, configuration. Ultrasound is much more widely used for locating defects in metal structures, where the uniform nature of the material allows higher frequency sound waves, with very high resolution, to propagate with little attenuation.

The use of ultrasound to inspect post-tensioning tendons is currently limited to attempting to inspect grouted ducts for voids [20-22]. A track mounted ultrasonic scanner (CANDI) [23] developed for this purpose has been successful in locating the ducts, but not at detecting voids. Problems have been encountered with noise from scattering in the concrete. The Ultrasonic Impact-Echo method of testing concrete that was initially developed by Sansalone to identify voids in grout [24], is being further developed by Watanabe and Ohtsu [25]. This method looks at the frequency content of the received ultrasonic signal to identify where voids may exist. The technique has achieved marginal success in concrete testing, although care must be taken to ensure that the impact frequency is high enough to detect defects. Ultrasonic Tomography is an application of this method, and is used to build up a 2-D or 3-D picture of voids in grouting ducts by measuring time-of-flight over different ray paths [26]. Ultrasonic methods are well discussed in two CAPCIS reports entitled *'Non-destructive methods for field inspection of embedded or encased high strength steel rods and cables'* [27, 28].

The use of guided ultrasonic waves in any application is more complicated than the use of bulk waves, and this has so far limited the use of guided waves for NDT. Guided waves exist in structures that do not behave as an infinite mass of material, and the sound propagation is constrained by one or more material boundaries. In these cases, sound propagation is complex and sound can travel in a large number of 'modes', which can be determined by the solution of the wave propagation equation. The complications arise from the fact that these guided waves are dispersive, and the frequency dependence of their properties such as velocity and attenuation must be known so that test results can be accurately interpreted. A more detailed introduction to guided waves is given later in this chapter. As understanding of guided waves increases, their commercial use is increasing, a particularly successful application has been the long-range inspection of pipes [29]. A major advantage of guided waves is that they propagate in the structure as a whole, and therefore have the potential to inspect the whole structure from a

single point. Thus, a guided wave excited at the exposed end of a tendon would be reflected from any defect in the tendon, allowing defects to be accurately located. This technique was first attempted by Weight [30], whose work was entirely experimental and without the advantage of a theoretical model. Later, development work was continued by Pavlakovic [5,31] who used modelling techniques to predict wave behaviour. Whilst Pavlakovic predicts shorter propagation distances than Weight, the experimental results by Pavlakovic are promising, with propagation over a 2m length being achieved. Some specific high frequency modes that have low attenuation have been identified as having potential for the inspection of tendons. This work is continued and discussed in more detail in chapter 5.

Acoustic Emission

Acoustic Emission techniques involve listening for acoustic events in a structure through permanently attached transducers. The characteristics of the signals can be correlated to identify failure events. The use of many transducers allows the event to be located accurately. Acoustic Emission was first used by Rebert and Brachet-Rolland [32] to detect fractures of individual wires in tensioned cables and active cracks in concrete. However, the method was limited by the need for better data interpretation of received signals. A successful acoustic emission technique has been developed in Canada and is being used to continuously monitor bridge tendons [33]. The commercial product is called Soundprint® and can be fitted to old structures as well as new. However, the test will only record new failures and not events that have already occurred. The test uses piezo-electric accelerometers that 'listen' for the acoustic energy emitted by break events, and can be used on grouted or ungrouted tendons, although a much higher density of transducers is required for grouted tendons.

Other methods

Numerous other techniques are used for bridge testing, and some can give limited information about the likely condition of reinforcing tendons, although they do not inspect the tendon itself. For example, chemical methods are often used in conjunction with visual techniques to determine if tendon corrosion is taking place. Core and surface samples are analysed in the laboratory for the chemicals produced by corrosion, and the levels are used to determine the likely tendon condition. Surface hardness methods are used to relate concrete hardness to strength, wear rate and uniformity. However, they are only useful up to a depth of about 30mm, and are therefore not suitable for tendon inspection.

Some inspection methods with the potential to inspect individual tendons are affected by the presence of the grouting ducts. Time domain reflectometry [34] is a technique that aims to detect electromagnetic reflections from defects. However, in real bridge structures the metal

ducts and tendons are often in electrical contact, which makes it difficult to examine a single tendon. An electrical reflectometry test (RIMT – Reflectometric Impulse Measurement Test) has been under development in Switzerland and Italy [35]. An electrical pulse is applied to a tendon, and it is claimed that tendon condition and voids in ducts affect reflections. Testing in England and France has not been successful so far, and the technique is not recommended [8], although it does have development potential. Ground penetrating and impulse radar have also been used to try and evaluate tendons, but radar is incapable of passing through the metal ducting. The method also suffers from poor resolution and the use of radar is therefore limited to duct location [36].

Dynamic response and load testing are also used for bridge analysis, but are generally very disruptive, as the bridge needs to be closed for the duration of the tests. Dynamic response tests range from a simple hammer test to check bridge deck condition, to more complex modal testing, which analyses the natural frequencies of the structure. The tests only provide general information on the condition of the bridge, and not on specific problem areas. Load testing is usually used in the form of a proof load test, where the structure is deliberately overloaded to prove that it can adequately support the design load. Strain and deflection can be measured using a variety of standard techniques [14] and this is useful for examining areas of stress concentration.

2.3 Rock Bolt Background Information

This section gives information on the use of rock bolts to reinforce mine roofs, and the typical problems that are encountered in service. Rock bolts have been increasingly used for roof support in British coal mines since 1990, and are now the main system of support. Their introduction has brought considerable safety and productivity improvements over the use of conventional steel supports [37]. Their introduction has involved 'design by measurement', using rock bolt and rock strata movement data to enhance the design and maintenance of rock bolted roadways [38]. Therefore, there is a considerable amount of data available to predict the condition of rock bolts, but there is currently no effective non-destructive test for their integrity. This thesis concentrates on the testing of the standard rock bolts used in UK coal mines, but the method also has potential for testing the grouted bolts that are used in the construction industry. Further research should also allow the inspection of other types of bolt, such as the under-reamed rock bolts [39] that are being developed specifically for soft rock applications. There are several texts available on the subject of rock bolting theory and practice, although a particularly useful introduction can be found in [40], which explores both tunnelling and mining applications.

2.3.1 Reinforcement of Mines Using Rock Bolts

A major consideration in supporting mine roofs is limiting the movement and expansion of the rock strata immediately above the roof. This is particularly significant close to the coal face, where large amounts of material are removed and the ground movement due to stress redistribution is high. Steel studs (rock bolts), threaded at one end only, are inserted into pre-drilled holes to limit the ability of the rock strata to slide over each other and/or expand downwards into the roadway. Standard rock bolts are usually between 2m and 3m long and 21.7mm in diameter, although 25mm diameter bolts are also in use. The rock bolts are held in place by a fast setting epoxy resin and are tightened against the rock face by a nut and plate assembly on the threaded (free) end. A steel mesh is sometimes inserted between the plate and the roof to prevent minor roof falls. A schematic of the complete installation in shown in figure 2.2, and a picture of a 1m long rock bolt prior to installation is shown in figure 2.3.

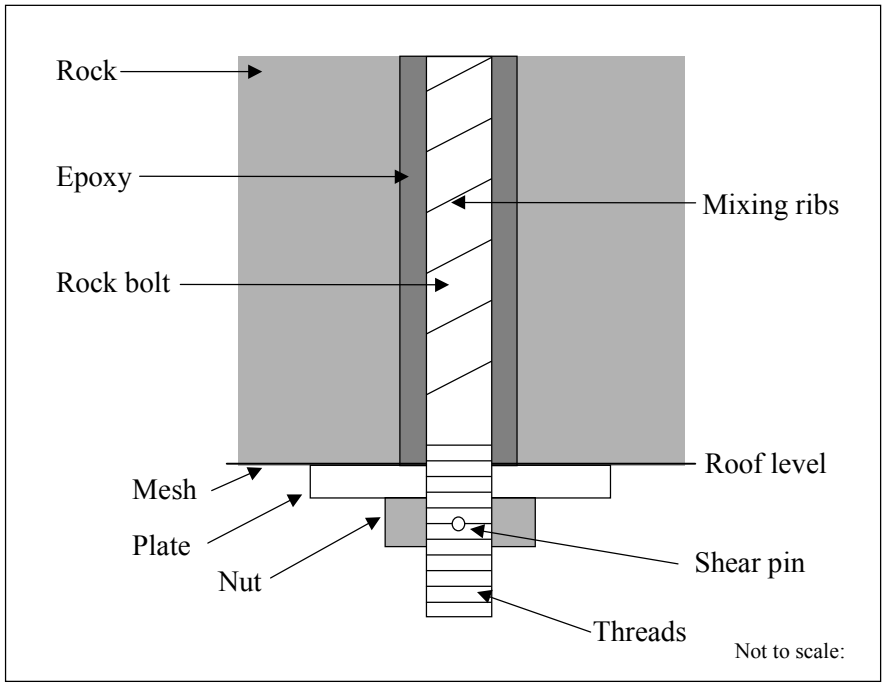

Figure 2.2: Schematic diagram of a typical rock bolt installation.

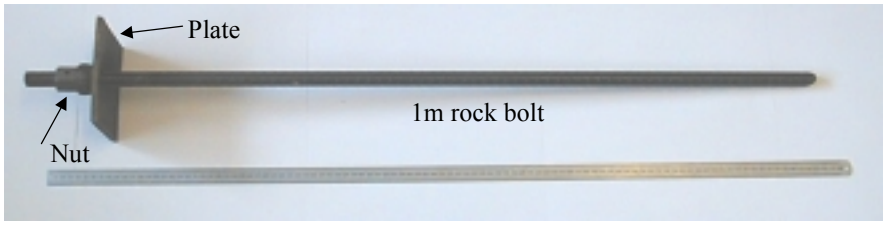

Figure 2.3: Picture of a 1m long rock bolt prior to installation.

The installation process begins with the pre-drilling of the installation hole. The hole is nominally 29mm in diameter, with a tolerance of ±2mm, which is equivalent to an epoxy layer thickness of about 3 to 5mm. The hole is then filled with plastic capsules containing the epoxy resin and a hardening agent. The assembled rock bolt is then inserted into the start of the hole and an installation machine is attached to the nut on the threaded end. This nut is held in place on the bolt with a shear pin, allowing the whole bolt assembly to be spun in the hole. Installation then takes place with the machine spinning the bolt further into the hole. The epoxy bags are punctured and their contents mixed, aided by a sharp angled end on the rock bolt and mixing ribs along the sides. Spinning continues after the bolt has filled the hole until the resin sets, usually after 10 to 120 seconds, depending on the resin type. The setting of the resin then causes the shear pin holding the nut in place to shear, and the nut is then driven up the bolt, forcing the plate against the roof.

The plate has a built in curved region that is designed to buckle before tensile failure of the bolt occurs, giving a visual indication of overload. However, this safeguard only protects against failure at the threaded end, which is likely if the bolt is resisting the expansion of rock into the roadway. A potentially more serious failure mechanism can occur if significant horizontal movement of the rock strata is occurring. In this case, the rock bolt would be subject to localised overload at the strata boundary, as illustrated by figure 2.4. Here the resin integrity will be lost as the strata slide over each other and the bolt will be formed into a crank handled shape as it crushes the rock in the deformation region. Necking of the bolt will occur in the deformed region prior to failure. In this way, the shearing motion of rock strata causes the bolt to fail locally in tension, in a similar way to that expected from expansion of the rock into the roadway. Localised corrosion may also cause the bolt to fail in regions where overload would not normally have occurred. A further defect that occurs is a loss of resin encapsulation near the free end of the bolt, which may be caused by an oversize hole or the insertion of insufficient resin capsules. Figure 2.5 shows pictures of a real rock bolt that was recovered from a roof fall after shearing of the rock strata caused deformation, overload, and eventual tensile failure. This figure also shows the detail of a rock bolt that has been over-cored and sectioned to reveal the epoxy layer and contamination by the resin capsules.

Because of the variety of loads that a rock bolt may experience, it is not always possible to assess the condition visually. A suitable non-destructive test is required to assess the integrity of the rock bolts. A basic test would need to be able to determine the residual bolt length, which could then be compared to the initial bolt length to detect failed bolts. The test could also be used as a form of audit to check that bolts of the correct length had been installed. Ideally, the test would also be able to determine the condition of the bolt [1]. This would include detecting loss of resin encapsulation, corrosion patches and necking or bending of the bolt.

There are other forms of rock bolt in use, which it would also be desirable to inspect. Fibreglass bolts are sometimes used instead of steel bolts, however these would present additional problems, as ultrasound is quickly attenuated in fibreglass. Seven-wire steel strand, similar to that used for concrete post-tensioning, is also used in lengths up to 8m. The smaller diameter of these strands and the longer length also make inspection more difficult, and so this thesis concentrates on standard steel bolts up to 3m in length, in order to prove the concepts.

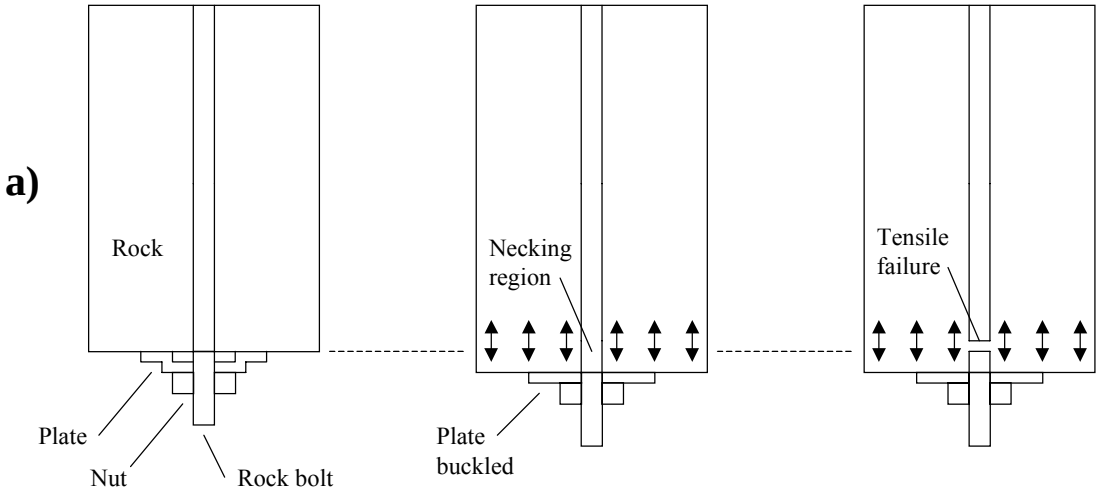

(i) Unloaded rock bolt, subject to strata expansion only.

(ii) Expansion of rock strata causes plate to buckle, then tensile overload and necking of the bolt close to free end.

(iii) Tensile failure of bolt occurs in the overloaded region.

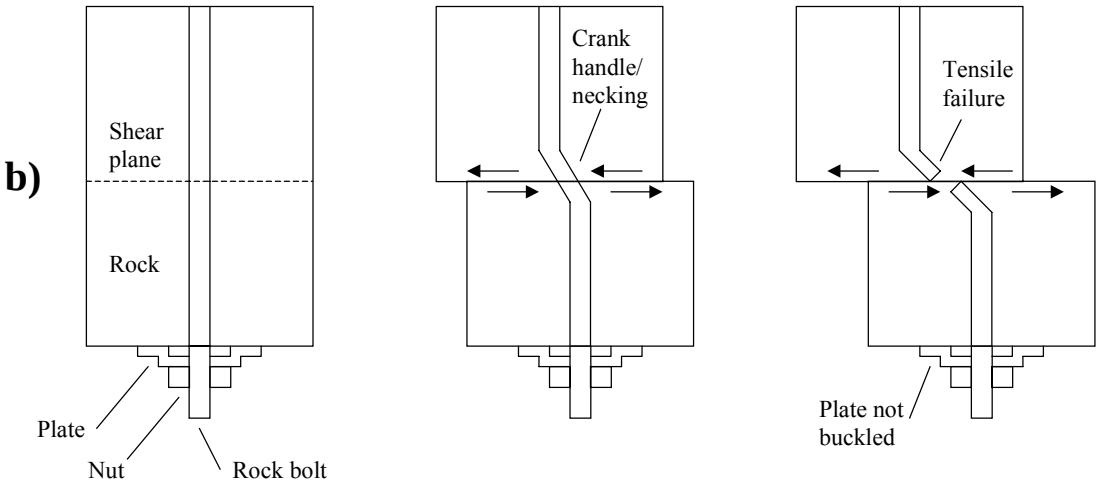

(i) Unloaded rock bolt subject to strata shearing only.

(ii) Shearing of strata causes localised deformation at the strata boundary. Tensile overload in this region leads to necking.

(iii) Tensile failure occurs in the overloaded region, but the plate has not buckled. Failure often just above deformed region.

Figure 2.4: Rock bolt failure mechanisms, (a) due to strata expansion, and (b) due to strata shearing.

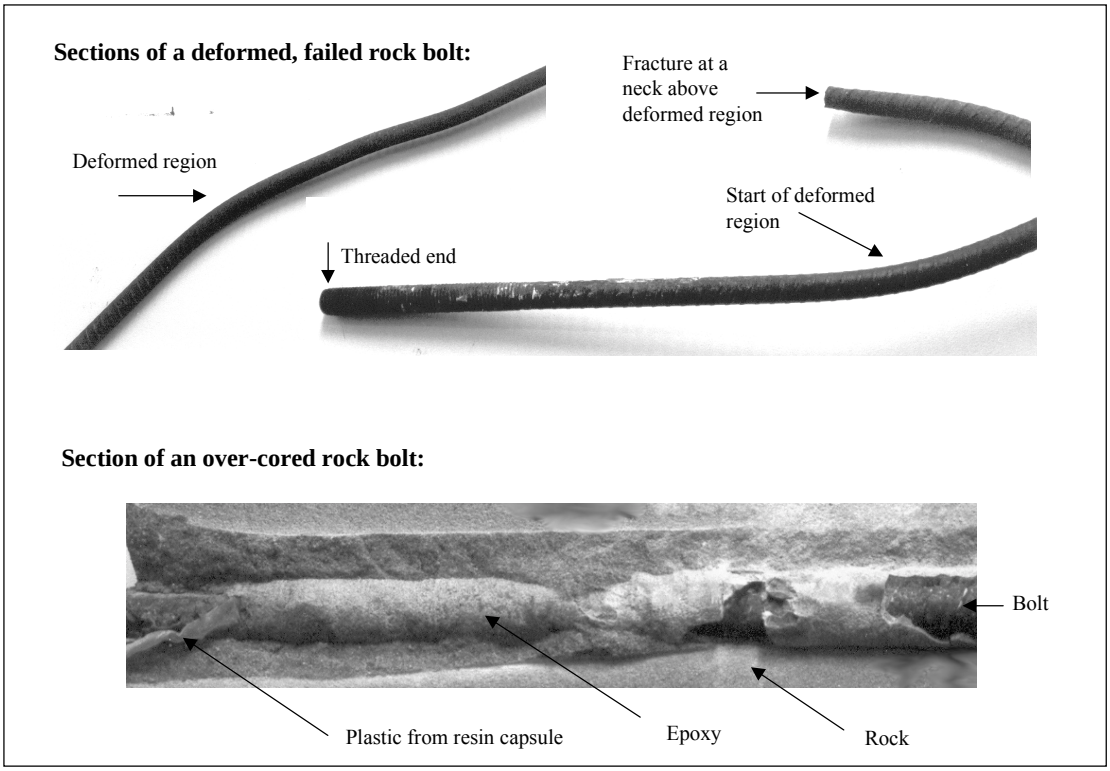

Figure 2.5: Pictures of a rock bolt that failed due to strata shearing and sections taken from an over-cored rock bolt.

2.3.2 Existing Inspection Techniques

There are currently no effective NDT techniques available for the testing of rock bolts in soft-rock applications such as in UK coal mines. A limited form of visual inspection is carried out to determine how much ground movement is occurring, and more rock bolts are installed if it is thought necessary. In addition, there is a pull-out test which is costly and time consuming to carry out, and can only be used on a very small sample of bolts. Some information on rock bolt condition can be gained from examining roof falls that occur as the coal face advances, but distortion may occur during collapse and it is difficult to tell the condition prior to failure.

A commercial testing instrument is available for the testing of grouted rock bolts [41]. The 'Boltometer' uses a low frequency guided ultrasonic wave to determine the quality of the bolt encapsulation on cement grouted bolts. The encapsulation is assessed by the amplitude of the flexural guided wave that is reflected from the bolt end. A report on an early version of the device identifies particular deficiencies [42], such as the need to prepare bolt ends and the need to calibrate on known good bolts. A major problem with the device is that good bolts are determined by a lack of return signal. It is therefore possible that an equipment malfunction such as problems with the transducers could result in a badly encapsulated bolt being wrongly classified as good. The attenuation of these reflections could also occur due to a variety of other

factors such as coupling conditions, rock conditions and exact bolt length and end conditions. Tests on the device by the mining consultancy company Rock Mechanics Technology Ltd. concluded that the device was not suitable for soft rock coal mining applications.

A test method based on the frequency response of rock bolts [43] is being developed to determine encapsulation conditions. The test determines the dominant frequency response when the rock bolt is struck with a hammer system attached to the bolt head. The measurements are made using accelerometers, aligned in the direction of the bolt axis. The aim is to identify a correlation between the dominant frequency and the percentage of the bolt that is grouted around the head area. However, for the technique to work, the grout must be properly fixed at least near the bolt head. The test has been devised for cement grouted rock bolts in hard rock mining applications, and it is considered unlikely that it will be able to determine bolt length reliably.

A method of determining bolt encapsulation quality based on the measurement of the frequency response function is claimed to be under development at the University of Queensland Mineral Research Centre. The method claims to be able to determine encapsulation conditions, and is being tested on bolts of different lengths. Although no literature on the method could be found, it is thought to be highly unlikely that the test will be capable of determining the bolt length or of locating defects.

2.4 Proposed Inspection Technique

There are many similarities between the rock bolt and tendon inspection problems, and guided waves offer new testing opportunities for both. The main similarity is that both involve long-range guided wave propagation in embedded cylindrical structures, and research in the understanding of these waves can be applied to both cases. In addition, easy access to both tendons and rock bolts can only be made from the exposed 'free' end that protrudes from the embedding material. In both cases, it is desirable to detect defects, and in the rock bolt case it is particularly desirable to detect the embedded end as well.

The proposed inspection technique involves exciting a guided wave in the tendon or rock bolt at the free end, which will then be reflected from the end or from defects and breaks, as shown in figure 2.6. The test is a pulse-echo test, and the same transducer that is used to excite the wave will then listen for reflections. The amplitude and time of arrival of these reflections can then be used to identify and locate defects. The test differs from most conventional industrial ultrasonic inspection techniques because a guided wave is used, rather than a bulk wave. Bulk waves can only exist in a bulk of material that is effectively infinite, and always travel at the speed of sound in that material. However, in structures with finite boundaries, guided waves are formed that have more complicated properties than bulk waves. These properties can be described by dispersion curves, and are discussed further in section 2.6.

The development of a guided wave test involves identifying suitable modes through modelling, assessing the sensitivity of the wave properties to changes in the specimen condition, and verifying the mode behaviour on site. In addition, the interaction of the wave with structure features and defects must be studied. The success of such a test will also depend on producing a suitable testing instrument and test equipment. The transducers need to be robust enough to withstand underground use, and the equipment must be capable of being transported several miles underground by one person. The amount of preparation needed must be minimal, to allow a large number of tendons or bolt to be inspected in a short time period. Equipment that is routinely used in coal mines must be certified as 'intrinsically safe', which ensures that there are no unsealed components that may cause sparks. This protects against the ignition of any natural gas pockets that may occur underground.

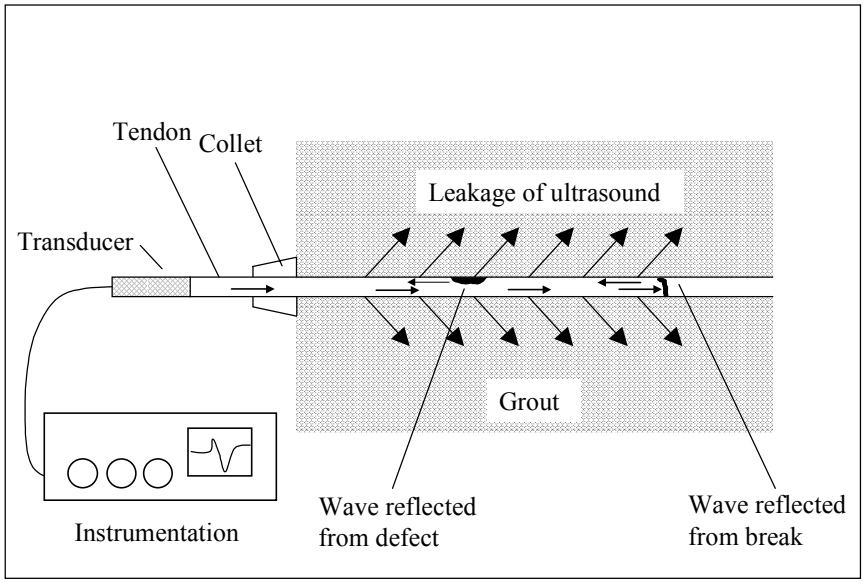

(a) Post-tensioning tendon.

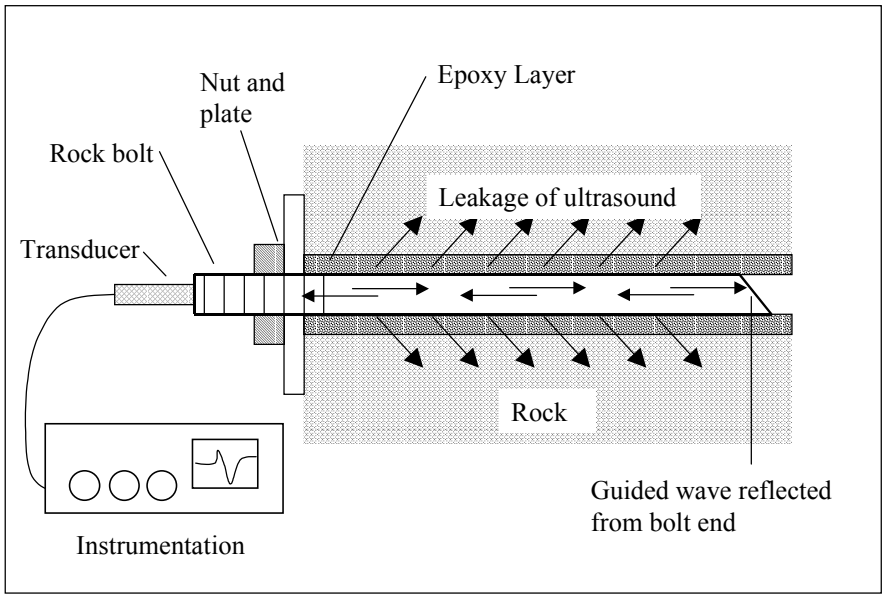

(b) Rock bolt.

Figure 2.6: Proposed inspection techniques.

2.5 Historical Development of the Understanding of Cylindrical Guided Waves

Guided wave propagation in a free bar was first studied numerically in the late 19th Century by Pochhammer [44] and Chree [45]. The next major achievements were made by in 1943 by Hudson [46], who studied the fundamental flexural mode in a free bar, and in 1948 by Davies [47], who studied the longitudinal modes. Later papers by Onoe, McNiven and Mindlin [48], Pao and Mindlin [49, 50], and Meeker and Meitzler [51] reported further developments in the understanding of elastic wave dispersion in a three dimensional solid bar.

Hollow isotropic cylinders were first studied by Gazis in 1959 [52], and his predictions were validated by Fitch [53] for both flexural and longitudinal modes. Kumar [54, 55] investigated the case of a hollow cylinder filled with fluid, such as would be found in a pipeline. Numerous developments have also taken place in the treatment of anisotropic materials, such as in [52, 56-61].

The extension of solution methods to the leaky case of embedded bars was limited by the ability to calculate complex Bessel functions. Thurston [62] was able to calculate dispersion curves for a clad rod, but only in the regions where the Bessel functions had wholly real arguments. Developments in the ability to calculate Bessel functions with complex arguments [63] has allowed researchers to calculate dispersion relationships more fully [64-66]. The discovery of high frequency low loss modes in embedded bars made by Pavlakovic [6] was made possible by the ability to calculate these functions efficiently.

The calculation of dispersion curves for systems with an arbitrary number of layers has been made much easier with the development of Disperse [7], a general purpose program for tracing dispersion curves. The software was originally developed by Lowe, who used the global matrix method to solve the wave propagation equation [67]. The general purpose nature of the software is a significant improvement over previous reported solutions, which were generally case specific. The software allows the modelling of elastic isotropic materials (with or without material damping), transversely isotropic materials, spring boundaries and fluids. Dispersion curves can be calculated in both Cartesian and cylindrical co-ordinates, and the solution method is valid for all mode types. The inclusion of multi-layered cylindrical embedded systems is a recent addition to the software [68], allowing leakage from a bar into an embedding material to be considered.

2.6 Introduction to Dispersion Curves

In an infinite bulk of a perfectly elastic material, a sound wave will spread out through the material as a bulk wave, decaying in amplitude because of the spread of the wave front. However, in a finite structure such as a perfectly elastic steel bar, the sound wave is reflected from the structure boundaries, and the energy is contained within the bar as a guided wave, which will propagate with constant amplitude. The complex effect of the boundaries means that the energy propagates in modes that have predictable frequency-dependent properties, which can be calculated by solution of the wave propagation equation. The mathematical solution to the wave propagation equation yields a number of solutions that form continuous propagating modes. The velocity-frequency relationships of guided waves can be displayed as dispersion curves. Figure 2.6 shows the phase velocity dispersion curves for a 20mm diameter steel bar in a vacuum. This case is discussed later in this section.

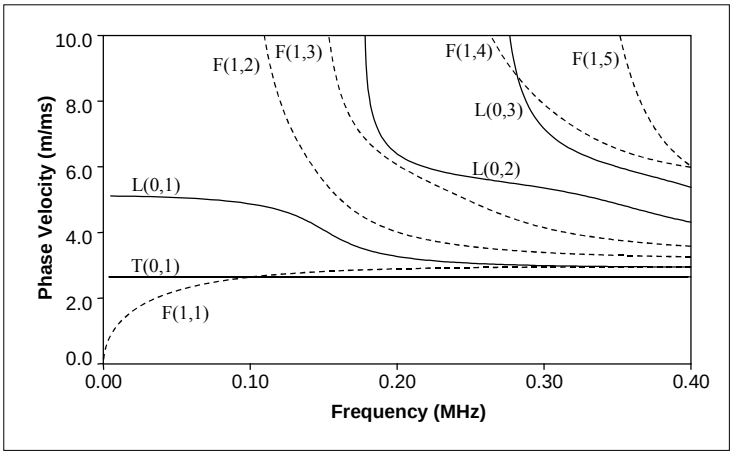

Figure 2.7: Phase velocity dispersion curves for a perfectly elastic, 20mm diameter steel bar in a vacuum.

Adding further finite layers around the steel bar, such as cladding, further complicates the waveguide, as energy can now be passed between the layers. In this case, a guided wave will still propagate in the structure as a whole, but with properties that depend on the elastic and damping properties of all the layers. Stress and displacement boundary conditions must be satisfied at the boundaries between layers. Generally, the level of interaction between two adjacent layers will be high if the bulk wave speed and density of the materials is similar, giving a low contrast in acoustic impedance between the layers. Attenuation through leakage can occur if the outermost layer may be considered infinite in extent. This important attenuation mechanism is discussed further in section 2.6.2.

The properties of guided waves are proportional to the dimensions of the structure, and can be expressed as a function of frequency-thickness. This means that a mode that exists in a 10mm

diameter bar at 1MHz, will also exist in identical form in a 20mm diameter bar at 0.5MHz etc. This also applies in multi-layer systems, although it is only of any use when all the layers are scaled by the same factor.

The remainder of this section discusses properties that are commonly used to describe guided wave behaviour. The properties of wavenumber, phase velocity and group velocity are introduced through the examination of the dispersion curves for a free, perfectly elastic bar. The properties of attenuation and energy velocity are introduced by extending this simple model to include an elastic embedding material, which introduces the possibility of leakage. The treatment is not intended to be complete, and further discussion is made in the relevant sections of chapter 3 on guided wave modelling. Good general references on guided waves are presented by Lowe [69] and by Alleyne [70] in their respective PhD theses, and also in [71].

2.6.1 Free Elastic Systems

This section examines the dispersion curves for a perfectly elastic, 20mm diameter steel bar in a vacuum, and defines the quantities of real wavenumber, phase velocity and group velocity.

Real Wavenumber

The tracing routines that are used by Disperse to search for solutions to the wave propagation problem in elastic systems operate in frequency-wavenumber space, or frequency-wavenumber-attenuation space in attenuative systems. The real wavenumber is simply inversely proportional to the wavelength of the guided wave, and is simply defined by equation 2.1, where ξ is the real wavenumber in radians per metre, and λ is the wavelength in metres.

$$\xi = \frac{2\pi}{\lambda} \tag{2.1}$$

Dispersion curves are often displayed as wavenumber plots in the literature. This solution space is also the one chosen by Disperse because it is the space in which the curves appear the most linear, and therefore the easiest to trace. However, the wavenumber plot does not contain much useful information for the application of guided waves to NDT; therefore other projections and derived data are also required.

Phase velocity

The phase velocity , v_{ph}, is calculated from the real wavenumber, ξ, by the relationship shown in equation 2.2, where ω is the circular frequency in radians/metre. Physically, the phase velocity is the speed at which the individual wave crests travel.

$$v_{ph} = \frac{\xi}{\omega} \tag{2.2}$$

The phase velocity dispersion curves for a 20mm steel bar in a vacuum have already been shown in figure 2.7. They show a number of propagating modes that can be categorised into two groups. The solid lines represent modes with an axially symmetric mode shape (longitudinal modes), and the dotted lines represent modes with a non-axially symmetric mode shape (flexural modes). An infinite number of modes exist at higher frequencies, but only the modes up to 0.4MHz are shown.

The modes are numbered according to the format used by Disperse, which closely follows that defined by Silk and Bainton [72]. Each mode is identified by the use of a letter and two reference numbers. The longitudinal modes are numbered in the series L(m,n) , and the flexural modes are numbered in the series F(m,n). The 'm' variable refers to the variation in displacement around the circumference of the bar. This variable is zero by definition for the axially-symmetric longitudinal modes. For the flexural modes the 'm' variable is determined by the number of displacement cycles around the outside of the bar, hence the displacement varies as cos(mθ) around the bar circumference. Only the first order flexural modes, numbered F(1,n), are plotted in figure 2.7. The second reference number 'n' is a counter variable, the modes being numbered sequentially as they appear with increasing frequency. The lowest frequency axially symmetric mode is therefore numbered L(0,1). A further mode exists at the shear bulk velocity of the steel, the fundamental torsional mode, numbered T(0,1). This is the only true torsional mode, as it exists with purely torsional characteristics at any frequency. Higher order modes that show torsional characteristics are also flexural in nature. Apart from T(0,1), all the other modes show some extensional and flexural characteristics at frequencies above zero, and therefore the use of the terms longitudinal and flexural to describe the other mode families is somewhat misleading. However, at zero frequency, the fundamental L(0,1) and F(1,1) modes do have purely extensional and bending characteristics respectively.

Group Velocity

The phase velocity tells us how fast the material particles are moving, but it does not tell us how fast the wave will propagate along a structure as a whole. In a perfectly elastic system, the group velocity is the rate of energy propagation along a structure, and is therefore the speed at which a guided wave packet will travel. The group velocity, v_{gr}, is defined by equation 2.3, where ω is the circular frequency and ξ is the real wavenumber in radians per metre.

$$v_{gr} = \frac{\partial \omega}{\partial \zeta} \tag{2.3}$$

The group velocity dispersion curves for the flexural and longitudinal modes in the same 20mm diameter steel bar are shown in figure 2.8. The group velocity curves show how dispersive a mode is, that is how much variation in velocity there is over a frequency range. This is

important, because any wave packet will contain energy over a range of frequencies, and all of these frequency components may travel at different speeds.

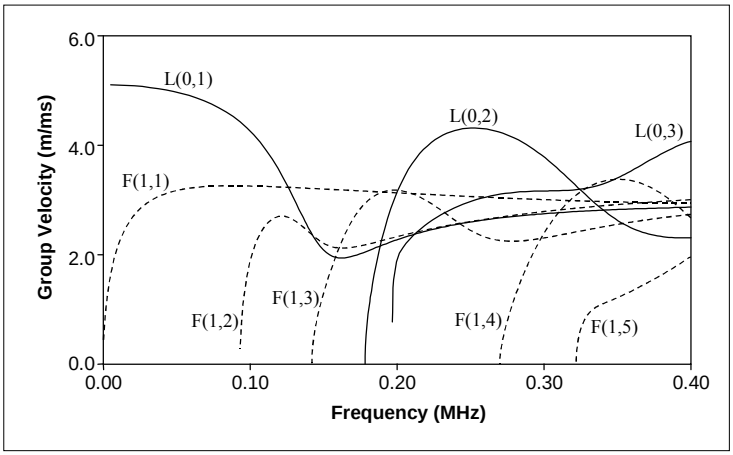

Figure 2.8: Group velocity dispersion curves for a perfectly elastic, 20mm diameter steel bar in a vacuum.

2.6.2 Leaky Elastic Systems

If a structure is embedded in a material and not in vacuum, energy is able to leak from the waveguide into the embedding material. In reality, this happens for simple cases such as a steel bar in air, but because the acoustic properties of the air and steel are so different, the amount of leakage is small. However, if the acoustic properties are more closely matched, as is the case for embedding the steel in another elastic solid, the leakage becomes very significant. The embedding material may alter all the other properties of the guided wave as well as introducing leakage. Energy can cross the boundary from the structure to the embedding material, but no energy will cross back from the embedding material to the structure. The leaked energy that crosses the boundary travels as a bulk wave in the embedding material, resulting in attenuation of the guided wave contained within the structure. Two additional properties that are useful to describe the behaviour of leaky waves are attenuation and energy velocity.

Attenuation

The introduction to this section has introduced the concept of wave attenuation through leakage into an embedding material. There is also another mechanism of attenuation, due to damping inherent in the waveguide material. This effect occurs because real materials are not perfectly elastic, and some attenuation of sound waves occurs because of viscoelastic losses. This effect will occur in a bulk wave and a guided wave, and can be calculated if the damping properties of the material are known. The standard model of damping used by Disperse assumes a constant attenuation per wavelength, which in a bulk wave means that attenuation generally increases

with frequency. Although this effect has some influence on guided waves, the frequency-attenuation relationship of guided waves is much more complex and is controlled by many other factors, including leakage.

The attenuation dispersion curves for a perfectly elastic 20mm diameter steel bar, embedded in a perfectly elastic rock with a Young's modulus of 12GPa are shown in figure 2.9. The attenuation is expressed in dB/m, therefore showing the decrease in the amplitude of a guided wave that would occur over any given propagation distance. In this perfectly elastic case, the attenuation is purely due to leakage, and would be higher if material damping was included in the model.

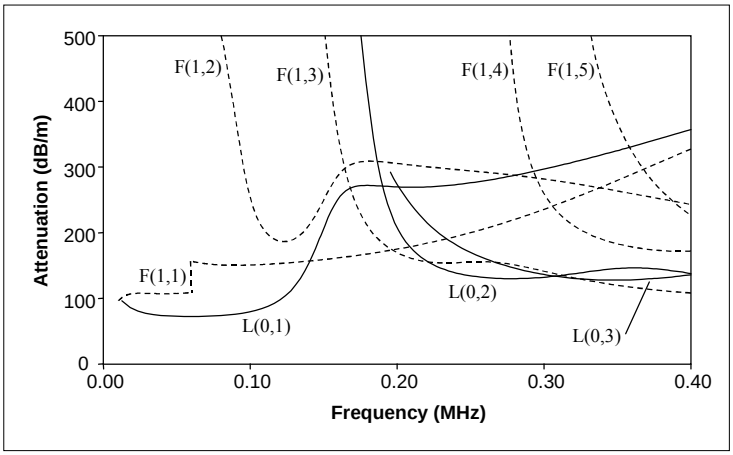

Figure 2.9: Attenuation dispersion curves for a perfectly elastic, 20mm diameter steel bar embedded in rock with a Young's Modulus of 12GPa.

Energy Velocity

The group velocity calculation is not valid for waves which are attenuating [73]. The speed at which a wave packet will propagate along a structure is known as the energy velocity, and can be obtained from data derived from the mode shapes (stress and displacement fields). The energy velocity is defined as the ratio of the power flowing along the structure to the strain energy stored in the structure as it passes. In cases such as the perfectly elastic steel bar in a vacuum, the energy velocity is equal to the group velocity. However, in leaky or attenuative systems there are differences between the group and energy velocities. The energy velocity dispersion curves for a perfectly elastic, 20mm diameter steel bar embedded in rock are shown in figure 2.10.

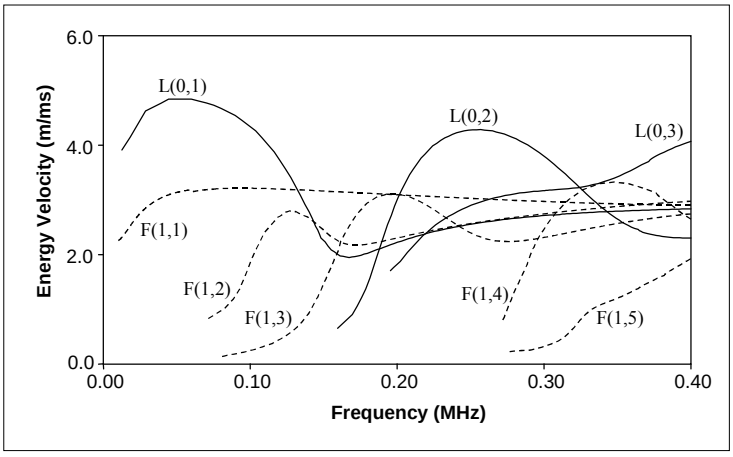

Figure 2.10: Energy velocity dispersion curves for a perfectly elastic, 20mm diameter steel bar embedded in rock with a Young's Modulus of 12GPa.

2.7 Project Collaborators

The research presented in this thesis was completed with the help of two industrial collaborators, and funded by the EPSRC [74]. The bridge tendon inspection work was assisted by the Transport Research Laboratory Ltd. (TRL) [75], who provided test specimens and background information for the project. The rock bolt inspection work was assisted by Rock Mechanics Technology Ltd. (RMT) [76], who provided specimens and access to the test site at Middleton. The work on rock bolt testing follows an initial feasibility study that was completed by Pavlakovic for RMT [77], who were working on a similar project funded by the HSE. The findings of RMT have been published in a report to the HSE [78], which includes details on practical testing results, the suitability of existing commercially-available instrumentation for bolt testing, and the development of a device to prepare bolt ends.

2.8 Conclusions

This chapter has shown that there is a need for the development of inspection techniques for both embedded rock bolts and grouted tendons. In the tendon case, it is desirable to be able to detect defects and breaks, and in the rock bolt case, it is desirable to be able to detect defects, and the bolt end. In both cases access is limited, and can only be achieved from the exposed end. It is proposed that an ultrasonic pulse-echo inspection method offers the potential to inspect these structures using guided waves, and that the work of previous authors can be built on to define a commercially viable inspection method. The various quantities that are used to describe wave behaviour have been introduced as a basis for the following chapter, which investigates the dispersion relationships of the rock bolt system in detail.

CHAPTER 3

MODELLING GUIDED WAVES IN AN EMBEDDED ROCK BOLT

3.1 Introduction

The previous chapter has outlined the historical development of guided wave understanding, and the various properties that are used to describe wave behaviour. Knowledge of these properties is necessary to identify modes that are suitable for testing a given system, and to interpret the often complex signals that can result from the excitation of multiple modes or the effects of dispersion. This chapter further examines the dispersion relationships for guided waves in cylindrical systems, and builds on the case of a free bar to describe wave behaviour in a simple embedded system, and then a multi-layer system that represents an embedded rock bolt. The modelling work presented in this chapter is compared directly with rock bolt site testing results in Chapter 4, and therefore uses a specific bar diameter of 21.7mm, rather than the more usual normalised dimensions. However, many of the principles discussed are general, and are also applied to the post-tensioning tendons discussed in chapter 5 of this thesis.

Conclusions are drawn about modes that could form the basis of a practical inspection technique, and at which frequencies these modes could be used. The effect of variation in material properties on the velocities and attenuation of these guided waves has then been examined, as significant variation in material properties is expected between sites, and possibly along the length of each individual bolt. For convenience, examination of the modes is split into the ‘low frequency’ fundamental modes, and ‘high frequency’, higher order modes. Particular attention is given to the high frequency modes that have a low attenuation due to leakage, as these offer the maximum potential test range. As a result, only the axially symmetric, ‘longitudinal’ family of modes has been considered in detail, as the ‘flexural’ modes are generally slower and more leaky, making them unattractive for long range inspection.

3.2 Modelling

This section examines the approach and methods used to model guided waves in an embedded rock bolt. The results of the modelling are presented separately for the low and high frequency modes in sections 3.3 and 3.4.

3.2.1 Calculation of Dispersion Relationships

All of the results presented in this chapter have been obtained using specialist software that calculates the dispersion curves for single or multi-layer, free or embedded systems [7,68]. The software uses the global matrix method [67] to avoid the problems of high frequency-thickness products associated with the Thomson-Haskell transfer function technique. Calculation can be performed in Cartesian or cylindrical co-ordinates, which allows both two dimensional plate models and axially symmetric bar models to be constructed. Embedding is modelled by an outer layer that is infinite in extent. Models are defined layer by layer and can include material damping and anisotropic material properties.

It is not possible to model three dimensional features such as the rock bolt threads and mixing ribs. However, the practical testing results presented in chapter 4 show that accurate predictions can be made if the rock bolt is modelled as a smooth bar. It is also not possible to model reflections from defects or from features such as the angled rock bolt end. Various authors have used finite element modelling for such predictions, but the technique is limited by model size at high frequency-thickness products. The effect of these features has been investigated experimentally, and is discussed further in chapters 4 and 5 of this thesis.

3.2.2 Model Construction

The following sections investigate the rock bolt modes using a variety of different models, starting with the simple case of a free steel bar in a vacuum. A simple embedded system is then examined by adding an outer embedding layer. The rock bolt model includes both an embedding layer and an epoxy layer. Figure 3.1 shows this model, which is a two-dimensional, axially symmetric representation of a real rock bolt. The inner steel core has a radius of 10.85mm, corresponding to the 21.7mm diameter of the real bolt. Limestone has been taken as a representative embedding material, and the epoxy thickness has been taken to be 4mm, which is an average thickness based on the tolerance of the installation hole. The effect of material, bond and geometric properties has been evaluated around this standard model, which is referred to throughout this thesis as the ‘basic rock bolt model’.

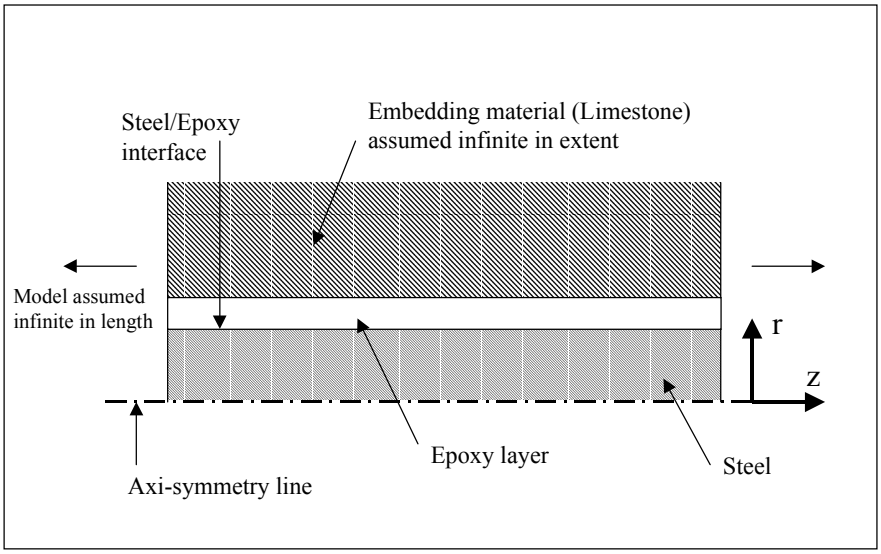

Figure 3.1: Geometry of the basic rock bolt model, which includes an epoxy layer and an outer embedding layer around a central steel core.

3.2.3 Range of Material Properties

The material properties used to define all the rock bolt models are given in table 3.1. The steel rock bolt has been modelled using the acoustic properties of a steel with a relatively low modulus, and the modulus of the actual steels used may be slightly higher. The error associated with this is small, primarily because the maximum difference in modulus is in any case small, and also because the modulus of the steel is very high compared to the other materials. There is a limited effect on the test frequencies predicted for the high frequency modes, this is examined further in section 3.4.8.

Epoxy properties have been taken from standard literature [79], and also from measurements made in the laboratory by RMT [76]. The actual epoxy used for the test specimens was 'Celtite AT for roof bolts', manufactured by Exchem Mining and Construction [80].

The elastic properties of rock are highly variable between rock types and locations. Limestone has been chosen for the basic studies, because most of the development testing has been undertaken in a limestone mine. This is a worst-case assumption, as coal mines are generally found in areas with a lower rock modulus where the leakage of ultrasound is likely to be less. The properties of limestone are taken from values supplied by the mining consultancy company, RMT [76], and are based on samples from Middleton Mine, where the specimen rock bolts were installed. In order to investigate the effects of different rock types, a generic material 'rock' has been defined, based on limestone, but with an elastic modulus in the range 10-60GPa.

Material attenuation values are extremely difficult to measure, particularly in highly attenuative materials such as epoxy and rock, and the values shown are estimates. However, the overall attenuation of the guided wave is dominated by leakage at low frequency, which is not affected by material damping properties [6]. At high frequencies material damping does contribute significantly to the overall attenuation, but since the ultrasonic energy is shown to travel mainly in the steel bar at high frequency, only the steel damping values are important.

Property/Material	Steel	Limestone	Rock	Concrete	Epoxy
Modulus, E (GPa)	207.0	40.0	10.0-60.0	30.0	14.0
Density, ρ (kg/m^3)	7900	2500	2500	2200	2000
Long. Attn. (np/wl)	0.003	0.03	0.03	0.2	0.03
Shear Attn. (np/wl)	0.01	0.1	0.1	0.5	0.1
Long. Vel (m/s)	5845	4360	2190-5370	4100	3070
Shear Vel (m/s)	3180	2520	1265-3100	2300	1640
Poisson Ratio, ν	0.29	0.25	0.25	0.27	0.30

Table 3.1: Material properties used to model an embedded rock bolt.

3.2.4 Contact Conditions

The amount of leakage that takes place into the embedding material is likely to be affected by the quality of the bond between the materials. In the case of the post-tensioning tendons, the contact conditions are likely to be generally good, as the grout is pumped into the ducts under controlled conditions. However, in the rock bolt case, the method of installation means that the bond line can easily become contaminated with water, debris from the drilling process and plastic from the resin capsules. In addition the completeness of the mixing process is not guaranteed, and it is possible that some areas of resin are improperly mixed and therefore have degraded properties. All these factors combine to reduce the strength of the bond. The effect of these factors on the overall strength of the bond is usually not a problem, as the mixing ribs mechanically interlock with the set resin, but the effect on the propagation of ultrasound may be much more marked, and needs to be investigated.

A simple method of modelling the variation in bond quality is to insert an additional interfacial stiffness layer between the two surfaces where bond quality is to be modelled. This layer has no thickness, but a fixed stiffness that represents the bond. Other authors have used simple spring models to simulate poor bonding between surfaces [81-85], and Disperse can be used to incorporate such layers into the model geometry.

To interpret the results from the model, it is necessary to define how the bond quality relates to the spring constants used to define the interfacial stiffness layer. Different authors have used

different methods of relating bond quality to stiffness, and there is no standard approach. In the case of a rock bolt, the bolt/epoxy bond has been identified as being the most likely to be degraded, and the method of defining the spring constants has been based on the stiffness of the epoxy layer. The ratio R has been defined as the ratio of the combined epoxy and interfacial layer stiffness to the stiffness of the original epoxy layer. The stiffness of the epoxy layer can be defined by three spring constants, as shown by figure 3.2a. The interfacial stiffness springs act in series with these springs, as shown by figure 3.2b. The ratio R can be expressed as a percentage, so that a 100% bond occurs when the original epoxy layer stiffness and combined epoxy layer and interfacial stiffness are the same, i.e. when the interfacial stiffness is infinite. A 0% bond occurs when the interfacial stiffness is zero, and the epoxy is effectively disconnected from the steel. It should be noted that in using this system, the epoxy layer is not replaced by springs in the Disperse model, and the equivalent stiffness of this layer is only used to define the bond quality. The following analysis in equations 3.1-3.4 shows how the interfacial boundary stiffness values are calculated for a given bond quality.

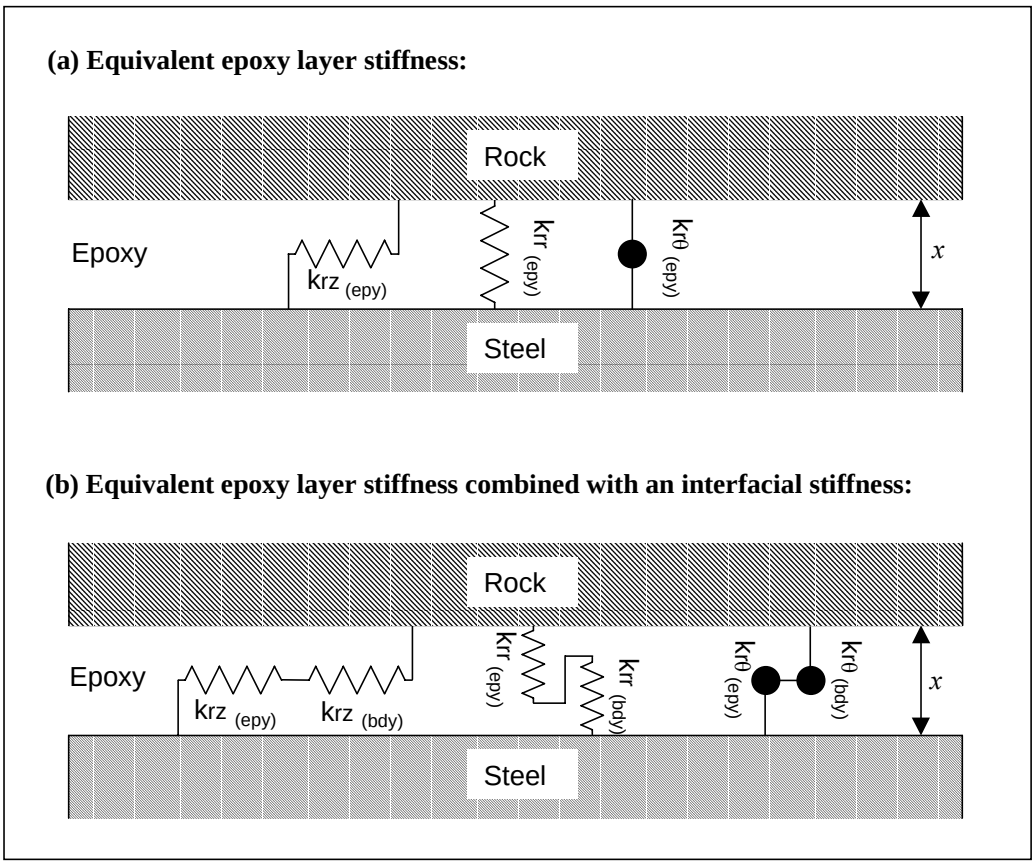

Figure 3.2: Spring models used to model poor bolt/epoxy bonding showing (a) how springs (subscript 'epy') can be used to represent the stiffness of the epoxy layer in the basic rock bolt model and (b) how additional boundary springs (subscript 'bdy') can be used to model the effect of poor bonding between the rock bolt and epoxy layers.

The equivalent stiffness of the epoxy layer in each direction is defined by equations 3.1, where the epoxy layer has bulk plane strain modulus 'E_{bulk}', shear modulus 'G' and thickness '*x*', and the spring constants are per unit surface area of the interface:

$$k_{rr} = \frac{E_{bulk}}{x}, \qquad k_{r\theta} = \frac{G}{x}, \qquad k_{rz} = \frac{G}{x} \tag{3.1}$$

If bonding is imperfect, then each of these epoxy equivalent springs (subscript 'epy') can be considered to act in series with an interfacial boundary spring (subscript 'bdy') as shown in figure 3.2b, so that for each of the three directions:

$$k_{total} = \frac{k_{epy} \cdot k_{bdy}}{k_{exy} + k_{bdy}} \tag{3.2}$$

This expression can be simplified by introducing the ratio 'R' of the combined epoxy layer and interfacial boundary stiffness to the stiffness of just the epoxy layer, as defined by equation 3.3.

$$R = \frac{k_{total}}{k_{epy}} \tag{3.3}$$

The ratio 'R' can be expressed as a percentage, and represents the quality of the bond. Equations 3.3 and 3.4 can then be combined and rearranged to give an expression for the stiffness of the interfacial boundary spring that is necessary to use to model a given bond quality:

$$k_{bdy} = \frac{R \cdot k_{epy}}{1 - R} \tag{3.4}$$

This expression can be used to specify the interfacial boundary stiffness in the two shear (*rz*, *rθ*) and one longitudinal (*rr*) directions for any given 'R'. These values are dependent on the original stiffness of the epoxy layer, and will therefore change with epoxy layer thickness. This definition of bond quality is used in sections 3.3.7 and 3.4.7 to investigate the effect of poor bonding on guided wave propagation.

3.2.5 Validation of Spring Layer Calculations

It was necessary to carry out some validation of the spring layer models, to demonstrate that the spring layer calculation was functioning correctly within Disperse, and to verify that the correct values of spring stiffness had been used within the model.

To verify that the spring layer was functioning correctly within Disperse, the epoxy layer of the basic rock bolt model was replaced directly with a spring layer of equivalent stiffness, calculated using equations 3.1. The maximum stress and displacement at either side of the spring layer was calculated in the normal direction, and one of the two shear directions. This calculation was made at a point on both a symmetric and an asymmetric mode, in both Cartesian and cylindrical geometry. If the spring layer is functioning correctly, the stress at either side of

each spring should be equal, and this stress divided by the difference in displacement at either end of the spring should be equal to the spring constant defined in that direction. Table 3.2 shows the stresses and displacements calculated by the model, and the resulting equivalent spring stiffness values, which agree exactly with those calculated from equations 3.1 and input into the model. This shows that the implementation of the spring layer in Disperse is correct. For completeness, the practicalities of this calculation are also included here for future reference. Disperse does not offer detailed information for layers that do not have finite thickness (such as spring layers), although some information can be extracted from the finite layers. The stress and displacement at either side of the spring layer was taken from the neighbouring points in the rock and steel layers, this is possible because the stresses and displacements are continuous across these boundaries. In addition, because the embedding rock layer is semi-infinite, an additional finite layer of rock was inserted between the epoxy and the semi-infinite rock layer. This does not change the overall geometry of the model, but allows disperse to calculate stress and displacements in a finite layer at the spring/rock boundary. The magnitude of the maximum stress and displacement was extracted from the calculated complex values.

Geometry/Calculation		**Spring layer calculated values**		
		Displacement magnitude (m)	Stress magnitude (N/m^2)	Equivalent stiffness per unit area of interface $(N/m)/m^2$
Cartesian S0, 80kHz	Normal:	u_x=4.118e-09	σ_{xx}=7745	k_{xx}=1.88e+13
	Shear:	u_z=9.216e-10	σ_{xz}=4957	k_{xz}=5.38e+12
Cylindrical L(0,1), 50kHz	Normal:	u_r=1.244e-09	σ_{rr}=23447	k_{rr}=1.88e+13
	Shear:	u_z=1.140e-08	σ_{rz}=61389	k_{rz}=5.38e+12

Table 3.2: Calculated stress and displacement at either side of a spring layer in Cartesian and cylindrical geometry, used to validate the spring layer implementation in Disperse.

To verify that the correct spring values had been used to represent the epoxy layer, the attenuation predictions of the basic rock bolt model were compared with the attenuation of the same model with the epoxy layer replaced by an equivalent spring layer. However, since the spring layer model has no mass in the equivalent epoxy layer, the density of the epoxy in the basic rock bolt model was set to be very low ($1.0e^{-5} kg/m^3$) to approximate the spring case as closely as possible. The original values of Young's Modulus and Poisson's Ratio were maintained, therefore the longitudinal and shear velocity in the low-density epoxy layer and the spring layer would be very high, allowing a direct comparison to be made. The attenuation dispersion curves, shown in figure 3.3, were chosen for the comparison because the attenuation

curves are very sensitive to differences in the relative shear and longitudinal layer stiffness. In addition, the change in attenuation with bond quality has important practical implications.

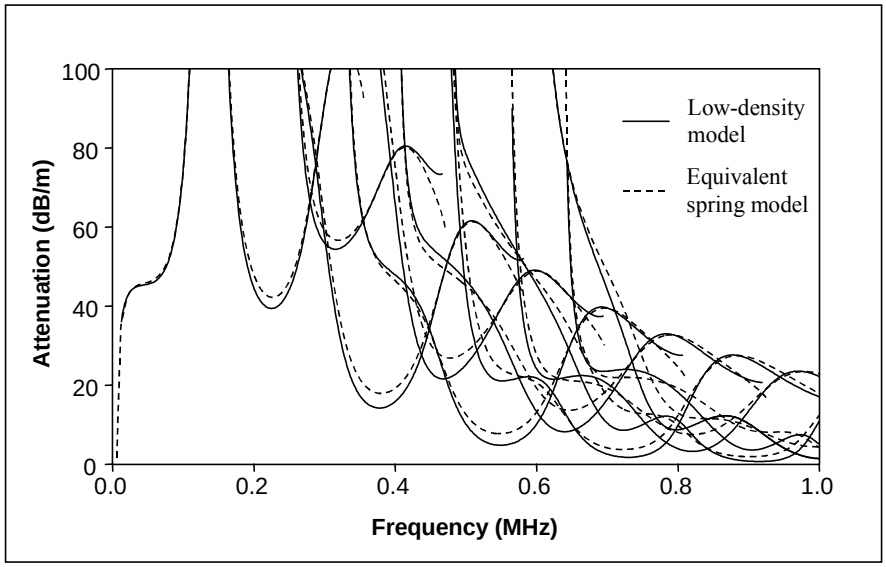

Figure 3.3: Comparison of the attenuation dispersion curves predicted by the basic rock bolt model with a very low density epoxy, and a similar model with the epoxy layer replaced by an equivalent spring layer.

The curves predicted by the two models match very well, indicating that the spring values used in the model are correct. The S0 mode matches very well, because the wavelength is long at low frequency, and the epoxy layer behaves as a spring boundary anyway. At higher frequencies, the attenuation is slightly overestimated by the spring model, this is probably caused by the fact that the spring layer has zero thickness, whereas the epoxy layer has a finite thickness of 4mm. It is likely that the reduced thickness results in better acoustic coupling to the embedding material and therefore higher leakage. This effect is only significant at high frequencies, where the wavelength is about the same, or smaller than, the thickness of the epoxy layer. The fact that the overestimation is relatively constant for all the modes confirms that the ratio of shear to normal stiffness is correct, as some modes are affected more by the shear coupling than others. The validation cases outlined in this section confirm that the interfacial layers used in the modelling work presented in this thesis are correctly implemented within Disperse, and that the method of calculating the equivalent stiffness of the epoxy layer that has been used is correct.

3.3 Low Frequency Modes

The following sections 3.3.1-3.3.8 examine in detail the low frequency modes in cylindrical systems, starting with the case of a free bar in a vacuum, and moving on to embedded cases, including that of the basic rock bolt model. The sensitivity of the basic rock bolt model to changes in geometry and material properties is then investigated.

3.3.1 Free Bar

The dispersion curves for a steel bar in a vacuum are well known, and are a good starting point from which to examine guided waves in an embedded rock bolt. This is commonly referred to as the 'free' bar case, and is the simplest cylindrical model that can be constructed. The phase velocity and group velocity dispersion curves for a 21.7mm steel bar in a vacuum are shown in figure 3.2. This case is representative of a standard diameter rock bolt without any embedding material. Each line represents a propagating mode, with velocities that vary with frequency. No attenuation dispersion curves have been shown, because although the bar has been modelled with material damping, the resulting attenuation per metre is small because of the long wavelength at low frequency.

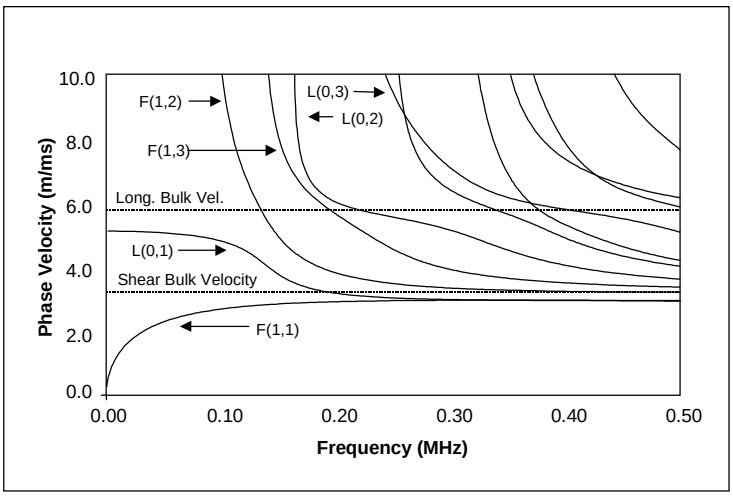

(a) Phase velocity.

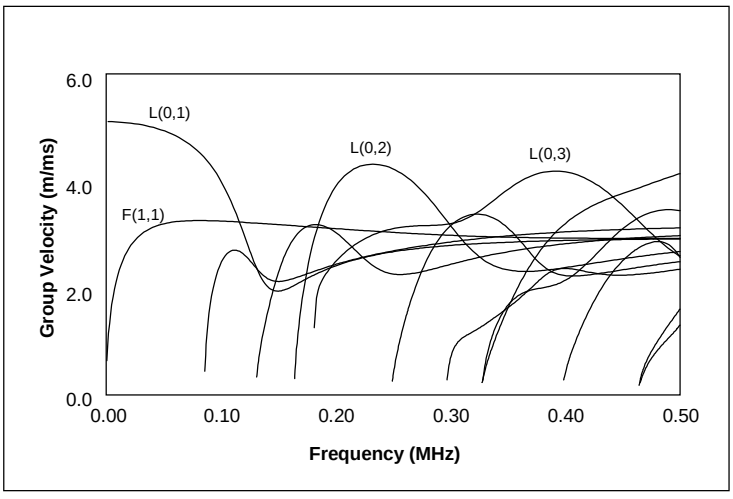

(b) Group velocity.

Figure 3.4: Phase and group velocity dispersion curves for a 21.7mm diameter steel bar in a vacuum.

At very low frequency, below about 100kHz, the phase velocity dispersion curves (figure 3.4a) show that only the fundamental modes can exist. The fundamental axially symmetric 'longitudinal' mode L(0,1), propagates with phase velocity equal to the bar velocity at near zero frequency, and tends to the Rayleigh velocity as the frequency is increased, behaving as a Rayleigh surface wave. At zero frequency, the L(0,1) mode shape is purely extensional, with only axial motion along the bar. As the frequency increases, radial motion becomes more significant and the mode shape becomes more complex, although always axially symmetric. The fundamental non-axially symmetric mode F(1,1) has zero phase velocity at zero frequency and behaves as a purely flexural mode, with only radial motion. As the frequency is increased, the F(1,1) mode shape also becomes more complex, with both axial and radial motion, and it also becomes a Rayleigh surface wave at high frequency. The F(1,1) mode shape is always non-axially symmetric, even at high frequencies where the Rayleigh waves on the top and bottom surfaces of the cylinder will be 180 degrees out of phase, with zero motion at the sides. A third fundamental mode, the purely torsional T(0,1) mode exists with a phase velocity that appears as a horizontal line at the bulk shear velocity of the steel. The global matrix method has difficulty calculating modes in the region of bulk velocities, and this mode is not shown. The T(0,1) mode is not considered in this thesis, as it has been found to be unsuitable for rock bolt testing.

The fundamental L(0,1) and F(1,1) modes are the lowest order modes in families of modes that are axially symmetric and non-axially symmetric in nature. Higher order modes first appear with infinite phase velocity at a cut-off frequency, which is a frequency at which a standing wave exists across the bar diameter. Successive modes have increasing numbers of displacement cycles in the standing wave. The higher order mode shapes are more complex, with an increasing number of displacement peaks through the cross section. The first few higher order modes of each type can be seen in figure 3.4b, but are discussed in detail in section 3.4.

The fundamental modes are an obvious choice for ultrasonic testing, because the simplicity of the dispersion curves in this region makes it easy to excite a single mode. This prevents interference between modes and simplifies data analysis, which can be complex if multiple modes are propagating in a system. The longitudinal mode is the easiest to use, as its axially symmetric shape allows excitation from the bolt end with a single compression transducer. The fundamental mode shapes can be seen in figure 3.5, which shows the axial and radial displacement for the L(0,1) and F(1,1) modes at 50kHz. The F(1,1) mode has one cycle of harmonic variation around the circumference of the bar (as denoted by the first '1' in the mode name). There is no variation around the circumference for the L(0,1) mode.

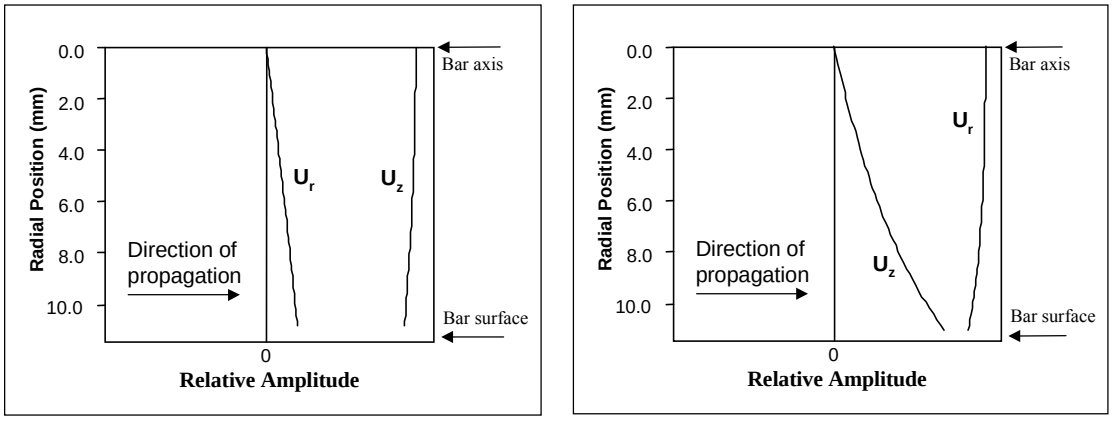

(a) L(0,1) Mode shape at 50kHz. (b) F(1,1) Mode shape at 50kHz.

Figure 3.5: Mode shapes of the fundamental flexural and longitudinal modes in a free bar at 50kHz, showing the axial (u_z) and radial (u_r) displacement components.

It is also important to test at a frequency where the effects of dispersion are minimal. Dispersion causes the different frequency components of a wave packet to travel at different speeds, which distorts the shape of the signal as it propagates, making accurate interpretation difficult. In general the points of minimum dispersion will be at points of maximum or minimum group velocity. The group velocity dispersion curves (figure 3.4b) show that the L(0,1) mode has a large non-dispersive region at very low frequency. An advantage of using a mode at a maximum group velocity point is that it will usually be the first part of the signal to arrive at the receiver, which can simplify interpretation.

3.3.2 Embedded Bar

Embedding the bar introduces the possibility of energy leakage from the bar into the embedding material, which causes attenuation of the wave modes. Ideally, the existence of a non-leaky mode would allow large propagation distances with little signal attenuation. Unfortunately, previous research [6] has shown the existence of a non-leaky mode in certain circumstances in embedded plates, but not in the cylindrical case. This section examines the dispersion curves for a bar embedded in an infinite expanse of rock, and highlights the differences that occur from the free case as a result of the embedding material. The basic rock bolt model, which includes the epoxy layer is examined in section 3.3.3. The predicted phase velocity, group velocity, energy velocity and attenuation dispersion relationships are shown in figure 3.6.

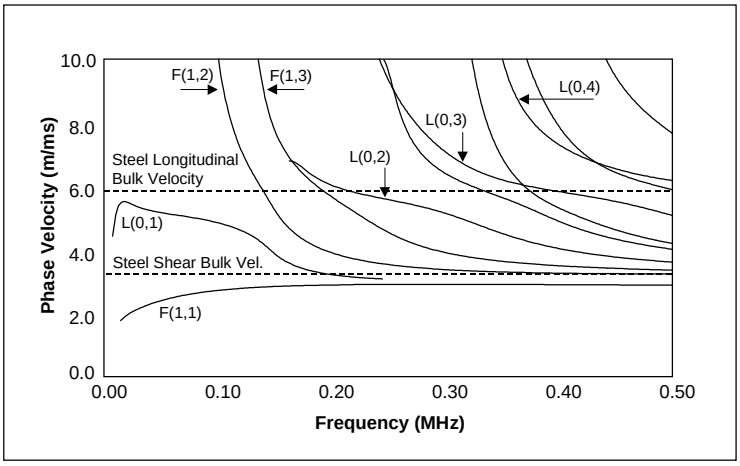

(a) Phase velocity.

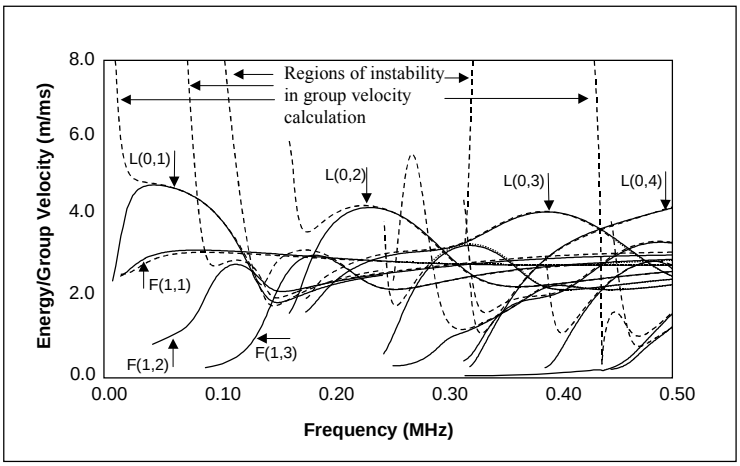

(b) Energy velocity (solid lines) and group velocity (dashed lines).

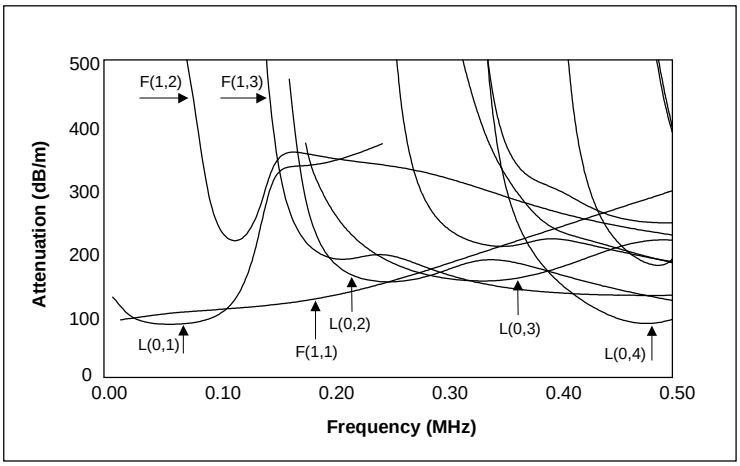

(c) Attenuation.

Figure 3.6: Dispersion curves for a 21.7mm diameter steel bar embedded directly in rock with a Young's Modulus of 20GPa.

The general form of the phase velocity dispersion curves for embedded case is unchanged from the free case discussed previously. The main difference is that the L(0,1) mode no longer exists at the bar velocity at zero frequency, but shows a peak in phase velocity before tending to zero at zero frequency. This phenomenon was first noticed by Nayfeh and Nagy [86]. The exact shape of the peak depends on the modulus of the embedding material and is discussed further in section 3.3.4. Higher order modes can also follow this trend, depending on the embedding material. Often the modes are highly attenuative in such regions, and are difficult to trace with the Disperse software - the L(0,2) mode has not been traced below about 170kHz in figure 3.6a.

The standard group velocity calculation can yield infinite solutions from complex wavenumbers such as those found in attenuating waves [73]. Figure 3.6b shows this as instabilities in the calculated dispersion curves, with the group velocity in some regions tending to infinity. The energy velocity is a more accurate measure of the wave packet speed, and is shown on the same plot. The energy velocity peaks at the same frequencies as the group velocity in the free case, indicating similar non-dispersive regions. The group and energy velocity dispersion curves are identical for a free, perfectly elastic material. However, as attenuation increases, the energy velocity is generally lower than the group velocity. The attenuation dispersion curves show that the L(0,1) mode has a point of minimum attenuation at the point of maximum energy velocity, making this mode attractive for long range inspection.

3.3.3 Resin Bonded Bar Embedded in Limestone

The basic embedded model can be refined further to include the epoxy layer that bonds the rock to the bolt. As outlined in section 3.2.2, the resulting basic rock bolt model is therefore a three-layer axially symmetric model, consisting of a central steel bar, diameter 21.7mm, surrounded by a 4mm layer of epoxy and an infinite expanse of rock. Limestone has been chosen as the embedding rock, to enable the predictions to be compared directly with site testing results. The dispersion curves predicted by this model are given in figure 3.7.

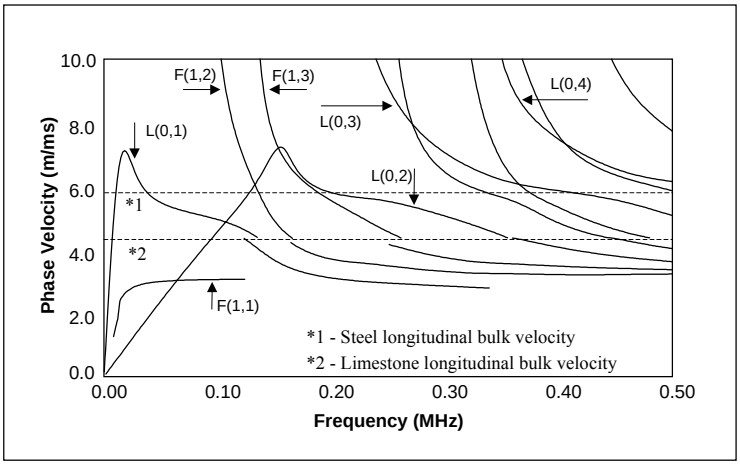

(a) Phase velocity.

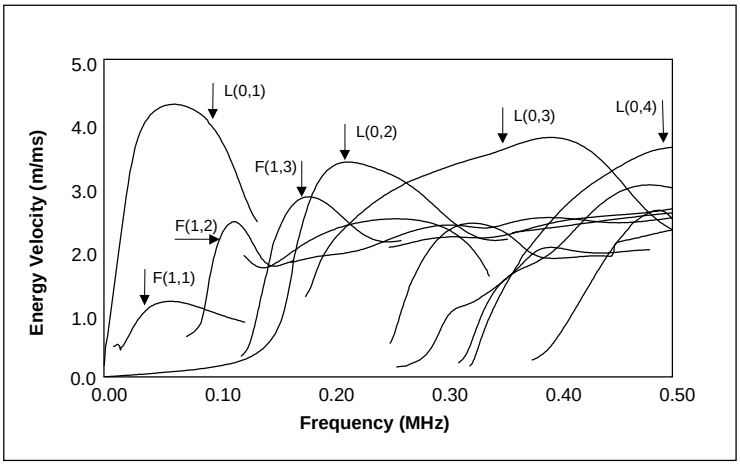

(b) Energy velocity.

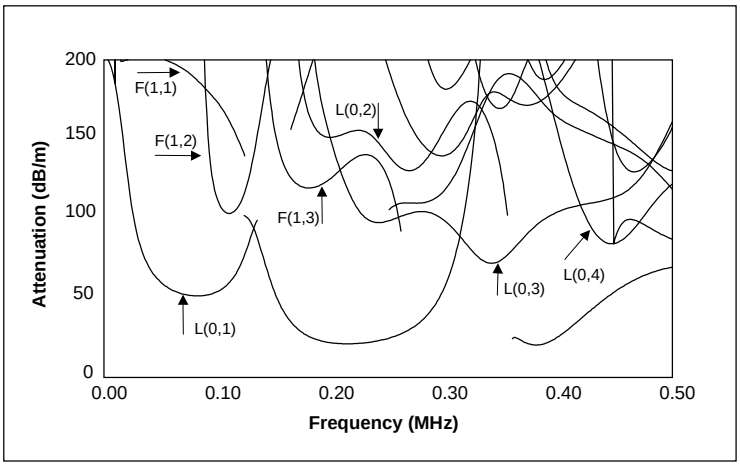

(c) Attenuation.

Figure 3.7: Dispersion curves for the basic rock bolt model, consisting of a 21.7mm steel bar, surrounded by a 4mm thick epoxy layer and embedded in limestone.

Comparison of figures 3.6 and 3.7 show that the dispersion curves for the basic rock bolt model are unchanged except in detail from the simplified case of a bar embedded only in rock. The epoxy layer has little effect at low frequency, because it is thin compared to the wavelength of the ultrasound (typical wavelength at 50kHz is 0.1m). The L(0,1) mode is by far the fastest mode, and at the velocity maximum has a predicted attenuation of around 50dB/m at 60-70kHz. The attenuation is largely due to leakage, as material damping effects are small at these frequency-thickness products. The attenuation curves show that the L(0,1) mode has another, lower attenuation minimum at higher frequency, but the energy velocity is low, and the mode shape is impractical for testing.

The predicted attenuation of the L(0,1) mode would limit the maximum inspection range to about 1m, as only around 100dB of amplification can be incorporated into the test equipment. However, in practice, longer propagation distances have been achieved, indicating that the actual attenuation is lower than the 50dB/m predicted by basic model. In addition, the preliminary experimental work found that the clearest results were obtained between 20kHz and 50kHz, which suggests that the actual attenuation minimum may occur below the 70kHz predicted by the basic model. The variation between the model predictions and experimental results can be explained by examining the sensitivity of the basic rock bolt model to changes in material properties and geometry, in the light of the likely specimen conditions. The effect of epoxy modulus, epoxy thickness, rock modulus and bond quality on the model predictions has been examined in the following sections, to enable better interpretation of the test results. This study also allows the effect of different rock types and epoxy conditions to be assessed, so that the test can be used at different sites with confidence.

3.3.4 Effect of the Embedding Material Modulus

The effect of the rock modulus on the predictions of the rock bolt model is important, because the modulus of the rock may vary considerably between test sites, and possibly locally within a mine. It is desirable to use a test that is affected as little as possible by the rock type. The effect of the rock modulus has been assessed by varying the modulus of the rock in the basic rock bolt model between 10GPa and 50GPa. Figure 3.8 shows the phase velocity, attenuation and energy velocity dispersion curves for the L(0,1) mode in a rock bolt embedded in different modulus rocks.

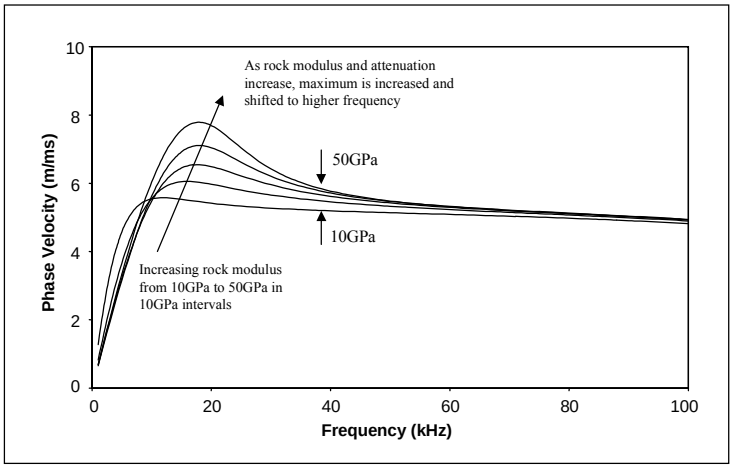

(a) Phase velocity.

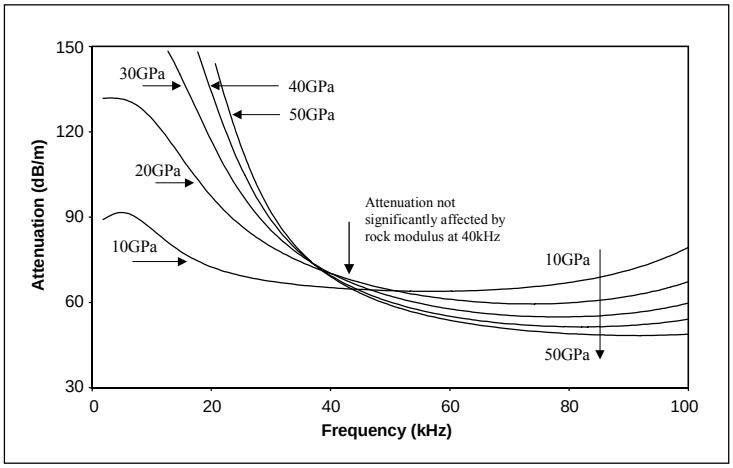

(b) Attenuation.

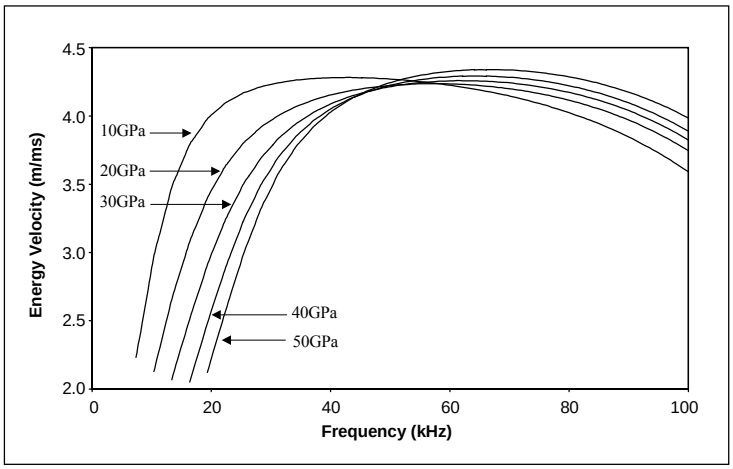

(c) Energy velocity.

Figure 3.8: Changes in the dispersion of the L(0,1) mode when the rock modulus of the basic rock bolt model is varied between 10GPa and 50GPa.

Figure 3.8a shows that the peak in phase velocity that occurs in embedded systems is shifted to a higher frequency, and to a higher maximum velocity as the rock modulus is increased. The shift in the phase velocity peak is related to the increase in attenuation. In the free case, with zero attenuation, there is no peak in phase velocity, and the L(0,1) mode is almost non-dispersive in the frequency range 0-40kHz.

The increase in attenuation that occurs with an increase in rock modulus below 40kHz can be explained by considering the contrast of acoustic impedance between the steel and the rock layers. At these low frequencies, the L(0,1) mode behaves as a simple compression wave, with a wavelength much longer than the epoxy layer thickness. Hence the epoxy layer acts much like an interfacial stiffness, and the leakage is controlled by the difference in elastic properties between the steel and the rock. Higher modulus rocks are better matched to the acoustic properties of the steel, and therefore more energy passes across the boundary, increasing the attenuation due to leakage. The effect of the contrast in acoustic impedance has been reported by Lowe [87], and can be illustrated by examining the predicted attenuation of the L(0,1) mode for the simplified case of a steel bar embedded only in rock, with no epoxy layer. Figure 3.9 shows the attenuation predicted by such a model, and the attenuation is consistently higher for higher modulus rocks.

However, the predicted attenuation does not increase with rock modulus for the whole frequency range shown in figure 3.8 for the basic rock bolt model. Above 40kHz, the mode shape is no longer a simple compression wave, which complicates the effect of acoustic impedance. In addition, as the frequency increases and therefore the wavelength decreases, the epoxy layer becomes more significant. The epoxy layer has a lower modulus than both the rock and the steel, and therefore the overall acoustic coupling is a combination of the rock/epoxy and bolt/epoxy interfaces. These factors produce the complex pattern seen in figure 3.8, where above 40kHz the trend seen at very low frequency is reversed. However, at 40kHz, the attenuation predictions are largely unaffected by rock modulus, and for this reason 40kHz would be an ideal test frequency. In fact, the variation in predicted attenuation between 30kHz and 60kHz is small, and it is likely that any frequency in this range could be used successfully in any rock type.

The link between the energy velocity and attenuation described in section 3.3.2 is illustrated by the fact that the points on the dispersion curves with lower attenuation have a high energy velocity, and that energy velocity generally decreases with increasing attenuation.

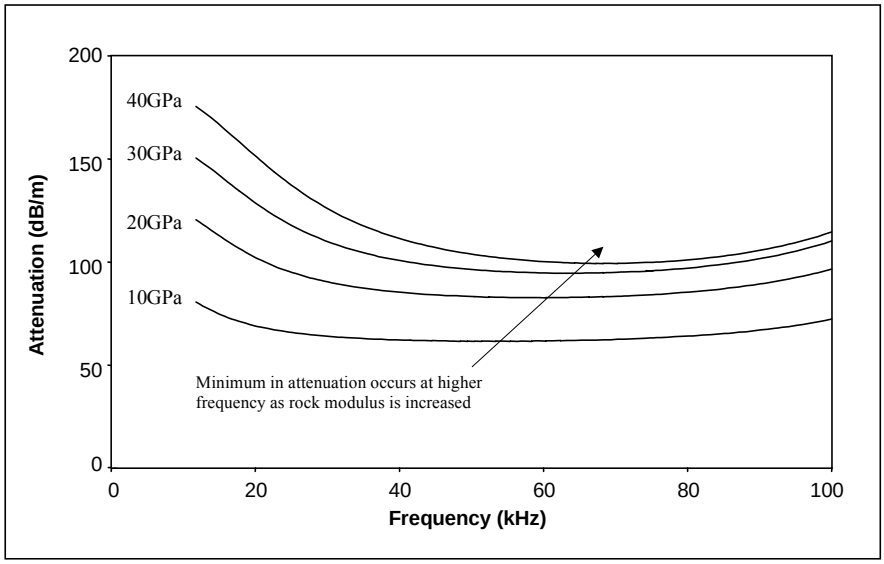

Figure 3.9: Changes in the attenuation dispersion of the L(0,1) mode with varying rock modulus, for the simple case of a steel bar embedded only in rock.

3.3.5 Effect of the Epoxy Layer Modulus

The basic rock bolt model uses a value of 14GPa for the epoxy layer modulus, which was obtained from laboratory measurements made by RMT, and data quoted by the manufacturer. This value is quite high for an epoxy, and although this may be achieved under ideal mixing conditions, in practice the apparent modulus of the installed epoxy will be affected by many factors. The conditions under which the epoxy is hardened are less than ideal, with debris from the drilling process and contamination from the plastic resin capsules acting to reduce the stiffness of the layer. In addition, variation in the amount of mixing that has taken place may cause some areas of the resin to be poorly mixed, and therefore not fully cured. This too will act to reduce the stiffness of the epoxy layer, lowering the apparent modulus.

The effect of the epoxy modulus has been investigated by varying the epoxy modulus of the basic rock bolt model from 2GPa to 14GPa. The predicted phase velocity, attenuation and energy velocity dispersion curves are shown in figure 3.10. Figure 3.10a shows that the peak in phase velocity that occurs in embedded systems is shifted to a lower frequency, and to a higher maximum as the epoxy modulus is decreased. This shift in the phase velocity peak to lower frequency is related to the decrease in attenuation. A similar trend was noticed for variation in the rock modulus, where the peak in phase velocity shifted to a higher frequency as the rock modulus and the attenuation increased. However, the increase in the height of the phase velocity peak was noticed for both the increased attenuation of the higher modulus rock and the reduced attenuation of the lower modulus epoxy, which highlights the complexity of embedded systems with intermediate layers.

The effect of the epoxy modulus on the predicted attenuation is much more straightforward. It can be seen that below 60kHz, a decrease in epoxy modulus causes a decrease in attenuation. This is because the wavelength is large compared to thickness of the epoxy layer, and the epoxy layer behaves like an interfacial stiffness. Since the modulus of the rock is higher than that of the epoxy, any decrease in the epoxy layer modulus results in the bolt being less well coupled to the rock, and therefore less leakage will occur. The effect at higher frequencies is again complicated by the mode shape no longer being a simple compression wave, and also because the wavelength is becoming more comparable with the epoxy layer thickness. This means that the acoustic impedance at both the epoxy/bolt and epoxy/rock interfaces becomes significant. It can be seen that the effect of lowering the epoxy layer modulus is actually to push the entire dispersion curve into a lower frequency range. The attenuation minimum occurs at a lower frequency as the modulus is reduced, and the 2GPa line also shows a subsequent attenuation maximum. This maximum is present in all the other cases, but occurs above 100kHz. The energy velocity can be seen to be relatively high for most cases where the attenuation is relatively low, although even this trend is complicated at the higher end of the frequency range.

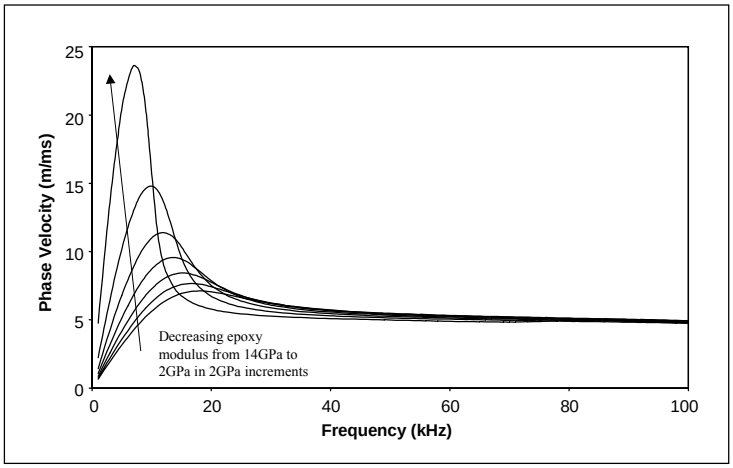

(a) Phase velocity.

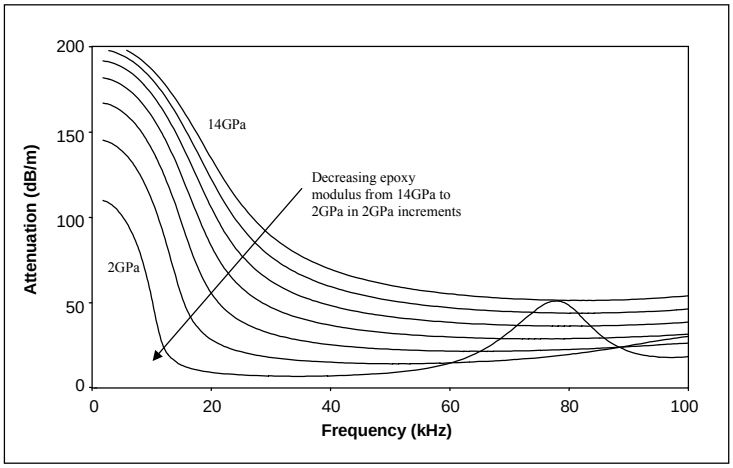

(b) Attenuation.

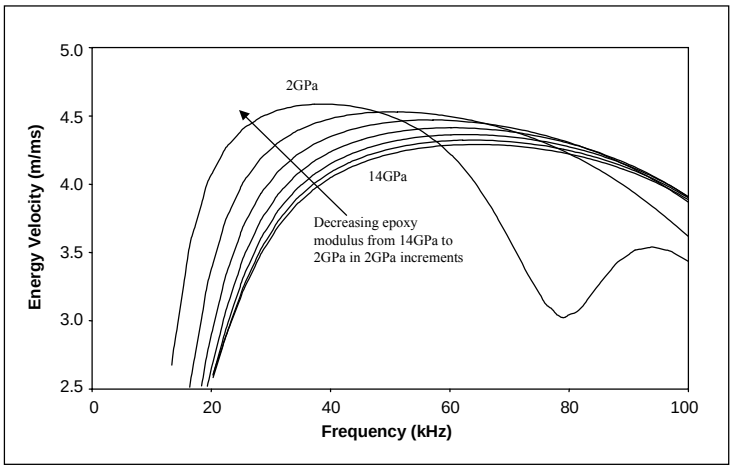

(c) Energy velocity.

Figure 3.10: Changes in the dispersion of the L(0,1) mode when the epoxy modulus of the basic rock bolt model is varied between 2GPa and 14GPa.

3.3.6 Effect of the Epoxy Layer Thickness

The epoxy layer thickness may vary between different bolts, as well as along the length of an individual bolt. The hole into which the rock bolt is installed has a nominal diameter of 27-31mm, which means that even if the epoxy layer is uniform around the bolt it can still vary in thickness from approximately 3-5mm. In addition, the hole may not be perfectly straight, and the bolt may not be perfectly aligned after the installation process. Hence there may be variations in thickness around the circumference of the bolt. Although variation around the circumference cannot be modelled directly, the possible effect can be evaluated by varying the overall epoxy thickness in the basic rock bolt model.

Figure 3.10 shows the phase velocity, attenuation and energy velocity dispersion curves for the basic rock bolt model when the epoxy thickness is varied from 0-10mm. The results show that an increase in epoxy thickness produces a similar effect to reducing the epoxy modulus. This is because the layer is thin compared to the wavelength, and increasing the epoxy thickness has the effect of reducing the apparent stiffness of the layer, exactly the same as reducing the layer modulus. The attenuation minimum is shifted to a lower frequency and a lower value as the thickness is increased, and the phase velocity is seen to reach a higher peak, at lower frequency. In the lower end of the frequency range, where the mode shape is simple, a thicker epoxy layer will therefore reduce the attenuation, and increase the energy velocity. However, this trend may be different for other embedding rock types. For example, in a rock with a modulus very similar to that of the epoxy, such as mudstone, the acoustic coupling would be largely unchanged by epoxy thickness and it is reasonable to assume that the attenuation would remain roughly constant.

Since the range of epoxy thickness likely to be encountered in site testing has a large effect on mode attenuation and energy velocity, it will be an important factor in interpreting test results, particularly in high modulus rocks. Changes in epoxy thickness along the bolt length may result in a large enough change in acoustic impedance to cause a significant reflection of the wave. These reflections may be detectable if the epoxy thickness changes dramatically over a short length of bolt. Gradual changes or continual variation along the bolt length are likely to result in increased attenuation of the wave, and additional background noise, decreasing the potential inspection range.

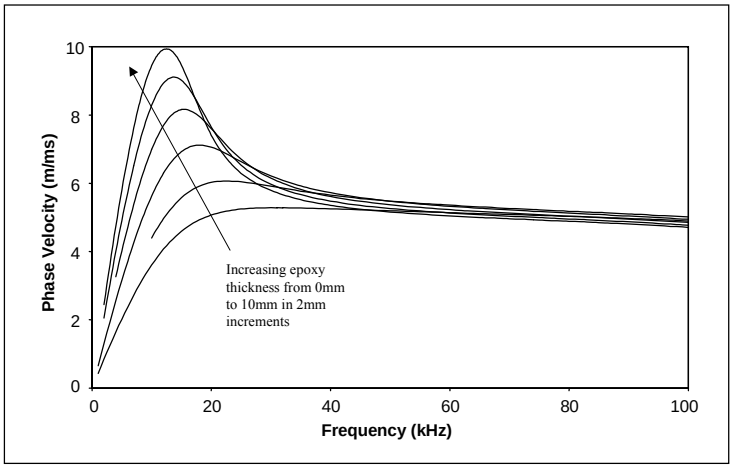

(a) Phase velocity.

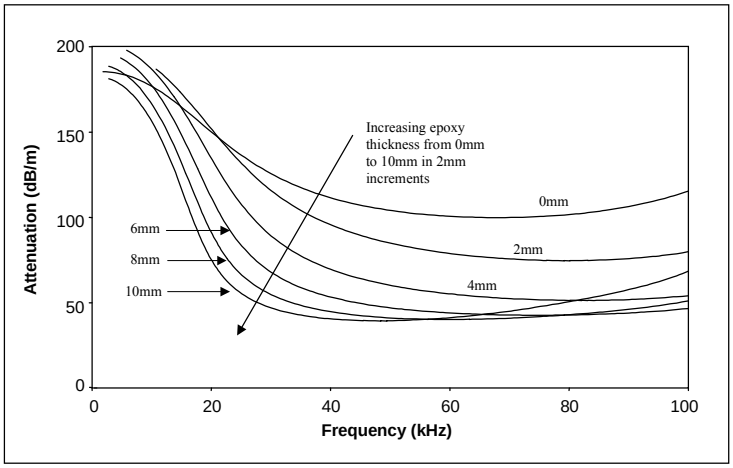

(b) Attenuation.

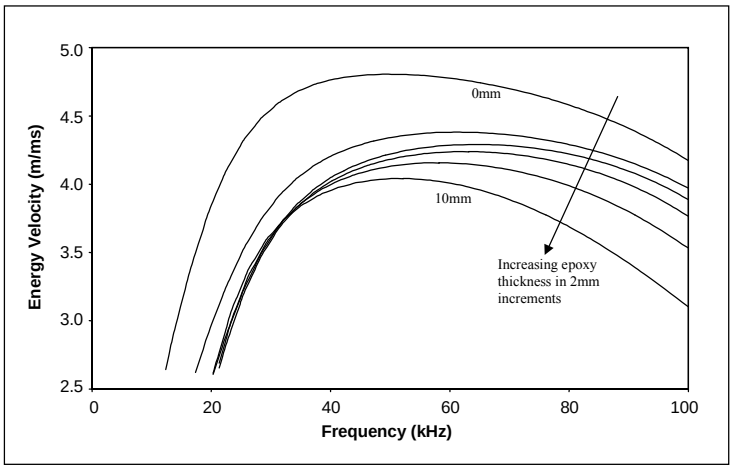

(c) Energy velocity.

Figure 3.11: Changes in the dispersion of the L(0,1) mode when the epoxy thickness of the basic rock bolt model is varied between 0mm and 10mm.

3.3.7 Effect of Imperfect Bonding

The coupling between the rock bolt and the epoxy is unlikely to be perfect, as outlined in section 3.2.4. Debris from the drilling process, water, and plastic from the resin capsules are likely to contaminate the bond line, and the fact that the rock bolt is spun into the setting resin will affect the bond strength at some points along the bolt. The effect of the bond condition between the bolt and the epoxy has been investigated using the interfacial boundary stiffness method and the definition of bond quality outlined in section 3.2.4. An additional interfacial stiffness layer has been defined for the full range of contact conditions, from a perfect bond to an almost totally degraded bond. The effect on the phase velocity, attenuation and energy velocity dispersion of the L(0,1) is shown in figure 3.12.

Figure 3.12 shows that at low frequency, reducing the bond quality has the same effect as decreasing the epoxy layer stiffness, with the phase velocity peak shifted to a higher value and a lower frequency, with lower predicted attenuation. This is expected, because at low frequency and long wavelength, a reduction in bond quality is similar to reducing the stiffness of the layer. However, further examination of the attenation dispersion predictions over the entire frequency range show that the behaviour at all frequencies is more predictable and consistent. The effect on attenuation is very significant, with a reduction in bond quality causing the attenuation to be reduced at all frequencies, with the shape of the dispersion curve unchanged. The frequency at which the attenuation minimum occurs is the same for all cases, showing that bond quality only really affects the coupling to the embedding material, and therefore the leakage, and not the optimum test frequency. The energy velocity is shown to increase as the bond quality, and therefore the attenuation, is reduced.

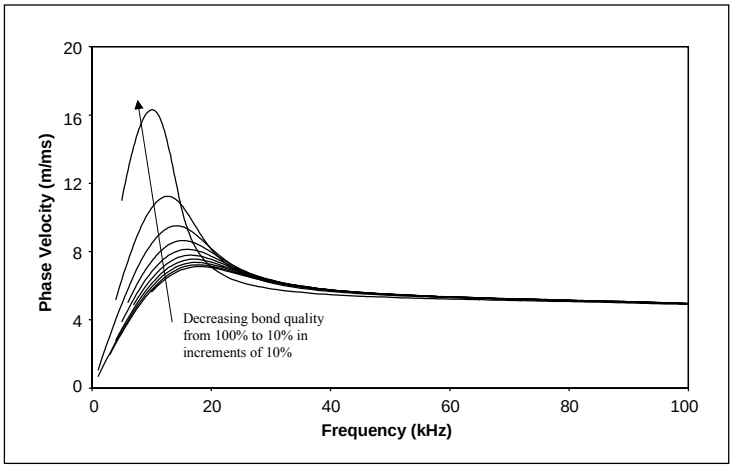

(a) Phase velocity.

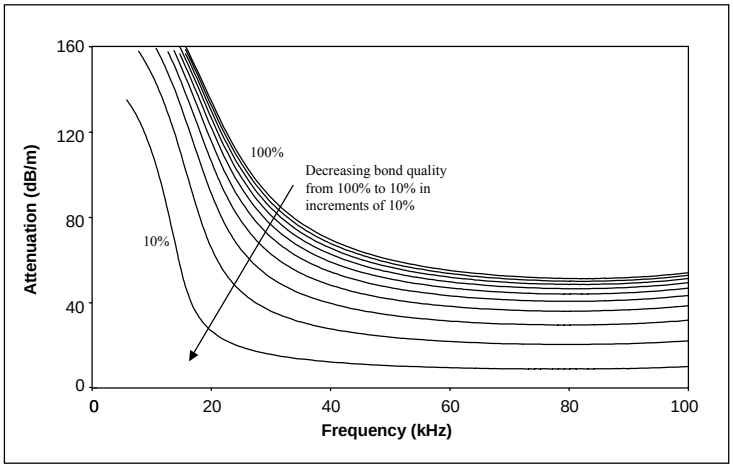

(b) Attenuation.

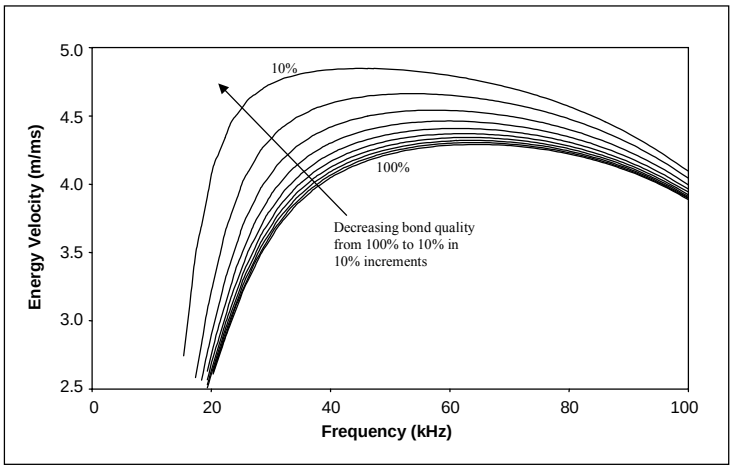

(c) Energy velocity.

Figure 3.12: Changes in the dispersion of the L(0,1) mode when the epoxy/bolt bond quality of the basic rock bolt model is varied between 10% and 100%.

3.3.8 Summary of Low Frequency Modes

Overall, the study of how variation in material properties and geometry affects the characteristics of the L(0,1) mode shows that the optimum frequency and predicted attenuation could be considerably different from those predicted by the basic model. This study has also given a good deal of information which will assist in the interpretation of test results.

It has been shown that reducing the bond quality and the epoxy modulus will both reduce the attenuation due to leakage. It is therefore highly likely that the attenuation in a real rock bolt will be considerably lower than the 50dB/m predicted by the original model, allowing the possibility of testing 2.4m rock bolts with the L(0,1) mode. The effect of a reduction in epoxy modulus is also likely to shift the attenuation minimum to a frequency considerably lower than 70kHz. The energy velocity of the mode is also likely to be faster than that predicted by the basic model.

The effect of the rock modulus and epoxy thickness are also significant. The modelling has shown that in the frequency range 30-60kHz, the L(0,1) mode is largely unaffected by the rock modulus, and this would therefore be an ideal frequency range for the test, as the mode would behave consistently in any rock type. It has been shown that any changes in the epoxy thickness could have a large effect on the attenuation and velocity of the L(0,1) mode. It is possible that any changes in epoxy thickness along the length of a bolt may be significant enough to cause the wave to be reflected. An abrupt change in thickness (such as a total loss of encapsulation) may well cause a reflection large enough to be detectable, and less severe changes may be detectable as increased attenuation or additional noise.

3.4 High Frequency Modes

The following sections analyse the higher order modes that can exist in a rock bolt by examining both a free bar and the basic rock bolt case of an epoxy bonded steel bar embedded in limestone. Many of the high order longitudinal modes exhibit regions of low attenuation, and this phenomenon is investigated using the simplified example of a bar embedded only in limestone, with no epoxy layer. The non-axially symmetric flexural modes exhibit much higher attenuation, and are therefore not considered. The effect of variation in material properties and geometry is also examined.

3.4.1 Free Bar

The dispersion curves for the high frequency modes have been produced using the same model as outlined in section 3.2.2. The dispersion relationships for the axially symmetric longitudinal modes up to 4MHz in a free 21.7mm steel bar are shown in figure 3.13. The phase velocity curves show the fundamental L(0,1) mode starting at zero frequency, with each successive higher order mode starting from a higher cut-off frequency.

The behaviour of each of the higher order axially symmetric modes is similar, with the phase velocity showing a plateau region around the steel longitudinal bulk velocity line. This plateau region becomes more noticeable with each successive mode order, extending further in frequency. The plateau region also becomes much flatter, and occurs at a slightly lower value of phase velocity as the mode order is increased. After the plateau region, the modes cross the bulk velocity line and tend to the steel shear bulk velocity at very high frequency (not the Rayleigh velocity as for the L(0,1) mode). The plateau regions also correspond with points of maximum energy velocity and minimum attenuation. The maximum energy velocity of each mode increases with the mode order, as shown in figure 3.13b. Figure 3.13c shows that the minimum attenuation attained by each mode increases with mode order. This is expected, as the only attenuation mechanism is material damping, and the damping effect is much greater at the small wavelengths associated with high frequency waves. This is a common observation in ultrasonic applications as frequency is increased, although the effect is not necessarily the same for other attenuation mechanisms, such as leakage. The fact that the attenuation minima and energy velocity maxima occur at the same points has been explained by Pavlakovic [6,31] with reference to the partial waves. In these regions the phase velocity is almost equal to the longitudinal bulk velocity, and the longitudinal partial wave is almost parallel to the bar axis. The amplitude of the longitudinal partial wave is also much greater than the amplitude of the shear partial wave, thus the wave propagates at a speed close to the bulk velocity, with a short apparent path length through the material, and therefore low attenuation.

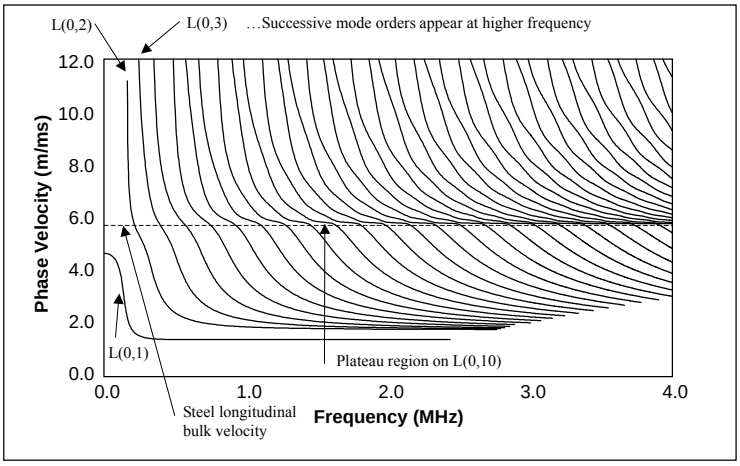

(a) Phase velocity.

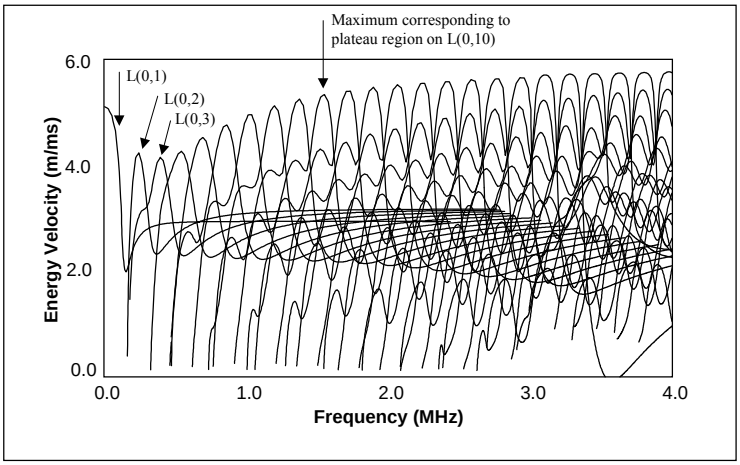

(b) Energy velocity.

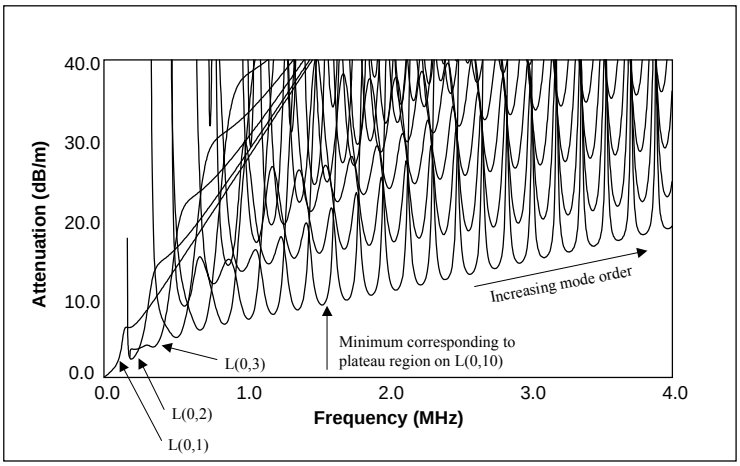

(c) Attenuation.

Figure 3.13: Dispersion of the axially symmetric longitudinal modes in a free 21.7mm steel bar, modelled with material damping.

3.4.2 Resin Bonded Bar Embedded in Limestone

The basic rock bolt model outlined in section 3.2.2 has been used to obtain the dispersion relationships for the higher order longitudinal modes in an embedded rock bolt, shown in figure 3.14. The phase velocity curves (figure 3.14a) show a difference in behaviour from the free case around the steel longitudinal bulk velocity line. Instead of the each plateau region belonging to a single mode, the L(0,11) mode breaks from this pattern and links the subsequent plateau regions together, to form a single mode that propagates close to the bulk velocity line. Other longitudinal modes then cross this mode, and the pattern is repeated at higher frequency, with L(0,20) also following this pattern to form a mode linking another group of plateau regions together. The exact pattern linking these regions depends on the properties of the embedding material [6], and is more complex if there are additional layers, such as the epoxy layer in this model, for example L(0,9) crosses one other mode in this model. The change in mode behaviour from repulsion to crossing has been observed by Chan [88] in polymers with a high level of attenuation due to material damping.

The attenuation dispersion curves in figure 14b show that, as observed in the free case, these plateau regions are associated with an attenuation minimum and an energy velocity maximum, suggesting that both material attenuation and leakage reach a minimum in these regions. The mode that forms to link all the plateau regions together therefore forms a single low-leakage mode. In this system, L(0,11) forms the low-leakage mode, although as the minima still exist in the plateau regions even if the regions are not linked, the actual mode that links the regions together is not particularly important. Section 3.4.3 examines the mode shape associated with the attenuation minima. The lowest values of attenuation are reached in the range 2-2.5MHz, with predicted attenuation of 15-20dB/m. This would make it possible to inspect a 3m rock bolt, assuming that 100dB could be compensated for by the testing instrument amplifier.

It is important to assess the sensitivity of the low-leakage modes to changes in material and geometrical properties. However, the large number of modes makes it impossible to look at the behaviour of each mode in detail, and the modes have only been studied at the points of interest, that is the attenuation minima. Four points on modes have been investigated, at attenuation minima occurring at 1.00MHz, 1.69MHz, 2.22MHz and 2.57MHz in the basic rock bolt model. Some parameter changes result in a very slight shift in the frequency of the attenuation minima, which is analysed further in section 3.4.8. However, for consistency, these frequencies are used to refer to the points, even though the attenuation and energy velocities were recorded at the actual frequency of the minima. The behaviour of the modes at these four points under varying rock modulus, epoxy thickness and bond quality is examined in sections 3.4.4-3.4.7.

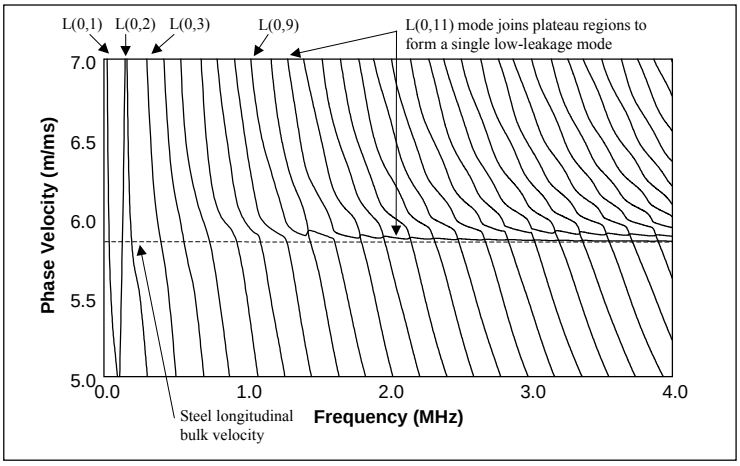

(a) Phase velocity.

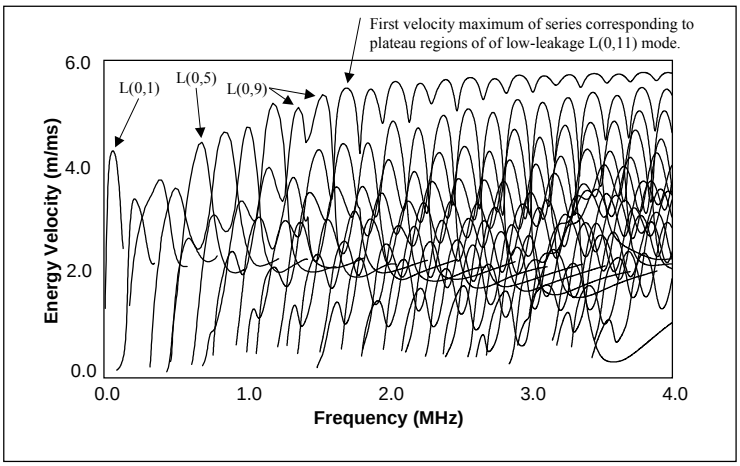

(b) Energy velocity.

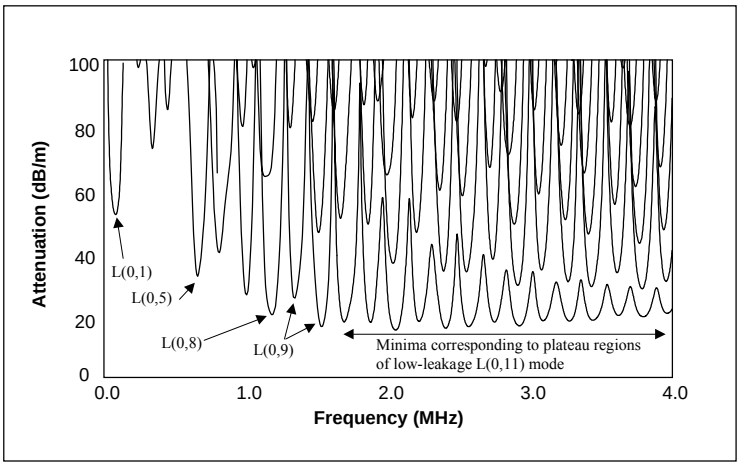

(c) Attenuation.

Figure 3.14: Dispersion of the axially symmetric longitudinal modes in the basic rock bolt model, consisting of a 21.7mm steel bar, surrounded by a 4mm thick epoxy layer and embedded in limestone.

3.4.3 Low-Leakage Modes

The low-leakage modes can be more easily examined in a simple embedded system. Figure 3.15 shows the phase velocity and attenuation dispersion curves for a 21.7mm bar embedded in limestone, with no epoxy layer. Figure 3.15a shows the phase velocity curves in the bulk velocity region, and in this case the L(0,7) mode can be seen to link the plateau regions to form a low-leakage mode. Figure 3.15b shows that all of the lowest attenuation minima from L(0,7) onwards are formed of this mode, although other modes show minima in their plateau region. Similar low-leakage modes are formed from the L(0,14) and L(0,21) modes, but in all of the cases examined, the lowest order low-leakage mode has the lowest overall attenuation, and is therefore the most useful in NDT.

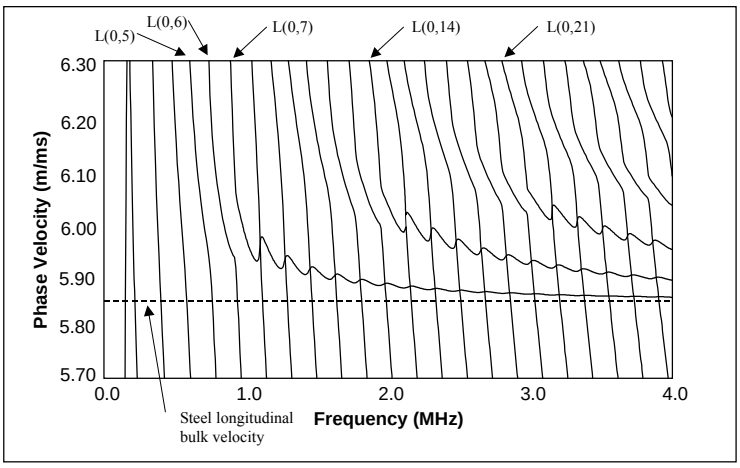

(a) Phase velocity.

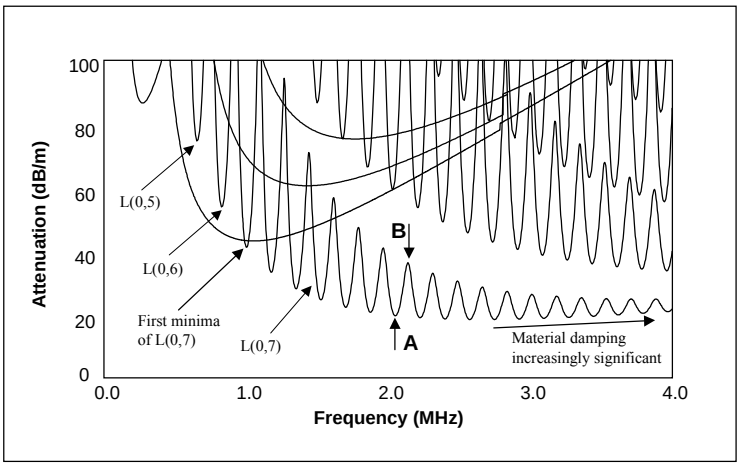

(b) Attenuation.

Figure 3.15: Dispersion of the axially symmetric longitudinal modes in a 21.7mm steel bar embedded in limestone, with no intermediate epoxy layer.

In this simple embedded system, the L(0,7) mode shows the trend of distinct attenuation minima, generally decreasing in value with frequency, as seen for the more complex rock bolt model. This is an unexpected observation, as the attenuation of ultrasound usually increases with frequency, due to the increase in material damping that occurs with decreasing wavelength. Figure 3.15b shows that eventually, the attenuation does begin to increase with frequency (after about 2.5MHz) as material damping effects become dominant. If the bar had no material damping, and the attenuation was due only to leakage, it would tend to zero as the frequency was increased.

The L(0,7) mode also shows regions of maximum attenuation in between the minima. This cyclic variation in attenuation can be explained by considering the mode shapes. Figure 3.16 shows the axial displacement profile for the high attenuation point labelled 'A' on figure 3.15b, and for the low attenuation point labelled 'B' on figure 3.15b. Figure 3.16a shows that there is very little axial displacement at the bar/limestone interface at the attenuation minimum at 2.05MHz. The predicted attenuation at this point is as low as 18dB/m. However, figure 3.16b shows that a slight increase in frequency to 2.13MHz results in a doubling of the attenuation and a significant axial displacement at the bar/limestone interface. Hence the mode shape characteristic that gives rise to the attenuation minima is the concentration of energy in the centre of the bar, with very low axial displacement at the surface of the bar. This means that there is very little interaction with the embedding material, and therefore the leakage is low.

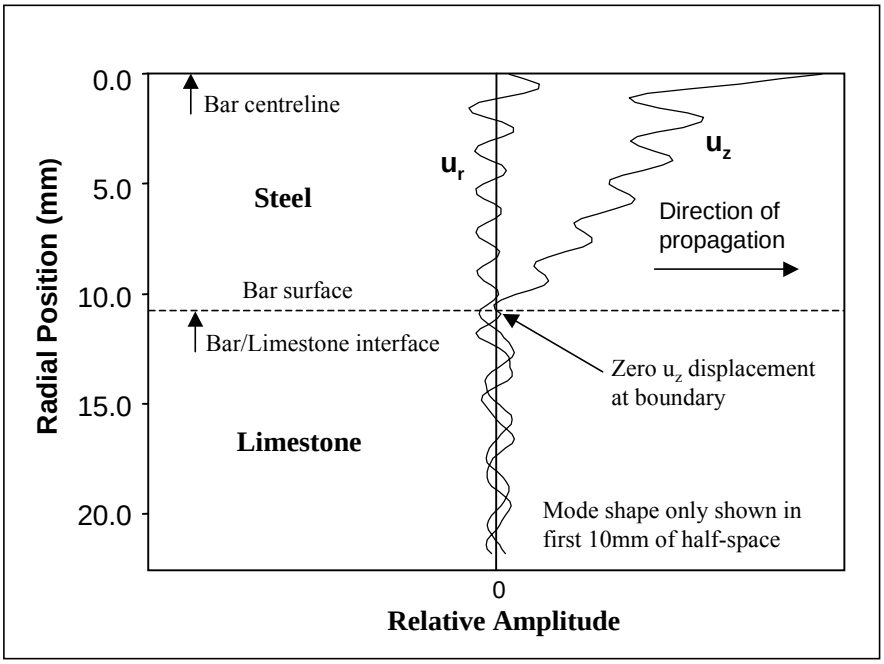

(a) Displacement at Point A on figure 3.15b (attenuation minimum).

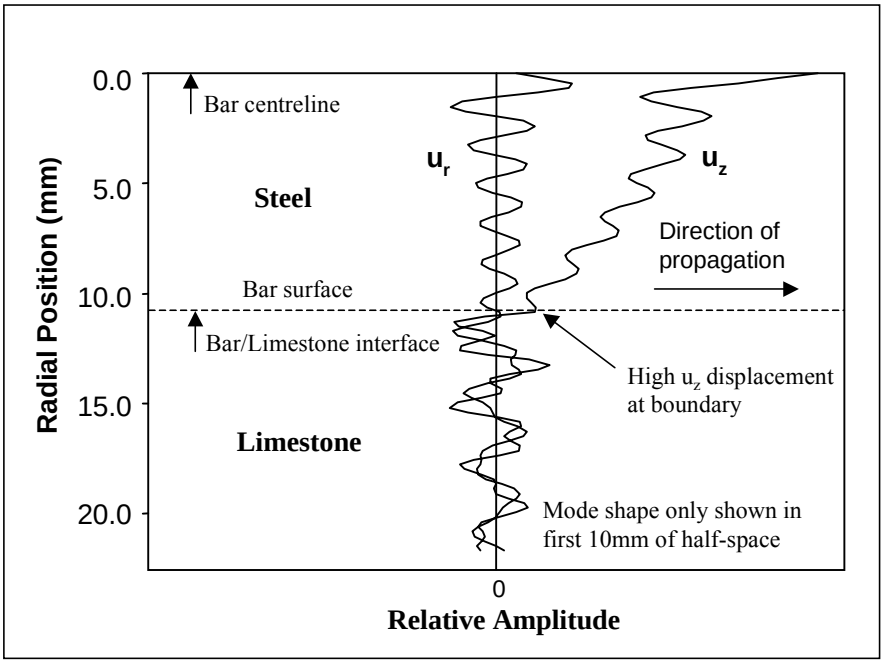

(b) Displacement at Point B on figure 3.15b (attenuation maximum).

Figure 3.16: Mode shape characteristic at a maximum and minimum attenuation point on a low-leakage mode.

3.4.4 Effect of the Embedding Material Modulus

Section 3.3.4 outlined the reasons why the effect of the embedding material was important, and showed that the embedding material has a significant effect on the properties of the L(0,1) mode at low frequency. At high frequency, low-leakage mode behaviour has been examined at the four reference attenuation minima identified in section 3.4.2. Figure 3.17 shows how the predicted attenuation varies with rock modulus for the basic rock bolt model.

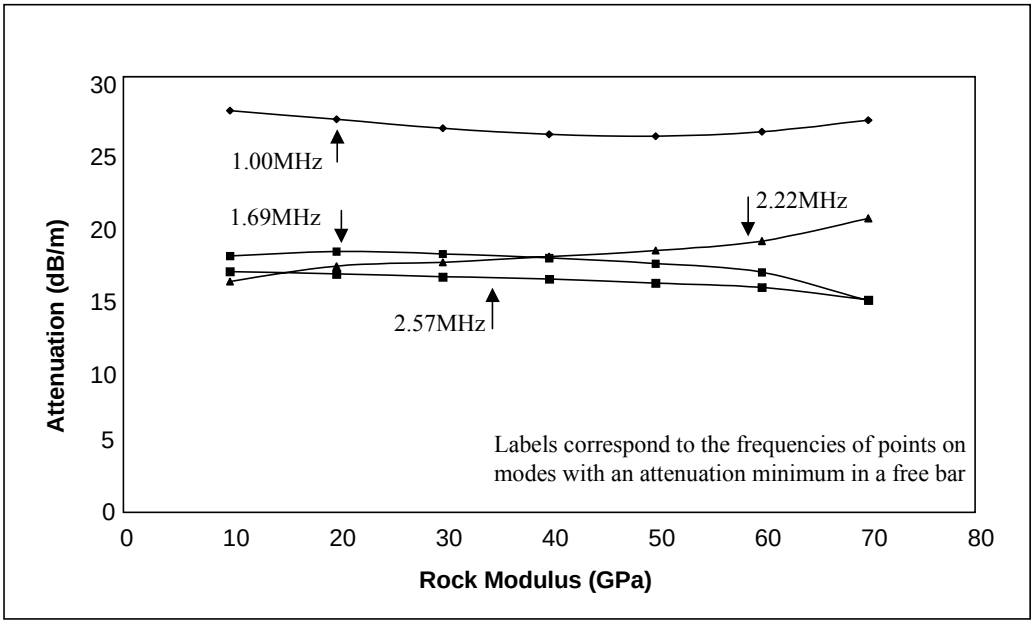

Figure 3.17: Changes in the predicted attenuation at the four reference attenuation minima when the rock modulus of the basic rock bolt model is varied between 10GPa and 70GPa.

Figure 3.17 shows that the rock modulus has little effect on the predicted attenuation, with no clear trend for any of the modes. It is likely that the concentration of energy in the centre of the bar at the low attenuation points limits the effect of the rock modulus, as the wave does not interact very much with the embedding material. At these high frequencies the wavelength of the guided waves is just a few mm, which is similar to the thickness of the epoxy layer, making them much more to be sensitive to the properties of this layer. Thus the epoxy layer acts as a buffer, with the high contrast in acoustic impedance at the epoxy/bolt interface isolating the wave from changes in the embedding material modulus. In addition, about half of the attenuation is due to material damping effects, which will not alter with embedding material properties. The energy velocity of the modes (not shown) does not change significantly with rock modulus. This is expected because the attenuation does not change very much, and also because the velocity of all the low-leakage modes is always close to the longitudinal bulk wave velocity of the steel.

3.4.5 Effect of the Epoxy Modulus

The effect of the epoxy modulus was also shown to have a significant effect on the L(0,1) mode at low frequency. The effect of the epoxy modulus on the four reference low-leakage points on modes has been investigated by varying the epoxy modulus of the basic rock bolt model. The results in figure 3.18 show that the epoxy modulus has little effect on the modes, although there is a slight trend to higher attenuation with increasing epoxy modulus. This is because increasing the epoxy modulus decreases the contrast in acoustic impedance at both the bolt/epoxy and epoxy/rock interfaces, and the leakage is higher. The effect is smaller than at low frequency because the nature of the low-leakage points is to interact very little with the embedding material anyway. It is interesting to note that the mode at 1.0MHz is affected more, as the low-leakage characteristics of this mode are less strong than the other modes. Once again, the energy velocity does not vary significantly for the cases examined.

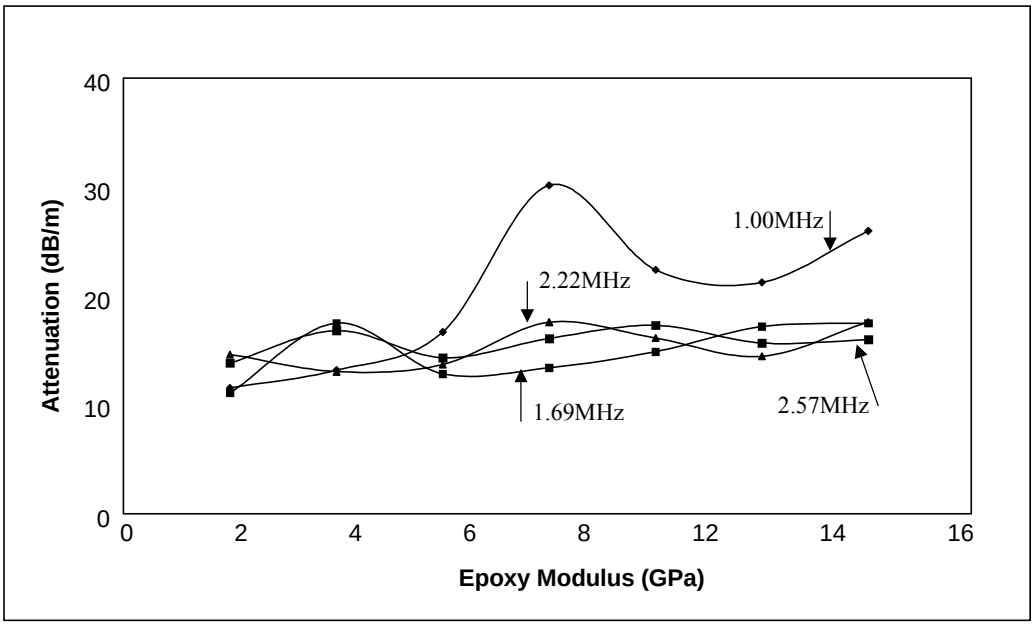

Figure 3.18: Changes in the predicted attenuation at the four reference attenuation minima when the epoxy modulus of the basic rock bolt model is varied between 2GPa and 14GPa.

3.4.6 Effect of the Epoxy Layer Thickness

The predicted attenuation at the four reference points has been calculated for the basic rock bolt model with varying epoxy thickness. The predicted attenuation is shown by figure 3.18 for thickness in the range 0-8mm. The epoxy thickness was shown to have a significant effect on attenuation at low frequency, but its effect is limited for these high frequency modes. At low frequency, the large wavelength meant that an increase in epoxy thickness showed a similar effect to reducing the epoxy modulus, but this effect is not seen at high frequency due to the

much shorter wavelength. It is noticeable that the zero epoxy thickness case yields slightly higher attenuation for all the modes, as the bar is then well coupled to the embedding material, without the buffering effect of the epoxy layer. The energy velocity (not shown) is close to the steel bulk longitudinal velocity, and is unaffected by epoxy thickness. This suggests that the high frequency modes are ideal for measuring rock bolt length, as any change in epoxy thickness will not cause significant changes in attenuation or wave speed. It is also likely that the high frequency modes will not be sensitive even to abrupt changes in epoxy thickness, such as the start of the resin encapsulation.

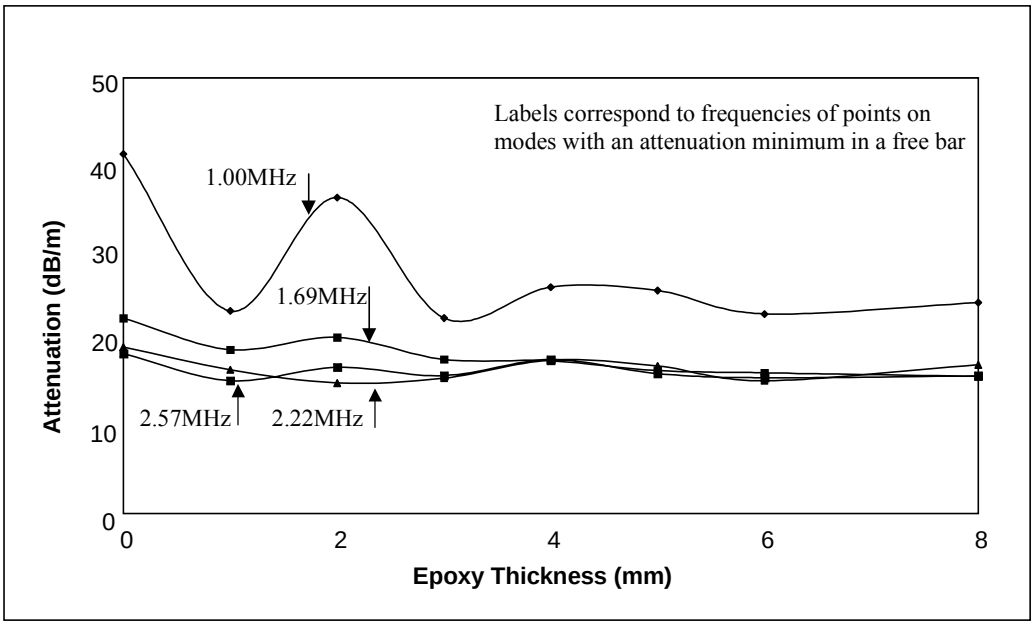

Figure 3.19: Changes in the predicted attenuation at the four reference attenuation minima when the epoxy thickness of the basic rock bolt model is varied between 0mm and 10mm.

3.4.7 Effect of Imperfect Bonding

The effect of imperfect bonding has been investigated by inserting an additional interfacial stiffness layer between the epoxy and rock bolt layers in the basic rock bolt model. This method of modelling the bond is outlined in section 3.2.4, and uses a definition of bond quality based on the relative stiffness of the epoxy layer and the combined epoxy/interfacial layer. The attenuation predicted at the four reference points when the bond quality is varied from 0% to 100% is shown in figure 3.19.

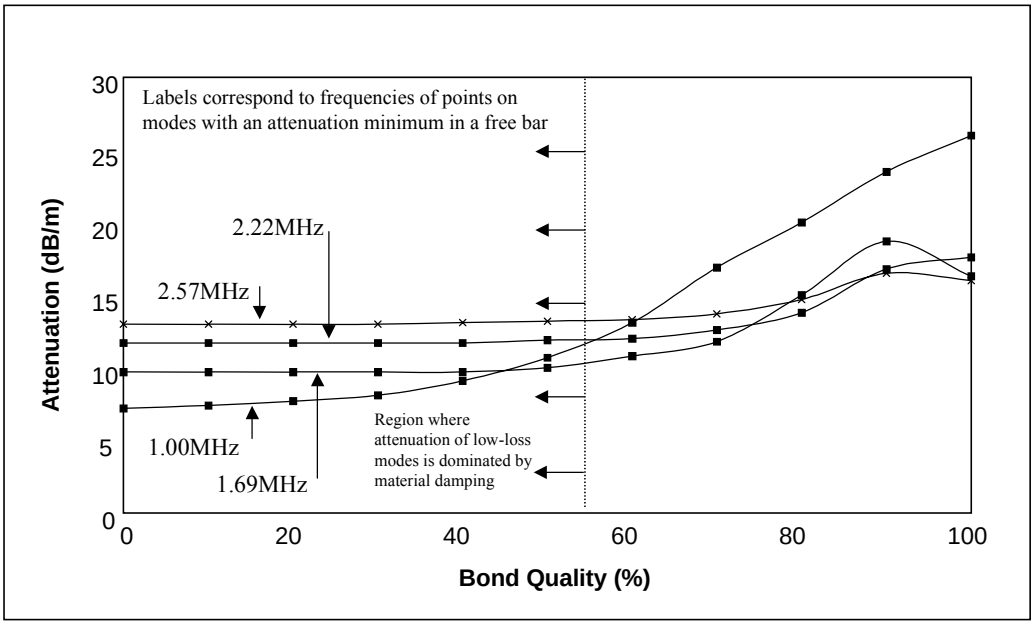

Figure 3.20: Changes in the predicted attenuation at the four reference attenuation minima when the bond quality between the steel and epoxy layers of the basic rock bolt model is varied between 0% and 100%.

Figure 3.20 shows that when the bond is perfect (100%), the attenuation is equal to that predicted by the basic rock bolt model. However, there is a rapid reduction in the predicted attenuation for all the modes as the bond quality decreases. When the bond quality falls below 85%, the 2.57MHz mode reaches a minimum attenuation value that is independent of the contact stiffness. The same effect occurs below about 55% bond quality for the 1.00MHz mode. This minimum value is that expected from material damping effects only, and is equal to the attenuation predicted for the free bar case, where material damping is the only mechanism of attenuation. This means that if the real bolt/epoxy bond quality is below 85%, as defined by the model, then the modes are essentially non-leaky above 2MHz. Therefore, in poor contact conditions, the lower order modes of the high frequency range will have lower overall attenuation, whereas in good contact conditions, the higher order modes in the high frequency range will have lower overall attenuation.

The implications for the use of these modes for practical inspection are good, as the attenuation will generally be expected to be lower than the basic rock bolt model predictions. It also raises the possibility of measuring contact conditions by measuring attenuation, as long as the steel damping properties are known accurately. These predictions have been compared with experimental results, and are discussed further in chapters 4 and 5.

3.4.8 Summary of High Frequency Modes

The low-leakage L(0,11) mode has been shown to have potential for rock bolt inspection as it has numerous points with low attenuation. Six frequencies at which this mode could be excited are shown in the first column of table 3.3. The study of the effect of variation in epoxy thickness and modulus, rock modulus and contact stiffness showed that the exact frequency at which these minima occur may vary slightly with these factors. The remainder of table 3.3 shows the predicted frequencies of the attenuation minima for a selection of the models used to investigate these factors. The variation in the frequency of the minima that occurs due to these factors is very small.

Basic Rock Bolt Model	Parameter changes to the basic model. Original values shown in brackets.			
	Rock Modulus 10GPa (40GPa)	**Epoxy Modulus 2GPa (14GPa)**	**Epoxy Thickness 1mm (4mm)**	**Bond Quality 50% (perfect)**
1.88 MHz	1.87 MHz	1.87 MHz	1.87 MHz	1.88 MHz
2.05 MHz	2.05 MHz	2.04 MHz	2.03 MHz	2.06 MHz
2.22 MHz	2.23 MHz	2.24 MHz	2.22 MHz	2.22 MHz
2.40 MHz	2.40 MHz	2.40 MHz	2.40 MHz	2.40 MHz
2.57 MHz	2.57 MHz	2.57 MHz	2.58 MHz	2.58 MHz
2.75 MHz	2.75 MHz	2.75 MHz	2.75 MHz	2.75 MHz

Table 3.3: Variation in the frequency of six attenuation minima on the L(0,11) mode when the parameters of the basic rock bolt model are varied.

The effect of the material factors on the attenuation and energy velocity of the points examined was also very small. This means that a high frequency test using these frequencies will be largely insensitive to changes in the rock type and the epoxy properties, and should be therefore be able to accurately measure bolt length in any conditions. The only significant factor was the quality of the bond between the epoxy and the bolt. If this bond is less than perfect, the attenuation will be reduced from the level predicted by the original model, and may be as low as that expected from material damping alone. Any estimates of inspection range made from the original model should therefore be conservative, providing the damping properties of the steel are known accurately.

The effect of the elastic properties of the steel will also affect the model predictions. All of the predictions in this model were made using properties typical of a steel with a Young's Modulus of 207GPa, which corresponds to longitudinal and shear bulk wave velocities of 5845m/s and 3180m/s respectively. Table 3.4 summarises the potential test frequencies using this steel, and also a higher strength steel with a Young's Modulus of 217GPa, which corresponds to longitudinal and shear wave velocities of 5960m/s and 3260m/s respectively. Table 3.4 also summarises the attenuation and energy velocity predicted for the 207GPa case.

Frequency (MHz) (207GPa Steel)	Frequency (MHz) (217GPa Steel)	Attenuation (dB/m) (207GPa Steel)	Energy Vel. (m/ms) (207GPa Steel)
1.88	1.92	17.4	5.45
2.05	2.11	14.9	5.60
2.22	2.29	17.6	5.57
2.40	2.46	15.5	5.64
2.57	2.65	16.0	5.67
2.75	2.82	17.4	5.65

Table 3.4: Summary of frequency, attenuation and energy velocity predicted by the basic rock bolt model at points on the L(0,11) mode suitable for inspecting rock bolts, also showing the corresponding frequencies for a higher strength steel.

3.5 Modelling Conclusions

The modelling presented in this chapter has shown that two longitudinal modes may be suitable for inspecting rock bolts, the fundamental longitudinal mode L(0,1), and the high frequency longitudinal mode L(0,11) in its low-leakage region. These modes have very different characteristics, and have the potential to interrogate a bolt for different types of defect. The sensitivity of these modes to different types of defect and other bolt features, such as mixing ribs, cannot be assessed using the modelling software. Further experimental work has been carried out in this area, and is reported in chapter 4.

The fundamental L(0,1) mode has a minimum in attenuation, and a maximum in energy velocity between 30kHz and 60kHz, depending on the exact epoxy thickness and rock modulus. The attenuation mechanism is primarily leakage into the rock, as material damping is limited by the long wavelength. The velocity maximum limits the effects of dispersion on wave propagation. The attenuation predicted by the basic rock bolt model is around 60dB/m, which in theory would limit the inspection range to about 1m. However, the predictions have been made for limestone, and lower modulus rocks may well give rise to lower attenuation, and poor contact conditions between the bolt and the epoxy have also been shown to reduce the predicted attenuation. It is therefore likely that the actual attenuation will be lower than this, and this has been confirmed by the experimental results presented in chapter 4. The L(0,1) mode shape has almost uniform axial displacement across the bar, and is therefore likely to be sensitive to surface defects and epoxy defects, such as loss of encapsulation - the mode has already been shown to be sensitive to epoxy thickness. This has been investigated further using experimental techniques and is discussed in chapter 4 of this thesis.

The L(0,11) mode in the rock bolt system behaves very differently. The mode has low-leakage regions with attenuation in the range 15-20dB/m at 1.88, 2.05, 2.22, 2.40, 2.57, and 2.75MHz.

These frequencies are close to the attenuation minima in a free bar modelled with material damping, and are also non-dispersive regions of maximum energy velocity, close to the longitudinal bulk velocity in the steel. This makes L(0,11) an ideal test mode at these frequencies, with the potential to inspect a full 3m bolt. The attenuation is due to a mix of material damping and leakage effects, and is found at points where the energy associated with the mode becomes concentrated in the centre of the bar. The mode is not sensitive to epoxy thickness or rock modulus at the attenuation minima, and in general it is expected that the energy travelling in the centre will also mean that the mode is not sensitive to surface defects in the bolt. The ideal application would therefore be to obtain a reliable indication of bolt length, without the complication of reflections or changes in velocity due to other features. The effect of bolt/epoxy contact conditions is very significant, a 10-20% reduction in the bond quality reduces the attenuation to the level expected for material damping effects in the steel only. This means that attenuation in the real case will be less than the basic model predicts, but the actual value needs to be determined experimentally. A potential problem is that the short wavelength of this mode may give rise to poor reflection from the bolt end or defects. Effects such as this cannot be modelled analytically and are investigated experimentally in chapter 4.

CHAPTER 4

APPLICATION TO TESTING ROCK BOLTS

4.1 Introduction

The previous chapter has investigated the behaviour of guided waves in embedded bars, and has shown that both the fundamental L(0,1) mode and the higher order L(0,11) mode have the potential to inspect rock bolts. This chapter presents the results of site and laboratory testing using these modes, and compares them with the modelling predictions. The sensitivity of the modes to material property and geometry changes is used to explain the observed test results. The effect of three dimensional features that cannot be modelled analytically is also investigated, along with the optimum excitation signal. Conclusions are drawn about the potential of guided waves for the industrial inspection of rock bolts.

4.2 Test Specimens

In order to develop a robust test, it was necessary to undertake testing work in conditions as close as possible to those found in a real coal mine. However, access to deep coal mines is limited, and there are strict safety regulations that restrict the use of equipment that is not ‘intrinsically safe’. The development of a rock bolt test required the use of mains voltage laboratory equipment, which does not comply with these regulations, and is also too bulky to transport underground. As a result, most of the practical tests were carried out on real rock bolts installed at a test site in a disused area of a shallow limestone mine (Middleton Mine, Derbyshire, UK). Access to this test facility was provided by the mining consultancy company, RMT [76]. Further experiments were conducted on laboratory specimens that were constructed in the Civil Engineering Department of Imperial College.

4.2.1 Laboratory Specimens

In addition to the site testing work, it was convenient to have a range of laboratory specimens to prove concepts and to test and develop transducers and instrumentation. The use of concrete as an embedding material also provided a further validation case for the modelling work. However, construction of laboratory test specimens was by no means an easy option, despite the strict safety and logistical problems of testing ‘on site’, primarily because of the difficulties associated with simulating an infinite mass of rock. The specimens must be large enough to

prevent the leaked bulk wave reflecting from the edges of the embedding material and interfering with the wave propagating in the rock bolt, or being detected directly by the transducer. This is relatively easy at high frequency, as the wavelength of the ultrasound is only a few millimetres, and the leaked bulk wave travelling in the embedding material quickly becomes scattered. However, at low frequency, the much longer wavelength of about 100mm is scattered less quickly, leading to the possibility of edge reflections being detected.

Concrete was chosen for the embedding material, to allow a single block to be cast, with similar acoustic properties to those of rock. The block was limited in size by a crane capacity of 5 tons, which equates to about 2 cubic metres of concrete. It was desirable to have an embedded length of at least 2 metres, which limited the cross section to about 1 square metre, giving only 2 wavelengths between a bolt in the centre of the block and the outside at 20kHz. As a result, several measures were taken to maximise scattering and reduce the risk of detecting stray edge reflections. The block was cast using two different mixes, with the main body being cast from a 20mm aggregate concrete mix, to encourage scattering of sound from the large aggregate particles. The outer edges of the block were channelled to minimise the coherence of reflected waves and to reduce the overall weight. A central circular core, into which the rock bolts were installed, was cast inside the main body using a mortar mix with no aggregate. The uniform nature of rock is better simulated by mortar, and the lack of aggregate also reduced the risk of reflections from aggregate particles close to the installed bolts. The installation holes were cast, rather than drilled, into the mortar core using a bar coated in a PVC covering. This removed the risk of shattering the block when drilling, and ensured the holes were straight. The PVC coating was included to provide sufficient flexibility to remove the bar from the hole after casting. The central core was cast whilst the concrete in the main body was still very green, thus maximising the bonding between the surfaces and minimising the possibility of reflections being detected from the interface.

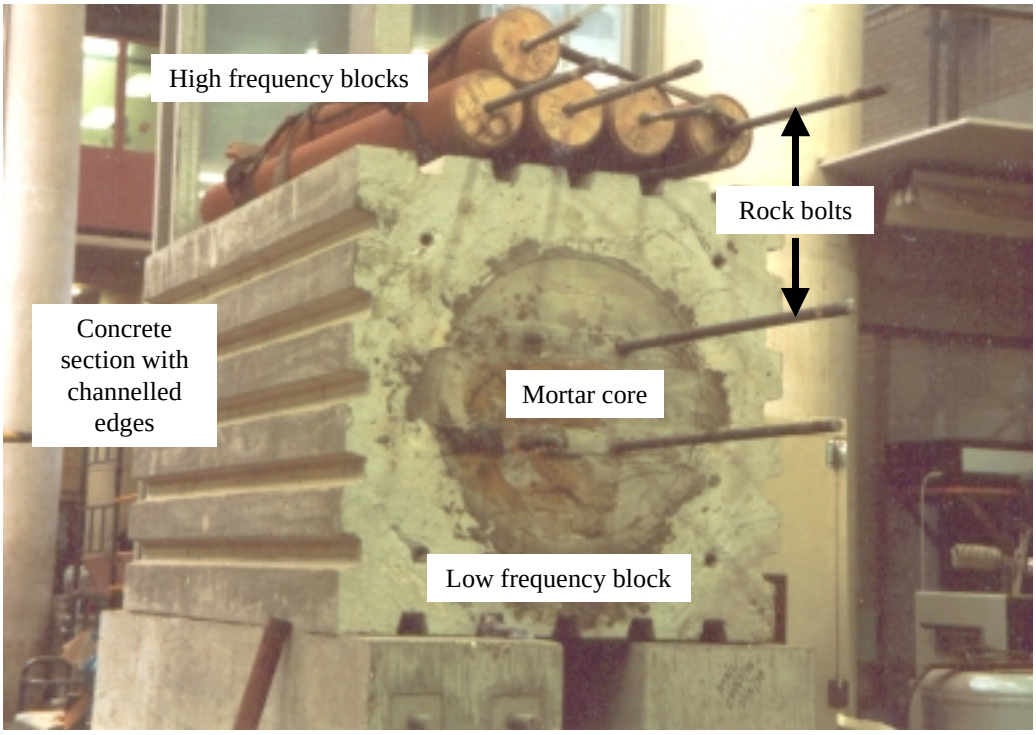

Figure 4.1: Picture of the specimens used for testing rock bolts in the laboratory, showing the large block test facility for low frequency work, and smaller blocks for high frequency work.

Four rock bolts were installed in the low frequency test block, three of which were installed into the central core using the industrial method described in chapter 2. Of these, one 2.4m flat-ended bolt, and one 2.4m angle-ended bolt were installed into 1.5m deep blind holes, leaving a 0.9m length of bolt protruding from the block. These specimens allowed the reflections from the start of the embedding material to be examined, as well as the end reflections. A third 2.3m rock bolt was installed into a temporary, removable end block, so that after the temporary block was removed, a short length of bolt protruded from each end of the main block. The purpose of this specimen was to allow the possibility of testing a 2m embedded length in both a pulse-echo and a through transmission configuration, and also to allow the possibility of changing the end conditions. The fourth rock bolt was formed into a crank-handled shape, manually coated with epoxy, and then cast into the mortar, to simulate a rock bolt that had been subject to a shearing movement of the rock strata. The geometry of this specimen is given with the test results in section 4.6.5, and a summary of these specimens, numbered LF1-LF4, is given in table 4.1.

Further specimens were required to test the sensitivity of the high frequency modes to defects and varying end angle. The small wavelength of these modes means that the leaked bulk waves will travel only a very short distance in concrete before becoming scattered, allowing the specimens to be much smaller. In addition, the modelling predicted very little difference in the wave properties with changes in the epoxy layer modulus and geometry, and therefore the

specimens were cast directly into concrete. The interaction of the high frequency modes with defects does not require an accurate simulation of bolt conditions, as long as the embedding material filters out the unwanted modes. Six rock bolt specimens were constructed by embedding rock bolts directly in mortar contained within lengths of 150mm diameter plastic pipe. Three of these specimens had lengths of rock bolt protruding from the mortar at both ends, to allow the end conditions and angle to be changed. Some of the bolts included a machined 'neck', representative of the geometry expected prior to failure from tensile overload. A summary of these specimens, numbered HF1-HF6, is given in table 4.1. All of the specimens were constructed with flat ends, except LF4, which had the standard manufactured angled end.

Specimen	**L_{thread} (m)**	**L_{embed} (m)**	**$L_{exposed}$ (m)**	**L_{total} (m)**	**L_{defect} (m) (Defect)**
LF1	0.19	2.00	0.11	2.31	n/a
LF2	0.92	1.48	n/a	2.40	n/a
LF3	0.10	2.05	0.10	2.25	1.00 (crank)
LF4	0.97	1.43	n/a	2.40	n/a
HF1	0.30	1.80	0.30	2.40	2.20 (neck)
HF2	0.30	1.80	0.30	2.40	2.20 (neck)
HF3	0.30	1.20	0.80	2.30	n/a
HF4	0.60	2.00	n/a	2.40	n/a
HF5	0.60	2.00	n/a	2.40	n/a
HF6	0.60	2.00	n/a	2.40	1.60 (neck)

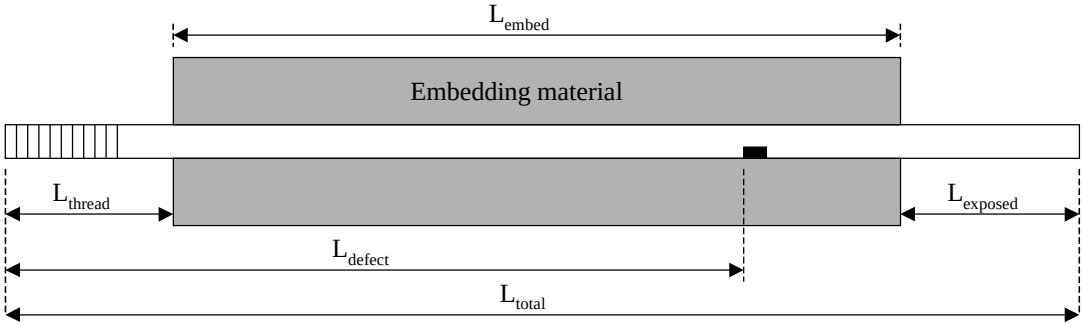

Table 4.1: Details of the laboratory specimens constructed for the development of the rock bolt inspection technique.

4.2.2 Middleton Mine

The test facility at Middleton was located in a disused area of a limestone mine that had been used to test machinery designed for the boring of coal mine roadways. The roof was low enough for easy access, and the surrounding rock was stable, minimising the risk of the installed bolts becoming deformed or broken from ground movement. There was no risk from naturally occurring gas, and the site had road vehicle access, allowing the transport and use of mains voltage laboratory equipment. Over fifty rock bolts, with a variety of lengths and end conditions, were available for testing, and all had been installed using the industrial method. The bolts could be identified by reference numbers, which are recorded throughout this thesis. Limestone has a higher modulus than rocks typically found in coal mines, such as Mudstone, but the modelling work presented in chapter 3 predicted that this would make little difference to the wave behaviour at the successful test frequencies.

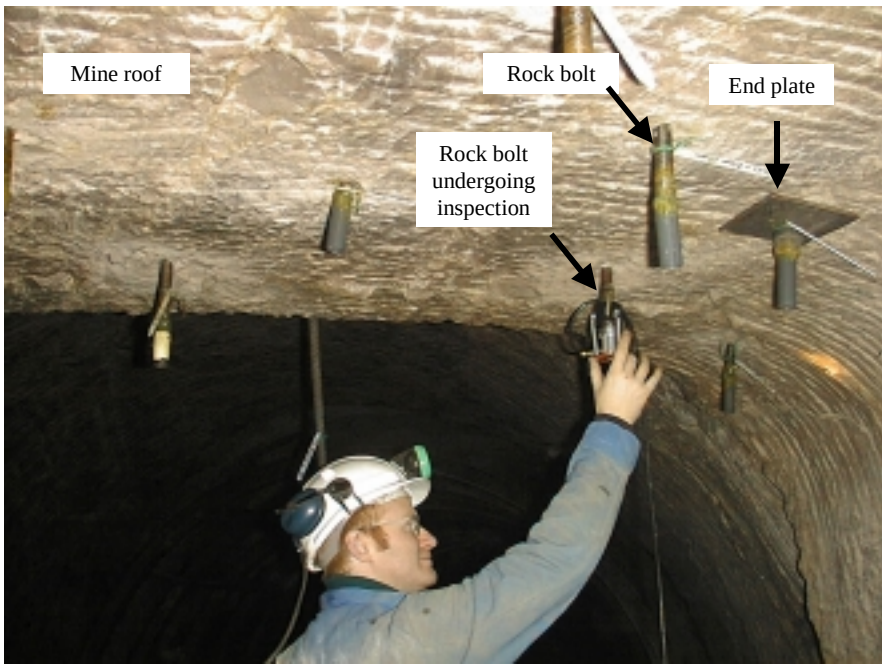

Figure 4.2: Rock bolts installed at the test facility in Middleton Mine.

4.2.3 Annesley Colliery

A limited amount of testing was carried out in a deep coal mine at Annesley Colliery, Nottinghamshire, UK. The opportunity arose from a consultancy contract undertaken by RMT Ltd. [76] to assess the condition of rock bolts in the mine. The tests were limited, as the only portable instruments available at the time were standard commercial units, with limited frequency control. Some successful tests were made at low frequency, but the high frequency results were unexpectedly poor, which brought about a closer study of the effect of curvature on guided wave propagation. This effect is discussed further in chapter 6.

4.3 Instrumentation

All of the ultrasonic tests reported in this thesis were made using the 'Wavemaker' range of instruments purpose built by Macro Design Limited [89]. The instruments are designed for guided wave testing, and can drive transducers with both pulse and toneburst signals at a controlled frequency. The instruments are capable of pulse-echo operation, and can apply up to 60dB of gain to the received signal, which can also be filtered. Wavemaker 'Duet', '10' and '16' models were used extensively during the testing program.

The 'Wavemaker Duet' can operate in the frequency range 50kHz-4MHz, and has a variety of pre-programmed excitation signals, including a selection of windowed tonebursts and pulses, although the unit can also be driven by an external function generator. The received signal must be captured by a digital oscilloscope, from where it can be transferred to a PC and analysed further.

The 'Wavemaker 10' is a development of the 'Duet', designed to operate up to a higher maximum frequency of 10MHz. The unit does not have any pre-programmed excitation signals, and so the required waveform was supplied and controlled by a PC, through a LeCroy 9101 Arbitrary Function Generator (AFG). The same PC was used to capture the received signal from a digital oscilloscope. Using this test configuration it was possible to carry out tests with a high number of cycles in the excitation signal, and also to carry out a series of tests at different frequencies automatically.

The modelling and early experimental work indicated that it would be necessary to carry out tests at frequencies lower than 50kHz. These tests were made using an adaptation of the 'Wavemaker 16' instrument developed for the long-range inspection of pipes at low frequency [29]. This instrument is capable of working at frequencies as low as 15kHz, and includes a function generator and digital sampling capability, controlled directly from a portable PC. The unit is portable, and also battery powered, making it very suitable for site testing work.

4.4 Bolt End Preparation

The condition of the contact area between the test specimen and the transducer affects the transmission of ultrasound across the boundary. As the frequency of the signal increases, and the wavelength decreases, the coupling between the transducer and the specimen becomes more important. All of the bolt ends were prepared prior to testing, either by turning the bolts on a lathe prior to installation, or by a portable bolt end preparing device fitted to a drill, This device was designed and produced by RMT Ltd. specifically for bolt inspection. Further details can be found in [78]. Both of these preparation methods were found to give a good enough surface

finish to test at all of the required frequencies. The transducer was coupled to the bolt with standard ultrasonic coupling gel, or grease, with no significant advantage found in using any particular product.

The consistency of the coupling is improved by clamping the transducer onto the bolt end, and a transducer holder was designed to screw onto the bolt threads. Figure 4.3 shows the clamp in use at Middleton Mine. The clamping force required to obtain good coupling is low, and there is no advantage in using higher clamping forces than necessary. Hand tightening of the 10mm cap head clamping screw pictured in figure 4.3 was more than sufficient to obtain consistent results.

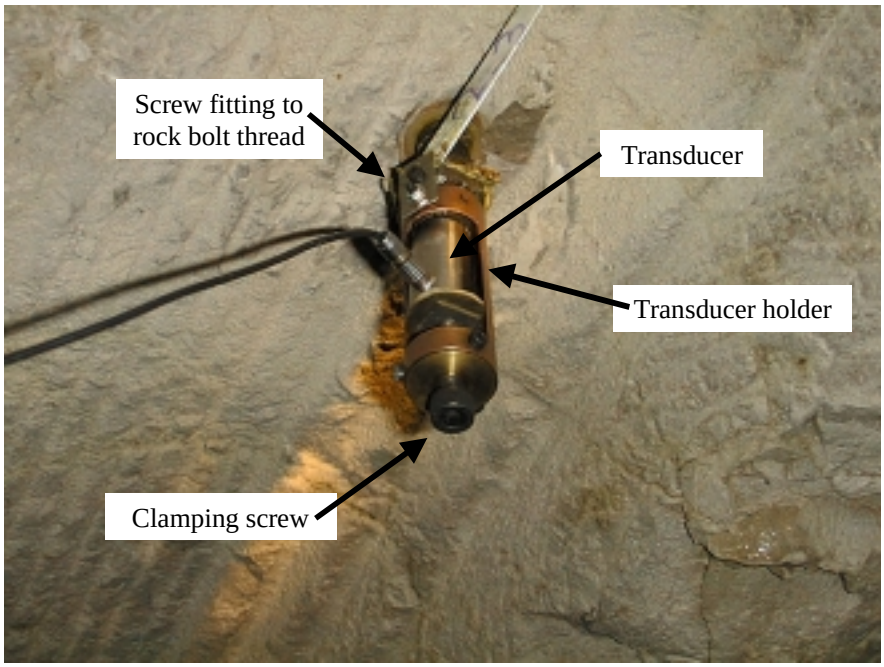

Figure 4.3: Picture of the holder designed to clamp the transducer firmly on to the end of a rock bolt.

4.5 Low Frequency Testing

4.5.1 Low Frequency Guided Wave Generation

In order to excite a specific guided wave in a structure, it is necessary to use a suitable combination of transducer and excitation signal. The frequency spectrum of the energy transferred to the structure is very important, and can be controlled either by the shape of the excitation signal or the resonant properties of the transducer. In both cases it is beneficial to use a transducer that has a displacement profile that matches the mode shape as closely as possible. The L(0,1) mode is relatively easy to generate, as it has a simple axially symmetric mode shape, which is already well matched to most transducers. Preferential excitation of other modes may be more difficult, for example, the F(1,1) mode is not axially-symmetric, and it is best generated

by a transducer that has two piezoelectric crystals with opposite polarity, as the resulting displacement at the surface of the transducer matches the mode shape better.

Resonant transducers

Preferential excitation of a given frequency through transducer design is achieved by selecting a suitable combination of piezoelectric element, backing material and casing so that the lowest natural frequency is equal to the desired excitation frequency. The transducer must be lightly damped, so that a sharp resonant peak is obtained. A disadvantage of a resonant design is that it is difficult to avoid ringing of the crystal and casing, therefore undamped reverberations within the transducer can mask received signals. Since the transducer will resonate at the target frequency, the bandwidth of the excitation signal is not important, providing that it contains some energy at the target frequency, and a simple voltage spike, such as that obtained from a capacitor discharge can be used. This 'pulse' will have a very wide frequency bandwidth, but only energy in the resonant frequency range of the transducer will be significantly transferred to the test specimen.

Non-resonant and damped transducers

A more controlled method of exciting a mode at a given frequency is to use a narrow bandwidth excitation signal, which removes the need for a resonant transducer and therefore reduces the risk of ringing. The transducer must either operate well away from the natural frequencies of the crystal, which in practice is difficult to achieve, or incorporate a high level of damping. Damping of the crystal through the use of backing materials widens and lowers the resonance peak, allowing the transducer to be effective over a wide frequency range. A windowed toneburst centred on the target frequency can then be used to excite the transducer. The toneburst will have a clearly defined frequency content that becomes narrower with increasing number of cycles. This is shown by figure 4.3, which shows the time and frequency domain signals for 5-cycle and 10-cycle Gaussian windowed tonebursts reaching a peak voltage of 1V. The higher cycle signal concentrates much more energy at the centre frequency of 50kHz, and limits the effects of dispersion. However, a disadvantage of the 10-cycle signal is that it is longer in time, and therefore early reflections may be hidden by the outgoing signal. The design of low-frequency non-resonant transducers is not straightforward, and has been developed and validated in other low frequency applications, such as [90].

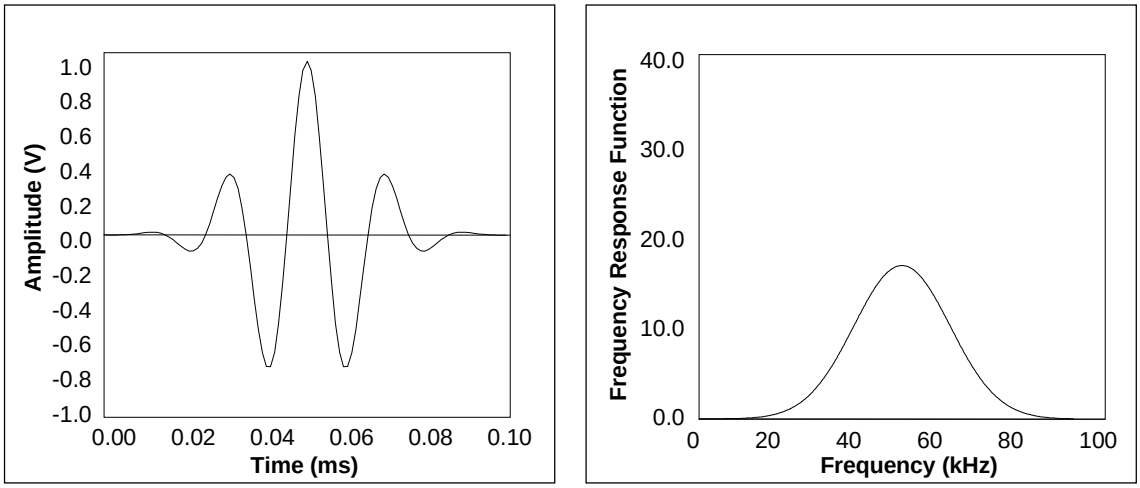

(a) 5-cycle toneburst.

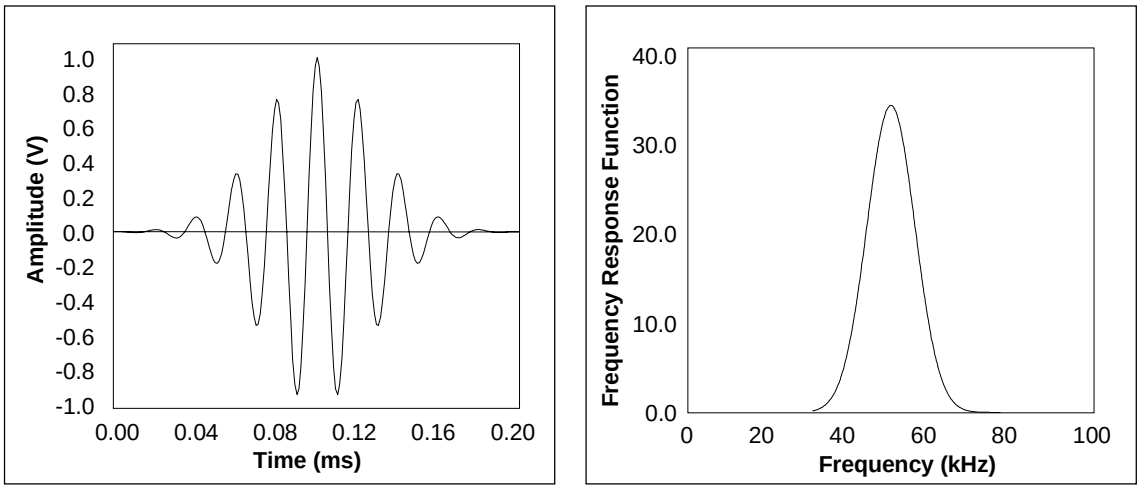

(b) 10-cycle toneburst.

Figure 4.4: Gaussian windowed tonebursts with (a) 5 cycles, and (b) 10 cycles, centred on 50kHz, with maximum amplitude of 1V, showing both the time and the frequency domain.

Following a feasibility study into the use of guided waves for rock bolt testing [77], initial investigations were carried out using resonant transducers with a centre frequency of 75kHz. This was primarily because the project collaborators, RMT Ltd. [76] were evaluating the potential of commercially available test instruments that were only capable of wide bandwidth pulse excitation. However, ringing of the transducer was found to cause problems at some frequencies, and most of the tests were inconclusive. To eliminate these problems, and to target the slightly lower frequency range predicted by the modelling outlined in this thesis, a highly damped transducer, with a centre frequency of 40kHz, was designed and constructed by Alltran Ltd. [91]. The risk of ringing was further reduced by the use of a thin piezoelectric crystal with a natural frequency above the required operating frequency.

4.5.2 Effect of Surface Features

An assumption of the modelling was that a rock bolt would behave like a smooth bar, as it is not possible to determine the dispersion relations for bars with 3 dimensional features analytically. The effect of the shear pin, threads and mixing ribs on the propagation of ultrasound along a rock bolt could be modelled at low frequency using finite element methods, but the models would be complex and time consuming to calculate, particularly if the embedding layers were included. A simpler method of verifying that this assumption is reasonable is to compare the signals recorded from a smooth bar and a rock bolt.

Figure 4.5 shows the recorded signals from a free rock bolt and a free 20mm diameter steel bar tested at 50kHz using the pulse-echo arrangement outlined in section 2.4. After some noise caused by the outgoing signal and switching from the send to the receive circuit within the instrumentation, the earliest clear reflection that can be seen in both cases is the L(0,1) mode reflected from the end of the specimen. This is followed by an end reflection from the slower F(1,1) mode, which is largely undamped in a free bar at this frequency. Although the transducer will preferentially excite the longitudinal mode, any slight misalignment or asymmetry in the crystal or transducer face can cause the flexural mode to be generated, hence the reflection has a lower amplitude than that for the L(0,1) mode. The third signal is a second reflection of the L(0,1) mode from the end of the specimen, that is a wave that has travelled from the transducer to the end and back twice. Note that the test in figure 4.5a used a resonant transducer, and some ringing can be seen on the tail of the echoes even at the low amplification required for this non-leaky case. The total travel time from the start of the outgoing signal to the start of the received signal was measured and used to calculate the wave speed. However, the start of the received signal can be difficult to distinguish, and it is easier to measure the time at the centre of the toneburst, where the maximum amplitude occurs. The arrival time has therefore been calculated from the time of the maximum amplitude, minus half of the initial toneburst duration. The measured and predicted wave speeds are shown together with percentage differences (shown in brackets) in table 4.2.

Specimen	**L(0,1) Predicted**	**L(0,1) (1)* Measured**	**L(0,1) (2)* Measured**	**F(1,1) Predicted**	**F(1,1) Measured**
20mm plain bar	4.97	4.91(1.2%)	5.00(0.6%)	3.17	3.19(0.6%)
21.7mm rock bolt	4.95	5.02(1.4%)	4.99(0.8%)	3.19	3.29(3.1%)

* (1) and (2) refer to measurements made from the first and second end reflections

Table 4.2: Comparison of predicted and measured wave speeds for a free bar/rock bolt. The percentage difference between the measured and predicted values is shown in brackets.

The results for a free bar and a free rock bolt are very similar, and no noticeable reflections are obtained from the rock bolt threads, shear pin hole or mixing ribs. The wavelengths of the L(0,1) and F(1,1) modes are about 100mm and 60mm respectively at this frequency, which is large compared with the surface feature dimensions of just a few millimetres, and therefore the wave is largely unaffected by such features. In addition, there is very little difference in relative amplitude between the first and second reflections for the two cases. The relative amplitude gives a measure of the amount of attenuation experienced by the wave in the bar/bolt, as it is independent of the properties of the transducer, and it is therefore unlikely that the surface features are causing any significant additional attenuation in the rock bolt case. Hence the modelling assumption of a smooth bar is accurate.

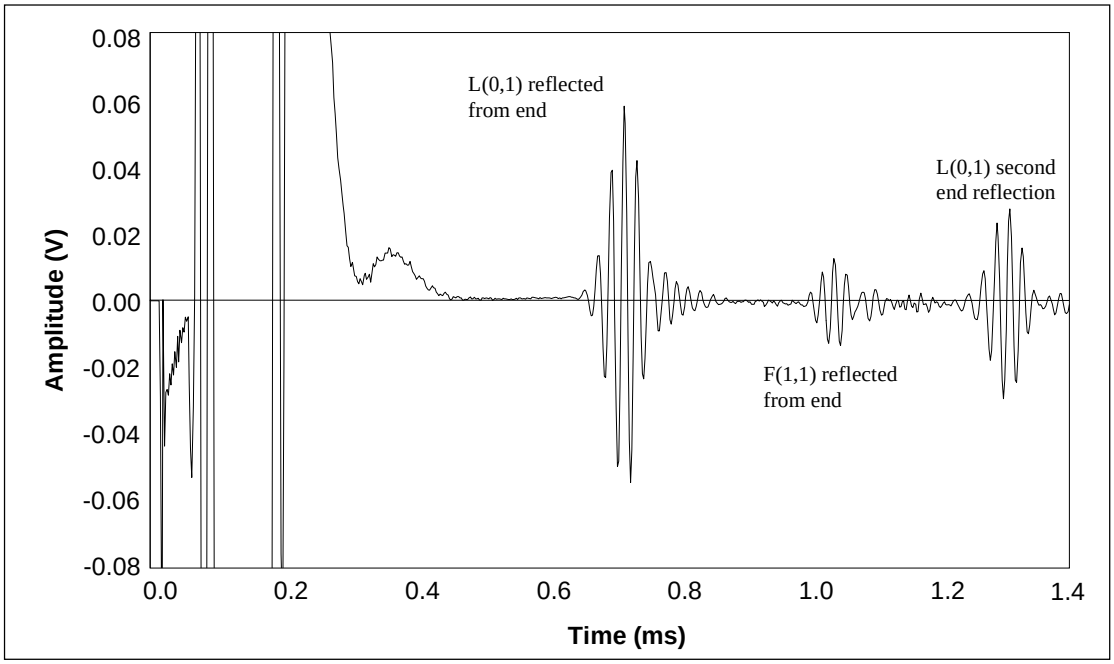

(a) Time trace recorded for a 1.8m free, smooth bar (non-resonant transducer).

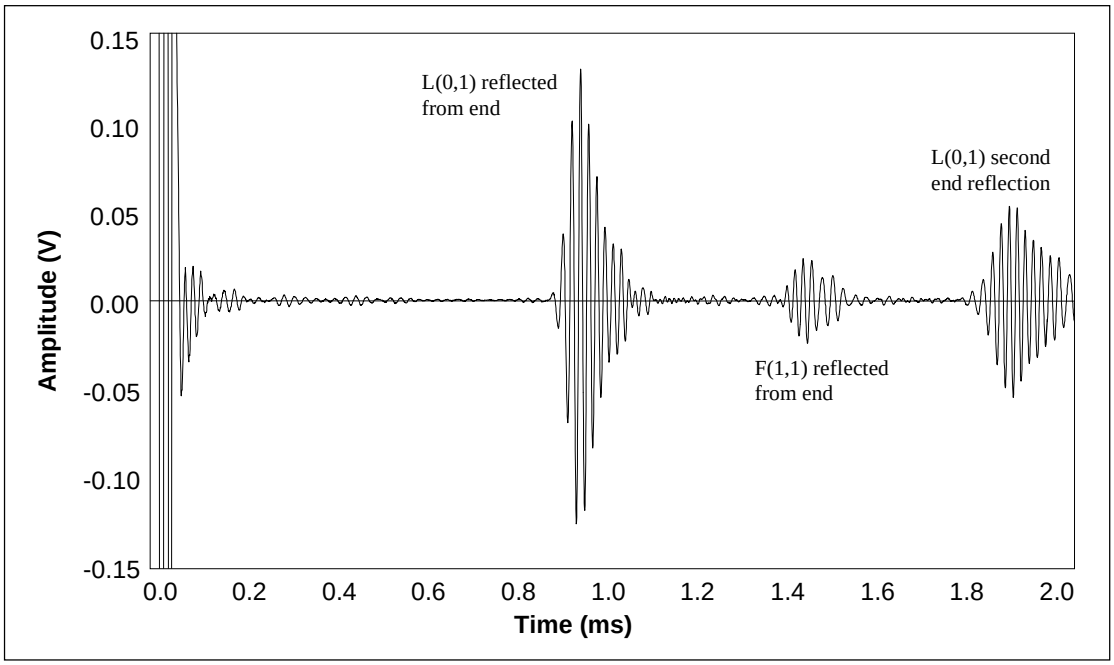

(b) Time trace recorded for a 2.4m free rock bolt (resonant transducer).

Figure 4.5: End reflections from a free bar and a free rock bolt, tested at 50kHz with a 10-cycle Gaussian windowed toneburst.

4.5.3 Effect of End Angle

Standard industrial rock bolts have a chamfered end that punctures the resin capsules and assists with installation into the pre-drilled hole. The precise angle of the chamfer can vary, but it is usually about 45° to the normal to the bolt axis. The effect this angle will have on the reflection of the L(0,1) mode from the end needs to be investigated, as it may cause significant mode conversion and therefore a reduction in signal amplitude.

Some finite element work into the reflection coefficient of L(0,1) from angled notches in free and embedded bars was carried out by Pavlakovic [92,31]. The study showed that a 100% reflection of the L(0,1) mode could be expected for a square or 45° notch extending through the full thickness of a free bar, whatever the orientation of the notch. The embedded case also showed a 100% reflection for a square notch extending through the full thickness of the bar, but the 45° results were slightly different, depending on the orientation of the notch. A reflection coefficient of 100% was obtained for a 45° notch initiating at the bar surface and aligned towards the centre of the bar, but this was reduced to 86% for a 45° notch that initiated at the bolt axis and was aligned towards the surface. A 50% loss of radius gave reflection coefficients of about 68% for all the free cases, and about 56% for all the embedded cases. This information suggests that the L(0,1) mode will be well reflected from any rock bolt end angle, but the results above are only for axially symmetric defects. The rock bolt end is not axially symmetric, raising the possibility of mode conversion to flexural modes, and therefore reducing the reflection coefficient of the L(0,1) mode. Modelling this type of defect requires a 3 dimensional finite element model, and is beyond the scope of the current finite element capability.

The reflection coefficient of L(0,1) from angled ends has been investigated experimentally, using the experimental procedure shown in figure 4.6. The L(0,1) mode was excited using a 10-cycle toneburst at 50kHz, 60kHz and 70kHz in plain steel bars with the chamfer angle cut at 0°, 10°, 20°, 30°, 40° and 45° to the normal to the bar axis. A laser interferometer was used to monitor the in-plane displacement at a location on the bar that allowed the incident and reflected signals from the end to be separated in time. The relative magnitude of these two signals gives a measure of the reflection coefficient at the end, neglecting any material losses.

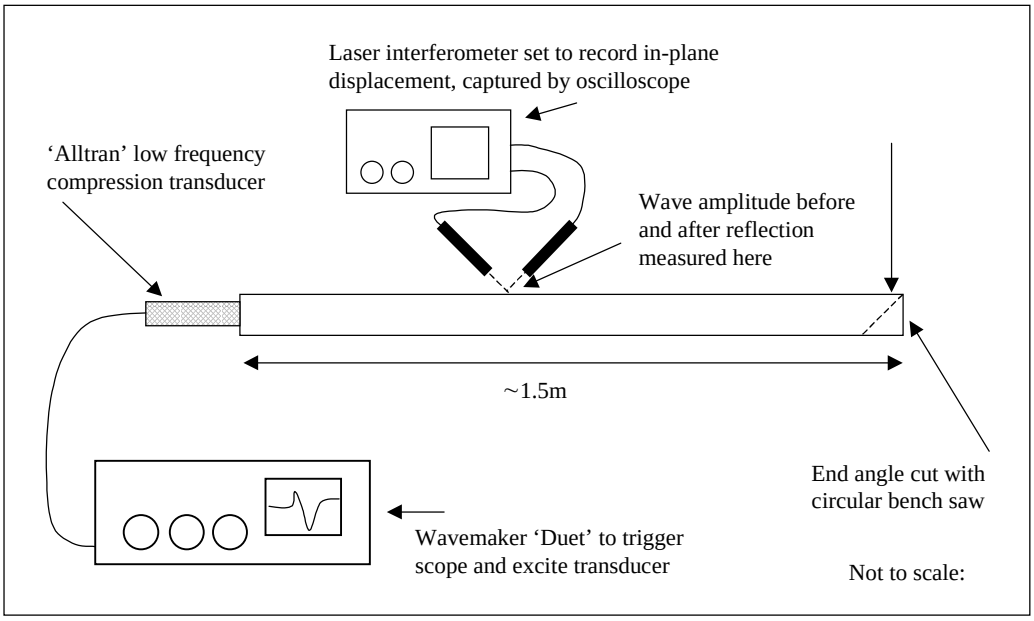

Figure 4.6: Low frequency end angle reflection coefficient - experimental set up.

The results of this experiment, given in figure 4.7, show that reflection of the L(0,1) mode is largely unaffected by end angle at these frequencies. However, there is considerable spread in the data, caused by the low signal to noise ratio obtained from the laser signal. This is due to the difficulties associated with measuring the in-plane displacement on a curved surface, where a low proportion of the laser signal is reflected directly towards the receiver. There is a trend towards lower reflection coefficient as the end angle increases, this is because an increasing amount of energy is converted to the flexural F(1,1) mode. However, the effect is small because the length of the end region of the bolt is still small compared to the wavelength. Whilst this experiment does not rigorously evaluate mode conversion and end effects, it does confirm that the attenuation due to end angle will be small compared to the attenuation due to leakage, and therefore the test can be used with confidence for any bolt end angle.

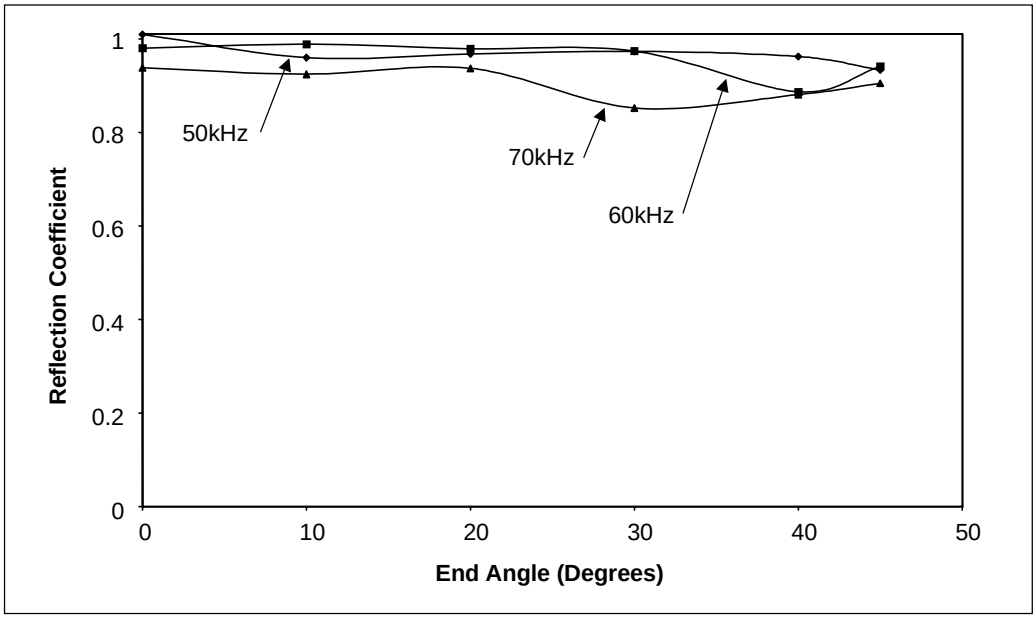

Figure 4.7: Reflection coefficient of the L(0,1) mode from the end of a 20mm diameter steel bar with varying end angle.

4.5.4 Laboratory Specimen Test Results

This section presents and discusses the results of the laboratory tests on the fully and partially encapsulated low frequency rock bolt specimens described in section 4.2.1. The laboratory tests have been used to prove the concepts of the technique, and to develop the instrumentation, transducers, and the application of data processing. It was found that because most of the noise tends to be coherent, signal processing and averaging does not greatly improve the signal to noise ratio. All the results presented were taken with 4 averages, but there is little difference from the 'live' signal. The amplifier gain was set between 30dB and 50dB, with higher gain needed for the specimens with a longer embedded length. Whilst a narrow band signal is desirable, it is not practical to use a high number of cycles at low frequency because the signal becomes very long in time. Tonebursts of 6 cycles have been found to give good results below about 40kHz, but at frequencies above this the shorter time duration allows the use of up to 10 cycles.

Fully encapsulated rock bolt

Figure 4.8 shows the time traces recorded at six different frequencies for a 2.3m rock bolt installed into a 2m length of concrete (specimen LF1). The threaded end was exposed by about 200mm, and in addition about 100mm was left free at the normally encapsulated end to assess the effect of changes in the end condition. No appreciable difference in signal was noticed for changing the end angle, varying the surface roughness, or coating the end with epoxy, verifying that the low frequency test is largely insensitive to the bolt end conditions.

Figures 4.8b-f all show clear L(0,1) end reflections at frequencies between 30kHz and 60kHz, with the best results obtained between 30kHz and 40kHz. These results are in the frequency range where the modelling predicts little variation in attenuation and velocity with material properties and geometry. Figure 4.8a shows that no clear end reflection was obtained for the 20kHz test. The apparent early reflection is probably caused by transducer ringing and reverberations in the free end of the bolt. The high attenuation that was predicted by the modelling work in chapter 3 prevents the end reflection from being large enough to be detected at this frequency. At frequencies above 50kHz, the amplitude and clarity of the end reflection is reduced. One explanation for this could related to the fact that as the wavelength of the guided wave decreases, the sensitivity to small changes in epoxy properties and materials increases. There will be a small amount of reflection and mode conversion as the wave encounters these changes, the cumulative effect of which will be increased wave attenuation, as the individual reflections will be too small to detect.

Table 4.3 shows the measured energy velocity of the L(0,1) mode in the specimen, together with the predictions made by the basic rock bolt model outlined in chapter 3, but with the embedding material changed to be concrete. The measured velocities have been adjusted to take into account the higher speed in the short free sections, using the measurements shown in table 4.2. In general the measured energy velocity is higher than that predicted by the basic model, and there is less variation with frequency. This difference could be explained by the effect of any of the model parameters discussed in sections 3.4.4-3.4.7. In particular the results for the model with 75% bond quality, also shown in table 4.3, would give a good match. The overall reduction in bond quality could be caused by a constant reduction along the whole length of the bolt, or localised badly bonded regions. The partially encapsulated specimen results given in the next section suggest that poor bonding and shrinkage effects may be significant close to the free ends, leading to speeds closer to the free bar velocity.

The observation that the energy velocity varies less with frequency than predicted by the basic model could be explained by a lower than expected embedding material modulus. However, since the concrete was mixed and cured under ideal conditions, and the material properties were measured after curing, this is unlikely. This effect is more likely to be caused by the bandwidth of the input signal. For example, the 30kHz signal contains energy at frequencies in the 20-40kHz range, and the energy velocity will to some extent depend on the energy velocity in the whole frequency range.

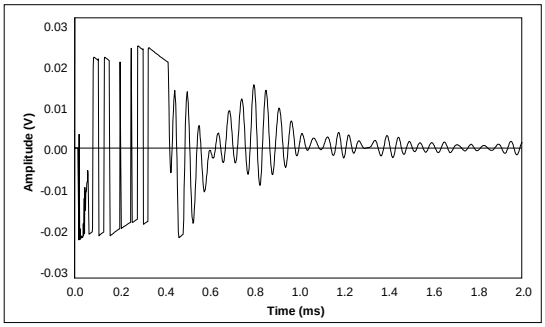

(a) 20kHz, 6-cycle toneburst.

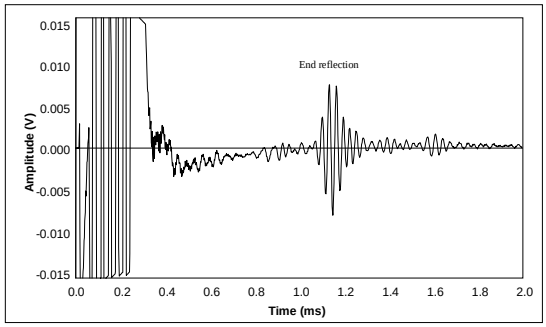

(b) 30kHz, 6-cycle toneburst.

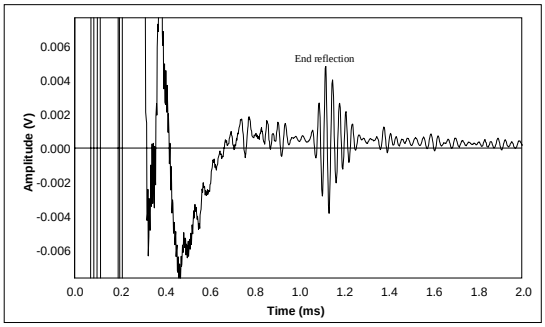

(c) 35kHz, 6-cycle toneburst.

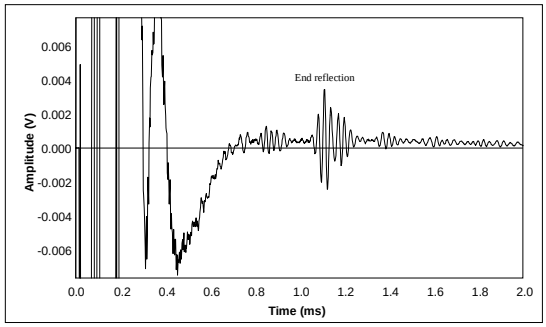

(d) 40kHz, 6-cycle toneburst.

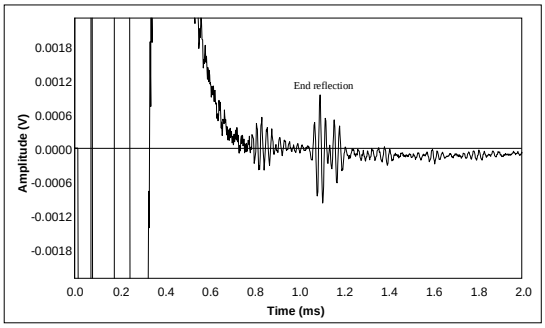

(e) 50kHz, 6-cycle toneburst.

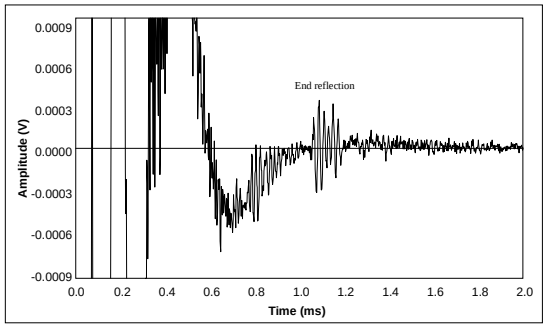

(f) 60kHz, 6-cycle toneburst.

Figure 4.8: Time traces recorded at different frequencies from laboratory specimen LF1, consisting of a 2.3m flat-ended rock bolt with the centre 2m embedded in mortar/concrete.

Frequency (kHz)	**Predicted E_{vel} (m/ms) (standard model)**	**Predicted E_{vel} (m/ms) (75% bonding)**	**Measured E_{vel} (m/ms)**
30	3.91 (9.9%)	4.10 (4.9%)	4.30
35	4.07 (7.6%)	4.23 (3.5%)	4.38
40	4.15 (5.8%)	4.32 (1.6%)	4.39
50	4.25 (2.8%)	4.40 (0.7%)	4.37
60	4.27 (2.3%)	4.42 (1.1%)	4.37

Table 4.3: Measured and predicted L(0,1) energy velocity for a rock bolt installed into concrete, based on the time traces shown in figure 4.8. The percentage difference between the predicted and measured values is shown in brackets.

Partially encapsulated rock bolt

Figure 4.9 shows the time traces recorded at six different frequencies for a 2.4m rock bolt installed into a 1.5m blind hole (specimen LF2). The 0.9m free length at the threaded end of the bolt simulates the case of partial resin encapsulation and allows the reflections from the epoxy boundary to be investigated. The embedded and free lengths have been chosen so that the end and resin reflections will not coincide, should multiple reflections from the resin be present. Partial resin encapsulation can occur if insufficient resin capsules are used, which may occur if the hole is oversized along any part of its length. It is not possible to inspect for this defect visually because the end plate and nut effectively seal off the end region.

The most promising results were obtained between 30kHz and 50kHz, where reflections can be seen from the start of the resin encapsulation and the bolt end. The 20kHz signal shows some evidence of end and resin reflections, but the long time duration and low amplitude signals are difficult to interpret accurately. A good reflection is obtained from the resin at 60kHz, but the end reflection is poor. The reflection of the L(0,1) mode in a steel bar as it enters a block of epoxy has been investigated by Vogt [93] using experimental and finite element methods. The reflection coefficient is only about 0.03 at 40kHz for this diameter bar, which is much smaller than the near unity reflection coefficient at the bar end. The epoxy reflection appears to be larger than the end reflection because of the high attenuation the end reflection has experienced in the embedded section. The epoxy boundary is also present in all fully encapsulated bolts, although in this case the free length is to short for the reflection to be separated in time from the transducer and amplifier noise in the early part of the recorded signals. The small reflection coefficient makes ringing due to multiple reverberations of the signal in this short free section of a bolt unlikely - the 35KHz and 40kHz cases show a possible second reflection of L(0,1) from this interface, but it is very small.

The 35kHz and 40kHz cases also show some evidence of a reflection of the F(1,1) mode from the start of the resin encapsulation. This mode will be generated by the transducer, and can also be reflected from the epoxy boundary. However, the F(1,1) mode may also be generated by mode conversion from the incident L(0,1) mode at the resin boundary, particular if the resin boundary is not axially symmetric. Similarly, small amounts of L(0,1) may be generated at the boundary by the incident F(1,1) mode. These mode converted reflections will arrive in between the F(1,1) and L(0,1) reflections, which may explain the complexity of the observed time domain signals around 0.6ms.

The calculated and predicted wave velocities for the free and embedded sections are shown in table 4.4. The embedded energy velocity is consistent with that measured on the fully

encapsulated specimen, and is within the range predicted by the modelling. It has been assumed that the wave travels at the free bar speed in the non-encapsulated length. However, the measured velocities for the L(0,1) mode that has been reflected from the epoxy boundary are much slower than expected for a free bar. It is unlikely that the wave does travel more slowly, and the boundary reflection is too early to be that from an incident L(0,1) mode and reflected F(1,1) mode. Therefore, it is likely that the wave is reflected further along the bolt than expected, possibly due to poor epoxy contact at the start of the bolt. This could be due to a combination of shrinkage during curing, movement of the bolt during curing, and resin loss close to the end. This effect has also been observed in separate experiments made by RMT [76].

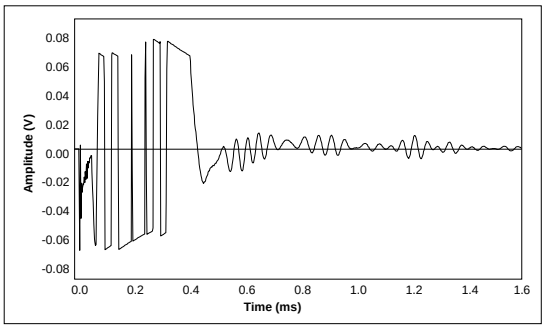

(a) 20kHz, 6-cycle toneburst.

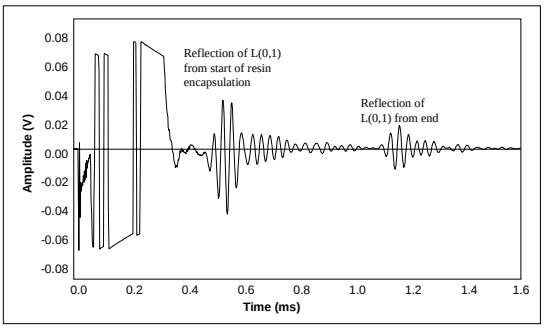

(b) 30kHz, 6-cycle toneburst.

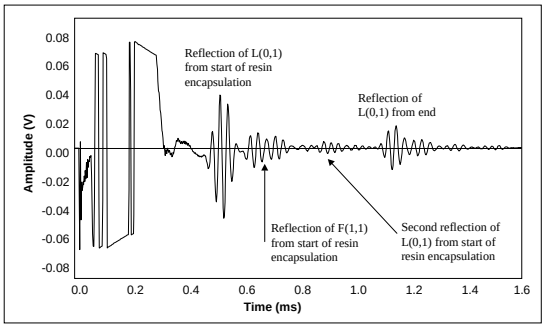

(c) 35kHz, 6-cycle toneburst.

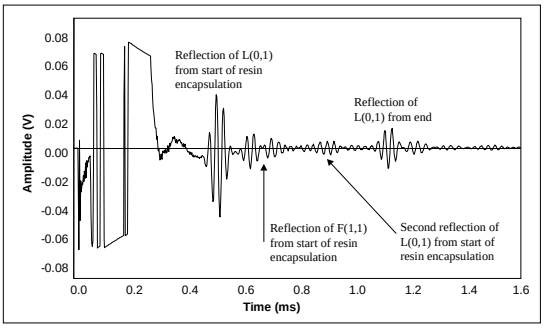

(d) 40kHz, 6-cycle toneburst.

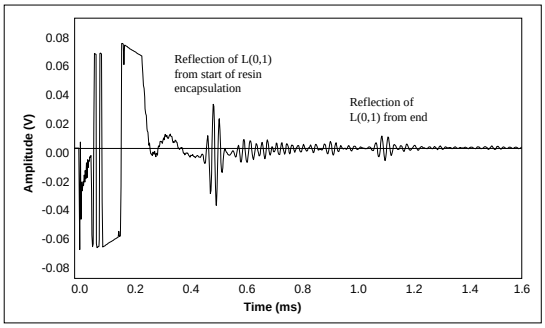

(e) 50kHz, 6-cycle toneburst.

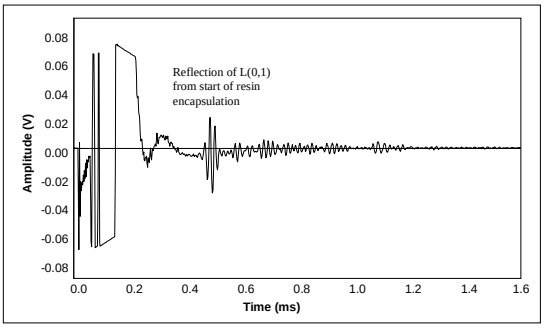

(f) 60kHz, 6-cycle toneburst.

Figure 4.9: Time traces recorded at different frequencies from laboratory specimen LF2, consisting of a 2.4m flat-ended rock bolt with the final 1.5m embedded in mortar/concrete.

Frequency (kHz)	**Predicted E_{vel} (m/ms) (embed)**	**Measured E_{vel} (m/ms) (embed)**	**Predicted E_{vel} (m/ms) (free)**	**Measured E_{vel} (m/ms) (free)**
30	3.91 (8.9%)	4.26	4.97 (18.1%)	4.07
35	4.07 (6.4%)	4.33	4.97 (17.9%)	4.08
40	4.15 (4.8%)	4.35	4.97 (15.3%)	4.21
50	4.25 (2.1%)	4.34	4.97 (15.5%)	4.20
60	4.27 (2.1%)	4.36	4.97 (15.9%)	4.18

Table 4.4: Measured and predicted L(0,1) energy velocity in the free and embedded sections of a rock bolt partially installed into concrete, based on the time traces shown in figure 4.9. The percentage difference between the predicted and measured values is shown in brackets.

4.5.5 Site Test Results

The laboratory results show that the L(0,1) mode has the potential to inspect a fully encapsulated 2.4m rock bolt for bolt length and loss of resin encapsulation. Figure 4.10 shows the results of tests undertaken on 1.0m, 1.8m and 2.4m rock bolts at Middleton Mine. These results were obtained using the non-resonant transducer and the 'Wavemaker 16' instrument, and are considerably improved over earlier results taken with a resonant transducer. In general, the optimum test frequency was in the range 30-45kHz, although the higher end of this range often gave better results. This is slightly higher than the optimum for the bolts tested in the concrete block, and reflects the change in the frequency of the attenuation minima with embedding material modulus predicted by the modelling in section 3.3.4.

Figures 4.9a and 4.9b show clear end reflections from 1.0m and 1.8m rock bolts, which both have flat ends. The L(0,1) mode energy velocity has been calculated from the echo arrival times at the successful test frequencies. These measured velocities are compared with those predicted by the modelling in table 4.5, and show excellent agreement. However, this does not necessarily mean that the site conditions are exactly as modelled, as there are many factors that can affect energy velocity and attenuation. Overall conclusions can only be made from a combination of the high and low frequency, site and laboratory, results.

Frequency (kHz)	**Predicted E_{vel} (m/ms)**	**Measured E_{vel} (m/ms)**
35	3.94 (1.3%)	3.99
40	4.08 (0.2%)	4.07
45	4.18 (0.5%)	4.20

Table 4.5: Estimated and predicted wave speeds in rock bolts embedded in limestone. The percentage difference between the predicted and measured values is shown in brackets.

Figure 4.10c shows the time trace recorded for a 2.4m rock bolt installed at Middleton. There is a signal starting at approximately 1.0ms that may be a reflection from the bolt end, but the time trace is dominated by earlier reflections. Assuming the bolt is defect-free, these early reflections could be from changes in the epoxy conditions, or from features in the rock such as a fault line. Numerous bolts at Middleton showed such early reflections, and this is likely to be a problem of testing in high modulus rocks, where the embedding material modulus is closer to that of steel than would be the case in typical coal mine conditions. High modulus rocks have acoustic properties closer to the properties of steel than lower modulus rocks, and the sensitivity of the L(0,1) mode to features in the rock is increased. A problem of the early reflections is that it is difficult to apply enough gain to the received signal to clearly see the end reflection. This is because the amplification is applied to the whole signal, and the resulting very high amplification of early reflections (including the start of the encapsulation) causes the amplifiers to saturate at high gain. The resulting amplifier recovery time is long, and can mask later reflections. This could be prevented by the use of amplifiers that could apply a time variable gain. This would allow attenuation due to leakage to be directly compensated for, so that equally sized reflectors would appear as equal size echoes, without amplifier saturation occurring. The issue of what is causing the early reflections is an important one, as they would indicate defects in a real test. Investigation into this could be achieved by over-coring the existing bolts for further examination, after testing with improved instrumentation.

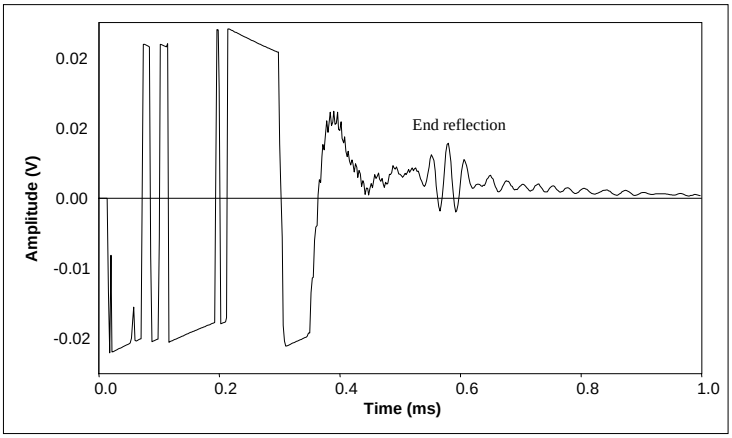

(a) Bolt 31 - 1.0m, tested at 35kHz with a 6-cycle toneburst.

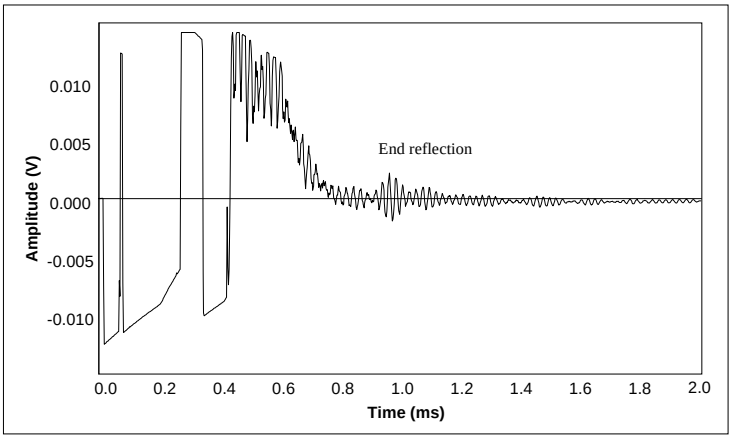

(b) Bolt 32 - 1.8m, tested at 45kHz with a 10-cycle toneburst.

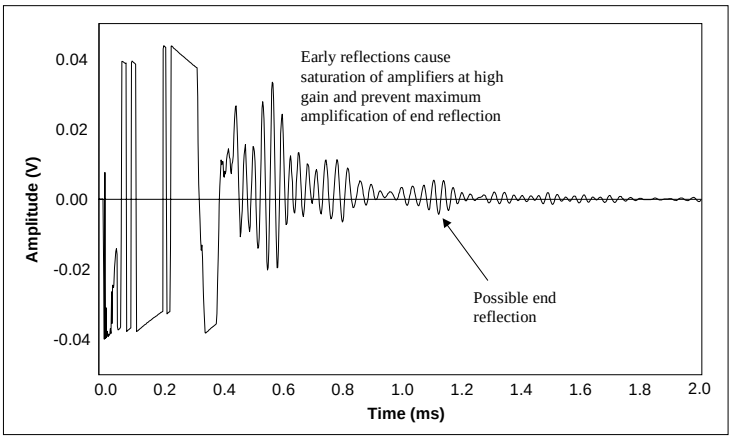

(c) Bolt 16 - 2.4m, tested at 30kHz with a 6-cycle toneburst.

Figure 4.10: Time traces recorded from rock bolt specimens installed at Middleton Limestone Mine.

4.5.6 Low Frequency Conclusions

The first part of this chapter has shown that the L(0,1) mode can be successfully used to detect the residual length of embedded rock bolts. The mode can also be used to detect the start of the resin encapsulation if the bolt has not been fully encapsulated. The F(1,1) mode was also reflected from the start of the encapsulation, which may provide a way of identifying resin loss from other defects, as the F(1,1) mode would be quickly attenuated if reflected from embedded defects. The L(0,1) mode should show sensitivity to partial depth defects such as deep corrosion patches, but this would require further research following instrumentation development.

The L(0,1) mode is best excited with a highly damped compression transducer with a centre frequency of about 40kHz. This allows testing to be undertaken over the whole 30-50kHz range with a single transducer, through the use of a toneburst excitation signal. The optimum number of cycles in the excitation signal is between 6 and 10, depending on the exact bolt conditions. Higher cycle signals are generally better, but are longer in time and reduce the resolution of the test, especially in the lower end of the frequency range. The use of a 20mm diameter transducer maximises the energy transferred to the bolt, and prevents the occurrence of coupling problems to the bolt edges, which may not be perfectly flat due to the presence of the threads. Coupling to the bolt can be achieved by hand, or by clamping the transducer to the bolt end, using grease or ultrasound coupling gel to maximise the acoustic transmission.

Very successful results have been obtained from a rock bolt embedded in a 2m length of concrete in the laboratory, which suggests that the end of a standard 2.4m rock bolt should be detectable using the method. Successful results have also been recorded from rock bolts up to 1.8m long installed in a limestone mine. The reduction in range was primarily caused by the numerous early reflections that were obtained, thought to be from some geological feature. These early signals prevented the use of very high amplifier gain, as the receiver amplifiers became saturated by the early reflections, and did not recover quickly enough to allow the end reflection to be resolved. It is believed that this can be overcome by instrumentation development that allows the use of time variable gain, which increases the gain over time to compensate for the attenuation due to leakage. Alternatively, amplifiers with a faster recovery time could be used, allowing the bolt to be screened in a number of sections, with the gain reset for each test.

The results of the testing have been compared to the modelling predictions outlined in chapter 3. The smooth bar assumption was shown to be accurate, and the measured speeds of the F(1,1) and L(0,1) modes in a free bolt matched the predictions well. The measured speeds also compared well with the predictions for embedded rock bolts, both for the laboratory specimens

embedded in concrete and those embedded in limestone at Middleton Mine. However, the variation in energy velocity across the 30-50kHz range was less than predicted. This is partly an effect of the bandwidth of the excitation signal, but it also indicates that the attenuation due to leakage is lower than predicted. This is expected, as the attenuation predicted by the modelling would be too high to produce the reliable test results that have been recorded. This lower than expected attenuation occurs because the bonding at the epoxy interfaces is not perfect, lowering the acoustic coupling and therefore the leakage. A further reason for the better results obtained in the laboratory may be that these interfaces were dry in the laboratory specimens. It is possible that the large amount of water present in the limestone mine improves the acoustic coupling between the epoxy and the rock/bolt and therefore increases the leakage. This is discussed further in section 4.7.

4.6 High Frequency Testing

4.6.1 High Frequency Guided Wave Generation

As at low frequency, a suitable combination of transducer and excitation signal must be used to generate the required L(0,11) mode in a rock bolt. The complex displacement pattern of this mode cannot easily be replicated by a single transducer, and since there are a large number of modes that can exist at high frequency, any transducer will generate a lot of modes. However, a simple compressional transducer, placed centrally on the specimen end, will preferentially excite the modes with axially symmetric mode shapes that are within the frequency bandwidth of the excitation signal. The transducers used for the testing were 'Aerotech' [94] ½ inch diameter immersion probes from the 'Alpha' and 'Gamma' range, with centre frequencies of 2.25MHz. The 'Alpha' probe incorporates a higher level of damping than the 'Gamma' probe, allowing use over a slightly wider bandwidth, but with less signal amplitude for a given excitation signal. The transducers were found to give good results when coupled directly to the bolts with either ultrasound coupling gel or grease. The use of transducers with a slightly smaller diameter than the bolt gave a good match to the L(0,11) mode shape, which has little displacement at the bolt edges.

All of the high frequency tests reported in this thesis were recorded using the 'Wavemaker 10' pulse echo instrument described in section 4.3. Signal averaging was used to reduce the high level of random noise that occurs at high frequency, with typical results having been averaged 50-100 times. A band pass filter incorporated into the instrument was also used to improve the signal to noise ratio.

The large number of modes generated at high frequency causes problems in examining the behaviour of specific modes at specific frequencies in a free bar. This is because most of the modes are highly dispersive, which leads to a complex end reflection that is much longer in time than the input signal. The same principles apply to an embedded bar, but the vast majority of the modes generated will not be low-leakage modes, and will therefore be attenuated through leakage into the embedding material. The embedding material therefore acts as a mechanical filter, removing all the unwanted modes, and allowing the low-leakage modes to be investigated. The modelling work outlined in chapter 3 shows that these low-leakage modes have distinct attenuation minima. Low-leakage modes will propagate at all of the frequencies with attenuation minima that are within the bandwidth of the excitation signal. The next section shows that there are significant advantages in controlling the frequency bandwidth so that only a single low-leakage mode is excited.

4.6.2 Optimum Excitation Signal

The short period of the high frequency waves means that a large number of cycles can be used in the input signal without a severe penalty in resolution. This means that a lot of energy can be put into a structure at a precise frequency, in order to excite a mode at a chosen point on the dispersion curves. This means that the high frequency modes can be used at points that would otherwise be too dispersive at low frequency. The number of cycles in the excitation signal has been investigated to determine the effect on the amplitude of the end reflection. Figure 4.11 shows the amplitude of the end reflection obtained from a 2m flat-ended rock bolt at Middleton Mine, with varying numbers of cycles. The excitation signal was a Gaussian-windowed toneburst, centred on an attenuation minimum at 2.6MHz, which was found by carrying out an FFT of the reflection obtained with wider bandwidth signals. This frequency corresponds to the minimum in attenuation on the L(0,11) mode at 2.57MHz that was predicted by the modelling in chapter 3. The actual frequency of 2.6MHz is well within the 2.57-2.65MHz range predicted for different types of steel in section 3.4.8.

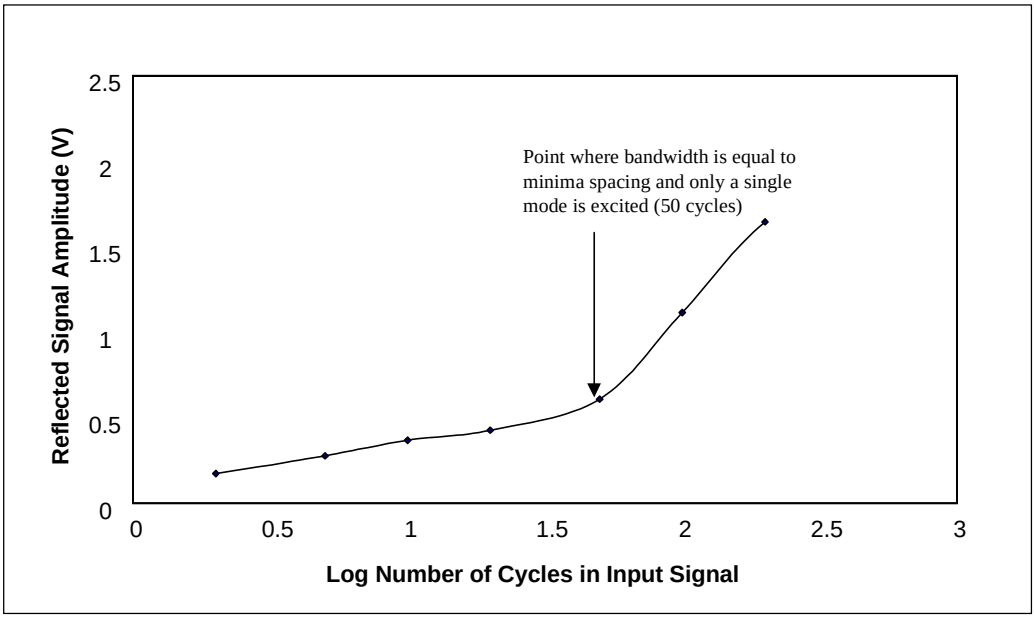

Figure 4.11: Amplitude of end reflection from a 2.0m embedded rock bolt at 2.6MHz, with varying number of cycles in the input signal.

Figure 4.11 shows that the amplitude of the end reflection initially increases linearly with the logarithm of the number of cycles, as the energy that is input to the rock bolt increases. This energy is increasingly concentrated at the centre frequency of the toneburst, which corresponds to one low-leakage point on the L(0,11) mode, hence increasing the end reflection amplitude. However, a step change in the improvement occurs at about 50 cycles, as shown on figure 4.11. This step change in improvement can be explained by looking at the signal bandwidth and the

frequencies of the other low-leakage points. Figure 4.12 shows the shape of a 50-cycle input signal in the time and frequency domains. The bandwidth is such that all of the energy is concentrated on just one attenuation minimum at 2.6MHz, with very little energy at the frequency of the nearest adjacent attenuation minima, approximately at 2.4MHz and 2.8MHz. This suggests that it is best to excite a single low-leakage point on a mode in order to obtain the clearest end reflections.

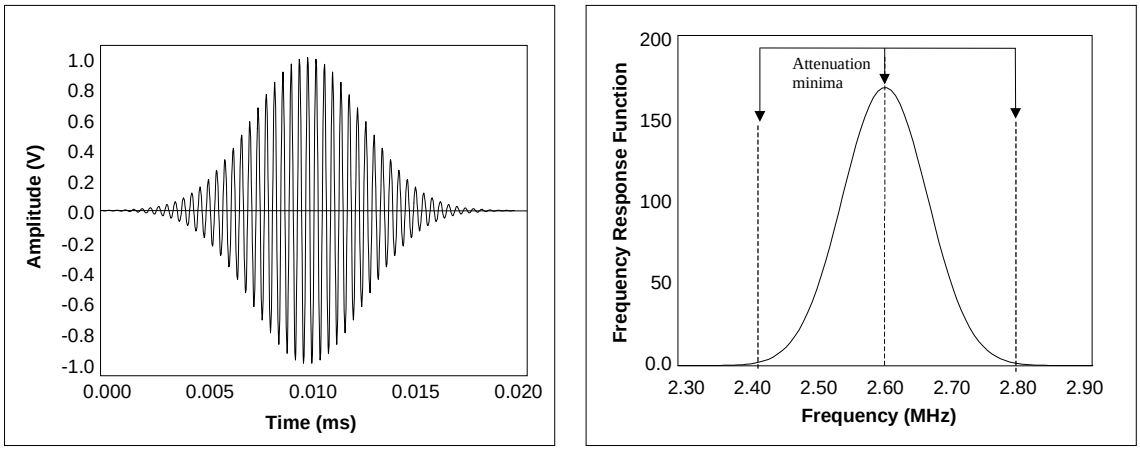

(a) Time Domain. (b) Frequency Domain.

Figure 4.12: Typical high frequency input signal consisting of a 50-cycle Gaussian windowed toneburst centred on 2.6MHz, showing (a) the time domain, and (b) the frequency domain.

It can be shown that the reason for exciting a single mode is that it prevents destructive interference between modes, which would otherwise occur if more than one mode was excited. Figure 4.13a shows the end reflection obtained from a 2m long rock bolt using a 10-cycle toneburst centred on 2.6MHz. The end reflection arrives between the times of 0.680ms and 0.720ms, and appears to be made up of several different packets. The FFT of the end reflection is shown in figure 4.13b, together with the bandwidth of the input signal. The FFT shows that energy is reflected in specific, narrow frequency ranges that correspond to the attenuation minima predicted by the modelling, and all of the low-leakage modes within the bandwidth of the input signal have been reflected from the bolt end. More information about each of these modes can be obtained by isolating one frequency peak from the FFT and converting from the frequency domain back to the time domain. This procedure was carried out for each mode shown by the FFT, and an example of a resulting time trace is shown in figure 4.13c for the 2.6MHz mode. The time trace shows that the reflection of the 2.6MHz mode is spread over the whole of the 0.680-0.720ms range that was occupied by the whole signal. A similar result was obtained for all the other modes, showing that the distinct packets observed in figure 4.13a are a result of an interference pattern between the modes. This is confirmed by the time trace shown

in figure 4.13d, which shows a sum of all the time traces extracted for each mode. As expected, the resulting signal resembles figure 4.13a, although there are some differences caused by the choice of window for each signal. In fact, not all the modes were received in exactly the same time window. It was noticeable that the higher frequency modes arrived very slightly earlier, which confirms the increasing energy velocity with increasing frequency predicted by the modelling. This analysis shows that it is best to use a very narrow bandwidth signal to test rock bolts at high frequency, so that the end reflection amplitude is maximised by avoiding interference and concentrating the energy at a single low-leakage frequency. However, lower bandwidth signals are longer in time, which reduces the ability to inspect the bolt in the region close to the transducer, and the ability to resolve defects that are close together.

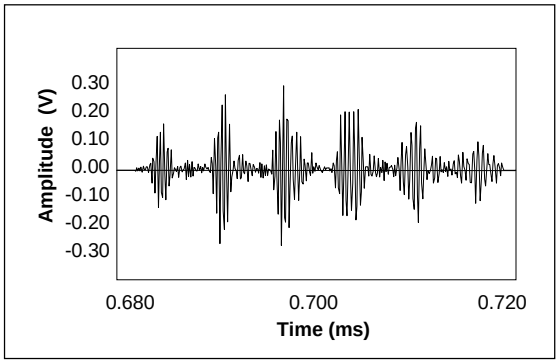

(a) Detail of the end reflection, which appears to consist of several distinct reflections.

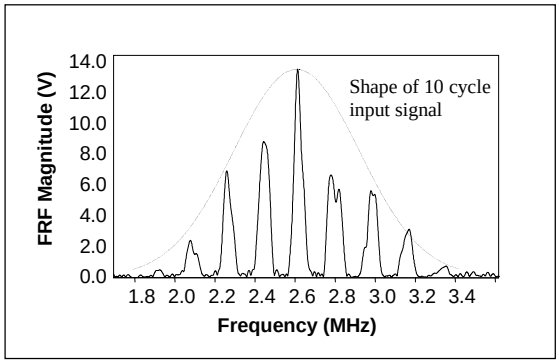

(b) FFT of the complete signal in (a) shows energy travelling at distinct frequencies, corresponding to attenuation minima.

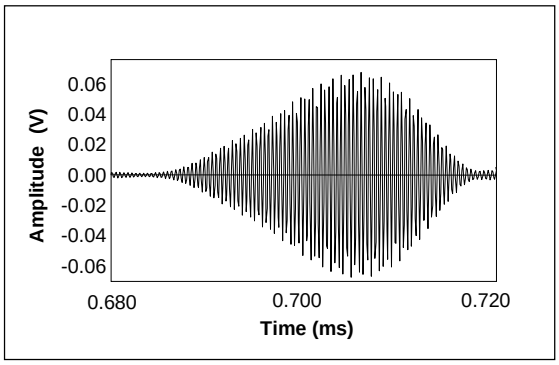

(c) Individual time domain signal for the 2.6MHz mode, obtained by isolating the mode from the FFT plot and converting back to the time domain. The mode arrives in the same time window as the complete signal.

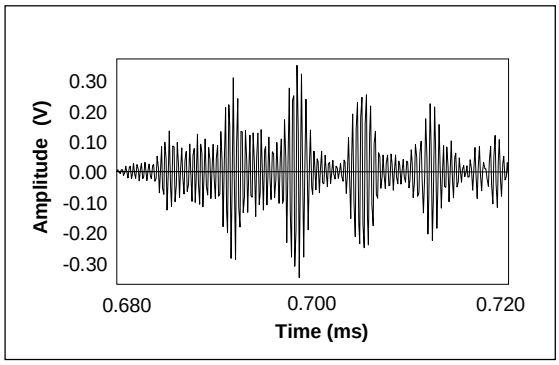

(d) The signal obtained by summing the individual time domain signals from each mode shown in figure (b). Closely resembles the original signal shown in (a).

Figure 4.13: Analysis of the end reflection from a 2m rock bolt with a relatively wide bandwidth (10-cycle) excitation signal, centred on 2.6MHz.

4.6.3 Effect of Surface Features

The effect of the rock bolt shear pin, threads and mixing ribs was evaluated at low frequency by comparing the time traces from a smooth steel bar and a rock bolt. The effect was found to be negligible because the feature dimensions are much smaller than the wavelength of the guided wave. However, at frequencies in the range 2-3MHz, the wavelength of the low-leakage modes is 2-3mm, and therefore could be much more sensitive to the surface features. It is difficult to repeat the low frequency experiment for the high frequency modes, because the large number of modes generated at high frequency in a free bar makes it impossible to examine the effect of a feature on just one mode. An embedded length could be used to filter out modes with high attenuation due to leakage, but it is likely that variations in the embedding material and transducer coupling between specimens would cause more changes in attenuation than the surface features. For this reason, the effect of the surface features is only discussed qualitatively at high frequency.

Numerous experiments have been conducted on bolts with and without shear pin holes, and on smooth bars throughout the testing program for rock bolts and tendons (chapter 5), and no particular differences have been noticed between the results. No ringing has been detected in the early part of the received signal, which suggests that the shear pin hole and threads are not significant reflectors. There will be some reflection from these features, and from the mixing ribs, but the reflections are too small to detect, and have little effect on wave propagation. It is likely that the combined effect of all these features is a small increase in the attenuation of the wave. The reason for the low sensitivity to surface defects is connected with the low-leakage mode shapes shown in chapter 3. The axial displacement is near zero at the bar/bolt surface, and therefore the modes are largely unaffected by surface features. The shear pin hole affects only a small proportion of the cross sectional area, and does not seem to have a major effect. In any case, the shear pin hole only exists in the free end of the bar, where the energy can propagate with low attenuation in a large number of modes. It is possible that there may be significant mode conversion both to and from the low-leakage modes, but this is only likely to result in a slight increase in the overall attenuation of the wave.

4.6.4 Effect of End Angle

The effect of the rock bolt end angle on the end reflection amplitude was measured at low frequency using a laser interferometer, and was found to be insignificant. The effect is likely to be greater at high frequency, because of the smaller wavelength of the sound waves. It was not possible to measure the effect using the laser interferometer method because the laser interferometer that was available was not sensitive enough to measure the very small displacements of the high frequency waves. In addition, embedding material would be required to filter out the unwanted modes, making access to the surface impossible.

An alternative method of measuring the effect of the end angle was devised, using a rock bolt laboratory specimen (HF3) with the centre section embedded in mortar, as shown in figure 4.14. A series of pulse-echo tests were then carried out on the specimen, with a new end angle cut between each test. The end angle was cut with a circular bench saw, and was varied from 0° to 55° to the normal to the bolt axis. The transducer was left firmly clamped in place during all the cutting operations to ensure the contact conditions were varied as little as possible between each test. The mortar section acts as a filter for both the outgoing wave and the reflected wave, ensuring that only the low-leakage modes can be incident on the angled end, and be received by the transducer. The many other modes that may be generated by mode conversion at the angled end and by the transducer are highly attenuated in the embedded section, allowing just the low-leakage modes to be examined.

The test was conducted at 2.61MHz, 3.32MHz and 4.02MHz, at known attenuation minima, to allow the frequency dependence of the reflection coefficient to be assessed. The difference in end reflection amplitude can be compared to the reflection from the flat end to determine the additional losses due to end angle. The reflection from a flat end can be assumed to be 100%, as discussed in section 5.5. Following the experiment, a repeat test was made at 0° and the end reflection amplitude was within 2dB of the original 0° test, demonstrating that contact conditions had remained reasonably constant throughout the experiment.

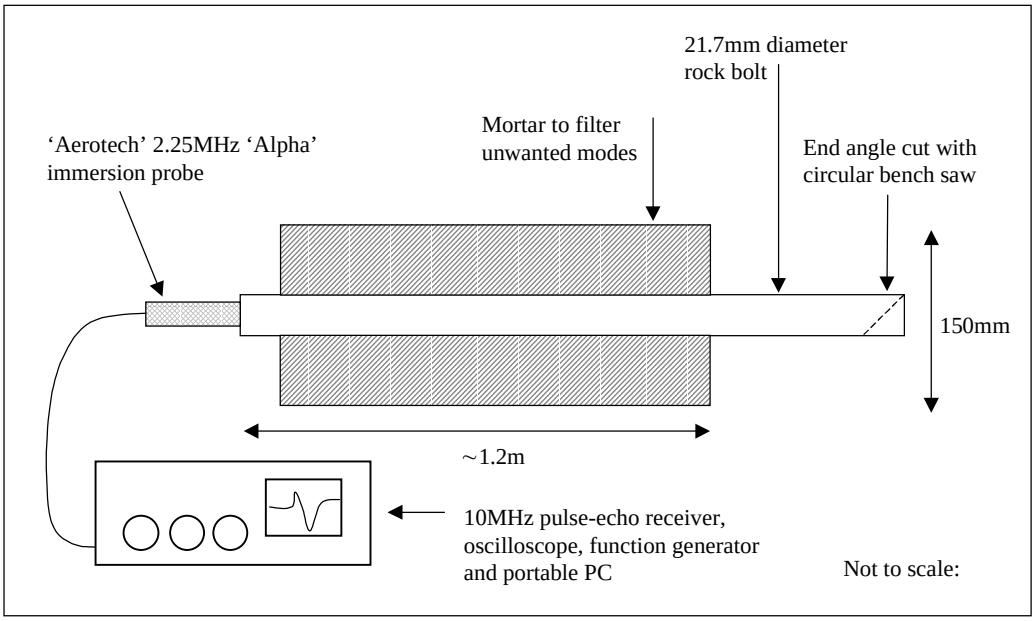

Figure 4.14: Experimental set up for measuring the reflection coefficient of high frequency, low-leakage modes from different bar end angles.

Figure 4.15 shows the measured loss for different end angles. There is a sharp and almost linear reduction in signal amplitude up to about 40dB loss at an angle of 10°. The loss then generally decreases to about 30dB between 10° and 55°. All three of the low-leakage modes are affected to about the same extent, irrespective of frequency. The poor reflection coefficient is primarily a result of the wavelength being only around 2mm, and so at 10° there is more than 1 whole wavelength difference in the length of the bolt across the diameter. This is likely to lead to a large amount of mode conversion taking place to both flexural and other, higher leakage, longitudinal modes. These modes will be filtered out in the embedding material. There may also be interference between different phases of the same mode, causing cyclic variation in reflected signal amplitude with angle and frequency. Figure 4.15 does show some cyclic variation in end amplitude, but this may also be due to spread in the experimental data, as the amplitude of the end reflections is very small, having been attenuated by leakage into the mortar as well as being poorly reflected from the angled end. The reflection from angled surfaces is not a widely researched area, and would benefit from further research using an analytical approach.

The results show that whilst it is possible to test rock bolts with angled ends using high frequency modes, the angled end may reduce the end reflection amplitude by as much as 40dB, leading to a more limited inspection range. If ultrasound is to be used to inspect new installations of rock bolts it would be beneficial to modify the design of bolts to incorporate a flat (0°) reflecting surface. If it is not possible to use flat-ended bolts, this could be achieved by a simple partial-depth saw cut, or an angled plastic cap fitted over a flat rock bolt end. A cap

would have two advantages, as it would allow the full surface area of the end to be a good reflector, and it could also protect the bolt end from becoming coated with epoxy. Better reflections would be obtained if there was an air gap at the end, as the contrast of acoustic impedance would be greater than for a steel/epoxy interface and therefore the reflection coefficient would be higher.

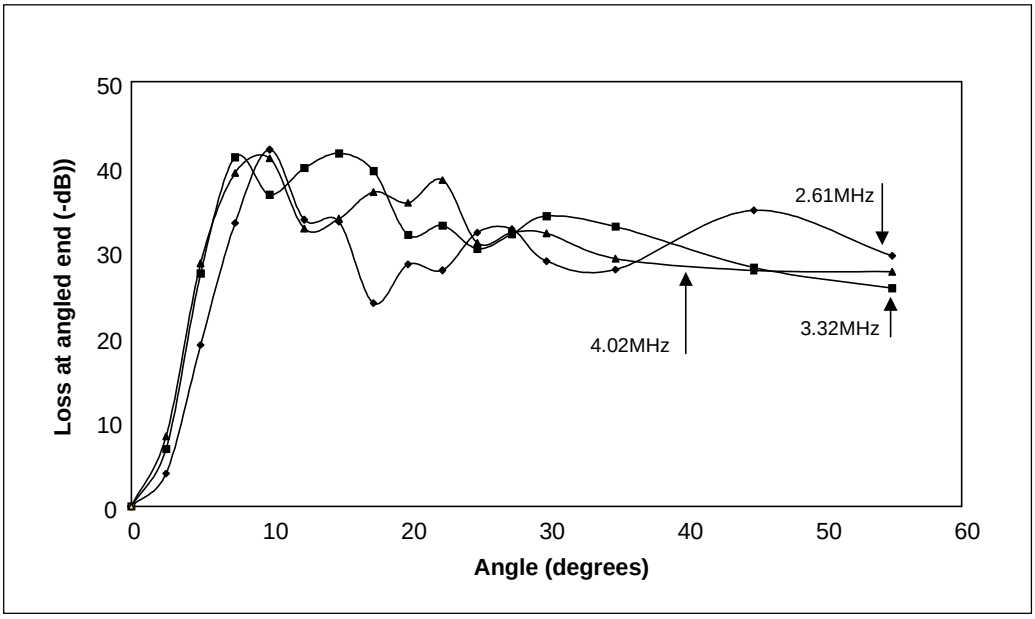

Figure 4.15: Attenuation experienced by high frequency, low-leakage guided waves when reflected from a bar with the reflecting end cut to different angles.

4.6.5 Laboratory Specimen Test Results

In addition to the end angle experiments, the laboratory specimens were used to examine the behaviour of guided waves at other types of defect. In particular, the interaction of high frequency, low-leakage modes with the start of resin encapsulation, severe bending, and necking was studied.

Loss of resin encapsulation

Figure 4.16 shows the end reflections obtained from two 2.4m partially encapsulated rock bolt specimens, with loss of resin on the first 1m. Figure 4.16a shows a clear end reflection from the flat-ended bolt, at a time that agrees well with the modelling predictions. The early part of the signal shows some undamped reflections and reverberations from features in the free part of the bolt, but no distinct echo showing the start of the encapsulation. The reason for this is related to the low-leakage mode shape. The low-leakage modes have very little displacement at the surface of the bolt and are therefore insensitive to changes in the properties of the embedding material. Figure 4.16b shows a similar test on a rock bolt with an angled end. In this case, the

extra gain required to overcome the attenuation at the angled end has increased the amplitude of the early reflections/reverberations to a level that obscures the end reflection. These results are in sharp contrast to the results for the L(0,1) mode, which showed good sensitivity to the start of the resin encapsulation on the same specimens. The L(0,1) mode has a much higher displacement at the surface of the bolt, and is therefore more sensitive to the embedding material properties.

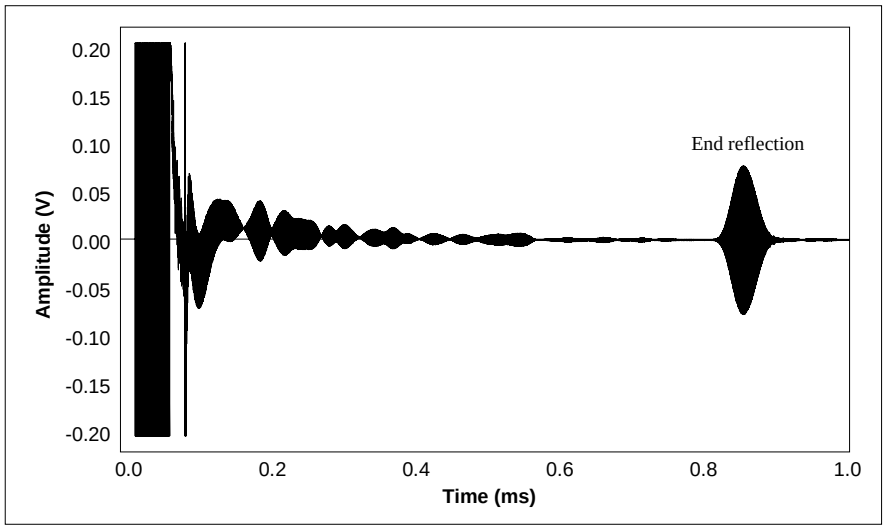

(a) Flat end.

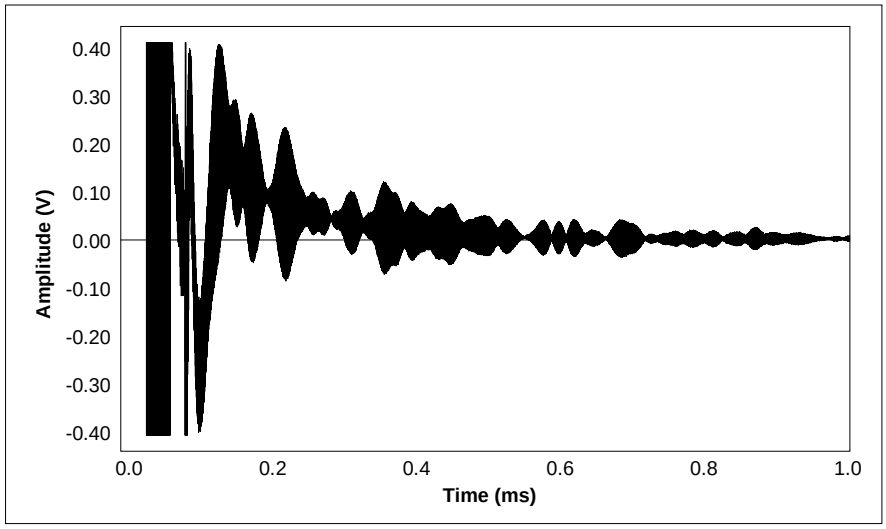

(b) Angled end.

Figure 4.16: End reflections from 2.4m rock bolts installed into the concrete laboratory test block with flat (LF2) and angled (LF4) ends, tested with a 200-cycle toneburst centred on 2.8MHz.

Necking prior to failure

Figure 4.17 shows the time trace recorded for a 2.4m rock bolt embedded in a 1.8m length of mortar, with 0.3m of the bolt exposed at threaded and reflecting end. The bolt had a defect representative of a typical neck that would be found in a rock bolt prior to failure, which had been pre-machined into the free section at the reflecting end. The geometry of the neck is also shown in figure 4.17, and was taken from measurements recorded by RMT Ltd. during a destructive tensile test carried out on a free bolt. The length of the neck was approximately 30mm either side of the final break, to which an approximately linear reduction in diameter to 15.5mm was measured. An end reflection can be clearly seen, together with a reflection from the neck. Note that the frequency that has been used is higher than those in the predicted optimum range, this was necessary to achieve the benefits of single mode excitation whilst having a signal short enough in time to resolve the end and neck reflections.

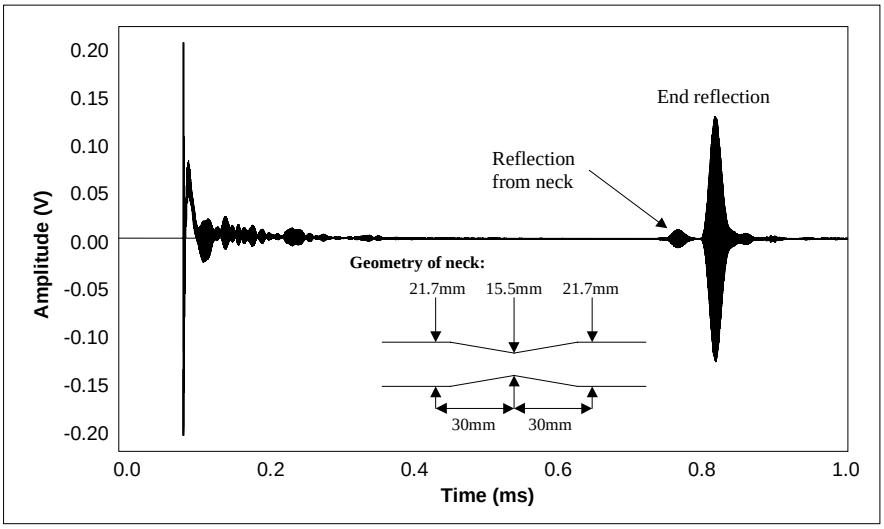

Figure 4.17: End reflection from a 2.4m rock bolt with a machined neck embedded in concrete (HF1), tested at 3.86MHz using a 100-cycle toneburst.

Severe bending

A feature of the failed rock bolts recovered from mines is that they are often bent into a crank-handled shape. This occurs because of stress relief in a plane normal to the bolt axis, which can cause the rock strata to slide over each other. In limiting this movement the rock bolt becomes bent at the strata interface, crushing the surrounding rock to form a crank-handled shape before tensile overload, necking and failure. Figure 4.18 shows the time trace recorded from a bolt with a crank-handled defect, with geometry as pictured in the inset. The time trace shows a reflection from the first bend and possibly also the second bend. This shows that the high frequency waves can be reflected by a severe change in curvature. No end reflection is visible, indicating that

insufficient energy was able to propagate to the end of the bolt. This means that it would be difficult to distinguish between a severe bend and a broken bolt using high frequency modes. Also, the bending radius used for this specimen is much smaller than that typically found in real rock bolts, and real bends may not be sharp enough to give a detectable reflection. Figure 2.5 shows a picture of a broken, crank-handled bolt recovered from a mine, and the bends are much less severe. Chapter 6 shows that the high frequency modes are attenuated very quickly in embedded curved bars, even if the curvature is very slight. Therefore, it is unlikely that reflection from, or propagation through, curves in rock bolts can be achieved with the high frequency, low-leakage modes.

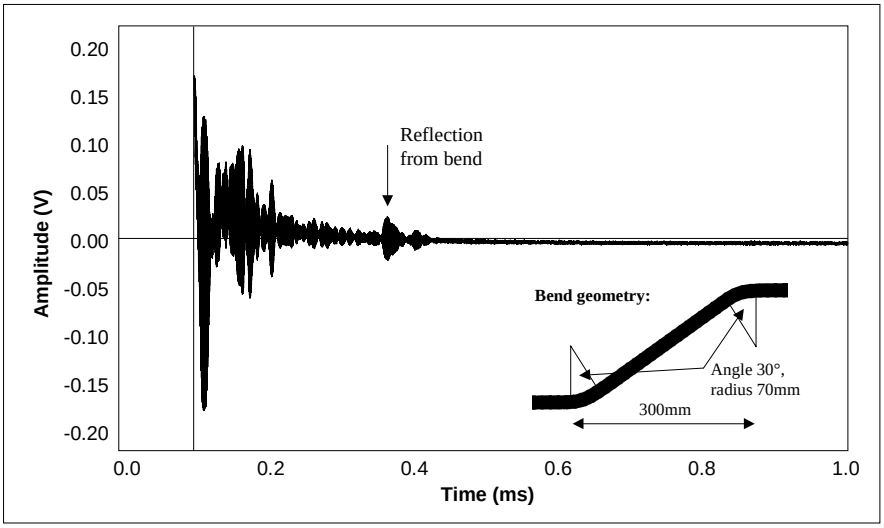

Figure 4.18: Reflection from a severe bend in a 2.4m rock bolt embedded in concrete (LF3), tested at 2.8MHz using a 50-cycle toneburst.

4.6.6 Site Test Results

The combination of laboratory test results and modelling work gives a good deal of information on how to make the best use of the low-leakage, high frequency modes for testing rock bolts. This section presents the results of some of the site tests made at Middleton Mine, and compares the results with the modelling predictions and similar laboratory tests. The results are split into 4 main areas:

- Use of a narrow bandwidth excitation signal to improve results
- Measurement of attenuation using a double reflection
- Applying signal processing to improve the end reflection from a 3m bolt
- Verifying the frequencies at which low-leakage modes exist

Application of narrow bandwidth excitation

The laboratory tests showed that single mode excitation can be used to improve the end reflection amplitude and clarity, through the elimination of interference and dispersion effects. Figure 4.19 shows the end reflection obtained from a 1m flat-ended rock bolt installed at Middleton Mine, tested using a 200-cycle toneburst centred on 2.6MHz. The first reflection is very clear, and a second reflection, corresponding to a wave that has travelled from the transducer to the end of the rock bolt and back twice can also be seen. The FFT of the first reflection shows a clear response with a bandwidth from 2.55-2.65MHz, which is exactly the same as the input signal bandwidth. This shows an efficient use of the energy input to the system, which minimises energy leakage at frequencies that do not correspond to the attenuation minimum at 2.6MHz. At this frequency signals with 200 cycles have given the best compromise between resolution and signal strength. Lower numbers of cycles can be used to scan the near field for defects.

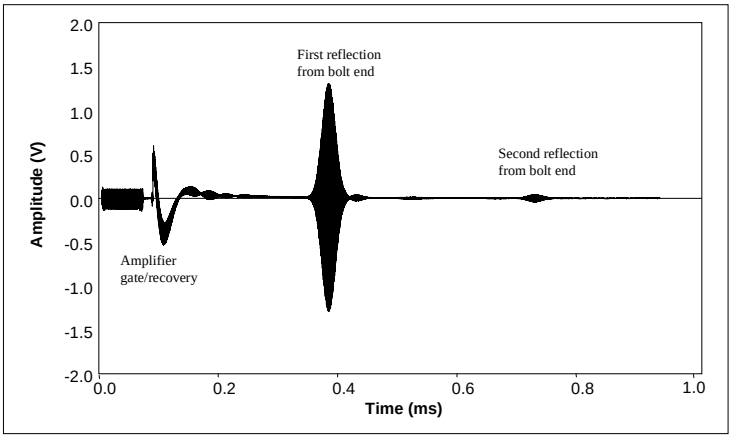

(a) Time domain.

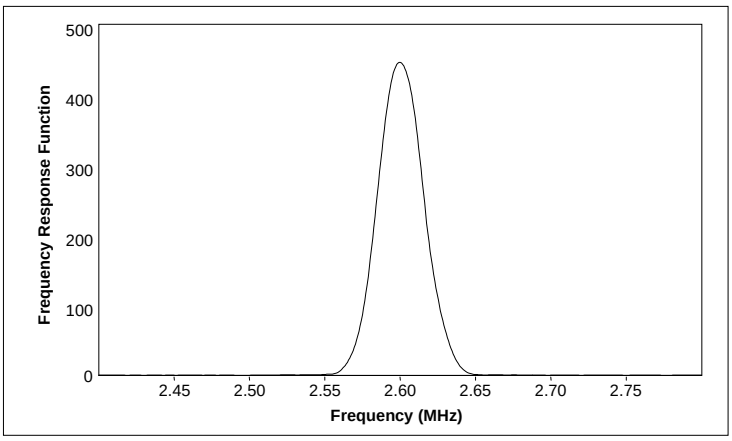

(b) Frequency content of the first reflection in (a).

Figure 4.19: Time and frequency domain signals recorded for a 1m flat-ended rock bolt installed at Middleton Mine (Bolt 23), tested at 2.6MHz using a 200-cycle toneburst.

Measurement of Attenuation

The fact that a double reflection can be obtained allows the attenuation of the wave to be estimated from the relative amplitudes of the first and second reflections, providing that the reflection coefficients at the bolt ends are known. Measurement of attenuation using this method formed a major part of the work on embedded tendons, and is described in detail in chapter 5, where it is shown that 100% reflections can be assumed from bar ends for the low-leakage modes. The same reasoning applies to the rock bolt case, and the attenuation can be measured in the same way. Figure 4.20 shows the measured attenuation for two 1m rock bolts with flat ends installed at Middleton. The measurements were carried out at six low-leakage points on modes with a sufficiently low attenuation for a double reflection to be obtained. The results show attenuation ranging from 12dB/m to 17dB/m, with one of the bolts having attenuation consistently higher by about 1dB/m. It is likely that this is due to poorer epoxy bond quality on

the bolt that shows lower attenuation. The measurements are all below the values predicted for the standard rock bolt model. However, the variation is well within the possible range of values predicted by the variation in factors examined in the modelling work.

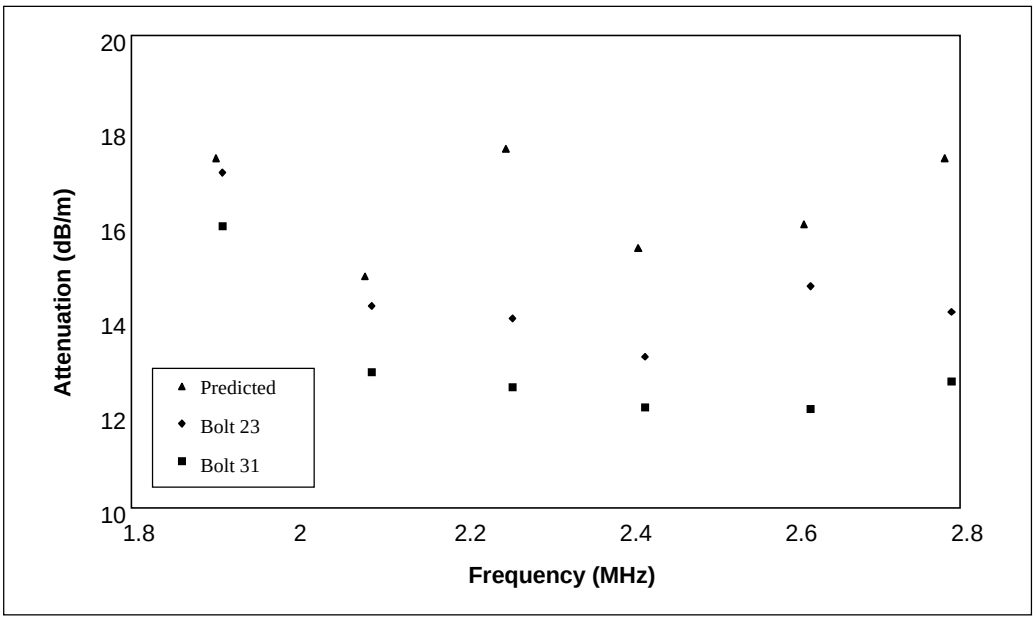

Figure 4.20: Measured and predicted attenuation for six low-leakage points on the L(0,11) mode for two similar 1m long rock bolts installed at Middleton Mine.

Tests on a 3m fully encapsulated rock bolt

The measured attenuation shows that it should be possible to test a 3m rock bolt using high frequency modes. Figure 4.21a shows the time trace recorded for a 3m flat-ended rock bolt, excited with a relatively wide bandwidth 20-cycle signal, centred on 2.6MHz. An end reflection can be seen just after 1.0ms, although there is a significant amount of interference and noise, and the end reflection is not clear. It has been shown that a narrow bandwidth signal would improve this result, but a clearer reflection can also be obtained by filtering out the unwanted frequencies by signal post-processing.

Figure 4.21b shows an FFT of the time trace obtained in 4.21a, with the first 0.4ms removed from the time domain signal as it consists largely of signals associated with amplifier recovery and ringing of the transducer. The FFT shows two distinct peaks, corresponding to the low-leakage modes at 2.44MHz and 2.62MHz. Figure 4.21c shows the time trace obtained after isolating just the 2.62MHz part of the signal using a band pass filter, and transforming back to the time domain. The end reflection is now clearly visible. This is a very satisfactory result, which is promising for the prospect of the technique as an industrial inspection method.

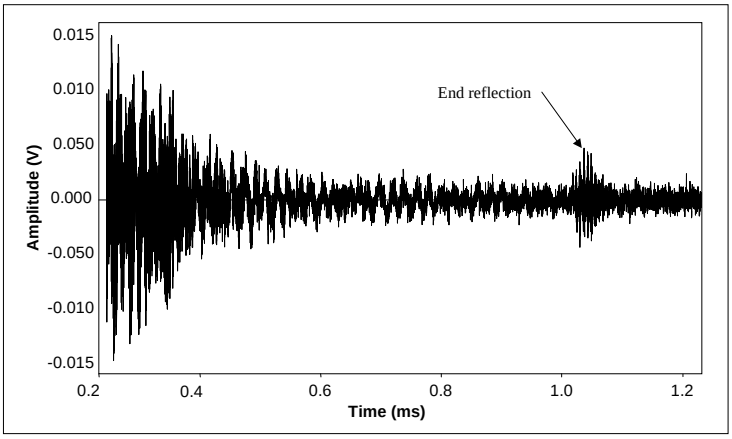

(a) Time trace recorded as raw data. Note that due to scope sampling limitations, the time axis begins at 0.2ms.

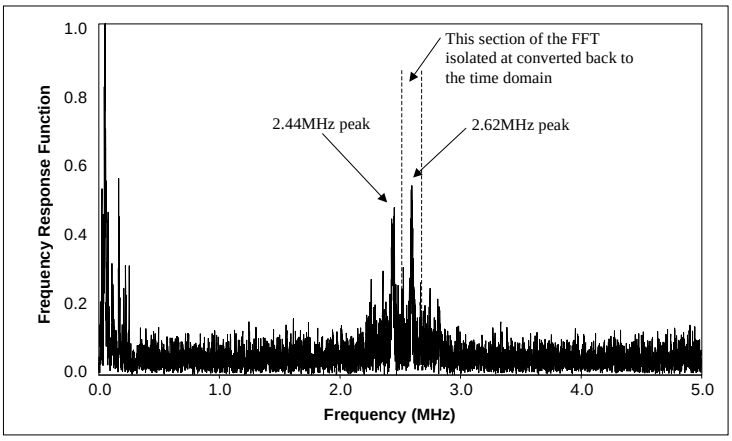

(b) FFT of 0.4-1.2ms region of (a), showing peaks corresponding to attenuation minima at 2.44 and 2.62MHz.

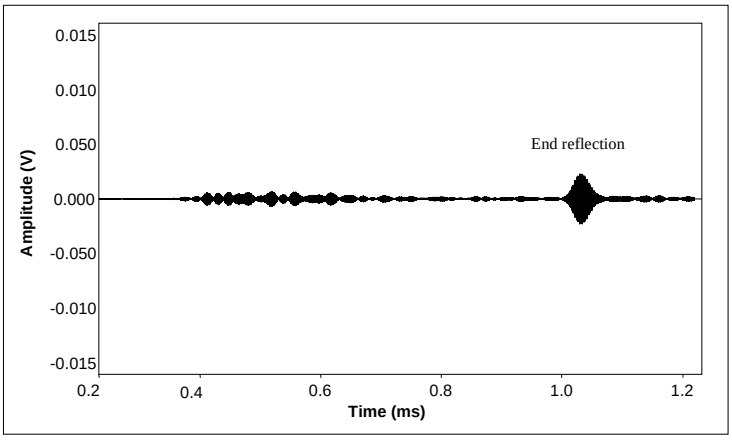

(c) Signal obtained by isolating the 2.62MHz frequency peak in (b) and reconverting to the time domain.

Figure 4.21: Time trace and FFT for a 3m flat-ended rock bolt at Middleton Mine, tested using a 20-cycle toneburst, centred on 2.6MHz.

Frequency sweep of 2.4m rock bolt with an angled end

The frequencies at which attenuation minima exist have been verified by carrying out a frequency sweep of a rock bolt, and measuring the amplitude of the end reflection at each frequency. This experiment was performed on three nominally similar 2.4m rock bolts with angled ends, using 350-cycle tonebursts, in 0.02MHz steps from 1.8MHz to 2.8MHz. A very narrow band excitation signal was used to maximise the energy input at each frequency, and to prevent interference occurring between modes travelling at different frequencies.

The results in figure 4.22 show the end reflection amplitude and predicted attenuation for the entire frequency range. It should be noted that no absolute attenuation measurement has been made, and only the frequencies of the minima and their relative amplitudes can be compared. The frequencies at which minima occur are within the range of frequencies predicted by the modelling for different types of steel, indicating that the modelling results are accurate. The results show that attenuation seems to vary between modes more than the modelling predicts. The mode at 1.91MHz gives a smaller end reflection amplitude than the predicted attenuation would suggest, as was also noticed in the attenuation measurements discussed earlier. In addition, the 2.26MHz and 2.44MHz modes show smaller end reflections than expected. This may be because particular modes are affected more by certain localised conditions on each bolt, such as a slight amount of curvature or a particular change in the bonding conditions or end angle. For example, the investigations into end angle reflections showed that there may be a complex relationship between wavelength, end angle and reflection coefficient. One or more of these reasons may explain why two other bolts tested in this way (not shown), all showed some, but not necessarily the same, modes being more successful than others. The results show that it will probably be necessary to test bolts at a number of frequencies over the full range of low-leakage modes, in order to ensure that reliable results are obtained.

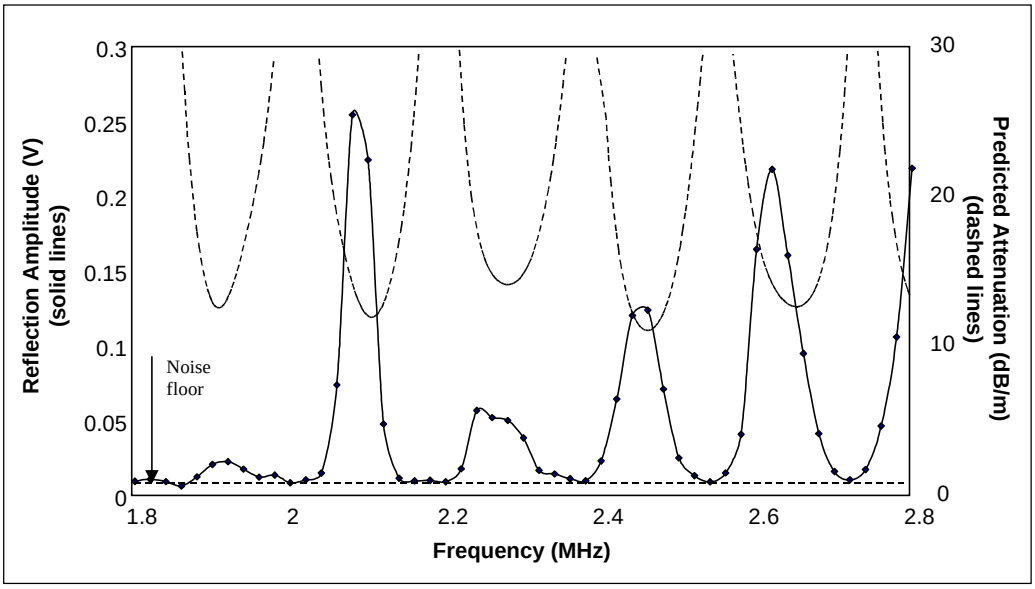

Figure 4.22: End reflection amplitude with varying frequency, for a 2.4m rock bolt with an angled end installed at Middleton Mine (Bolt 16), tested in steps of 0.02MHz with a 350-cycle toneburst signal.

4.6.7 Effect of Curvature

The limited amount of site testing undertaken in the deep coal mine at Annesley Colliery did not detect any end reflections using the high frequency test. The rock bolts that were tested were close to the coalface, where there is high stress relief in the rocks and therefore significant movement of the rock layers. It was possible to recover some rock bolts from partially collapsed areas of the mine. These bolts showed that a significant amount of deformation had taken place prior to failure, as shown in figure 2.5. The effect of this deformation on the high frequency modes has been investigated, and is reported in chapter 6. The effect has been found to be unexpectedly large, and it is unlikely that the low-leakage modes will be useful for bolts that have become deformed. It is possible that a dual high/low frequency test could be used to determine whether or not rock bolts are deformed.

4.6.8 High Frequency Conclusions

This chapter has shown that low-leakage high frequency guided waves have the potential to inspect straight 3m flat-ended rock bolts for some defects and residual length. The modelling work identified low-leakage points on high order longitudinal modes as they approach the steel longitudinal bulk velocity. The existence of these modes has been confirmed, and site testing at a limestone mine has found modes at 2.08, 2.26, 2.44, 2.62, and 2.80MHz, which is within the range predicted by the modelling for different steel types.

The attenuation of these modes has been measured by comparing the amplitude of subsequent end reflections from bolts, and is in the range 13-15dB/m, with some variation between nominally similar bolts and between different modes. This compares to attenuation values of 15-18dB/m predicted by the modelling. The difference can be attributed to poor acoustic coupling between the rock bolt and the epoxy layer, with the presence of drilling debris, plastic coating and partially cured epoxy acting to reduce the stiffness of the joint. The measured attenuation corresponds to predicted values for the model with an 85-90% reduction in stiffness of the epoxy layer in both shear and longitudinal directions. Differences can also be expected from changes in epoxy thickness and localised rock properties.

The effect of bolt features and various defects on the propagation of the high frequency modes has also been investigated. Surface features, such as threads and mixing ribs do not affect the modes significantly, and therefore surface defects are not likely to be detectable using this method. This is because the energy is concentrated in the centre of embedded bars at the low attenuation points. The effect of end angle is very significant. A severe loss in reflected signal amplitude of 40dB occurred in laboratory tests when the end angle was cut from 0° to 10°. For larger angles, the reflection coefficient was slightly better. This means that for these modes to be used effectively, the ends of the rock bolts would need to be redesigned, to incorporate a flat reflecting surface. This could be achieved by making a simple saw cut close to the end of the bolt and through most of the bolt diameter, or through the use of a plastic angled end cap, fitted onto a flat-ended bolt. Both of these solutions would allow effective NDT on new installations, but the high frequency test method could not be used to its full potential on existing bolts. The effect of end angle makes real defects difficult to detect, and the variation in reflection coefficient expected for different angled defects such as corrosion patches would make accurate defect sizing impossible.

To achieve the best results, the modes must be excited using a narrow bandwidth signal to concentrate as much ultrasonic energy as possible into a given low attenuation frequency. This can be achieved by using a toneburst of at least 50 cycles, with a centre frequency that corresponds to an attenuation minimum. This removes the effect of destructive interference between modes, which reduces the end reflection amplitude. However, if this is not possible, e.g. if the number of cycles in the outgoing signal is restricted by the length of the signal in time, then good results can be achieved by isolating a small frequency range on the received signal by post processing. The use of electronic filters and averaging can also help to improve the signal to noise ratio.

Significant variation in the results was noticed for different bolts, and a major factor in this may be the effect of curvature. All rock bolts will be deformed to some degree, however small, and it

is believed that this is the cause of poor results from some test specimens. However, variations in epoxy thickness, end angle, and epoxy bonding conditions will also have a limited effect.

4.7 Effect of Environmental Exposure

Although successful results have been obtained from both laboratory and site specimens, the signals obtained in the laboratory have generally been clearer, and more consistent over several tests. The large-scale laboratory specimens were installed using the industrial method, so it is unlikely that differences in the consistency of the epoxy layer between the sites can account for this. The rock is stable at Middleton Mine, and it is therefore also unlikely that the rock bolts have become deformed at that location. The main difference between the specimens is that the specimens installed in the mine are subject to exposure to water seeping through the rocks. This has probably already led to some corrosion, which may affect the attenuation of the waves, but it may also affect the coupling between the epoxy and the rock, if the bonding is not perfect. If the rock and epoxy were not fully bonded, then coupling of ultrasound into the rock would be improved by the presence of water, therefore increasing the attenuation due to leakage. This effect has not been investigated, but is an area that requires further research.

4.8 Rock Bolt Testing Overall Conclusions

The modelling predictions showed that both the L(0,1) and L(0,11) modes have the potential to be used to inspect rock bolts, and this has been confirmed by practical experiments in the laboratory and at a limestone mine. The L(0,1) mode has been successfully used between 35kHz and 45kHz, and the L(0,11) mode at a variety of frequencies between 1.8MHz and 2.8MHz in its low-leakage region.

A major focus of the research work has been to reliably detect reflections from the end of rock bolts to confirm their residual length. The high frequency test has successfully detected the end of a 3m long rock bolt with a flat end, and a 2.4m rock bolt with a standard angled end. The attenuation of the mode has been measured to be as low as 13-15dB/m, against modelling predictions of 15-18dB/m. The L(0,1) mode has been successfully tested on bolts up to 1.8m and 2.0m long on site and in the laboratory respectively, which also suggests lower attenuation than the modelling predicted. The difference between the predicted and measured attenuation is due to two main factors. Firstly, the material attenuation may have been slightly overestimated, as found for the tendon examples in chapter 5, which will particularly affect the high frequency results. Secondly, the modelling assumes that there is perfect bonding between the layers, and it is likely that the bolt/epoxy bond is less than perfect due to the presence of drilling and encapsulation debris, water, and incomplete mixing of the epoxy. This will reduce the acoustic coupling into the rock, and therefore reduce the attenuation due to leakage. The energy velocity predictions compare well to the measured values for the high and low frequency modes.

The two modes show a very different sensitivity to bolt features and different types of defect. Neither the L(0,1) or L(0,11) modes are sensitive to the rock bolt surface features or plate assembly, but for different reasons. The wavelength of L(0,1) is about 100mm at the test frequencies, and is therefore unaffected by surface features of only a few millimetres in length. The energy of the L(0,11) mode is concentrated in the centre of the bolt, and although the wavelength of 2mm makes it sensitive to small features, the wave is not affected greatly if these features are near the bolt surface. The low frequency L(0,1) mode is reflected from the start of the epoxy encapsulation. The reflection coefficient is small at about 3%, but as the reflection only travels in a section of bolt that is not encapsulated, and is therefore not attenuated, it can be used to detect loss of resin encapsulation on the lower part of the bolt. The high frequency L(0,11) mode was insensitive to this interface, again because of the lack of surface displacement. High frequency modes have also been used to successfully detect the necking of bolts and severe bending.

The rock bolt end angle has been found to be very significant. The reflection coefficient of the L(0,1) mode from a bolt end is almost 100%, irrespective of the end angle, but the high frequency L(0,11) mode is poorly reflected when the bolt end is not flat. An angle of 10° results in a 40dB loss of signal amplitude, and although the loss decreases as the angle is increased further, a 45° angle will still cause a loss in signal amplitude of roughly 30dB. This means that some design changes would need to be made to rock bolts so that the inspection method could be used to its full potential. The rock bolt ends need to incorporate a flat reflecting surface, either by making a simple saw cut through part of the bolt, or by fitting a plastic angled end cap to bolts with a flat end. The high frequency mode is more sensitive to end angle because of the smaller wavelength. Even at small angles, there can be more than 1 wavelength across the length of the reflecting surface, leading to significant mode conversion. This effect is an area that would benefit from further research, as there may be some cyclic behaviour of the reflection coefficient with wavelength.

The high frequency modes are severely affected by curvature. This has also affected the post-tensioning tendon testing discussed in chapter 5, and the effect has been reported in detail in chapter 6 of this thesis. It is unlikely that the high frequency modes can be used on rock bolts that have become deformed due to ground movement. This is a unfortunate, as the L(0,11) mode has very low attenuation and produces clear end reflections. A limited number of experiments conducted on free bars suggest that the L(0,1) mode is not significantly affected by curvature, and therefore a dual frequency could be used to determine whether deformation had occurred.

The optimum excitation of the modes has also been investigated. At high frequency, the best combination of transducer and excitation signal is to use a highly damped probe, excited with a very narrow bandwidth toneburst centred on the frequency of an attenuation minimum. Gaussian windowed tonebursts with up to 200 cycles have been used for the testing. This maximises the energy propagating in the bolt and avoids the detrimental effects caused by interference between modes. Averaging and passive filtering of the signals has been found to improve the signal to noise ratio, with 50 averages being used as standard. However, the improvements in the signal are less noticeable if narrow bandwidth excitation is used. At low frequency, the bandwidth of the excitation signals cannot be very narrow, as the signals become too long in time. Tonebursts of between 4 and 10 cycles have been used, depending on the bolt length and test frequency. A specially designed damped transducer, with a centre frequency of 40kHz, has been produced for the test, which gives good signal strength with minimal ringing. Further improvements in the inspection range are likely to be made through developments in the instrumentation. Problems were encountered at Middleton with early reflections, thought to be

from geological features or changes in epoxy condition. These early reflections were quickly amplified to a level that saturated the receiver amplifiers. The subsequent ringing and recovery time was often long enough to prevent the end reflection being visible, meaning that insufficient gain could be applied to detect the end reflection, limiting the inspection range. The use of an amplifier with gain that was variable in time would allow later signals to be amplified more, giving a clearer picture of later signals without saturating amplifiers with early reflections.

Overall, the rock bolt inspection has been a success, and the findings of this chapter are sufficient to develop a testing instrument that would be suitable for commercial use. With developments in instrumentation, it should be possible to detect the ends of rock bolts that are at least 2.4m in length. High frequency testing is very successful for straight bolts and has been used successfully on 3m fully encapsulated specimens with flat ends. However, the high frequency low-leakage modes are affected by curvature, and are not suitable for use on deformed bolts.

As well as instrumentation development, further research in several areas would improve scientific understanding to the benefit of the method in the long term. The interaction of the low frequency modes with defects could be modelled further, and the over-coring of bolts installed in the test mine with unknown, but detectable defects would also be of use if the test is to be used commercially. A related area of study is the modelling of an angled end, which has only been investigated experimentally in this thesis. There is also great deal of work that could be carried out on the effect of curvature, and the practical testing of curved embedded sections. Some of the issues regarding curvature are discussed further in chapter 6.

CHAPTER 5

APPLICATION TO TESTING CONCRETE REINFORCING TENDONS

5.1 Introduction

Post-tensioning increases the load bearing capacity of concrete and is a common form of construction in applications such as bridge decks. A compressive load is applied to the concrete through the tightening of post-tensioning cables after the concrete has been cast. The cables are enclosed in a duct, which, after tensioning, is pumped full of an alkaline grout to protect the cables from corrosion. The cables can either be single wires, typically 5mm or 7mm diameter, or multiple wire 'strand' cables. A common strand configuration is a 15.9mm diameter, seven-wire strand, with six 5.2mm diameter wires wrapped spirally around a 5.5mm diameter core wire. The inspection of both strands and wires is considered in this chapter.

Guided wave inspection of rock bolts has been thoroughly investigated through modelling and experimental work in the previous two chapters. Many of the principles are general, and also apply to the inspection of grouted post-tensioning tendons. This chapter continues the work of previous researchers [5,30] into tendon inspection, and draws conclusions about the potential of guided waves for such a test. This has been achieved principally through the measurement of attenuation in grouted tendon specimens, and also through experimental work into the reflection of modes from different angled ends. Guided wave behaviour is predicted through modelling the tendon system using Disperse, and the experimental results are compared directly with these predictions.

This chapter only considers the use of high frequency, low-leakage modes for tendon inspection. The rock bolt research has shown advantages in using the fundamental L(0,1) mode for testing, but this is not practical for tendon inspection because the ducting that contains the tendons could reflect the leaked bulk waves and make the method unreliable. In addition, the attenuation due to leakage is radius dependent, and the already very high predicted attenuation for the L(0,1) mode in a rock bolt would be much higher for small diameter tendons. A limited number of low frequency experiments were attempted on grouted tendons in a simulated bridge deck, but without success.

5.2 Background to Guided Wave Inspection of Grouted Tendons

Previous Work

Some of the earliest work on the use on ultrasound to inspect post-tensioning tendons was carried out by Weight [30], of City University. His approach involved sending long bursts of high frequency ultrasound along tendons, and it indicated potential propagation distances of 20m. His work was largely experimental.

The development of the guided wave modelling software 'Disperse' [7,68], reported elsewhere in this thesis, allowed further investigation into the technique. Pavlakovic used this software to model guided wave propagation in embedded tendons and his research led to the discovery of high frequency, low-leakage modes [6]. A number of experiments were conducted to validate the results, and the existence of low attenuation modes at the frequencies predicted by the modelling was confirmed [5]. Using this technique, Pavlakovic was able to detect 2mm and 4mm deep saw cuts in an 8.1mm diameter bar embedded in grout at a distance of 450mm into the grout. An end reflection was also obtained from a 2m long, undamaged section of embedded 8.1mm diameter bar. Full breaks, at 45° to the axis of 15.9mm strands were detectable at distances up to 1.5m, but no further.

A further important area of research conducted by Pavlakovic was the reflection coefficients of waves from defects, which was investigated using Finite Element methods [92,31]. Pavlakovic studied the L(0,1) mode in detail, concluding that for both the embedded and free bar cases, almost 100% reflection of the L(0,1) mode would be obtained from a square or a diagonal notch cutting completely through the bar. Pavlakovic also examined the behaviour of the L(0,4) mode, which is the first mode to show the trend of attenuation minima that reduce in value with increasing frequency. The reflection coefficient for the L(0,4) mode from a square notch cutting completely through a free bar was 90%. Work was also carried out on partial depth notches, with the reflection coefficient reducing to about 0.6 for a square notch cutting though half of the radius. Limitations on the size of the finite element model prevented the study of higher order modes.

The conclusions of Pavlakovic and Weight generally agree, with the exception that Pavlakovic predicts a shorter maximum test range. Pavlakovic concluded that 'up to several metres' of tendon could be inspected from a single inspection point, and also that the signal was mainly carried in the inner wire of the strand samples, thought to be due to lower acoustic coupling into the grout. Pavlakovic concluded that the lower attenuation experienced in the centre wire was the reason for the long propagation distances measured by Weight.

Further progress reported in this thesis

The modelling and experiments conducted by Pavlakovic led him to conclude that the original propagation distances predicted by Weight were unlikely to be possible. However, he concluded that short lengths of tendon could be inspected either from the tendon anchorage points or from transducers attached to the sides of the tendon through bore holes. Inspecting tendons from the anchorage points is particularly attractive, as the ends of the cables are already exposed and it is difficult to inspect tendons in this region using traditional methods. However, only limited conclusions were drawn about the level of attenuation and the interaction of the wave with defects and other features, such as the tensioning clamps and the entry point to the grout.

The primary work of the author of this thesis has been to measure the actual attenuation levels in grouted tendons, in order to enable a more thorough comparison with the modelling predictions. Experimental work into reflection of high order modes from different angled bars was carried out for the study of rock bolts, and this information has been used to assess the likely reflection coefficients from defects in tendons. The different behaviour of the inner and outer wires of strand specimens has also been investigated experimentally, and is backed up by the detailed study of curvature reported in chapter 6. Overall conclusions have been drawn about the maximum tendon inspection range that can be achieved by using guided waves, and the types of defect that can be detected.

5.3 Dispersion Relationships

Modelling the guided wave dispersion relationships is important in understanding the results of non-destructive tests. The dispersion relationships for a grouted steel bar were first calculated by Pavlakovic [5,31] and have been repeated by the author of this thesis to allow further investigation to take place. This section presents and discusses these dispersion calculations, although many of the trends observed for the high frequency rock bolt modes also apply to grouted tendons, and are discussed more fully in chapter 3.

The material properties used to model the tendon are shown in table 5.1. The steel values are based on a steel with a relatively high modulus, although some steels may have velocities that are up to 2% lower. In practice, this makes no difference to general trends, but it does affect the exact frequency at which attenuation minima occur. For example, such a shift in velocity will cause the L(0,9) mode attenuation minima to shift in frequency by about 150kHz in a 5mm diameter tendon. This is significant compared to the spacing of the minima, and therefore the test frequencies will need to be closely matched to a particular steel.

Material Property	**Steel**	**Grout**
Modulus, E (GPa)	216.9	11.2
Density, ρ (kg/m^3)	7932	1600
Longitudinal Attenuation (np/wl)	0.003	0.043
Shear Attenuation (np/wl)	0.008	0.100
Longitudinal Bulk Velocity (m/s)	5960	2810
Shear Bulk Velocity (m/s)	3260	1700
Poisson's Ratio, ν	0.29	0.21

Table 5.1: Material properties used to model grouted tendons.

The phase velocity dispersion curves for the axially symmetric modes in a steel bar, embedded in an infinite expanse of grout are shown in figure 5.1. The simplicity of the model, with no intermediate layers, allows the dispersion curves to be expressed in terms of frequency-radius, as all the layers can be scaled by the same factor. One set of curves can therefore be used for all tendon diameters. The form of the dispersion curves is similar to the rock bolt case discussed in chapter 3, showing peaks in phase velocity for lower-order modes, and a general flattening of the curves around the steel longitudinal bulk velocity line as the mode order increases. As for the rock bolt case, these flat regions are associated with low material attenuation and low-leakage. The reason for this is discussed in detail for the rock bolt case in chapter 3, and the same principles apply here, with the mode shape showing little displacement at the steel/grout boundary. In this particular case, the regions become linked from the L(0,12) mode, upwards in frequency, to form a low-leakage mode. Lower-order modes, such as L(0,9) show a single low-leakage region.

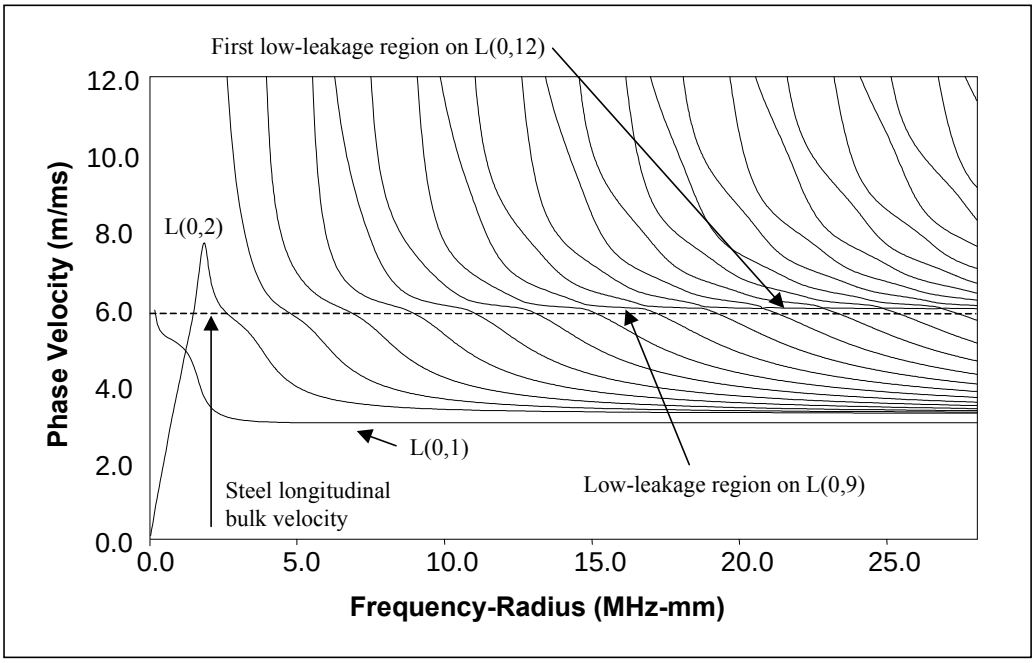

Figure 5.1: Phase velocity dispersion curves for the longitudinal modes in a steel bar embedded in grout.

The predicted attenuation and energy velocity can be seen in figure 5.2, also expressed in terms of frequency-radius. The attenuation is also radius dependent, and is plotted as attenuation-radius. This means that the leakage from the surface will be relatively high in small diameter tendons, this is a consequence of having a large surface area to volume ratio. Attenuation due to material damping also increases as radius decreases, as each mode shifts to a higher frequency and thus a shorter wavelength. The attenuation curves show a relatively high attenuation for L(0,1), with a clear trend to lower minimum attenuation shown by the L(0,4) mode onwards. The L(0,8)-L(0,11) modes have been found to give the best experimental results, and these modes are investigated in detail in the following sections. All of the minima at higher frequency in this series are points on the low-leakage L(0,12) mode. Theoretically this mode has the lowest attenuation, but the problems of generating the large output high frequency signals required for small diameter tendons outweigh the small gains in attenuation over the L(0,8)-L(0,11) modes. If the frequency is increased above the frequency of first one or two attenuation minima on the L(0,12) mode, then the overall value of the predicted attenuation minima increases. This is because the increase in attenuation due to material damping is more than the reduction in attenuation due to leakage, and is discussed fully in chapter 3. The energy velocity dispersion curves show a maximum in energy velocity close to the frequency of the attenuation minimum for each mode. It can be seen that the energy velocity and attenuation are closely related, with lower attenuation modes having higher velocities. The energy velocity curves clearly show L(0,12) as a low-leakage mode linking low attenuation regions.

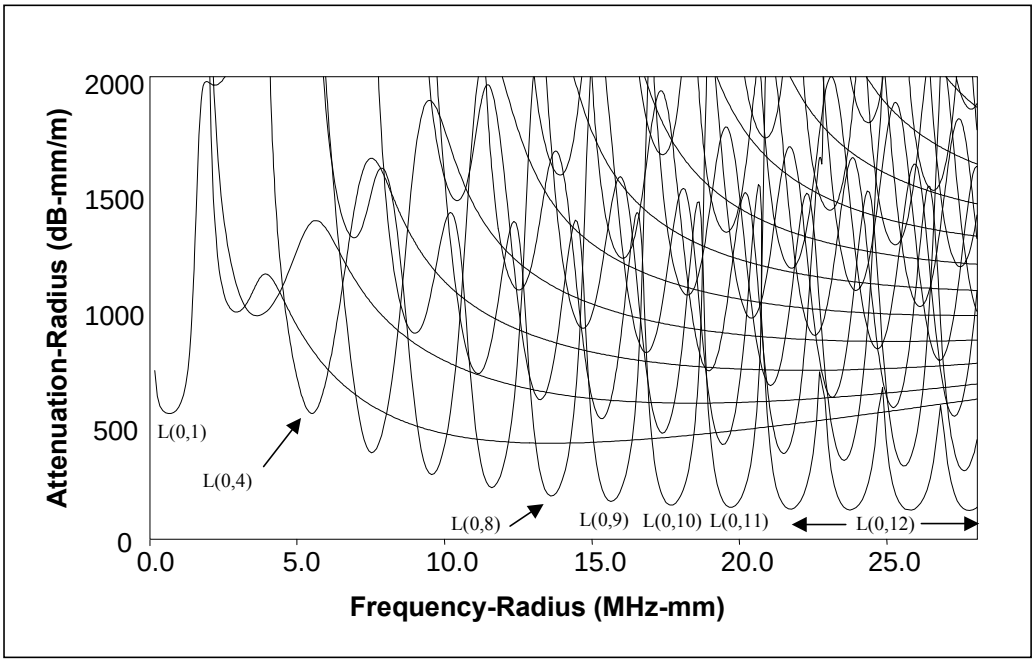

(a) Attenuation.

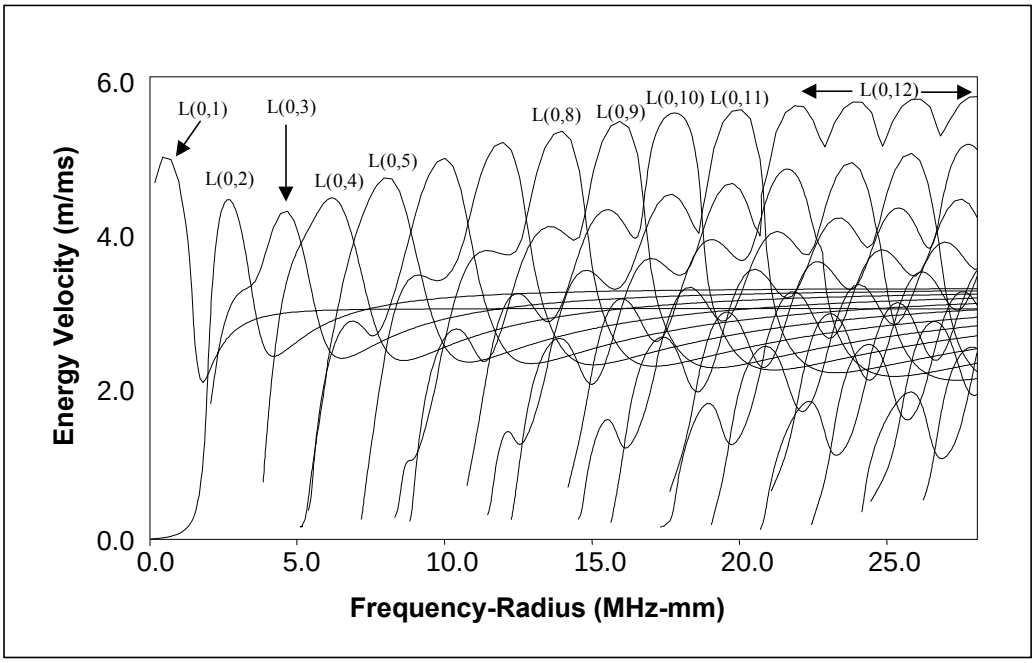

(b) Energy velocity.

Figure 5.2: Attenuation and energy velocity dispersion curves for the longitudinal modes in a steel bar embedded in grout.

Table 5.2 shows the predicted attenuation and energy velocity at the frequency of the attenuation minima of the L(0,8)-L(0,11) modes. Table 5.2a shows the predicted values for a free bar, where the attenuation comes from material damping only. Table 5.2b shows the predicted values for a bar embedded in grout, where the attenuation comes from leakage as well as material damping. It should be noted that although the attenuation minima follow the same pattern for the free and embedded cases, the precise frequency at which they occur is slightly different. For example, the attenuation minimum on the L(0,8) mode occurs at 13.3MHz in a free bar, but 13.1MHz in a grouted bar. It is interesting to note that the difference decreases with increasing frequency, with the L(0,11) mode having minima at 19.0MHz in both the free and grouted cases. This effect occurs because the leakage decreases with increasing frequency, and therefore the overall attenuation is increasingly dominated by material damping. The grouted bar therefore behaves more like a free bar as the frequency is increased. Since the modes will be excited at frequency of the attenuation minima in a grouted tendon, the energy will also travel at that frequency in the free section of the tendon. Table 5.2a also shows (in brackets) the predicted attenuation and energy velocity in a free bar at these frequencies. The values are only slightly different from those expected at the actual free bar minima, and the slight frequency shift will have little effect on wave propagation. The predictions show that there is less than 0.5% difference between the energy velocity in embedded and free sections of bar. Roughly half of the overall attenuation is due to material damping, although this proportion increases with frequency.

Mode	**Frequency-Radius (MHz-mm)**	**Attenuation-Radius (dB-mm/m)**	**Energy Velocity (m/ms)**
L(0,8)	13.3 (13.1*)	81.1 (82.1*)	5.25 (5.21*)
L(0,9)	15.2 (15.1*)	88.0 (88.3*)	5.38 (5.35*)
L(0,10)	17.1 (17.0*)	94.8 (95.2*)	5.47 (5.46*)
L(0,11)	19.0 (19.0*)	101.9 (102.0)*	5.55 (5.55*)

** Values shown in brackets are at the frequencies corresponding to the attenuation minima in a grouted bar, as shown in table 5.2b.*

(a) Free bar.

Mode	**Frequency-Radius (MHz-mm)**	**Attenuation-Radius (dB-mm/m)**	**Energy Velocity (m/ms)**
L(0,8)	13.1	205.7	5.23
L(0,9)	15.1	183.7	5.36
L(0,10)	17.0	171.0	5.44
L(0,11)	19.0	163.9	5.54

(b) Embedded bar.

Table 5.2: Attenuation and energy velocity at attenuation minima on four modes in a free steel bar and a steel bar embedded in grout.

5.4 Transducer, Excitation and Instrumentation

All of the experiments reported in this chapter were carried out using a 'LeCroy' 9101 Arbitrary Function Generator, and the 'Wavemaker 10' pulse/receive amplifier described in section 4.3. Filtering and signal averaging were used to improve the signal to noise ratio on all of the tests. A highly damped transducer from the Aerotech 'Alpha' series [94] with a centre frequency of 5.0MHz allowed good signals to be obtained over the required frequency range. The transducer was coupled to the tendon ends with a standard industrial coupling gel, and was mounted in a holder, clamped onto the exposed tendon end for stability. Good transducer contact was obtained through a screw clamp acting on the back of the transducer, with a rubber washer to correct slight misalignment and reduce ultrasound reverberations in the holder. This arrangement, shown in figure 5.3, was found to be more successful at producing repeatable results than an earlier sprung-loaded design. Although the results presented in this chapter are largely independent of the clamping force, more reliable averaging and therefore better signal resolution can be obtained through the use of the clamp.

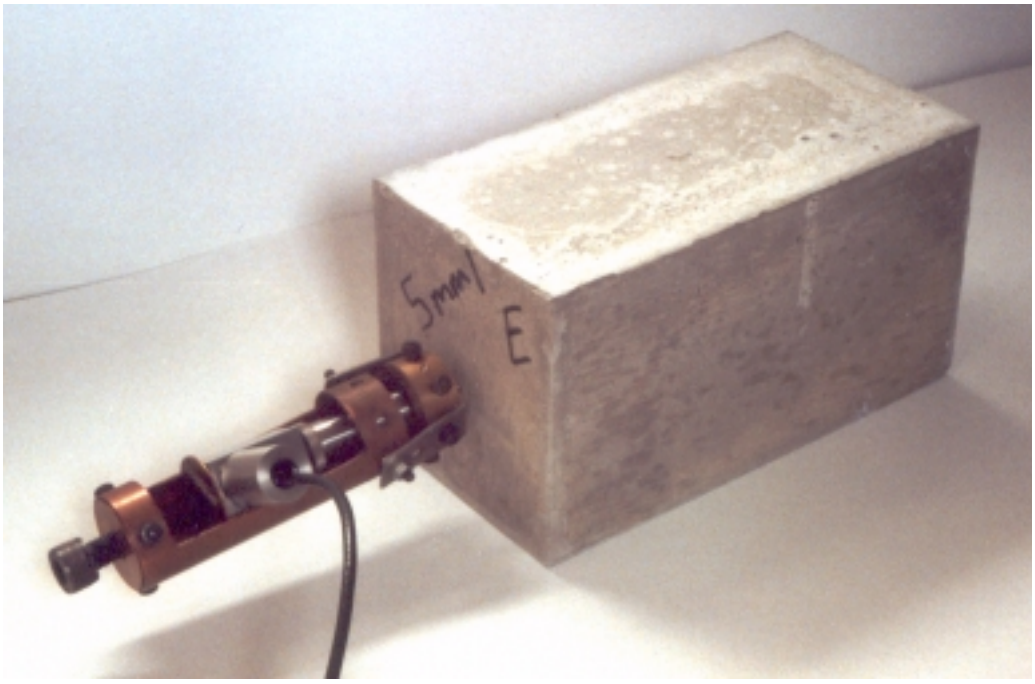

Figure 5.3: Grouted tendon specimen showing the transducer and clamp.

Frequency control was achieved by using a narrow bandwidth toneburst to excite the transducer. As discussed in chapter 4, using such a signal to excite a single mode has significant benefits. Figure 5.4 illustrates this for the tendon case, by showing the end reflection amplitude from a grouted strand at 4.76MHz against the number of cycles in the input signal. There is a steady improvement in amplitude with cycles, as more energy is put into the mode at the low-leakage frequency. The step change in improvement at 20 cycles is the point where a single mode only is excited. The nearest low-leakage modes are at 4.0MHz and 5.5MHz, and the insert in figure 5.4 shows that there is virtually no energy at these frequencies for a 20-cycle toneburst, hence destructive interference between modes is avoided. At very high numbers of cycles the benefit is diminished due to the limits of the receiver amplifier and limitations on the length of the outgoing signal.

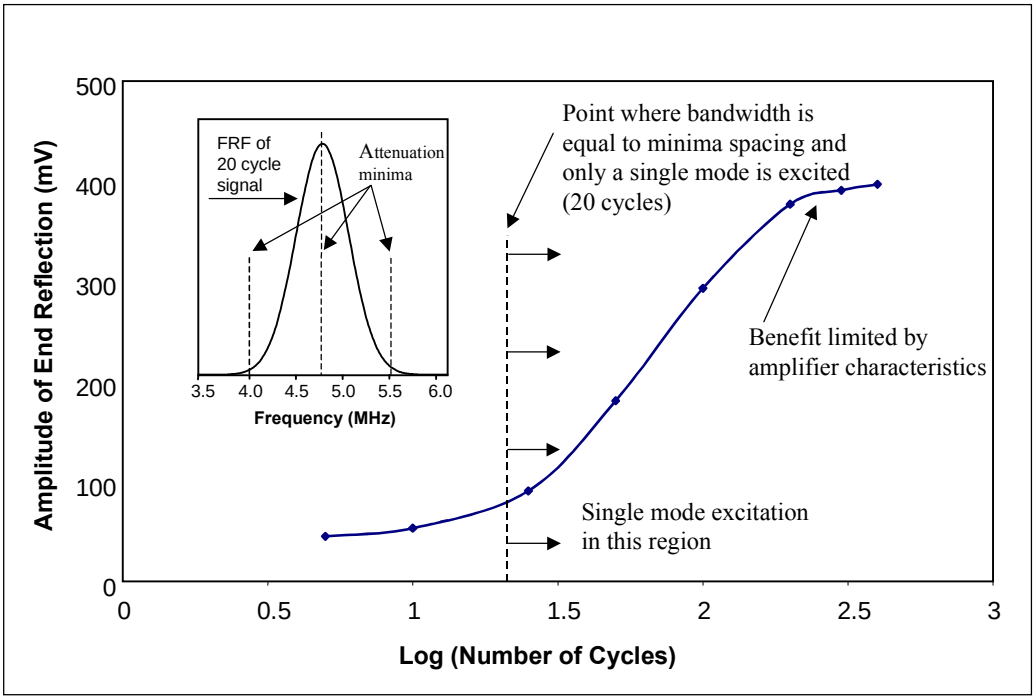

Figure 5.4: Effect of varying the number of cycles in the input signal on the end reflection amplitude from a 15.9m diameter grouted strand.

5.5 Method of Attenuation Measurement

It is relatively easy to measure the frequencies at which attenuation minima occur, simply by examining the strength of the end reflections obtained while varying the frequency of a narrow bandwidth excitation signal. If the attenuation is not too high, it is also possible to examine the FFT of an end reflection obtained with a wide bandwidth signal. Measuring the value of the attenuation is more difficult, as the signal must be compared at two points along an embedded length. The use of calibrated piezo-electric sensors at the surface of the bar could enable this to be done, and was attempted by Pavlakovic. However, since the edge displacement at the surface

of the bar is close to zero for the low attenuation modes, the received signals would be small. It would also be possible to measure attenuation by comparing signals from two similar bars, with different embedded lengths. However, the maximum difference in embedded length would be limited by the high attenuation, and also the need to maintain the same test configuration. As this method would also be subject to variations in transducer contact conditions, bond quality and grout properties, the overall uncertainty in the results would be high.

The method that has been used to measure attenuation in grouted tendons is to compare the relative amplitude of multiple end reflections from a short length of embedded bar. Specimens were constructed with an embedded length that would allow a signal to be detectable after it had travelled from the transducer to the end and back at least three times. The observed signal attenuation between subsequent reflections is a measure of the attenuation due to material damping and leakage, but also includes factors such as the reflection coefficient from the end of the bar, the transducer/bar interface, and the location where the bar enters the grout. However, these effects can be shown to be negligible. A typical signal obtained from this experiment is shown in figure 5.5, which shows 4 distinct end reflections from an 8mm diameter, 330mm long bar, completely embedded in grout apart from the first 30mm, which was left free for the transducer clamping assembly. The grout was contained within a rectangular box, with a 100mm square cross section, which allowed enough distance between the bar and the grout edges to scatter the leaked bulk waves.

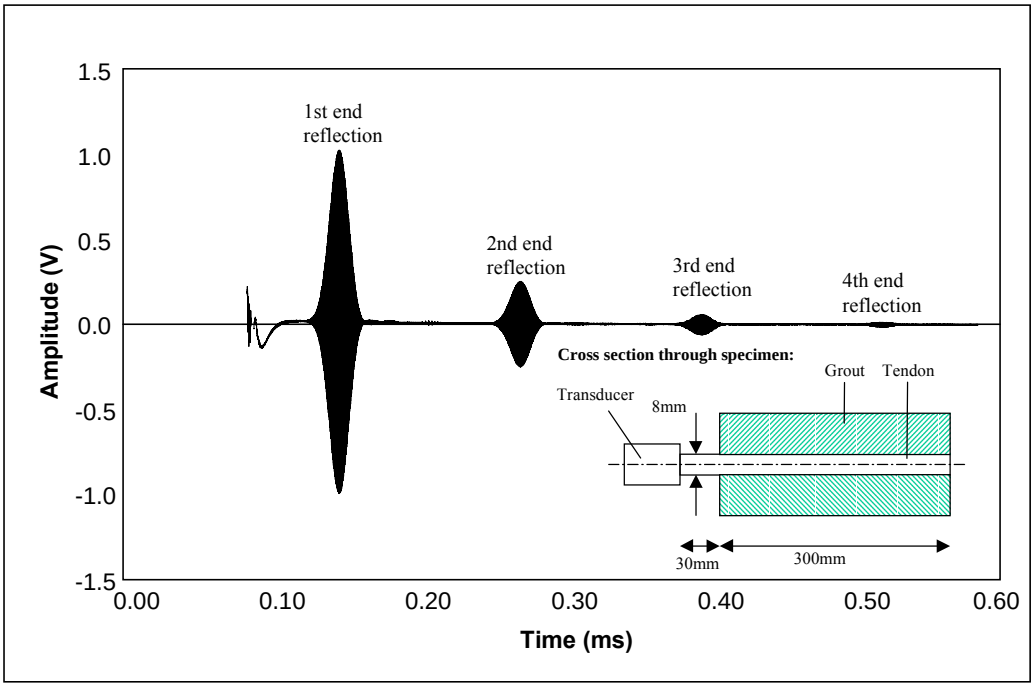

Figure 5.5: Multiple end reflections of the L(0,10) mode from the end of an 8mm diameter, 330mm long bar, excited by a 100-cycle toneburst centred on 4.75MHz.

The assumption that the high frequency low-loss modes are almost perfectly reflected from bar ends that are flat can be justified by examining the behaviour of the lower order modes. Pavlakovic [31,92] showed by Finite Element methods that the reflection of L(0,4) from a complete, flat break in a free bar is around 90% at the low-leakage point. The losses are due to mode conversion, rather than transmission to the air, because the acoustic impedance between the air and the bar is high. The amount of mode conversion is also small, and this can be related to the mode shapes at the low-leakage points. At these points, the axial displacement is high relative to the radial displacement, and the axial stress is high compared to the shear stress, as shown in figure 5.6 for the L(0,10) mode. The sum of all the stresses of the incident and reflected waves must be zero at the reflecting end, to satisfy the required stress free boundary condition. This condition can be met almost entirely by the incoming and outgoing low-leakage mode, because the total stress is dominated by the axially symmetric in-plane stress (σ_{zz}). This means that only a very small amount of mode conversion to other propagating and non-propagating modes is required to meet the boundary condition. Hence, the reflection coefficient for these modes is high. This effect has been investigated by Lowe [95] for the case of a free plate.

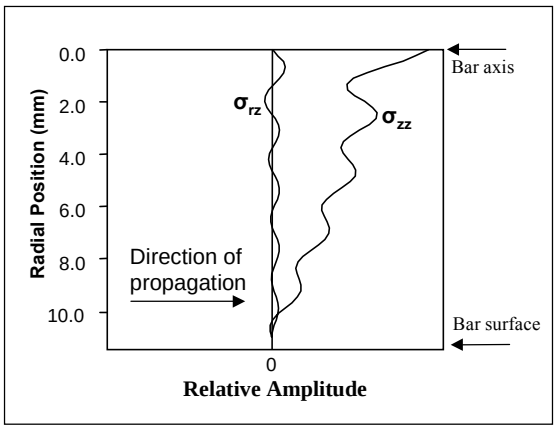

(a) In-plane (σ_{zz}) and shear (σ_{rz}) stress.

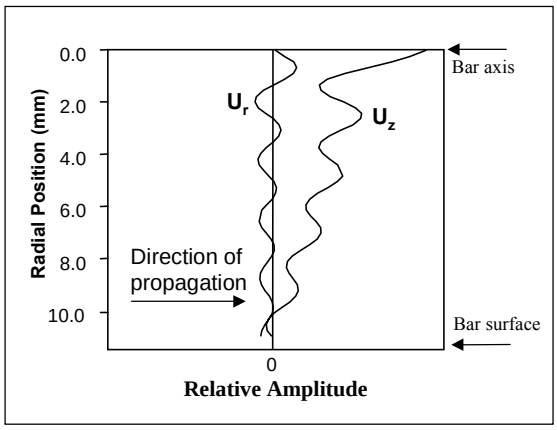

(b) Axial (u_z) and radial (u_r) displacement.

Figure 5.6: Stress and displacement mode shapes for the L(0,11) mode at a frequency-radius of 19MHz-mm in grouted bar.

The high number of elements needed for the simulation means that the reflection coefficients for the L(0,8)-L(0,11) modes cannot currently be calculated using finite element methods. However, examination of the mode shapes show that as the mode order increases, the relative amount of in-plane stress to shear stress increases, and the shear stresses become increasingly less significant. Hence it is likely that for these modes, the amount of mode conversion at flat ends will be less than that for the L(0,4) mode. The reflection coefficient of the high order low-

leakage modes from a flat break in a bar can therefore be assumed to be almost unity. Even if the reflection coefficient is only 90% at both ends of the specimen, the overall error in attenuation (dB/m) for the typical case of a 6mm diameter wire would only be about 5%.

This estimation of error assumes that the reflection coefficient from the transducer/bar interface is also close unity. In reality, there will be some additional losses over those that occur at a flat end in air, due to transmission of energy to the transducer face. The additional attenuation has been measured by comparing the end reflection amplitude from a grouted bar exposed to air at free end, with the end reflection amplitude from a grouted bar with a transducer well coupled to the free end. The additional transducer was placed without removing the measuring transducer, to ensure the coupling conditions remained constant. The measured change in end reflection amplitude ranged from +5% to -5%, indicating that the change in reflection coefficient was smaller than the error associated with the measurement. Clearly some energy must pass to the transducer face, but the amount is small compared to the leakage and material damping attenuation, and can be ignored.

The final attenuation mechanism that must be considered is reflection from the point where the bar enters and leaves the grout. Vogt [93] has shown that the expected amplitude reflection coefficient for the L(0,1) mode in a steel bar entering a block of epoxy is approximately 3% at a frequency-radius product of 0.4MHz-mm. The reflection coefficient of this mode is only significant at very low frequency-thickness products. At the higher frequency attenuation minima, the higher order modes show much less interaction with the outside of the bar and it is likely that the reflection from such an interface will be at least an order of magnitude lower. Hence the losses at the grout boundary will be extremely small, and can be ignored. This is confirmed by the fact that only end reflections were visible on the time traces from the grouted bar experiments, despite having been attenuated through leakage into the grout.

5.6 Wire Specimens

5.6.1 Experimental Results

Table 5.3 shows the predicted and measured values of energy velocity and attenuation in 5mm, 6mm and 8mm wire specimens, and the same information is shown graphically in figure 5.7. The predicted values were calculated from the frequency and attenuation-radius products shown in table 5.2. The measured attenuation values were obtained using the method outlined in section 5.5, and the energy velocities were calculated from an average of the time between the subsequent reflections. All of the results have been averaged between two nominally similar specimens. The variation between the pairs of samples was at most 5%, showing a good degree of consistency in the grouting conditions.

Frequency (MHz)	**Predicted E_{vel} (m/ms)**	**Actual E_{vel} (m/ms)**	**Predicted Atten. (dB/m)**	**Act. Attenuation (dB/m)**
3.29 - L(0,8)	5.23	5.15	51.4	18.8
3.78 - L(0,9)	5.36	5.26	45.9	19.0
4.25 - L(0,10)	5.44	5.33	42.8	19.2
4.75 - L(0,11)	5.55	5.27	41.0	20.4

(a) 8mm diameter (specimen length 330mm, 300mm embedded).

Frequency (MHz)	**Predicted E_{vel} (m/ms)**	**Actual E_{vel} (m/ms)**	**Predicted Atten. (dB/m)**	**Act. Attenuation (dB/m)**
4.38 - L(0,8)	5.23	5.11	68.6	26.6
5.04 - L(0,9)	5.36	5.23	61.2	28.7
5.67 - L(0,10)	5.44	5.34	57.0	29.8
6.33 - L(0,11)	5.55	5.33	54.6	32.1

(b) 7mm diameter (specimen length 280mm, 250mm embedded).

Frequency (MHz)	**Predicted E_{vel} (m/ms)**	**Actual E_{vel} (m/ms)**	**Predicted Atten. (dB/m)**	**Act. Attenuation (dB/m)**
5.26 - L(0,8)	5.23	5.10	82.3	40.4
6.04 - L(0,9)	5.36	5.23	73.5	42.6
6.80 - L(0,10)	5.44	5.27	68.4	43.1
7.60 - L(0,11)	5.55	5.26	65.6	48.3

(c) 5mm diameter (specimen length 220mm, 200mm embedded).

Table 5.3: Measured and predicted attenuation and energy velocity in different diameter steel bars embedded in grout.

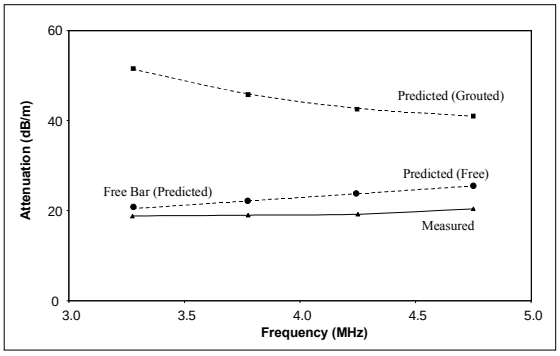

(a) 8mm diameter bar.

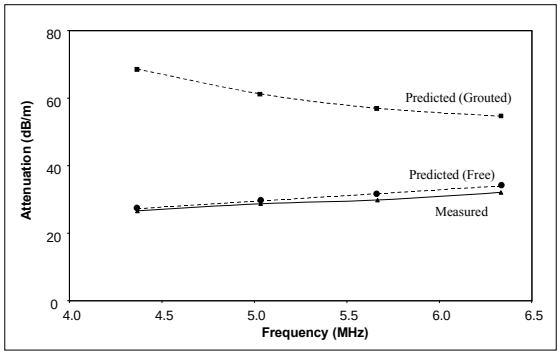

(b) 6mm diameter bar.

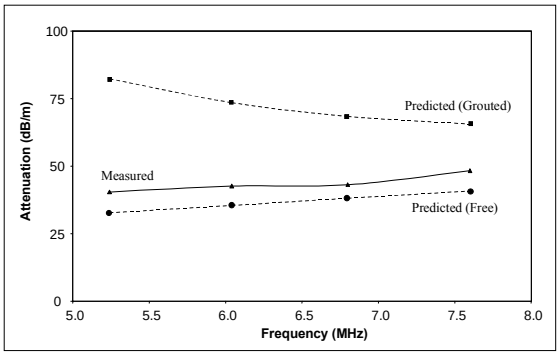

(c) 5mm diameter bar.

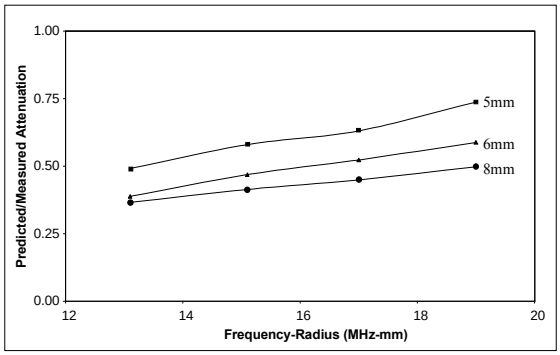

(d) Ratio of predicted to measured attenuation in 5,6 and 8mm diameter bars.

Figure 5.7: Measured and predicted attenuation for different diameter steel bars embedded in grout, and predicted attenuation for different diameter free steel bars.

5.6.2 Discussion of Measured and Predicted Results

Comparison of Energy Velocity

The results for the measured energy velocity are highly consistent, and all the measured values fall between 95% and 98% of the predicted values. The reason for the lower measured velocity is probably due to small errors in the assumed material properties. The bar shear and longitudinal velocities are based on a steel with a very high modulus, and the actual bulk velocities may be slightly lower. This will also lower the predicted energy velocity at the attenuation minima. It is not possible to obtain much information about the accuracy of the modelling from the energy velocity values, as table 5.2 shows that the free and embedded bar velocities are very close anyway. Changes in velocity due to factors such as grout/bar contact conditions would therefore be very small.

Comparison of Attenuation

Table 5.3 shows that there are large differences between the measured and predicted values of attenuation in all of the bars embedded in grout. This information is presented graphically in figure 5.7, which shows the measured and predicted attenuation together with the predicted free bar attenuation. In general, the measured attenuation is lower than the predicted values, and is closer to that predicted for a free bar than that predicted for an embedded bar. The overestimation of attenuation can be seen to be worse in the smaller diameter tendons. The differences could be due to an overestimation of the material damping properties used by the model, or an overestimation of the leakage brought about by the assumption of perfectly bonded layers.

More information can be obtained by examining the frequency dependence of the attenuation. In general, it is expected that the attenuation due to leakage decreases with frequency, and that the material attenuation increases with frequency. The exact frequency at which the minimum overall attenuation is found is therefore highly dependent on the steel damping properties, the embedding material properties, and the bonding quality. The attenuation predictions for the modes that were examined generally decrease with frequency, but the measured attenuation values do not show this trend, and show much less frequency dependence than the predictions. This suggests that the optimum balance between leakage and material damping occurs at a lower frequency. It is unlikely that the material damping has been underestimated, as some of the measured attenuation values are already below the free bar predictions, and so it is probable that the leakage component of the attenuation is greatly overestimated by the modelling. The main reason for this is likely to be poor bonding between the tendon and the grout, the effect of which is discussed for the rock bolt case in chapter 3.

In general, the results show that the predicted attenuation values are not reliable. There are two main reasons for this, firstly the difficulty in measuring precise material damping properties, and secondly, the unknown conditions at the grout/bar interface. The measured attenuation values are subject to an error of about 5% because of the assumptions of the method, plus approximately a further 5% for variations between samples and the effect of noise on the recorded time traces. The assumptions of the method will result in an overestimate of attenuation being made, and therefore the attenuation measurements can be considered reliable enough to determine maximum inspection ranges.

5.6.3 Effect of Post-Tensioning

A major difference between the laboratory specimens and real tendons is that the real tendons are carrying a high tensile load to pre-stress the concrete. Each tendon is held under tension by a collet assembly at the anchorage point, which clamps firmly onto each tendon. The loading stress in the tendon is unlikely to affect the propagation of ultrasound, as the elastic properties are unchanged by the load, and the additional stresses caused by the sound wave propagation are small. However, the three-jaw clamp that forms part of the collet assembly is directly in contact with the tendon, and has the potential to act as a reflector of ultrasound.

The effect of the collet assembly has been investigated by comparing the amplitude of the end reflection from a short length of grouted bar with and without a collet fitted. However, the collet could not be fixed using the real method, as it is not possible to tension the wires after the grout has hardened, and the grout is needed to prevent the propagation of non low-leakage modes. It would be possible to use separate tensioned and free specimens, but the differences in grouting conditions and transducer coupling would probably have a greater effect than the collet. The collet was therefore firmly attached to the tendon using a clamp. Before clamping, the inside of the collet was lightly coated with grease to maximise the acoustic coupling to the tendon to simulate the good coupling that may occur as a result of the collet teeth engaging with the surface of the tendon. Experience with clamping the transducer onto the bolt ends has shown that the amount of energy transferred to and from the tendon quickly reaches a maximum as the clamping force is applied, and it is therefore reasonable to assume that this experiment is a good approximation to the real situation.

The additional attenuation due to the clamp was measured to be less than 0.5dB for the pulse-echo test, or 0.25dB per single pass. The transmission coefficient per pass is therefore 97%. This implies that the combined reflection coefficient from both of the ends of the collet is less than 3% for the low-leakage modes, as some of the attenuation will be due to leakage into the jaws. The rest of the attenuation is due to mode conversion at the ends of the collet. This very low reflection coefficient from a boundary with a material that is almost perfectly acoustically matched to the tendon gives further confidence in the assumption that the reflections from the entry points into the grout are negligible. The experiment was not repeated for strands, as the next section shows that ultrasound can only propagate long distances in the centre wire, which is not in direct contact with the collet. Overall, this experiment shows that the presence of collets on real tendons will make virtually no difference to the range that can be inspected.

5.7 Strand Specimens

5.7.1 Experimental Results

The major emphasis of the experiments on grouted strands was to measure and compare the attenuation in the inner and outer wires. The motivation for this was to firmly establish how the sound wave propagates in the tendon, and to confirm and explain the suggestions of previous authors that the sound travels mainly in the centre wire. The work of Pavlakovic [5,31] included tests on strands with different numbers of component wires broken. The tests were only successful on specimens that had the centre wire broken, leading to the conclusion that most of the energy was transmitted in the centre wire. The successful testing frequencies were also found to correspond to those predicted for a bar of the same diameter as the centre wire. Pavlakovic suggested that the lower attenuation experienced in the centre wire could be explained by poor coupling into the grout, and that this was the reason for the long propagation distances reported by Weight [30].

The attenuation experienced by the low-leakage modes in the centre and outer wires of strand tendons has been measured using the multiple reflection technique outlined in section 5.5. Two 300mm long, 15.9mm diameter strand specimens were prepared and embedded in a 250mm length of grout. As for the wire specimens, the grout was contained within a rectangular box, with a 100mm square cross section, allowing sufficient embedding material around the strands to scatter any leaked bulk waves. Before embedding, each of these specimens had some wires shortened at the free end by grinding, to allow access to either an outer wire or the centre wire. The separate wires were then tested individually, at frequencies corresponding to the four attenuation minima previously examined. Note that the test frequencies were different for the inner and outer wires, because the diameters are different. The measured and predicted attenuation and energy velocity are shown in table 5.4, and also graphically in figure 5.8. The predictions are based on those for a fully grouted individual wire. The results show that the individual wires in the strands behave very differently to individual wires of the same diameter, even though the optimum test frequencies were found to be the same. As expected, there are also major differences between inner and outer wires.

Frequency (MHz)	Predicted E_{vel} (m/ms)	Actual E_{vel} (m/ms)	Predicted Atten. (dB/m)	Act. Attenuation (dB/m)
4.76 - L(0,8)	5.23	4.92	74.8	20.5
5.47 - L(0,9)	5.36	5.04	66.8	22.1
6.18 - L(0,10)	5.44	5.06	62.2	23.4
6.91 - L(0,11)	5.54	5.07	59.6	25.6

(a) Inner wire (5.5mm diameter).

Frequency (MHz)	Predicted E_{vel} (m/ms)	Actual E_{vel} (m/ms)	Predicted Atten. (dB/m)	Act. Attenuation (dB/m)
5.06 - L(0,8)	5.23	4.75	79.1	59.5
5.81 - L(0,9)	5.36	4.94	70.7	57.6*
6.54 - L(0,10)	5.44	**	65.8	56.9*
7.30 - L(0,11)	5.54	**	63.0	51.0*

* Minimum values of attenuation due to the second reflection being below the noise floor.
** Accurate measurement not possible to due poor propagation at the centre frequency.

(b) Outer wire (5.2mm diameter).

Table 5.4: Measured and predicted attenuation and energy velocity in the inner and outer wires of a 15.9mm grouted seven-wire strand.

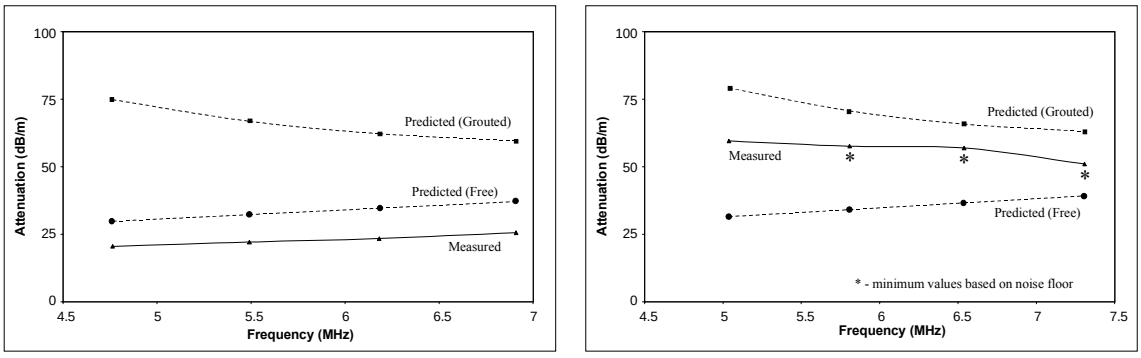

(a) Centre wire (5.5mm diameter). (b) Outer wire (5.2mm diameter).

Figure 5.8: Measured and predicted attenuation in a 15.9mm grouted seven-wire strand.

5.7.2 Discussion of Results - Centre Wire

The attenuation in the centre wire of the strand is much lower than in the 5mm wire specimen, which suggests that the leakage is very low due to limited contact with the grout. The measured values are also below the predicted free bar attenuation, which was not the case for the fully grouted 5mm wire. This suggests that all the tendon models have overestimated the material attenuation, as well as the attenuation due to leakage. Further evidence that the leakage is very low can be seen from the time traces recorded for the centre wire, an example of which is shown in figure 5.9. The time trace shows evidence of other modes propagating, which would only be possible if poor coupling to the grout was reducing the leakage of these modes. It is possible that much of the leakage that does occur is into the surrounding steel bars, and therefore the other modes that are observed are modes that propagate in the tendon as a whole.

The energy velocity is also lower than that predicted for a wire. This is partially an effect of the lower attenuation and the factors discussed above, but may also be due to the high steel velocities assumed in the modelling. The attenuation measurement samples are made from a lower strength steel, and this will lower the longitudinal bulk velocity, and also the energy velocity of the low-leakage modes.

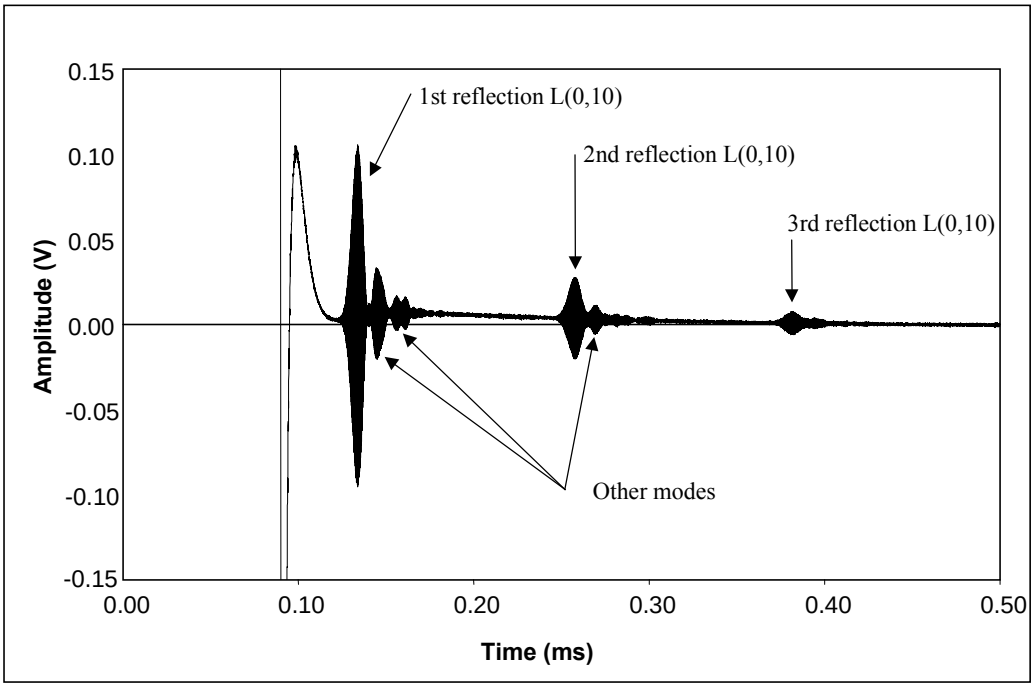

Figure 5.9: End reflections of the L(0,10) mode obtained from the centre wire of a 300mm length of 15.9mm grouted strand, tested at 6.18MHz using a 100-cycle toneburst.

5.7.3 Discussion of Results - Outer Wire

Figure 5.8b shows that the measured attenuation for the spirally wound outer wire is 2-3 times higher than for the inner wire. Accurate results could only be obtained for the L(0,8) mode at 5.06MHz, as at the other frequencies the second reflection was below the noise floor. The measured attenuation for other modes is therefore a minimum value, based on the size of the first reflection relative to the noise floor. The minimum value decreases with frequency because the transducer output (and therefore the size of the first reflection) decreases with frequency, whereas the noise floor is relatively constant. The fact that a second reflection could only be obtained for the L(0,8) mode suggests that attenuation increases with mode order. The increase in attenuation over the centre wire is too high to be explained only by better coupling into the grout, suggesting that the curvature itself is a significant factor.

The energy velocity was also found to be lower for the outer wire. This is linked to the high attenuation values; the modelling studies presented in chapter 3 show that the high attenuation regions on these modes are associated with low energy velocity. Measurement of the energy velocity was not possible in all cases, due to poor definition of the first reflection. Closer examination of this signal provides insight into the high attenuation levels recorded in the outer wire. Figure 5.10 shows the FFT of the first end reflection from the outer wire of a strand tested at 6.54MHz with a 100-cycle toneburst. The FFT shows that very little energy has propagated at the centre frequency of 6.54MHz, but some energy has propagated at frequencies away from the expected attenuation minima. This has been found to be a direct effect of curvature, and this phenomenon is investigated further in chapter 6.

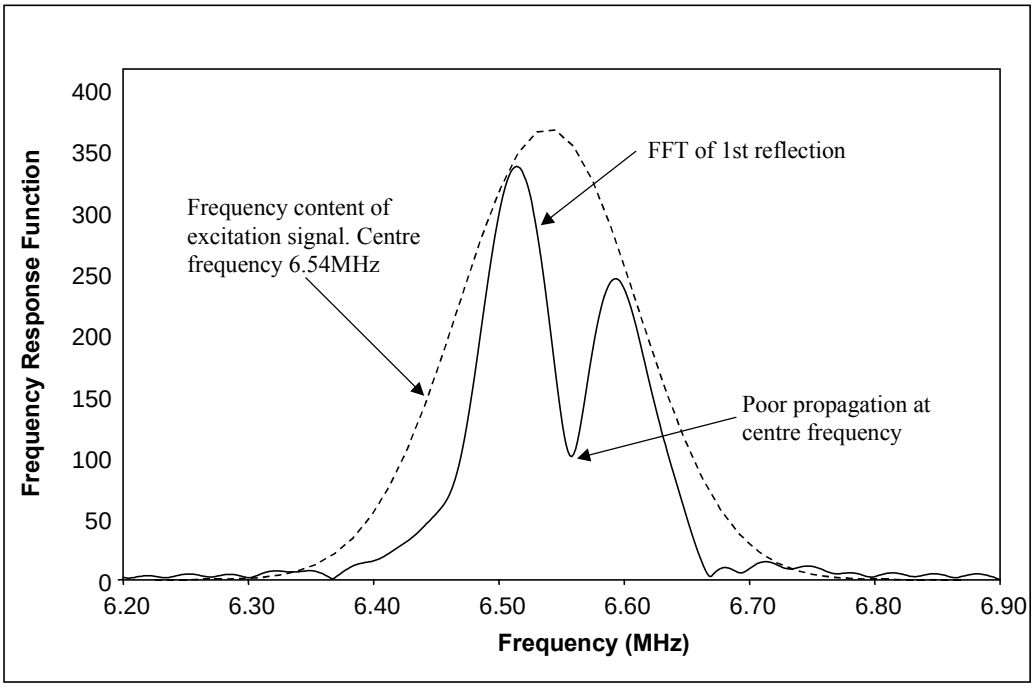

Figure 5.10: FFT of the first end reflection from the outer wire of a grouted strand, tested with a 100-cycle toneburst centred on 6.54MHz.

5.8 Effect of Defect Geometry

The likely effect of defect geometry can be estimated from the experimental work carried out on the reflection of modes from different end angles reported in chapter 4. This experiment shows that, at a frequency-radius of 25MHz-mm, a deviation of just 10° from a flat end results in a reduction in end reflection amplitude of about 40dB. Increasing the end angle still further increases the reflection coefficient slightly, but the loss is still 30dB for an angle of 45°.

The reflection coefficient would be even less for partial depth defects such as corrosion patches or breaks with a poor surface finish. Finite Element studies carried out by Pavlakovic [31,92] show that the reflection coefficient of L(0,4) from a defect resembling a square notch extending halfway through the radius of a bar would be about 0.6, and from a quarter depth defect about 0.2. However, as the frequency is increased the energy of the modes becomes more concentrated in the centre of the tendon, and it is likely that the L(0,8)-L(0,11) modes would have lower reflection coefficients from surface defects than L(0,4). Even if this is not the case, the L(0,4) figures suggest that a corrosion patch extending a quarter of the way through the radius (removing roughly half the surface area) would cause the reflection amplitude to be reduced by an extra 14dB over a full depth defect. The amplitude of a reflection from such a defect could therefore be between 44 and 54dB lower than that from a flat break. It is therefore unlikely that real partial depth defects such as corrosion patches could be detected reliably.

5.9 Tendon Testing Conclusions

The research presented in this chapter has been used to assess the maximum potential inspection range for different defects in a range of wires and strands. The predictions are based on an assumed maximum amplifier gain of 100dB, which is close to the upper limit for the NDT equipment that is currently available. Some of the predictions take into account the fact that the defect may not have a reflecting surface that is normal to the bolt axis. It has been assumed that the reflection amplitude from such a defect will be 40dB lower than that from a flat break. This is based on the worst-case example of a reflecting angle at 10° to the normal to the bolt axis. The predictions also assume a smooth reflecting surface. Further surface roughness caused by corrosion may increase the overall attenuation at the reflecting surface.

The dispersion curves for a grouted tendon have been calculated, and the L(0,8)-L(0,11) modes were shown to have attenuation minima at frequency-radius products of 13.1, 15.1, 17.0 and 19.0MHz-mm. Lower attenuation was predicted for the first low-leakage mode L(0,12), but the high frequencies required to generate the mode in small diameter tendons make its use impractical. The energy velocity predictions showed good agreement with the measured velocities, although the attenuation predictions were found to be unreliable. In general the attenuation was overestimated by the modelling. The main reasons for this are thought to be an overestimation of the steel damping properties, and a general overestimation in the amount of leakage that takes place because of the assumption that the steel/grout interface is perfectly bonded. The frequencies of the attenuation minima agree with the predictions, although some slight shift in frequency can be expected due to differences in the bulk wave speeds of different types of steel.

The optimum excitation signal has been found to be a very narrow bandwidth toneburst, containing about 200 cycles. This concentrates all the ultrasonic energy at the low-leakage frequency, and avoids the detrimental affect of interference between modes, which can occur if multiple low-leakage modes are excited. The received signal needs to be averaged at least 50 times to remove the effects of random noise, and filtering can be used to remove unwanted frequencies, either from the live signal, or from the recorded time trace as part of the post-processing. However, the benefit of filtering is reduced by the use of narrow bandwidth signals, as the all of the ultrasonic energy is already propagating at the target frequency.

The modes used for testing are largely unaffected by the collet assembly that holds the post-stressing tendon in tension. The lack of surface displacement of the modes makes the reflection coefficient for such boundaries very small, and no reflections were obtained from this interface. This also means that the mode would be very difficult to generate from the sides of the tendon

(e.g. through bore holes), and the inspection would be limited to the tendon anchorage region through the tendon ends.

The 15.9mm strand has a minimum measured attenuation of 20dB/m, which gives a test range of 1.5m for a complete break, for any break angle. This is consistent with the findings of Pavlakovic [5,31], who was able to detect a complete 45° break in a strand at 1500mm, but not at 2000mm. The lowest measured attenuation in the outer wire was 60dB/m, limiting the inspection range to 0.5m. The test would need to be conducted at the optimum frequency for both the 5.2mm outer wires and the 5.5mm inner wires. Detection of a corrosion patch removing half of the wire cross-sectional area would reduce the range to 1.0m for a centre wire, and about 0.3m for an outer wire. Smaller diameter strands would have a reduced inspection range. The large difference in attenuation between the inner and outer wires occurs because of the curvature in the spirally wrapped outer wires. This effect is examined further in chapter 6.

The minimum attenuation measured for the 8mm, 7mm and 5mm diameter wires was 19dB/m, 27dB/m and 40dB/m respectively. The inspection range for a complete break would be limited to about 1.2m for a 7mm wire, and 0.8m for a 5mm wire. The measurements are consistent with the findings of Pavlakovic [31], who was just able to detect a flat break in an 8mm diameter, 2m long grouted wire, which would have experienced around 80dB of total attenuation. Detection of corrosion patches removing half the wire cross-sectional area would reduce the range to 0.8m for a 7mm diameter wire, and about 0.5m for a 5mm diameter wire.

Overall it is felt that the opportunity for guided wave inspection of concrete reinforcing tendons is limited. The attenuation due to leakage is lower than the predictions suggest, but still very high, especially in small diameter wires. The testing of strands is extremely limited by the fact that only the centre wire could be inspected reliably, and even full breaks in the other six wires could not be detected if more than 0.5m from the test point. There are also other problems of inspecting tendons using this method. The modelling predicts a much higher maximum attenuation than that measured, and therefore any factors such as slight corrosion improving the grout/bar bond, may increase the attenuation. This presents a problem in a blind test such as this, where no positive confirmation of the inspection length can be obtained, and therefore guided waves do not offer a complete solution to testing even localised areas of tendon. The method may be used to provide positive confirmation of defects in the anchorage region, but not as a reliable screening technique. There are two main reasons why the tendon testing is not as successful as the rock bolt application. Firstly, the tendons have a much smaller diameter, which increases the attenuation of the waves, and secondly, the shorter length of the rock bolts gives the possibility of detecting an end reflection, which provides positive confirmation that the test is working properly and that the entire length has been screened.

CHAPTER 6

EFFECT OF CURVATURE

6.1 Introduction

The practical testing of both concrete reinforcing tendons and rock bolts has shown that there are issues concerning the propagation of ultrasonic guided waves through curved structures. In particular, the high frequency, low-leakage guided waves investigated in chapter 3 are attenuated strongly in the outer, spirally wound, wires of stranded tendon, and problems have also been encountered in testing rock bolts that are thought to have become deformed due to ground movement. This chapter investigates this 'curvature effect' by examining a series of experiments designed to show that attenuation occurs in both free and embedded bars, and then by calculating, examining and comparing the mode shapes in curved and straight plates. Finally, the dispersion curves for a curved bar have been calculated using a finite element method, as there is currently no analytical guided wave solution for this geometry. Conclusions are drawn about the behaviour of low-leakage modes in curved structures.

6.2 Experimental Confirmation of Effect

It was necessary to confirm that curvature could cause the additional attenuation observed in curved strand and rock bolt specimens. However, since it is difficult to measure attenuation directly, it was necessary to compare the end reflection amplitude from different straight, curved, free and embedded bars in order to estimate the attenuation.

6.2.1 Curved Embedded Bar

Ideally, it would be desirable to test a single bar specimen with curvature that could be changed, to remove the possibility of variations in the embedding material affecting the results. Clearly, it is not possible to do this with an embedded bar, and therefore similar specimens, with different amounts of curvature, were constructed and cast within the same concrete block. The effect of variations in the embedding material on the attenuation was in any case thought to be small compared to the effect of curvature.

Four 1.2m long, 16mm diameter, smooth steel bars were used for the experiment, with the centre 1m embedded in concrete. Curvature was applied by tightening bolts against the surface

of the bars before the concrete was cast. The bars were supported at each end of the embedded section, and the bolts were located at 0.25m and 0.75m along the embedded section to give as constant curvature as possible, as shown in figure 6.1. A length of 100mm was left protruding from both ends of the concrete block, allowing a pulse echo test to be made from each end. The curvature was measured in terms of the amount of deflection at the centre of the embedded length. Three bars were deformed, with 10mm, 20mm and 30mm of lateral deflection at the bar centre, and the fourth bar was left straight. This amount of centre deflection roughly corresponds to curvature radii of 12.5m, 6.8m, and 4.1m respectively, with the arc made by the bars turning through 2.3°, 4.6° and 6.9°. This level of curvature is very slight, with the ratio of curvature radius to bar diameter being 780, 420 and 260.

Guided waves were then excited in each bar at 5 frequencies corresponding to attenuation minima using a 350-cycle Gaussian windowed toneburst. This high cycle signal was necessary to examine the behaviour of the modes over a very narrow frequency bandwidth, and was the maximum number of cycles that would fit into the outgoing signal window of the 'Wavemaker 10' instrument that was used for the experiments. The transducers used were from the Aerotech 'Alpha' immersion probe range [94], with centre frequencies of 2.25MHz and 5.0MHz. These transducers are highly damped, and therefore it was possible to conduct tests over the entire frequency range of interest with just the two probes. The transducers were clamped on to the bars with the transducer holder shown in figure 4.3, using an adapter to allow it to be clamped on to a smooth bar. A standard coupling gel was used to improve the transmission of ultrasound. The end reflection amplitude was measured three times from each end of the block and all the results averaged, to reduce the effect of variation in end conditions and transducer contact conditions.

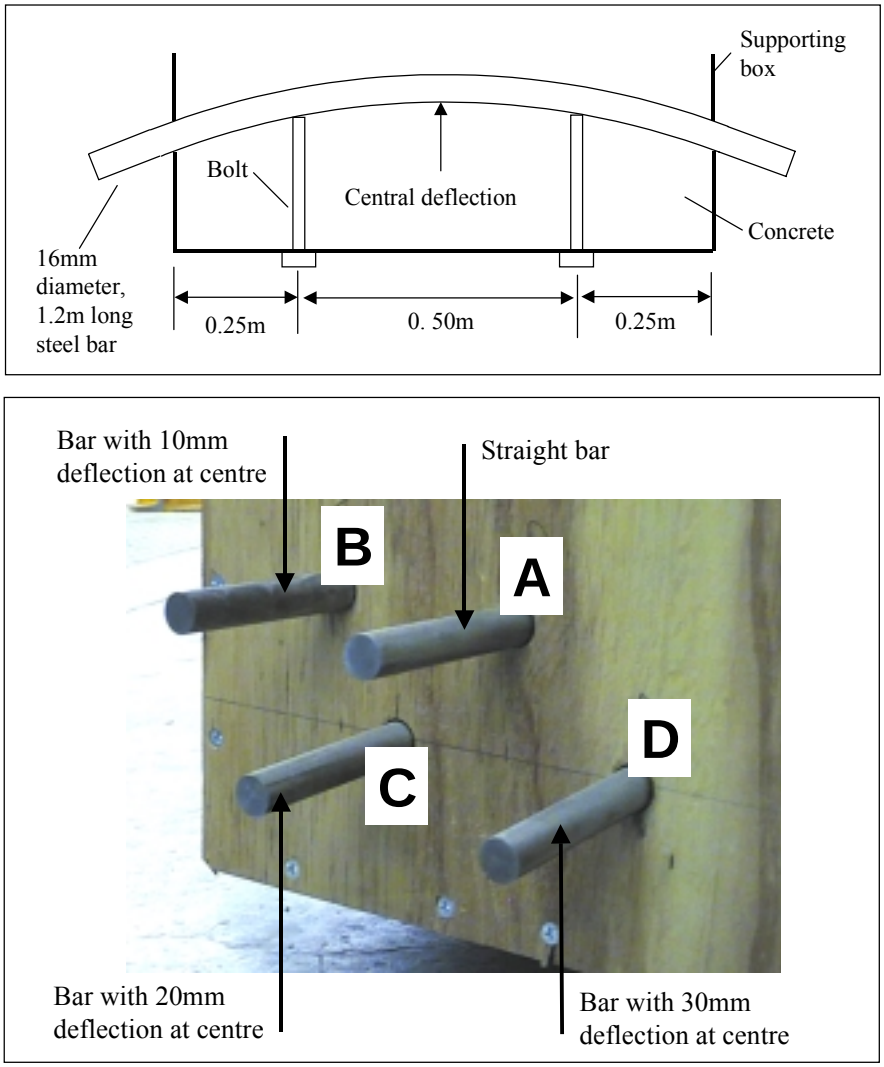

Figure 6.1: Experiment to compare the attenuation of high frequency, low-leakage modes in 16mm diameter embedded bars with different amounts of curvature.

The relative amplitude of the end reflections obtained is shown in figure 6.2. The results have been normalised so that the amplitude of the straight bar reflection is unity at each frequency. The test frequencies shown can be related to the rock bolt test modes by the frequency-diameter dependence of the dispersion curves. The 2.52MHz and 3.28MHz test frequencies correspond to the frequencies of minima at 1.88MHz and 2.40MHz in a rock bolt. It can be seen that increasing the curvature of the bar reduces the end reflection amplitude considerably. The lowest frequency mode (2.52MHz) is affected least by the curvature, with higher frequencies being attenuated more. However, at frequencies over 4MHz, there is little difference between the end amplitudes recorded for any of the modes.

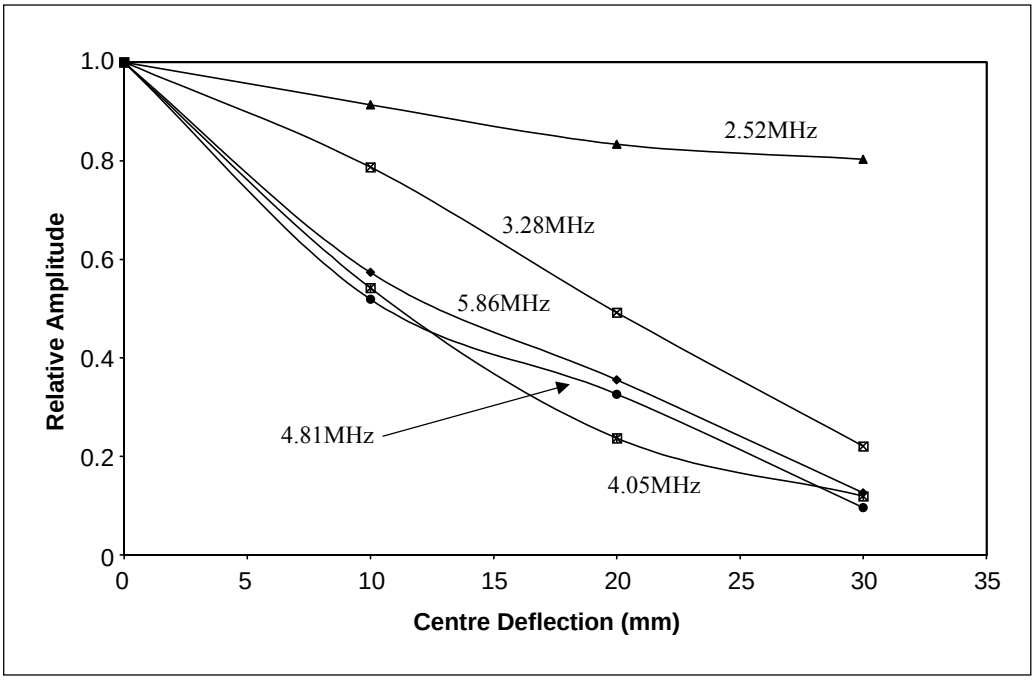

Figure 6.2: End reflection amplitude for different low-leakage modes in 16mm diameter curved bars embedded in concrete. Amplitudes have been normalised against the end reflection amplitude from a similar, straight bar.

Further information about exactly how the modes are affected by curvature can be obtained by examining the end reflection closely at a range of frequencies around an attenuation minimum. A series of tests were recorded around 4.05MHz (equivalent to about 3MHz in a rock bolt), using a 350-cycle signal to give a bandwidth of less than 50kHz at 50dB below the maximum signal level. The results of this experiment are summarised in figure 6.3, with sample time and frequency domain signals shown in figure 6.4. As expected, the straight bar shows a maximum in signal amplitude at the attenuation minimum at 4.05MHz. However, as the curvature is increased the end reflection at this frequency is almost completely attenuated. The response of the curved bars is significantly better away from this frequency, so from a practical point of view it may still be possible to test curved bars at a frequency shifted from the predicted optimum, although this would increase the attenuation due to leakage in the straight sections.

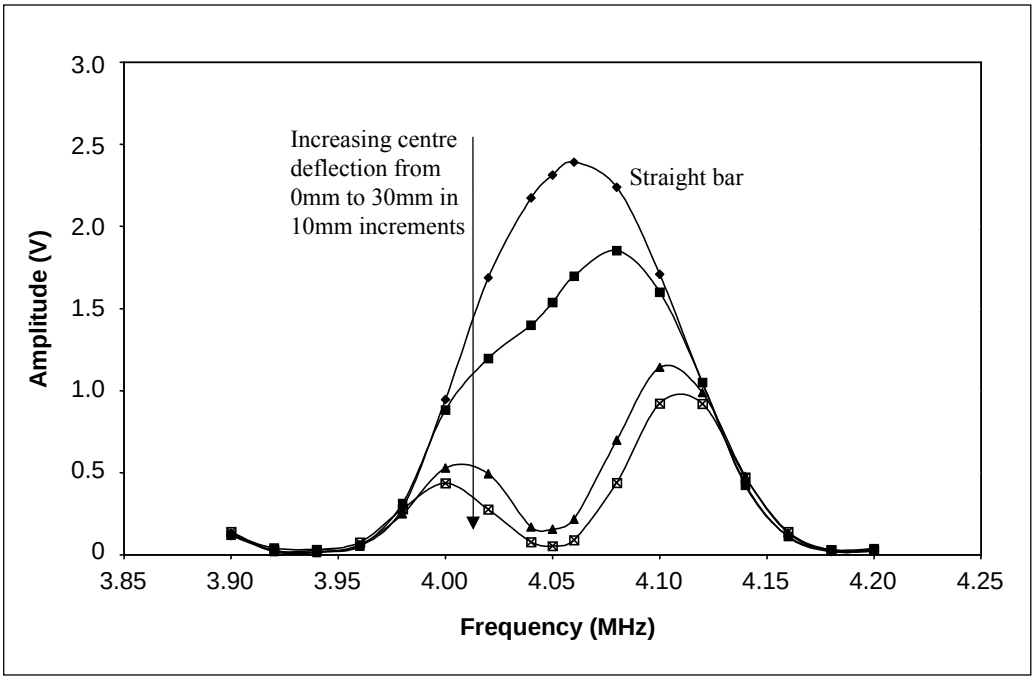

Figure 6.3: End reflection amplitude obtained from different 16mm diameter curved steel bars embedded in concrete, at frequencies close to a straight bar attenuation minimum at 4.05MHz.

The time trace for the straight bar in figure 6.4 (Bar A) shows a clear first and second reflection from the bar end, and the FFT is a smooth curve resulting from the shape of the input signal and the filtering effect of the embedding material. As the curvature is increased, the end reflection decays in clarity and amplitude (note the different scales), and the FFT information shows that less energy is able to propagate at the centre frequency of 4.05MHz. The bar with the most curvature (Bar D) shows that almost no energy propagates at the optimum frequency for a straight bar, even though the curvature radius is still over 4m. The time domain signals also shows signs of interference between the different frequency components.

It is clear that the attenuation minima that exist in a straight bar do not exist in a curved bar at the same frequencies. One possible reason for this is that the low-leakage mode shape characteristic does not occur in curved bars, increasing the attenuation due to leakage. Another possible reason is related to mode conversion at the transition between straight and curved sections of the bar. If the mode shapes in these sections are significantly different then there will be attenuation of the low-leakage modes through mode conversion to other, more leaky, modes at straight/curved section boundaries. If this is the case, then it would be expected that the observed attenuation at the low-leakage frequency in an embedded bar could also be observed in a free bar.

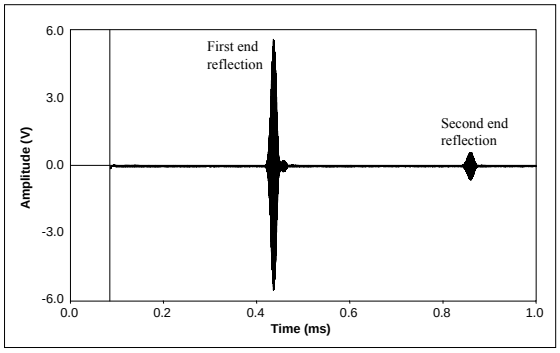

Bar A (straight): Time domain.

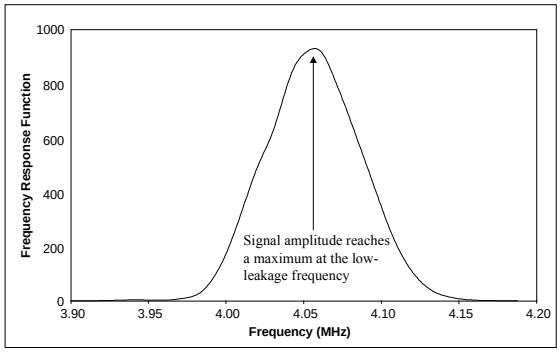

Bar A (straight): Frequency domain.

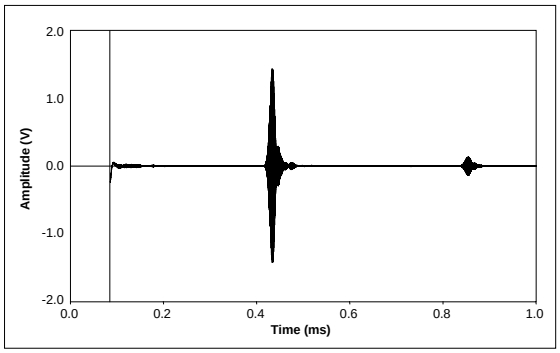

Bar B (10mm deflection): Time domain.

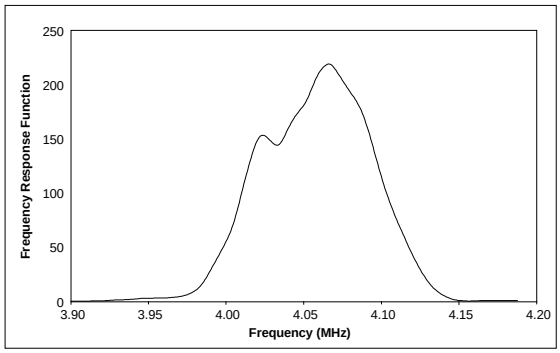

Bar B (10mm deflection): Frequency domain.

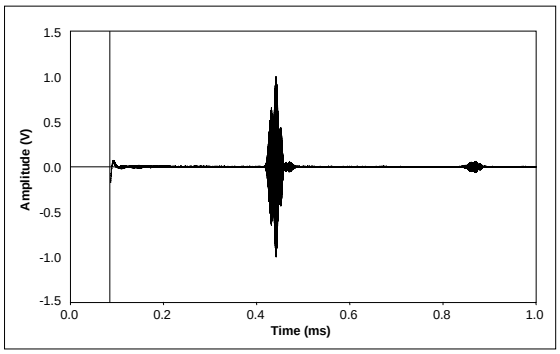

Bar C (20mm deflection): Time domain.

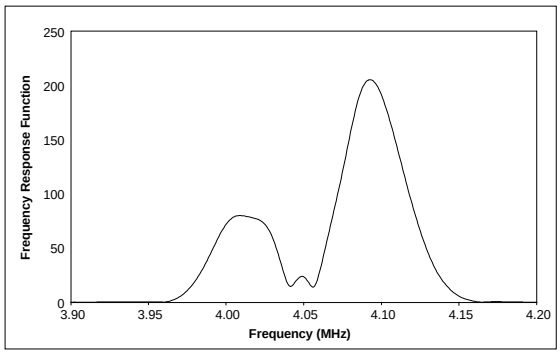

Bar C (20mm deflection): Frequency domain.

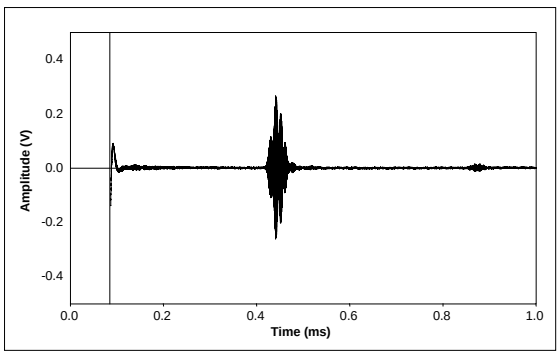

Bar D (30mm deflection): Time domain.

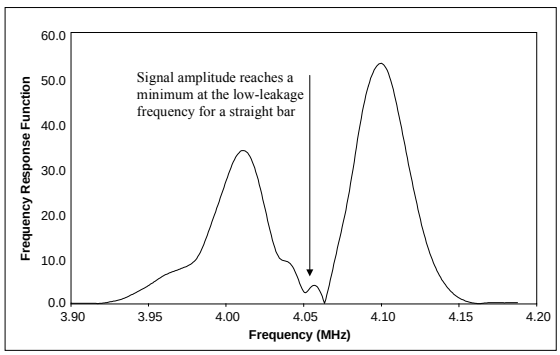

Bar D (30mm deflection): Frequency domain.

Figure 6.4: Example time traces and Fourier transform for the 4.05MHz end reflection results presented in figure 6.3.

6.2.2 Curved Free Bar

It has already been discussed elsewhere in this thesis that it is not easy to study high frequency modes in free structures, because of the large number of modes that can exist. It is not possible to excite a single mode, even if a very narrow bandwidth signal is used. However, it is possible to examine low-leakage modes if an embedded section is used to filter out the unwanted modes. Figure 6.5 shows the experimental set-up that was designed to examine low-leakage mode propagation through a free curved bar. The experiment uses a single bar specimen, 1360mm long, with two 400mm embedded sections, and one 375mm free section. The remainder of the bar protrudes from the ends of embedding blocks to allow a transducer to be attached.

Variable curvature can be applied to the free section by moving one of the embedding blocks, and clamping it so that constant curvature is maintained through the curved section. The embedded sections need to be long enough to filter out unwanted modes, and therefore a 7mm diameter bar was used to keep the experiment to a reasonable scale. Any unwanted, leaky modes that are generated by the transducer and at the straight/curved boundaries are filtered before reflection from the end of the bar, and before reaching the transducer. A low-leakage mode was excited at 7.05MHz, which is equivalent to the 2.26MHz test frequency in a rock bolt.

This experiment is designed to show that the attenuation of low-leakage modes in bars increases when a section of the bar is deformed, even if the deformed section is not embedded. Since there can be no significant leakage from the free section into the surrounding air, it is likely that most of this attenuation arises from mode conversion at straight/curved boundaries. This effect would occur if a low-leakage mode in the straight section was not well matched to a similar mode in the curved section, and is discussed further in section 6.7. However, this is not the only explanation, as the attenuation due to material damping may also be increased by curvature. The modelling work presented in chapter 3 showed that minima in attenuation exist in a free bar, modelled with material damping, at approximately the same frequencies as the minima in embedded bars modelled without material damping. This is related to the fact that the longitudinal partial wave is much more significant than the shear partial wave at the minima. If the shear wave is more significant in a curved bar, then it is possible that the material attenuation is also increased by curvature.

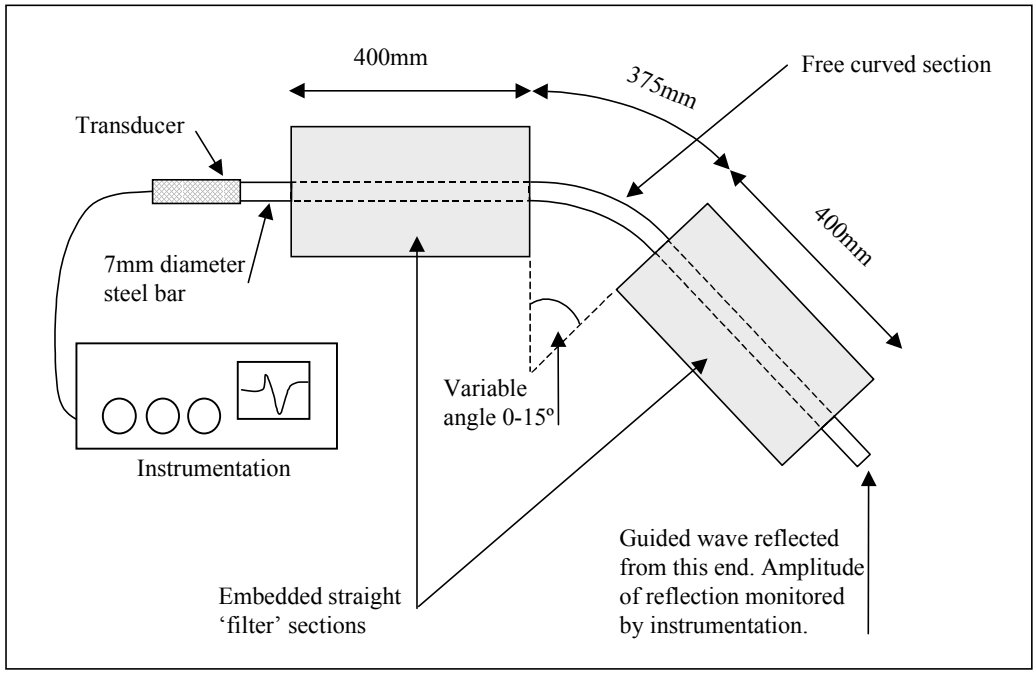

Figure 6.5: Experiment to determine the effect of curved sections on the attenuation of high frequency, low-leakage modes in a 7mm diameter free bar.

The measured end reflection amplitudes around the frequency of the attenuation minimum at 7.05MHz are shown in figure 6.6. The results are shown for a straight bar, and for arc angles of 5°, 10° and 15°,which roughly corresponds to curvature radii of 4.3m, 2.1m and 1.4m respectively. As for the embedded bar experiment, the amount of curvature is slight, with the ratio of curvature radius to bar diameter being approximately 600, 300 and 200 respectively. The results show that as the curvature increases, the attenuation increases at the frequency of the attenuation minimum for a straight bar. However, the effect is less severe that that observed for the embedded curved bar, suggesting that mode conversion, increased leakage and possibly also increased material attenuation all cause the effects observed in curved bars. The following sections look closely at the dispersion curves of curved structures around low-leakage points, to explain this effect further.

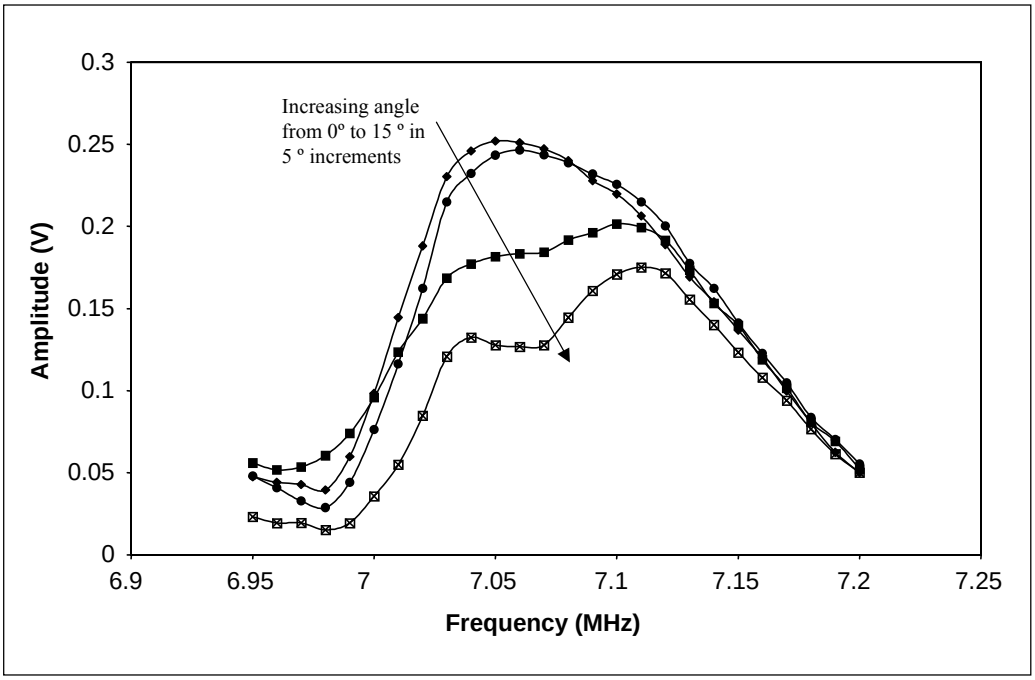

Figure 6.6: End reflection amplitude measured for different arc angles in the experiment shown in figure 6.5.

6.3 Guided Waves in Plates

6.3.1 Introduction

It has been shown that high frequency, low-leakage modes are very significantly affected by curvature in bars. The underlying principles behind this phenomenon would best be investigated by comparing the dispersion curves and mode shapes in embedded curved and straight bars. However, solution of the wave propagation equations for a curved bar using an analytical method is difficult, because the usual Helmholtz differential equation is non-separable when written in toroidal co-ordinates [96]. A considerable amount of research effort is necessary to solve this problem, as it is highly unlikely that a straightforward analytic solution can be found. Instead, this section examines Lamb waves in free and embedded plates, and shows that meaningful conclusions about the dispersion curves and mode shapes in curved embedded bars can made by the examination of free plates. The information obtained will be useful for the future validation of a full curved bar model, as well as giving insight into the use of low-leakage modes for the inspection of rock bolts and tendons.

6.3.2 Dispersion Curves for a Free Plate

The dispersion curves for a flat free plate are well known, and can be readily calculated by analytical and numerical methods. The existence of propagating waves on the surface of a semi-infinite elastic isotropic solid was first shown by Rayleigh in 1885 [97]. In 1917, Lamb [98]

solved the wave propagation equation for an elastic, isotropic plate in a vacuum to obtain the dispersion relationships. For this reason, guided waves in plates are often referred to as 'Lamb' waves. Many authors have since contributed to the field, and the Disperse software [7] can solve problems containing anisotropic materials, inelastic materials, and multi-layer and embedded systems.

Figure 6.7 shows the dispersion curves for a free steel plate, calculated using the Disperse software. Material damping has been included in the model, and all the material properties are given in table 3.1. The model is created in Cartesian co-ordinates, with plane strain conditions assumed in the 'y' direction. The 'x' direction denotes the plate thickness, with modes propagating in the 'z' direction. As for the cylindrical case, there are two basic families of modes, symmetric and asymmetric. The symmetric modes have a 'z' displacement profile that is symmetrical about the plate centreline, and are numbered sequentially from S0. All of the modes up to S5 are shown in figure 6.7. The asymmetric modes are numbered sequentially from A0, and have 'z' displacement that is anti-symmetric about the plate centreline. All of the modes up to A5 are shown in figure 6.7. There is a further family of modes (not shown), known as SH modes, which have displacement only in the 'y' direction, but these modes are not considered in this thesis.

The fundamental S0 and A0 modes are the only modes that exist at very low frequency, and at higher frequencies they both become Rayleigh surface waves, propagating at the Rayleigh velocity. As for the bar case, higher order modes begin at infinite phase velocity at a cut-off frequency and tend to the shear velocity of the steel at high frequency. The symmetric modes are analogous to the longitudinal modes in a bar, and like the longitudinal modes, can be seen to flatten in phase velocity as they approach the steel bulk velocity line. These flattened regions are again associated with maximum values of group and energy velocity.

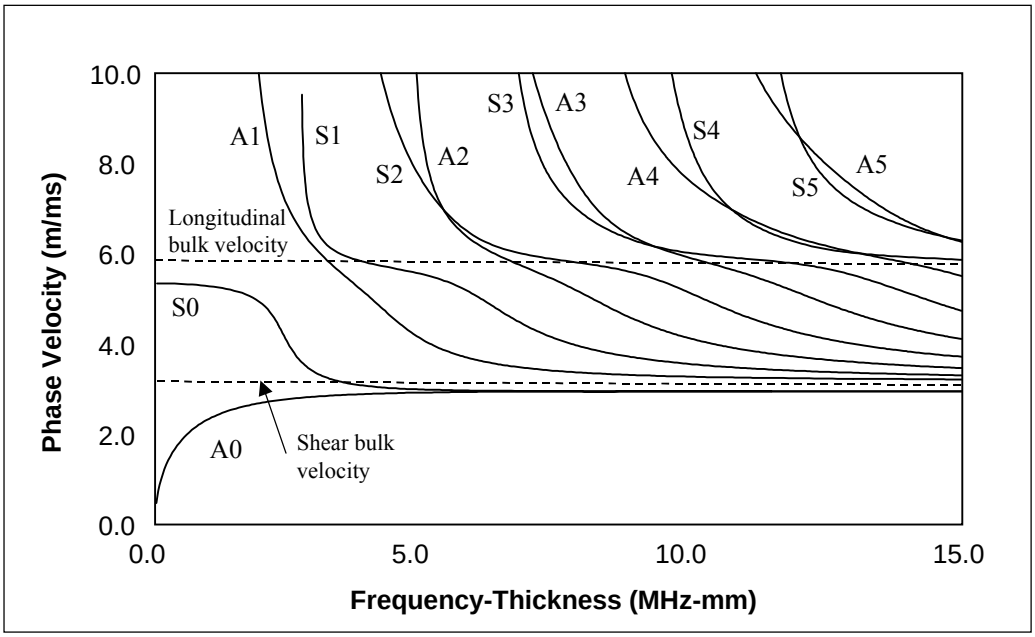

Figure 6.7: Phase velocity dispersion curves for a free steel plate.

6.3.3 Dispersion Curves for an Embedded Plate

It is possible to model embedded plate structures using Disperse by adding a semi-infinite layer of material to each side of the free plate. Figure 6.8 shows the phase velocity dispersion curves for a steel plate embedded in an infinite expanse of rock, with a Young's modulus of 20GPa. The other material properties are as given in table 3.1. Material damping is included in all the model layers, although only the damping properties of the steel have any significant effect. The dispersion curves are similar to those predicted for the free case, the main difference being that the S0 mode tends to zero phase velocity at zero frequency. As observed for the bar case, this trend is also followed for some of the higher order modes.

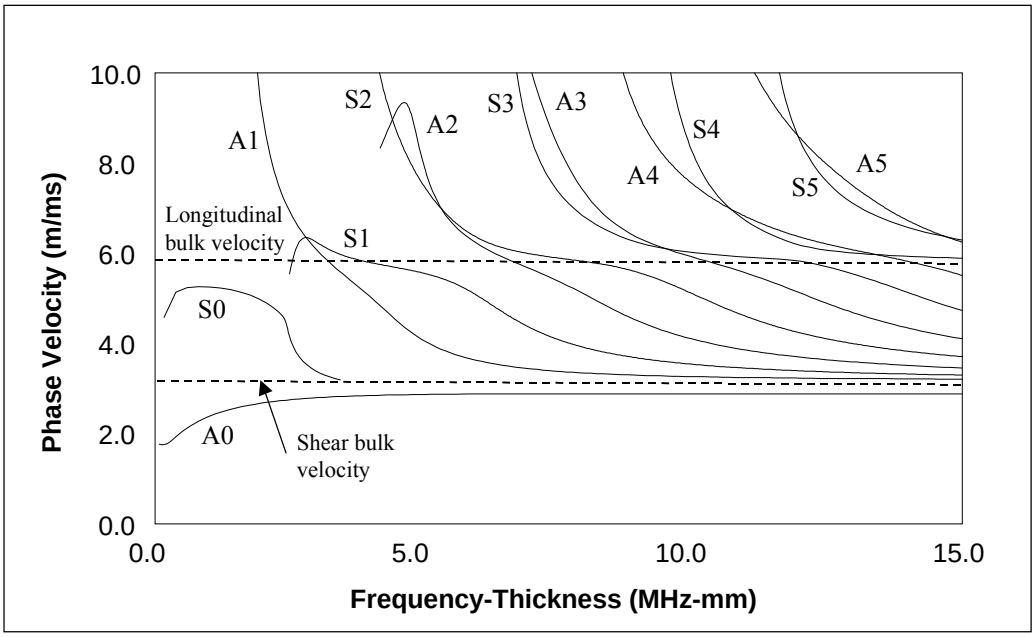

Figure 6.8: Phase velocity dispersion curves for a steel plate embedded in an infinite expanse of rock with a Young's Modulus of 20GPa.

6.3.4 High Frequency, Low-Leakage Modes in Embedded Plates

Chapter 3 showed that the high frequency, axially symmetric mode dispersion curves in steel bars tend to flatten as they approach a phase velocity equal to the longitudinal bulk velocity of the steel. In the embedded bar case, each flat region was shown to be associated with a minimum in attenuation. This flattening behaviour can also be seen for the plate cases in figures 6.7 and 6.8, and in the embedded plate case, the plateau regions are also associated with attenuation minima. As the frequency increases, a mode forms that links the plateau regions together to form a low-leakage mode, in the same way as has been observed for the bar case. Figure 6.9 shows the phase velocity and attenuation dispersion curves for selected symmetric modes in the embedded plate discussed in the previous section. In this case, it is the sixth symmetric mode (S5) that forms the low-leakage mode. For the same embedding material in a bar, the seventh axially symmetric mode, L(0,7), forms the low-leakage mode, which highlights the fact that the behaviour of the different geometry systems is very similar.

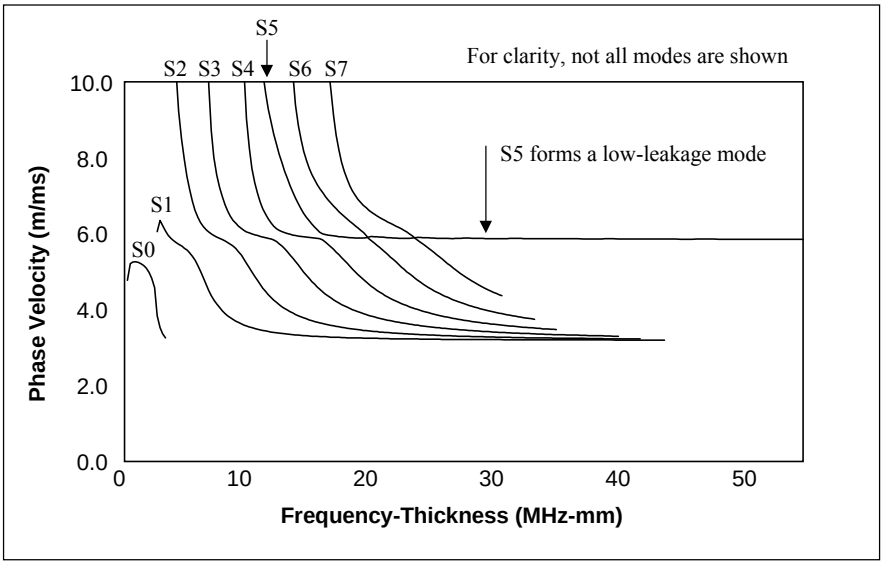

(a) Phase velocity.

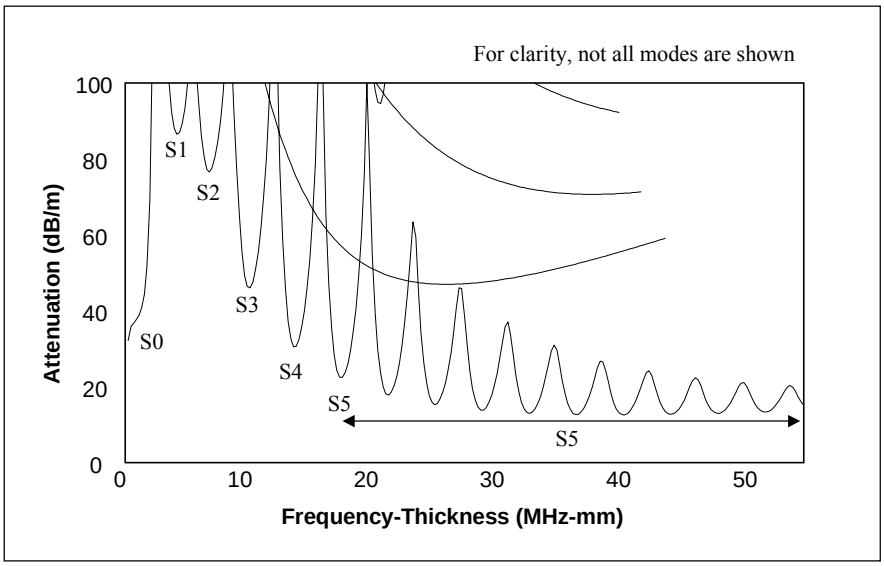

(b) Attenuation.

Figure 6.9: Dispersion curves for selected symmetric modes in a steel plate embedded in an infinite expanse of rock with a Young's Modulus of 20GPa.

The reason for the minimum in attenuation in these regions is related to the low-leakage mode shape characteristic outlined in chapter 3 for case of an embedded bar. Figure 6.10 shows, using the example of S4, that the attenuation minimum is associated with small in-plane displacement (u_z) at the plate edges, and the concentration of energy in the centre of the plate. Figure 6.10 shows that this mode shape characteristic occurs at the same frequency in both an embedded and free plate, which allows inferences about the embedded mode shapes to be made from studying the free mode shapes at the same frequency.

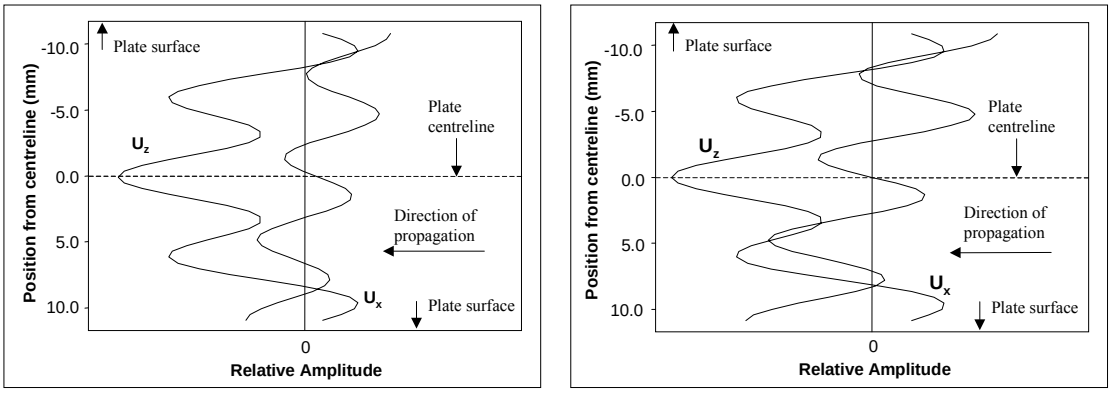

(a) Free plate. (b) Embedded plate.

Figure 6.10: S4 mode shape at 13.09MHz-mm in a free and embedded plate, showing the low-leakage mode shape characteristic.

6.3.5 Mode Crossing Points and Attenuation Minima

Close examination of the phase velocity dispersion shows that the low attenuation points occur at points where symmetric and non-symmetric modes have the same phase velocity, i.e. where the modes cross. Figure 6.11 shows the detail in the region of the attenuation minima for the embedded plate discussed in the previous section, and the minima occur at points where the 'A' and 'S' families of modes intersect, close to the steel longitudinal bulk velocity. Figure 6.12 shows the corresponding region for a steel bar embedded in the same material. In this geometry, the attenuation minima occur at points where the longitudinal and flexural modes intersect. Comparison of figures 6.11 and 6.12 shows that the attenuation minima occur at similar frequencies in a plate and bar when the plate thickness is equal to the bar diameter. For example, the first attenuation minimum of the sixth symmetric mode (S5) in an embedded plate occurs at a frequency-thickness of 17.3MHz-mm. In an embedded bar, the sixth axially symmetric mode (L(0,6)) has an attenuation minimum at a frequency-diameter of 17.9MHz-mm.

The existence of mode crossing points has been discussed in literature published by a number of authors, but has not been related to mode shapes or attenuation minima. Zhu and Mayer [99] found that there was no solution to the wave propagation equation at a mode crossing point at around 8.5MHz-mm in an aluminium plate, implying that no mode could exist. However, the frequency-thickness range over which no solution could be found was very small, being just 8.45435146 to 8.45435157. This means that although no mathematical solution can be found at the crossing points, the affected bandwidth is so small that a practical test would be unaffected, because the bandwidth of the excitation signal would be very much larger than the bandwidth of the affected crossover region.

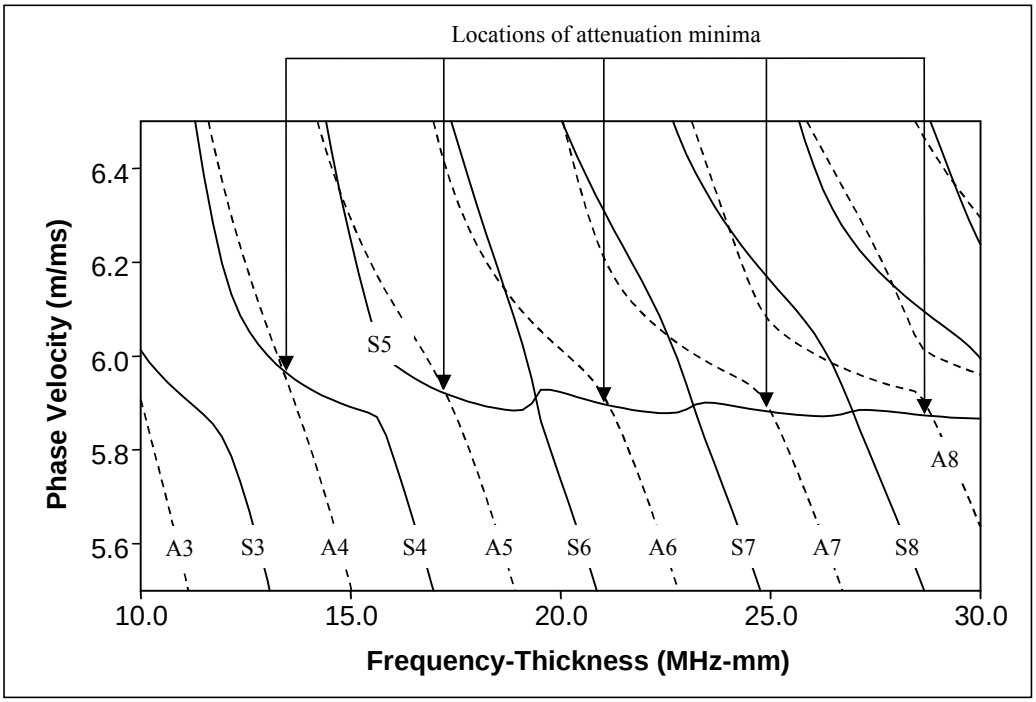

Figure 6.11: Phase velocity dispersion curves in the low-leakage region of a steel plate embedded in a rock with a Young's Modulus of 20GPa.

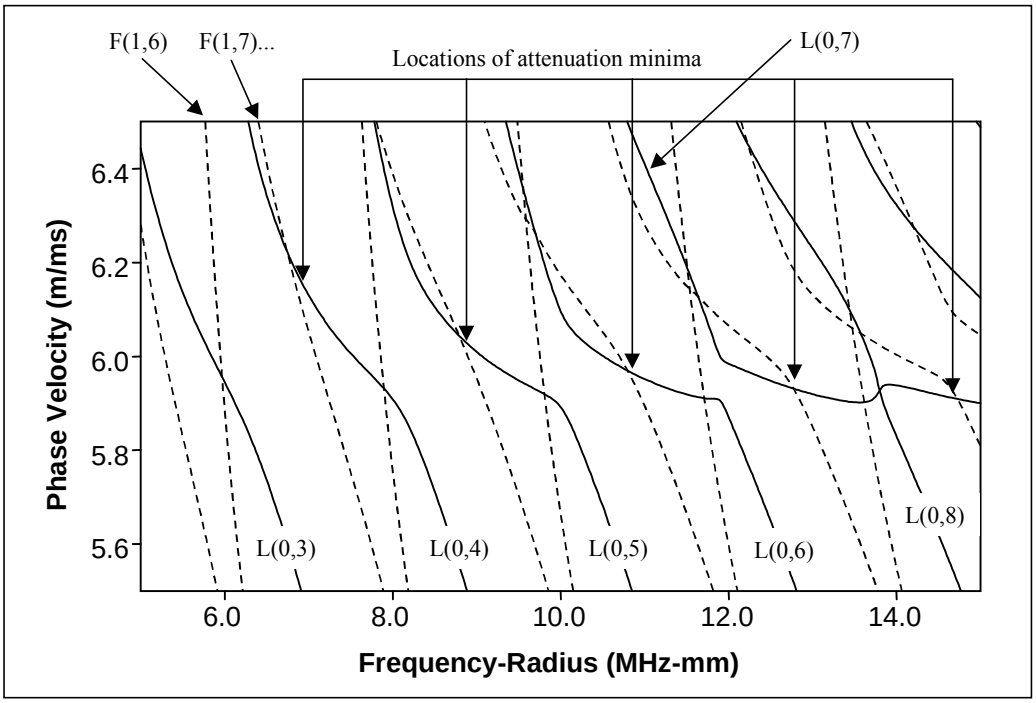

Figure 6.12: Phase velocity dispersion curves in the low-leakage region of a steel bar embedded in a rock with a Young's Modulus of 20GPa.

6.3.6 Use of Curved Plates to Study Wave Propagation in Curved Bars

It has been shown that guided waves in plates and bars show similar behaviour in embedded systems. In particular, both show attenuation minima that can be explained by a very small axial displacement at the interface with the embedding material. Furthermore, this mode shape characteristic also occurs on the same modes, and at the same frequencies, in free (vacuum bounded) bars and plates. The low attenuation points occur at frequencies on the phase velocity dispersion curves where the symmetric and asymmetric modes cross in plates, and where the flexural and longitudinal modes cross in bars. In both cases, where two modes cross more than once, the attenuation minima can be found at the crossing point that occurs at the highest frequency.

The similarity of wave behaviour in plates and bars makes it possible to make inferences about wave behaviour in bars from the study of wave behaviour in plates. In addition, the similarity of the mode shapes at attenuation minima in embedded cases and corresponding points in free cases makes it possible to make inferences about embedded systems from the study of free systems. Therefore, it is possible to predict the nature of the wave behaviour in curved, embedded bars from the study of free, curved plates. The following sections investigate the mode shapes in free flat and curved plates, and use the information to draw conclusions about the behaviour of low-leakage modes in embedded curved bars.

6.4 Calculation of Dispersion Curves and Mode Shapes in Free Curved Plates

The previous section has shown that it is possible to study guided waves at low-leakage points in curved, embedded bars by making comparisons with the case of a free plate. However, although the wave propagation equations for a curved plate have been solved analytically and published, the solution is not necessarily trivial, and requires a significant amount of computational effort. This section examines previous work in this area, and presents the equations governing wave propagation in such a form as to allow solution using standard mathematical software. The solution method is discussed, and the dispersion and mode shape predictions are validated against published literature and comparisons with the flat plate case.

6.4.1 Previous Work

Two authors have recently published the dispersion equations for a curved, isotropic, perfectly elastic solid plate in a vacuum. Wilcox [100] investigated the inspection of large structures such as oil tanks using guided waves. As many of these structures consist of slightly curved plates, Wilcox needed to demonstrate that there was little variation between the dispersion curves of flat plates and the dispersion curves of curved plates with a large radius of curvature. This was achieved through derivation of the equations necessary to plot phase and group velocity in a

curved plate. Wilcox showed that guided waves were affected little when the radius of curvature was at least 10 times greater than the plate thickness. Wilcox also noticed that some of the mode crossing points observed for flat plates did not occur in curved plates, and gave examples of modes repelling away from each other at these points. Although Wilcox compared flat and curved plate dispersion curves, no calculation or comparison of mode shapes was made. At about the same time, the equations for wave propagation in a curved plate were published by Qu [101]. This work included the calculation of some mode shapes, but no comparisons were made with the straight plate case.

Other authors have investigated the use of circumferential creeping waves for inspecting weep holes in airframe stiffeners [102], and also for crack detection on the surface of small annular components. These creeping waves are analogous to Rayleigh Waves in flat plates, and are not useful for the inspection of embedded systems. Some work has also been reported on the modelling of circumferential waves in layered cylinders [103]. The coupling of extensional and bending motion in long slender rods at frequencies as low as 1kHz has been investigated by Drumheller [104], who investigated the attenuation of extensional waves in drill strings. This work concluded that the slight curvature of the drill string caused an increase in the attenuation of the extensional wave due to interaction of the extensional and bending waves. However, at the time of writing, it has believed that no work has been published on guided waves in embedded curved plate structures or curved bars.

6.4.2 Curvature Ratio

It has already been discussed that the dispersion curves can be presented as a function of frequency-thickness for plates, and a function of frequency-radius for bars. This geometrical dependence was shown by Qu [101] to extend to the curvature of plates. This means that the modes in a 1mm thick curved plate with a 10mm radius of curvature have the same characteristics as the modes in a 2mm thick plate with a 20mm radius of curvature, except that they occur at half the frequency. This means that the dispersion curves for a curved plate can be plotted for any given ratio of thickness to curvature radius. The later sections of this chapter examine plates and bars with different curvature radii, and it is useful to define the curvature ratio R_c, based on the ratio of the thickness or diameter to the radius of curvature. Equation 6.1 defines this ratio for the plate and bar cases. In both cases, r_c represents the curvature radius from the axis to the plate or bar centreline.

$$R_c = \frac{t}{r_c} \text{ for the plate case, where 't' is the plate thickness.}$$

$$R_c = \frac{d}{r_c} \text{ for the bar case, where 'd' is the bar diameter.} \qquad (6.1)$$

6.4.3 Governing Equations

This section presents a brief explanation of the relevant equations that are needed to calculate the dispersion relationships and the power-normalised mode shapes in curved, free, perfectly elastic plates. It is not intended to be a rigorous derivation, as this has been well reported by the other authors discussed in the previous section. The equations are presented in a form that allows them to be easily solved using standard mathematical software, as the final equations are extremely cumbersome. Software such as Maple, Mathematica or Matlab can be used compute the algebraic equations for stress, velocity and displacement, which can then be used directly in further calculations.

The equations governing the propagation of waves in curved plates can be obtained by following the well known methods for the equivalent equations for a flat plate, although the algebra is considerably more complex. The differential 'wave equations' that must be satisfied by all propagating waves can be derived by applying Hooke's law to an infinitesimally small volume of perfectly elastic material. The solution method adopted by Wilcox [100] and by Qu [101] involves the use of the potential functions, φ and ψ, to separate the displacement field into two distinct fields, one associated with longitudinal waves, and one associated with transverse waves. These potential functions can then be shown to satisfy the wave equation. Figure 6.13 shows how the curved plate can be represented by a 2-dimensional annulus using the polar co-ordinate system. Plane strain conditions are assumed through the thickness of the annulus, which is therefore assumed infinite in extent. The following equations summarise the solution method used by the previous authors.

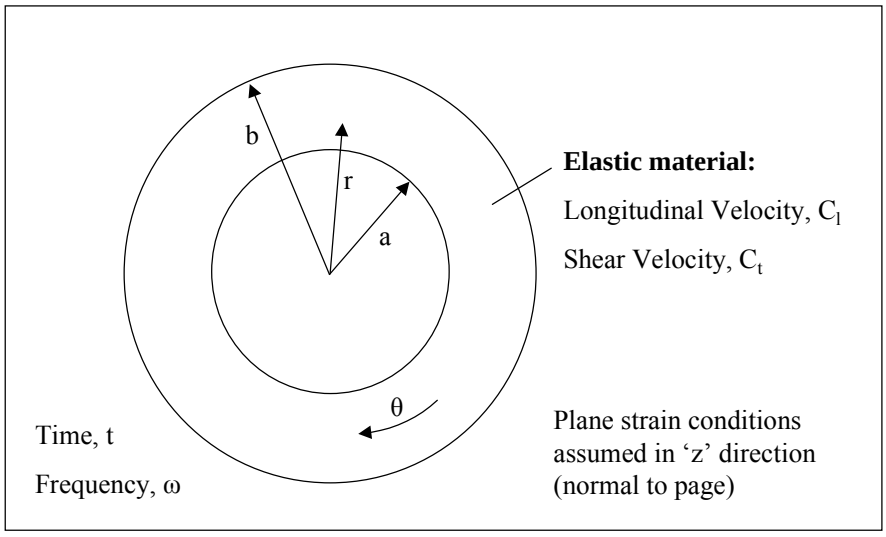

Figure 6.13: Two dimensional representation of a curved plate, used to solve the wave propagation equations.

The relationship between the displacement potentials φ and ψ, and the radial and hoop displacements u_r and u_θ, are given in equations 6.2. The third displacement u_z is zero by the definition of plane strain conditions.

$$u_r = \frac{\partial \phi}{\partial r} + \frac{1}{r}\frac{\partial \psi}{\partial \theta}$$
$$u_\theta = \frac{1}{r}\frac{\partial \phi}{\partial \theta} + \frac{\partial \psi}{\partial r} \tag{6.2}$$

The circular wavenumber for the geometry in figure 6.13 is defined by equation 6.3, where C_b is the linear phase velocity at the outer radius and ω is the circular frequency.

$$k = \frac{\omega}{C_b} \tag{6.3}$$

The potential functions that can be shown to satisfy the displacement functions are given by equations 6.4. 'BesselJ' and 'BesselY' refer to Bessel functions of the first and second kinds, respectively, and C_l and C_t are the longitudinal and transverse velocities of the material. A_1 to A_4 are constants determined by the boundary conditions, which are discussed later in this section. The time and spatial dependence of the waves is governed by the exponential terms.

$$\phi = e^{i\left(k\theta - \frac{\omega C_t t}{b}\right)}\left(A_1 BesselJ\left(k, \frac{\omega C_t r}{C_l b}\right) + A_2 BesselY\left(k, \frac{\omega C_t r}{C_l b}\right)\right)$$
$$\psi = e^{i\left(k\theta - \frac{\omega C_t t}{b}\right)}\left(A_3 BesselJ\left(k, \frac{\omega r}{b}\right) + A_4 BesselY\left(k, \frac{\omega r}{b}\right)\right) \tag{6.4}$$

Substitution of the potential functions (6.4) into the displacement equations (6.2) allows expressions for the displacements at a given radius to be derived in terms of the guided wave frequency and wavenumber, and various material and geometric constants. It is also necessary to obtain expressions for the stress field to enable the combinations of frequency and wavenumber that satisfy the equations to be found by the substitution of boundary conditions. The standard cylindrical form of the strain-displacement relationships defines the strain field, which is included for completeness in equations 6.5.

$$\varepsilon_{rr} = \frac{\partial u_r}{\partial r}$$
$$\varepsilon_{\theta\theta} = \frac{u_r}{r} + \frac{1}{r}\frac{\partial u_\theta}{\partial \theta}$$
$$\varepsilon_{r\theta} = \frac{\partial u_\theta}{\partial r} - \frac{u_\theta}{r} + \frac{1}{r}\frac{\partial u_r}{\partial \theta} \tag{6.5}$$

The strain relationships can be can then be substituted into the stress-strain relationships defined by Hooke's law to obtain expressions for the stress field in terms of the particle displacements, as shown by equations 6.6.

$$\sigma_{\theta\theta} = (\lambda + 2\mu)\left(\frac{u_r}{r} + \frac{1}{r}\frac{\partial u_\theta}{\partial \theta}\right) + \lambda \frac{\partial u_r}{\partial r}$$
$$\sigma_{rr} = (\lambda + 2\mu)\frac{\partial u_r}{\partial r} + \lambda\left(\frac{u_r}{r} + \frac{1}{r}\frac{\partial u_\theta}{\partial \theta}\right)$$
$$\sigma_{\theta r} = \mu\left(\frac{\partial u_\theta}{\partial r} - \frac{u_\theta}{r} + \frac{1}{r}\frac{\partial u_r}{\partial \theta}\right) \qquad (6.6)$$

The velocity field is also required to calculate the power-normalised mode shapes, and can be calculated from the derivative of the displacement field, as shown by equations 6.7.

$$v_\theta = \frac{\partial u_\theta}{\partial t}$$
$$v_r = \frac{\partial v_r}{\partial \theta} \qquad (6.7)$$

6.4.4 Solution Method

The full algebraic expressions for the displacement, stress and velocity fields in terms of the constants A_1 to A_4 can obtained by working through the above equations. However, the resulting equations are extremely complex, and are not reproduced in full here. The simplest and most reliable way to solve the equations is to derive and calculate the expressions within the same mathematical spreadsheet, as this avoids excessive handling of the very cumbersome equations. To solve the wave propagation equations, the values of the constants A_1 to A_4 must be known. These can be found by substituting four appropriate boundary conditions into the wave equations. It is required that both the radial stress (σ_{rr}) and shear stress ($\sigma_{r\theta}$) must be zero at the surfaces of the annulus, so that:

$$\sigma_{r\theta(r=a,b)} = 0 \quad , \qquad \sigma_{rr(r=a,b)} = 0 \qquad (6.8)$$

Substituting these boundary conditions (equations 6.8) into the equations for the stress field (equations 6.6) leads to a system of four homogeneous equations, which can be written as a 4 by 4 matrix problem. For non-trivial solution to the equations, the determinant of the matrix must be zero, which yields an infinite number of ω,k pairs that satisfy the wave equations. These are the points that define the dispersion curves. Once the ω,k pairs are known, the subsequent calculation of the stress, displacement and velocity fields is relatively straightforward. Only the relative amplitudes of the constants A_1 to A_4 can be found, and for the work presented in this thesis, the amplitude of A_1 has been assumed to be unity. Physically, this means that only the relative amplitudes of the stress and displacements fields are calculated for each case. To compare different mode shapes with each other, it is necessary to normalise the mode shapes: in the case of power normalisation, the stress, displacement, and velocity fields are normalised so that 1W of power is carried by the propagating wave.

For all the work presented in this thesis, the equations were solved and the dispersion relationships calculated using the mathematical software 'Maple 4'. It should be emphasised that this is not an efficient method of solution, and the worksheet was slow in calculating the many complex Bessel function values required. However, it was not felt worthwhile developing dedicated software, as it is hoped to fully include the calculations within Disperse, which will then be able to handle embedded and multi-layer systems using the global matrix method. The results presented in this thesis will provide a validation case for Disperse, once the solution is fully implemented. It should be noted that the curved plate dispersion curves presented by Wilcox were calculated using an early version of Disperse, but no mode shape calculations or multi-layer capability was included in the implementation.

The worksheet written for the research presented in this thesis was able to trace a dispersion curve from a given starting point. The power-normalised mode shape was then calculated at each point. The spreadsheet then used data from Disperse files to obtain the roots of the straight plate equations at the same frequency, and calculate those mode shapes. A comparison of the mode shapes was then made using a simple dot product method, outlined in section 6.6.1.

6.4.5 Validation of Results

The ω, k dispersion relationships and the calculated mode shapes that were obtained were compared with the results published by Qu [101] and were found to agree exactly. The results were also validated against the case of a plate with a very large radius of curvature, which approximates the case of a flat plate. Table 6.1 shows the calculated frequency/wavenumber combination for points on the S3 and A4 modes, together with the same information for a flat plate, calculated using Disperse. The corresponding power-normalised mode shapes are shown for the stress and the displacement fields in figure 6.13. The mode shapes match so closely that is impossible to distinguish between them, indicating that the calculated power normalised mode shapes are correct.

Mode	Frequency-Thickness (MHz-mm)	Wavenumber (1/mm)	
		Straight Plate	Curved Plate
S3	7.50	1.012175	1.012185
A4	9.00	0.987939	0.987957

Table 6.1: Calculated wavenumber for points on the S3 and A4 modes in a free straight plate, and a free curved plate with a curvature ratio of 100.

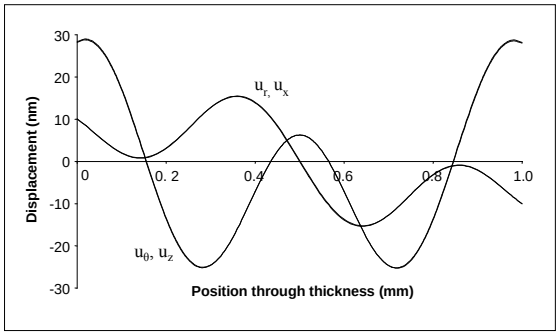

(a) S3 Displacement at 7.50MHz-mm.

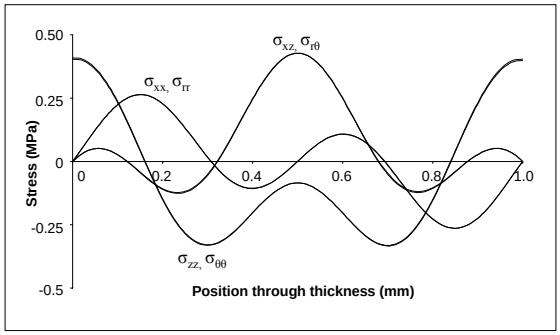

(b) S3 Stress Distribution at 7.50MHz-mm.

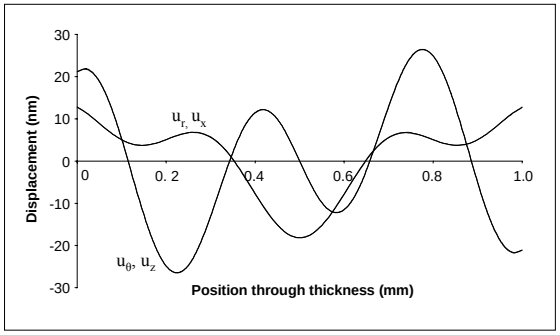

(c) A4 Displacement at 9.00MHz-mm.

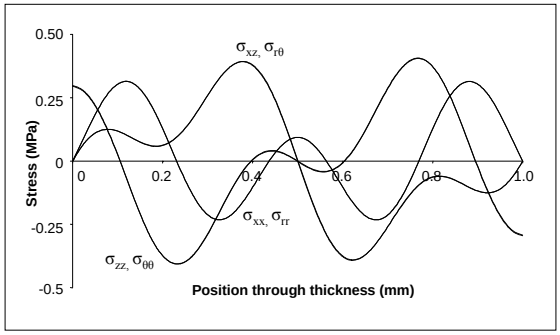

(d) A4 Stress Distribution at 9.00MHz-mm.

Figure 6.14: Comparison of the displacement and stress mode shapes at two frequencies for a straight plate and a curved plate with a curvature ratio of 100. The mode shapes for the straight and curved cases are superposed on each plot.

6.5 Curved Plate Mode Numbering

Although the curved plate mode shapes given in the previous section show similar characteristics to straight plate symmetric/asymmetric modes at the points examined, the following sections show that this is not always the case, and it is necessary to introduce a different numbering system. The work presented in this thesis follows a simple convention for curved plate modes consisting of a number followed by a letter. The number represents the equivalent straight plate mode reference number, for example, the modes that are equivalent to S4 and A4 are both numbered 4. The following reference letter can be A or B, with the letter A representing the mode which has the lowest cut-off frequency. The curved and flat plate dispersion curves have been found to overlay very closely at the cut-off frequencies. Since A4 has a lower cut off frequency than S4, the curved plate mode that is equivalent to A4 at high phase velocity is numbered 4A, and the curved plate mode that is equivalent to S4 at high phase velocity is numbered 4B. The fundamental modes do not have a cut-off frequency, and the mode equivalent to A0 is simply numbered 0A, and the mode equivalent to S0 is simply numbered OB.

6.6 Comparison of Phase Velocity Dispersion Curves in Free Straight and Curved Plates

6.6.1 General Dispersion Relationships

Wilcox [100] concluded that the differences in the dispersion curves between straight and curved plates were slight if the radius of curvature was at least 10 times greater than the plate thickness (i.e. the curvature ratio is greater than 10). However, he also noticed that certain points were affected more than others, including the points where pairs of symmetric and asymmetric modes cross. In the curved case, some of the modes were found to repel away from each other at these crossing points, after which each mode following the locus of the other. However, these points were not examined in detail. The work published by Qu [101] showed some modes crossing and not others, although he did not conduct a detailed examination of the crossover points. Since the low-leakage points on high frequency modes occur at these crossover points, a detailed study of these points is made in the next section.

Figure 6.15 shows the phase velocity dispersion curves for the first 6 symmetric and asymmetric modes in a free straight plate and a free curved plate with a curvature ratio of 5. Even at this sharp radius of curvature, the curves can be seen to be almost identical, except at the crossover regions. It is interesting to note that the A1/S1 pair are affected in the region of phase velocity where the crossover points occur, even though the straight plate modes do not actually cross.

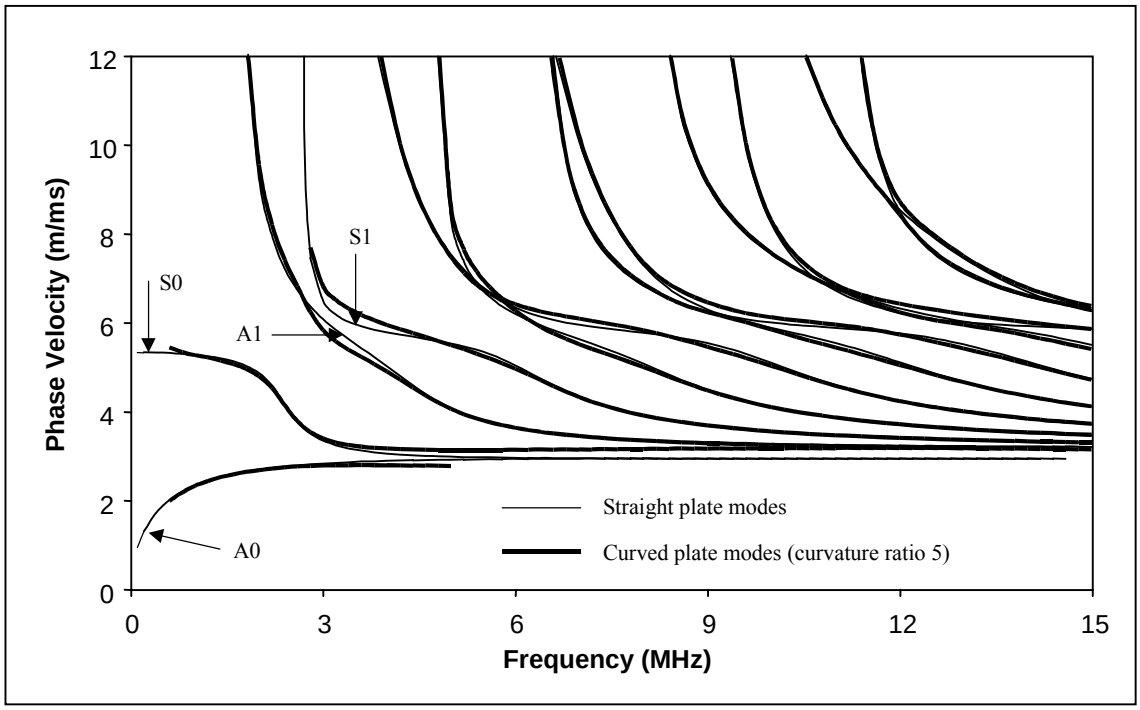

Figure 6.15: Comparison of the phase velocity dispersion curves for a straight plate and a curved plate with a curvature ratio of 5.

6.6.2 Mode Crossing Points

The previous section showed that the general form of the dispersion curves for straight and free plates is similar, but that there are differences at the crossover points that have not been investigated fully by other authors. Figure 6.16 shows the detail of the phase velocity dispersion curves in the region of the last A4/S4 crossing point for plates with different curvature ratios. The modes always repel away from the crossing point, even when the curvature ratio is as much as 50. The long calculation time prevents calculation of the curves for even greater radii, but it is likely that the modes will always repel in a curved plate. This is consistent with the limiting case of a straight plate, where the findings of other authors show that there is no straight plate solution actually at the crossing point.

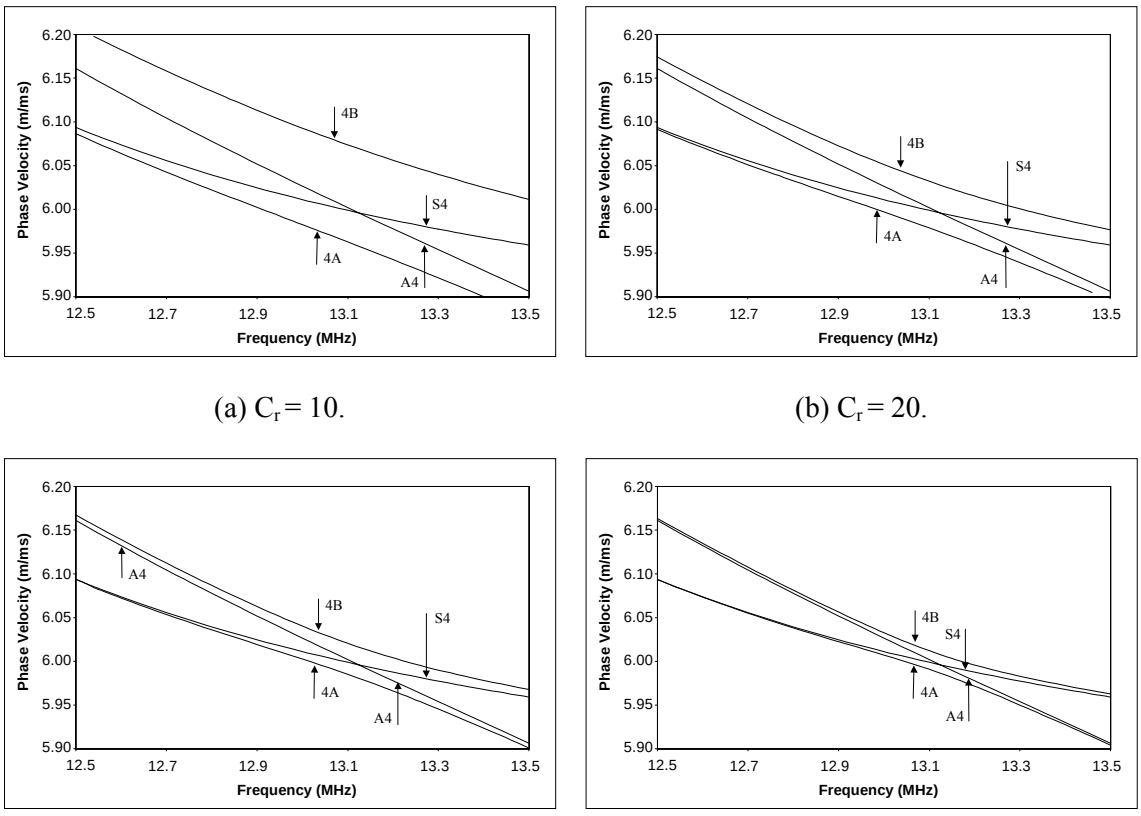

(a) $C_r = 10$. (b) $C_r = 20$.

(c) $C_r = 30$. (d) $C_r = 50$.

Figure 6.16: Comparison of the phase velocity dispersion curves, in the region of an S4/A4 crossover point, for a straight plate and curved plates with different curvature ratios.

The behaviour of the modes around the crossing points raises the possibility that the modes equivalent to symmetric and asymmetric modes never cross in a curved plate, even at high mode orders. Figure 6.17 examines the final crossing point of the S10/A10 modes, which is the point equivalent to a low-leakage point on the L(0,11) mode in a bar. The equivalent curved plate modes are also shown not to cross at this point. This shows that the behaviour of the modes at

crossover points is similar for high and lower order modes at low-leakage points. The following sections investigate the effect of the modes repelling on the mode shapes, and the consequences that this has for guided wave propagation through embedded, curved structures.

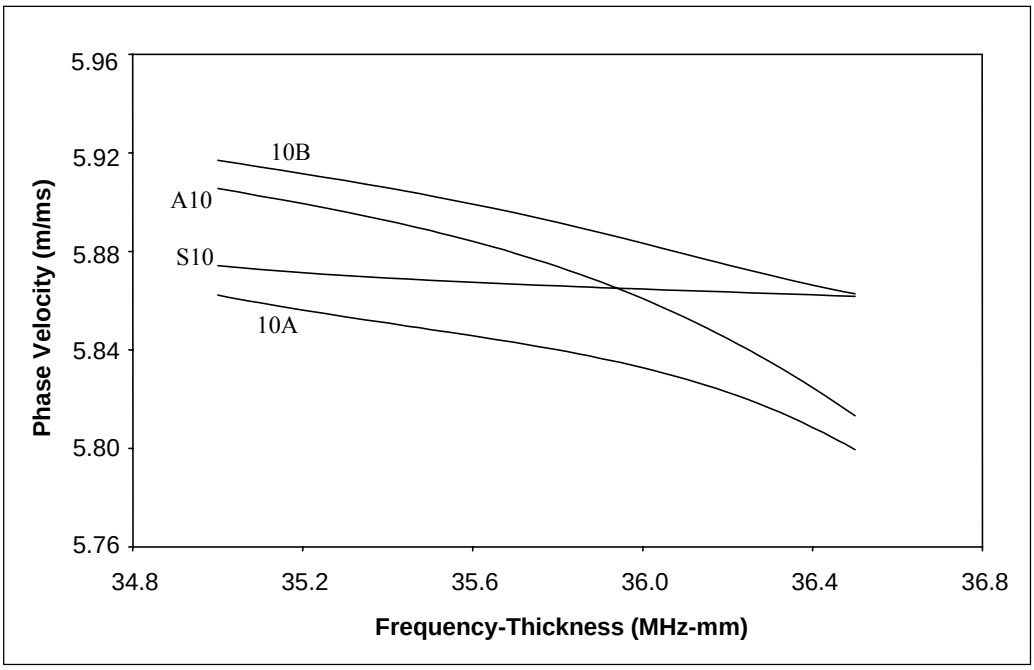

Figure 6.17: Phase velocity dispersion at a crossing point of the S10/A10 modes in a straight plate, showing the behaviour of the corresponding 10A and 10B modes in a curved plate with a curvature ratio of 30. The A10/S10 crossing point is equivalent to a low-leakage point on the L(0,11) mode in an embedded bar.

6.7 Attenuation due to Mode Conversion at Straight/Curved Plate Boundaries

6.7.1 Introduction

The variable angle bar experiment described in section 6.2 showed that the low-leakage modes were attenuated when the free section of the bar was curved. It is not possible for the modes to be attenuated through leakage in this section of bar, and therefore the observed attenuation must come from some other effect. The most likely explanation is that the attenuation is caused by poor mode coupling between the straight and curved sections of bar. If a narrow bandwidth signal is used, the first embedded section ensures that only a single low-leakage mode arrives at the free curved section. If no similar mode can exist in the free curved section, then many modes may be generated by mode conversion at the straight/curved boundary. This is also likely to lead to modes being reflected from the boundary, but if the generated modes are not low-leakage, then they will be rapidly attenuated in the embedded section, and will not be detectable. The many modes that propagate in the free section will then mode convert again as they reach the following straight section, and will not all be converted back into the low-leakage mode. This effect will occur at every change of curvature, resulting in attenuation of the wave, and

because the mode shapes in free and embedded bars are similar at the low-leakage points, it will affect both free and embedded systems.

Section 6.3.6 shows that it is possible to evaluate the likely effect of mode conversion at boundaries between straight and curved sections of bar by examining the mode shapes in straight and curved plates. A rigorous analysis may be possible using the S-Parameter technique [105], but this method would require information on all the modes that exist in the frequency bandwidth under investigation, including the non-propagating modes. The calculation would therefore be extremely complex for the higher order modes, and a simpler analysis based on a dot product comparison between the displacement vectors of the straight and curved plate mode shapes has been used here. This method is described further in section 6.7.2.

6.7.2 Displacement Dot Product Method of Mode Shape Comparison

It is reasonably straightforward to compare the mode shapes in straight and curved plates visually, but it is also desirable to evaluate them quantitatively. A rigorous evaluation would need to include all the displacement and stress vectors, but a good deal of information can be obtained by examining just the principal displacements. For a comparison between a straight and a curved plate, this means comparing the in-plane 'z' and 'θ' displacement vectors with each other, and also the out of plane 'x' and 'r' displacement vectors with each other. The mode shapes are therefore identical if the 'z' and 'θ' displacement vectors, and the 'x' and 'r' displacement vectors are the same. If the vectors are similar, it is reasonable to assume that good mode transmission will be obtained between straight and curved sections. However, if the vectors are very different, then energy will be converted and reflected in other modes and the transmission of the low-leakage mode will be poor.

The similarity of two vectors can be evaluated mathematically by taking the dot product of the vectors, after first normalising them such that the dot product of each vector with itself is unity. This principle can be applied to the in plane and out of plane displacement vectors as shown by equation 6.7 to give a measure S of the similarity of the two vectors.

$$S_{z,\theta} = \overline{u}_z \cdot \overline{u}_\theta , \qquad S_{x,r} = \overline{u}_x \cdot \overline{u}_r \tag{6.7}$$

The overall quality of the match between the two mode shapes can be determined by simply averaging the in plane and out of plane results, as shown by equation 6.8. This method gives equal importance to the in plane and out of plane vectors, and therefore information regarding the relative magnitude of these displacements is lost. However, in most of the cases examined, $S_{x,r}$ and $S_{z,\theta}$ are in any case similar for each comparison.

$$S = \frac{1}{2}\left(\left(\overline{u}_z \cdot \overline{u}_\theta\right) + \left(\overline{u}_x \cdot \overline{u}_r\right)\right) \tag{6.8}$$

The similarity factor 'S' reaches a maximum value of 1 if the mode shapes are identical, and the minimum value is zero. A similarity factor of zero indicates that the mode shapes are completely different, for example, when symmetric and asymmetric modes are compared. Good mode shape matches will give a result closer to unity than poor matches. Negative results can be obtained if the displacement vectors have different phases. For example, a factor of -1 indicates a perfect mode match, but that the compared modes are in opposite phase. It is therefore important to ensure that the phase and propagation direction of each mode is same before the comparison is made.

6.7.3 Mode Shape Comparisons at Mode Crossing Points

The mode shapes of straight and curved plates have been compared visually, and using the dot product method outlined in the previous section. The behaviour of the modes at crossing points is of particular interest, and the S4/A4 pair of modes have been chosen for this study as they have two crossover points, the second of which is associated with the low-leakage mode shape characteristic.

Visual Comparison at Crossover Point of S4/A4

Figure 6.16d shows the detail of the second S4/A4 crossover point (where S4 exhibits the low-leakage mode shape) and the corresponding A and B modes in a curved plate with a curvature ratio of 50. The crossover occurs at 13.12MHz-mm for the A4/S4 modes, but the curved plate modes 4A and 4B repel away from this point and do not cross. Figure 6.18 shows the displacement mode shapes for the 4A mode at five frequencies around the crossover point, and also the A4 and S4 mode shapes. It can be seen that before the crossover point, the 4A mode in a curved plate is very similar to the S4 mode in a straight plate. However, the shape gradually changes around the crossover region, and after the crossover point the 4A mode is very similar to the A4 mode. Figure 6.19 shows the same information for the 4B mode. Before the crossover point, this mode is very similar to A4, but changes in the crossover region to be more like S4. Hence, actually at the crossover frequency, the curved plate modes 4A and 4B are not well matched to either of the corresponding straight plate modes.

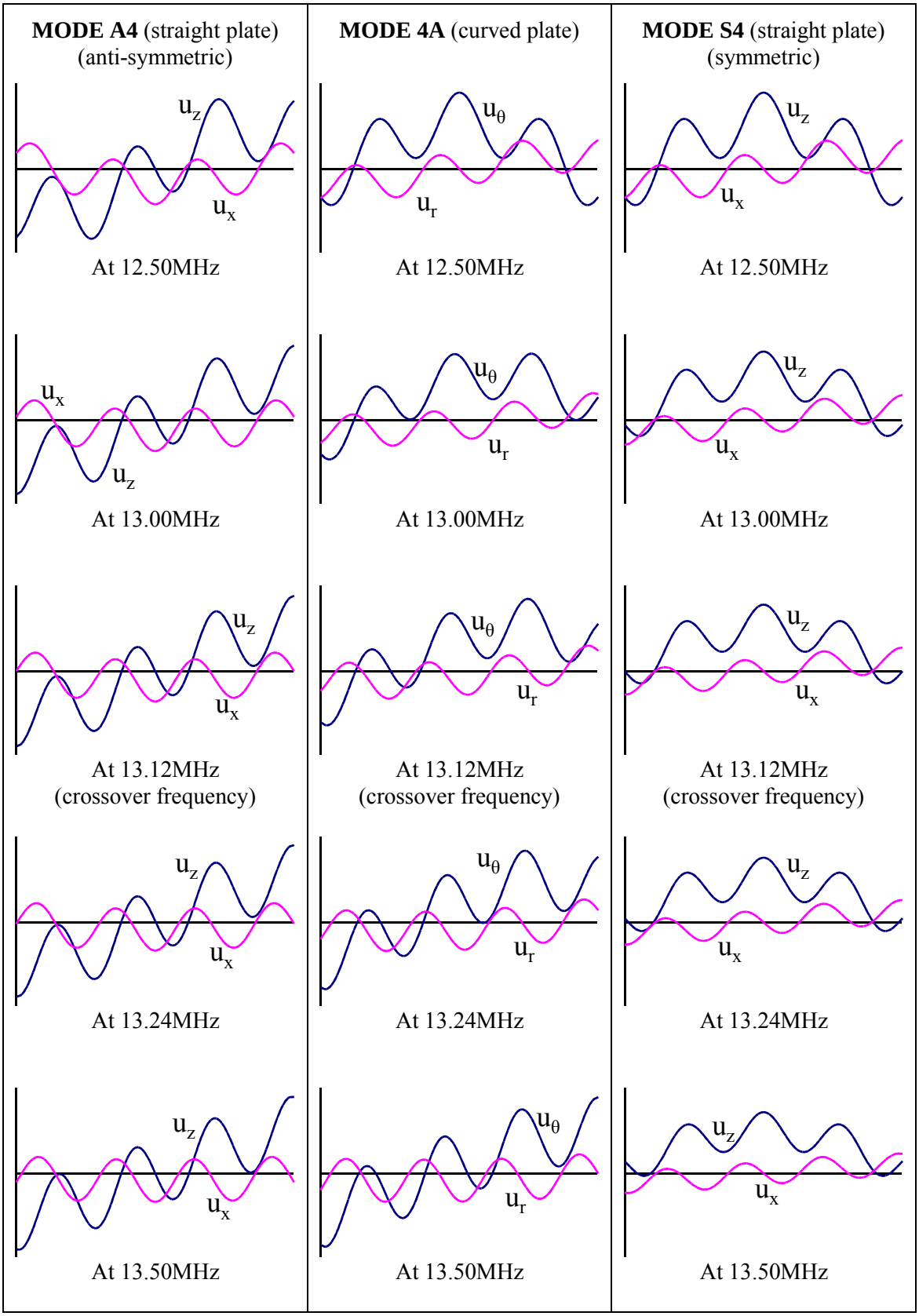

Figure 6.18: Displacement mode shapes of the 4A mode in a curved plate with a curvature ratio of 50, compared to the displacement mode shapes of A4 and S4 in a straight plate, showing the displacement amplitude (y-axis) through the thickness of the plate (x-axis).

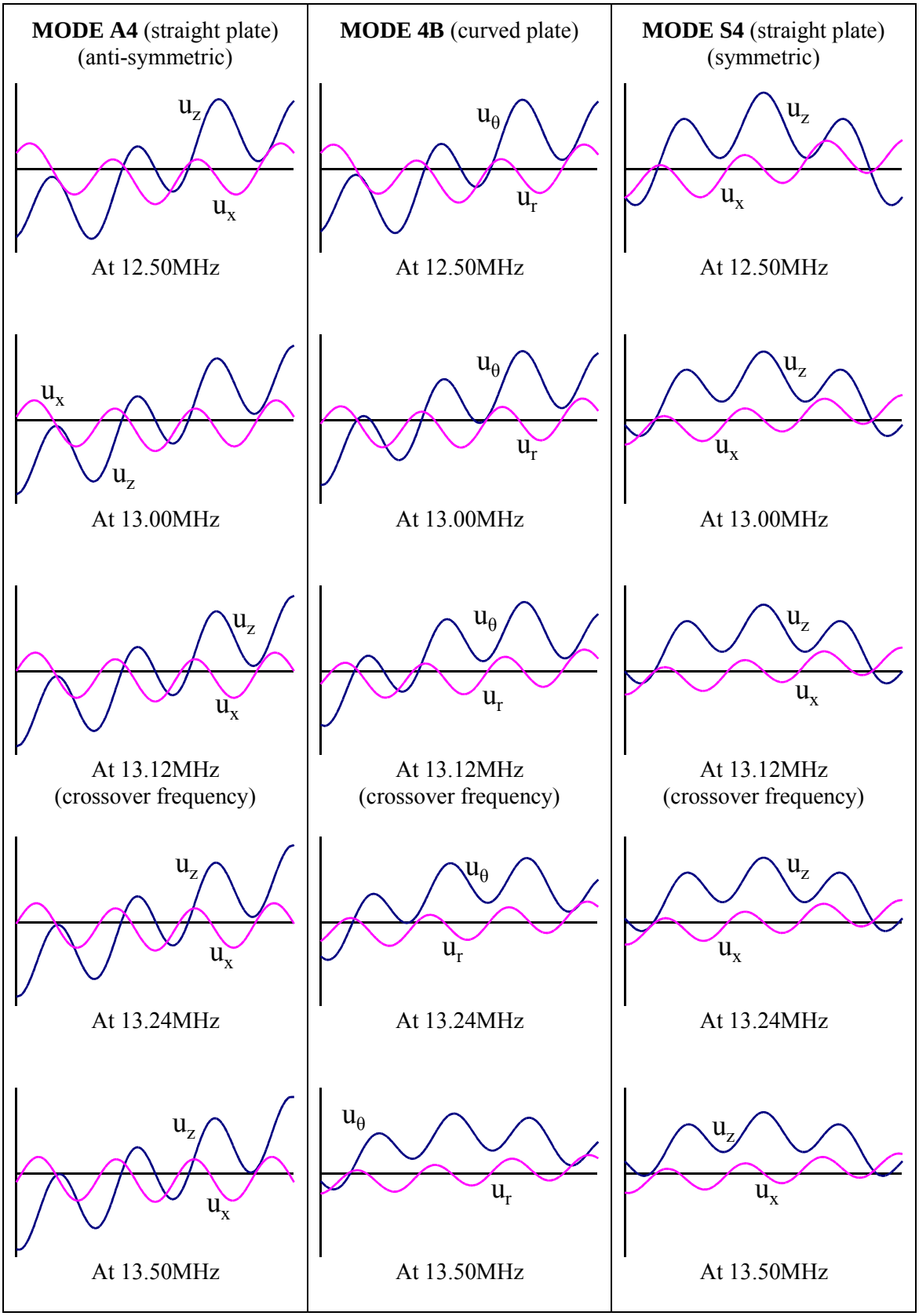

Figure 6.19: Displacement mode shapes of the 4B mode in a curved plate with a curvature ratio of 50, compared to the displacement mode shapes of A4 and S4 in a straight plate, showing the displacement amplitude (y-axis) through the thickness of the plate (x-axis).

Dot Product Comparison at Crossover Point of S4/A4

Although a lot of physical understanding can be gained by visually examining the mode shapes around the attenuation minima, a bigger range of data can be studied by comparing the mode shapes using the dot product method outlined in section 6.7.2. Figure 6.20 shows the dispersion curves for the S4/A4 case examined above over a wider frequency range, encompassing both crossover points. As discussed in section 6.7.2, the curved plate modes overlay the straight plate modes at all frequencies, except close to crossover regions. At the cut-off frequency, the A4 mode overlays the 4A mode, and the S4 mode overlays the 4B mode. These modes 'swap' at the first crossover point, and thereafter S4 and 4A overlay, and A4 and 4B overlay. At the second crossover point, the modes swap back to overlaying the same modes as at the cut-off frequencies.

The dot product comparison shown in figure 6.21 shows that the mode shapes of the curved plates are very similar to the straight plate modes when the phase velocity dispersion curves overlay, with similarity factors close to unity. At 9.5MHz, S4 and 4B are virtually identical, and so are A4 and 4A. The match changes at each crossover point, so that at 11.5MHz, modes S4 and 4A, and A4 and 4B are virtually identical. This means that good mode conversion between straight and curved sections can be expected in regions where the dispersion curves overlay. This confirms the results of Wilcox, who concluded that very little difference in the propagation characteristics could be expected for straight and curved plates, providing that the radius of curvature was at least 10 times greater than the plate thickness.

Although the mode shape match is good over the majority of the dispersion curves, the match is poor at the crossover points. Figure 6.21 shows that the similarity factor falls to about 0.7 at the crossover points, even for a curvature ratio of 50. Since some of these crossover points are associated with the low-leakage mode shape characteristic, then the frequencies used for testing tendons and rock bolts will be affected significantly. The next section examines the mode shapes at a crossover region on the higher order S10 mode.

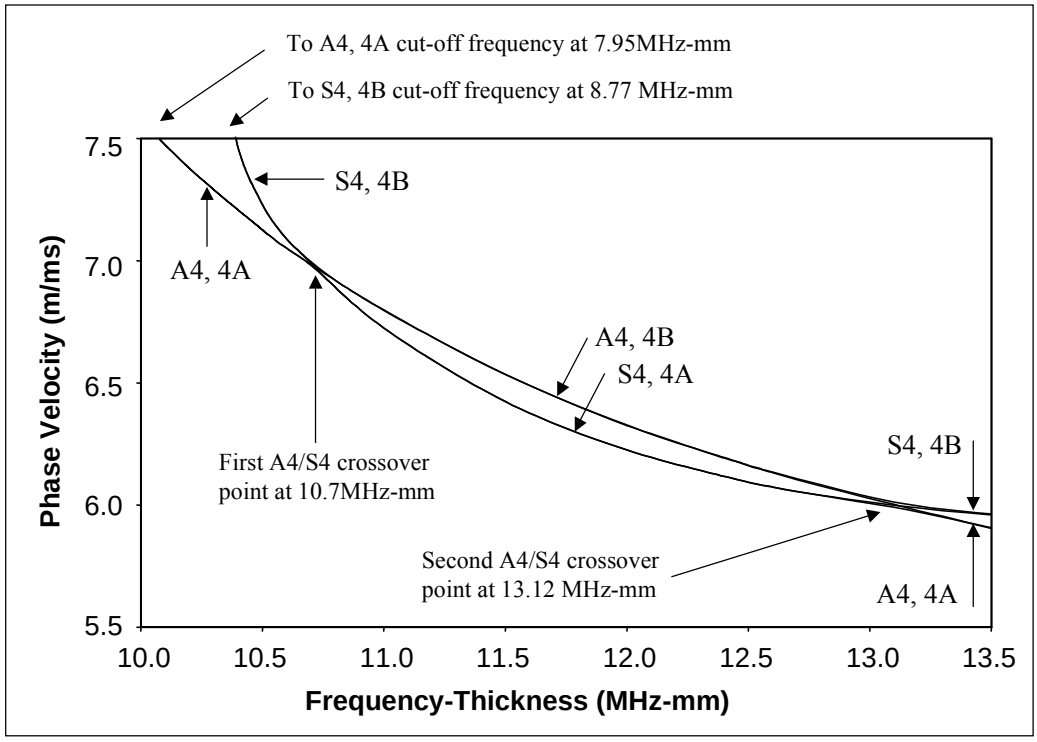

Figure 6.20: Dispersion curves for the S4 and A4 modes in a straight plate, and the 4A and 4B modes in a curved plate with a curvature ratio of 50, showing both mode crossing points.

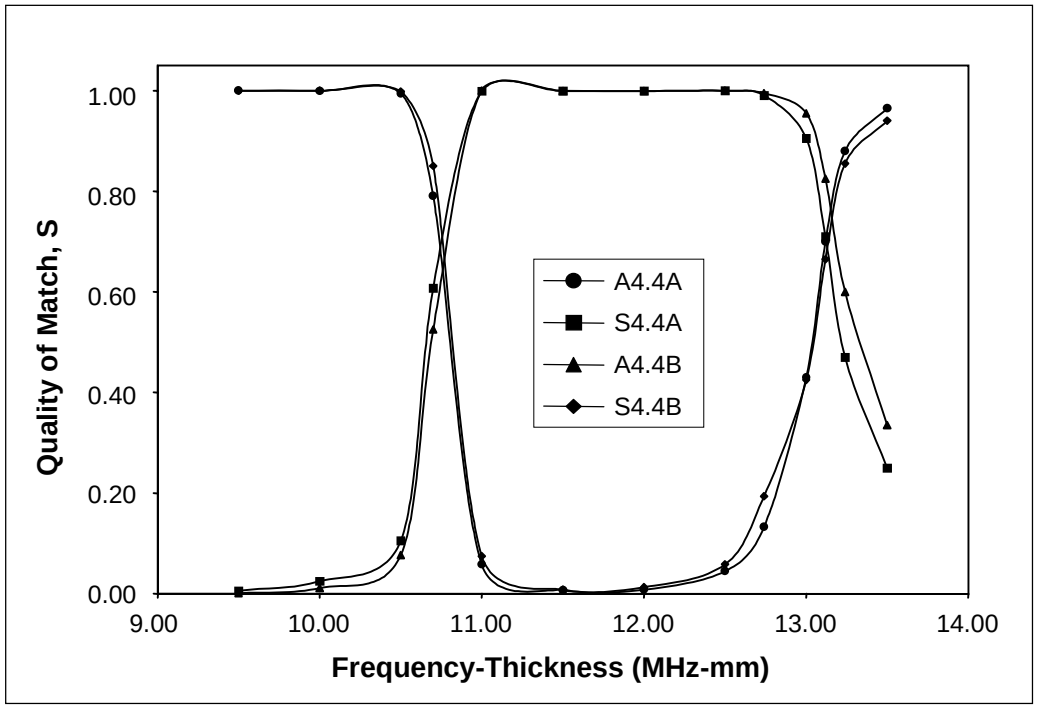

Figure 6.21: Dot product mode shape comparison for the modes and frequency range shown in figure 6.20.

Dot Product Comparison at Crossover Point of S10/A10

Figure 6.22 shows the results of a dot product comparison of the S10 mode with the corresponding 10A and 10B modes in a curved plate with a curvature ratio of 30. The frequency range includes the A10/S10 crossover point where S10 exhibits the low-leakage mode characteristic. The phase velocity dispersion curves in this region are also shown in figure 6.22. The shapes of the curved plate modes changes from symmetric to anti-symmetric around the crossover region, with the result that both the 10A and 10B modes are equally poorly matched to S10 at the frequency where an attenuation minimum would exist in the embedded case. Only the in-plane displacement has been compared in this case, as the displacement of S10 in the 'x' direction is small compared to the displacement in the 'z' direction, and this was found to distort the results.

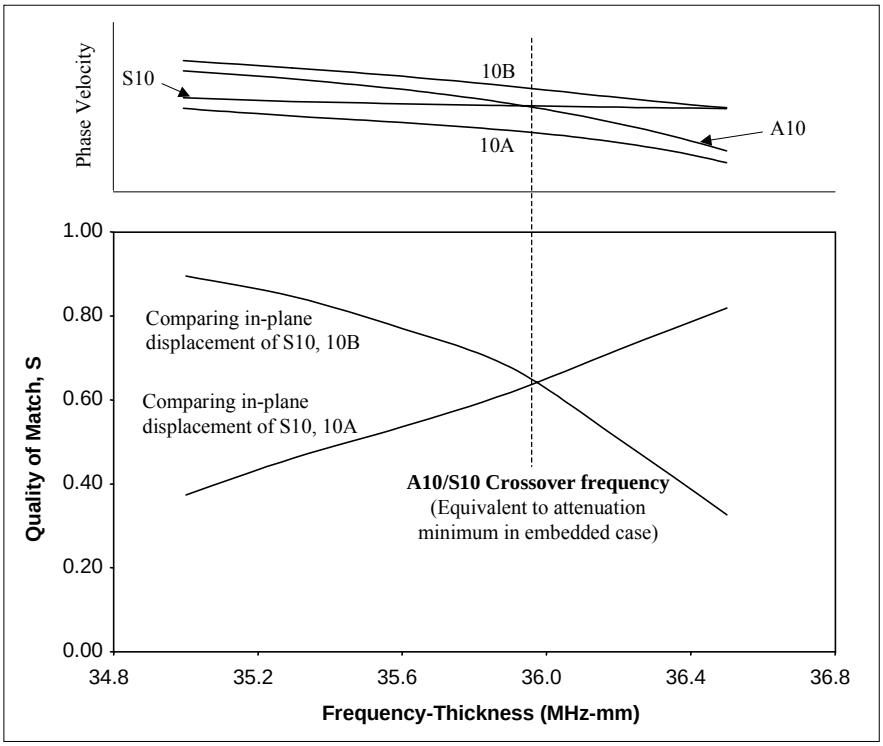

Figure 6.22: Phase velocity dispersion curves and mode shape comparison for a straight plate and a curved plate with a curvature ratio of 30, in the region where S10 exhibits the low-leakage mode shape characteristic.

6.7.4 Estimated Effect of Mode Conversion at Straight/Curved Plate Boundaries

The fact that the mode shapes are not well matched between straight and curved sections at the low-leakage frequencies means that several modes may be generated by mode conversion at straight/curved boundaries. In the both the S4 and S10 cases examined previously, the quality of the match between the low-leakage mode shape and the A and B modes at the same frequency was approximately equal. This means that, if no other modes are generated, the incident S4 or S10 mode will convert equally to the corresponding A and B modes in the curved section, as shown in figure 6.23, so that half of the incident energy will propagate in each. In reality, there will also be other modes generated, which will reduce the energy propagating in the A and B modes. At the end of the curved section, the A and B modes will convert back to the straight plate modes. However, the analysis of both the S4 and S10 cases has shown that the curved plate modes are equally well matched to the straight plate asymmetric mode as well as the symmetric mode. This means, again assuming that no other modes are generated, that the incident A and B modes will both convert equally to the A and S modes in the straight section. In reality, other modes will be generated and reflected, but this simple analysis shows that at least 50% of the energy propagating in the symmetric mode in the initial straight section will be converted to other modes by the curved section.

This analysis is not intended to be rigorous, but it does show the principle that half of the energy travelling in a low-leakage symmetric mode in a plate can be converted to energy travelling in an asymmetric mode by a curved section. The effect of other modes being generated and reflected at the straight/curved plate boundaries will increase the attenuation of the low-leakage mode still further. In addition, the low-leakage mode propagating after the curved section will be mode converted from both the A and B modes, and it is likely that there will be phase differences between the two mode converted components that will further increase the overall attenuation of the low-leakage mode [96].

The free curved bar experiment described in section 6.2.2. measured a loss in end reflection amplitude of up to one half with curvature, even though the free bar curvature was very slight. This corresponds to a 75% loss of energy, suggesting that for each of the two passes through the curved section, up to 50% of the energy propagating in the low-leakage mode was converted to other modes. This level of attenuation is of the same order as predicted by this simple analysis, although the results of the experiment will clearly be affected by curve length, angle and curvature radius.

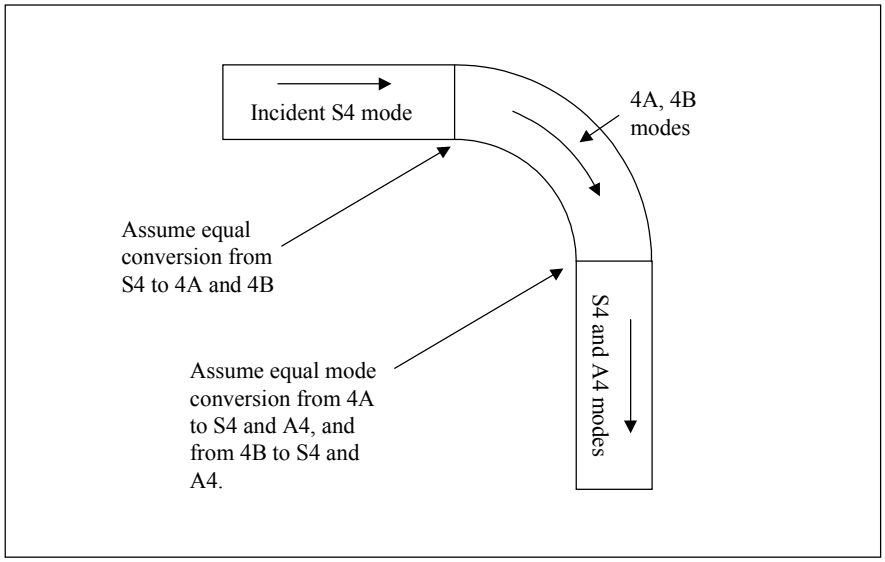

Figure 6.23: Effect of mode conversion on the modes propagating before and after a curved section of plate at a low-leakage frequency.

Overall, it can be seen that poor low-leakage mode transmission will certainly cause some attenuation of low-leakage modes at straight/curved boundaries in a free bar. The effect of mode conversion would be less away from the low-leakage frequencies, where the curved/straight plate dispersion curves overlay. It is likely that this effect will also occur in an embedded plate and in free and embedded bars, and therefore contributes to the increased attenuation observed in curved rock bolt specimens. In reality, the curve transitions will not be abrupt, and the radius of curvature will change constantly over a deformed section of rock bolt. This may have the effect of increasing the attenuation in deformed specimens still further.

6.8 Attenuation due to Leakage in a Curved Plate

Mode conversion explains some of the attenuation that has been observed in embedded and free bars. However, the embedded bar experiment discussed in section 6.2.1 shows much greater attenuation than the free case discussed in section 6.2.2, suggesting that there is another increased attenuation mechanism in an embedded bar. The likely cause of this attenuation is through leakage, and ideally it would be possible to examine the predicted mode shapes and attenuation in curved embedded plates. In the future, it is envisaged that Disperse will be developed further to include curved plate geometry, which would make the treatment of embedded cases straightforward. However, it has already been shown that the low-leakage points in embedded plates have characteristic mode shapes that also exist in free plates at the same frequency, and the likely effect of curvature on these mode shapes can be examined from the free case.

Figure 6.24 shows the displacement mode shape of S10 and A10 in a straight plate and the corresponding 10A and 10B modes in a curved plate with a curvature ratio of 30. The frequency-thickness has been chosen to be 35.9MHz-mm, which corresponds to an attenuation minimum of S10 in the embedded straight case. The mode shape of S10 clearly shows the low-leakage mode shape, with near-zero axial (u_z) displacement at the plate edges. The A10 mode shows a very high axial displacement at the plate edges at this frequency. If the plate was embedded in rock of modulus 20GPa, then the Disperse model predicts an attenuation-thickness of about 250dB-mm/m for the S10 mode, but over 20 times higher for the A10 mode. Figure 6.24 shows that the near-zero edge displacement condition is not met in either the 10A or 10B mode in a curved plate, and therefore the attenuation is likely to be very high. The large difference in edge displacement between the curved plate modes and low-leakage straight plate mode suggests that the attenuation could be at least an order of magnitude higher in the curved embedded case at the low-leakage frequency. This would explain the high attenuation of these modes that has been observed in curved embedded structures. This confirms that because the crossover points observed in a straight plate do not occur in a curved plate, then the low-leakage mode shapes observed in a straight plate at these frequencies do not exist in a curved plate. The following sections examine the modes in curved bars using a finite element technique, to verify that curved bars and curved plates both behave in this way.

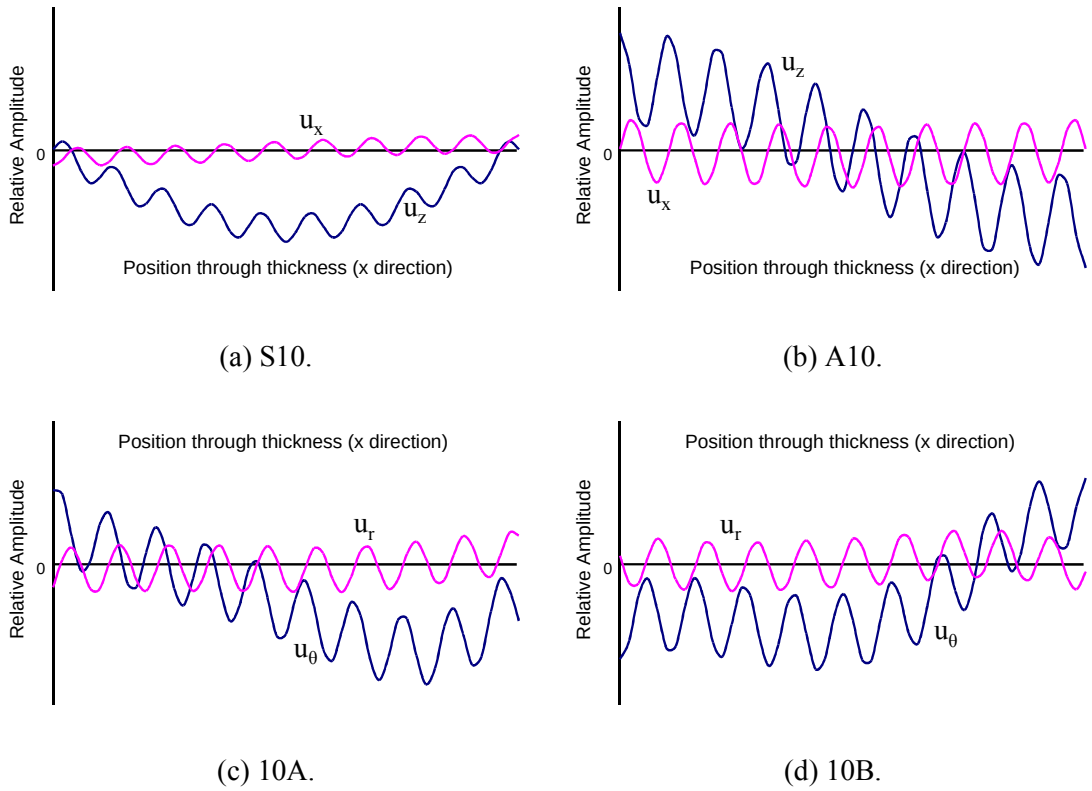

Figure 6.24: Mode shapes at the low-leakage frequency of S10 in an embedded plate, for a free straight plate and a free curved plate with a curvature ratio of 30.

6.9 Calculation of the Dispersion Curves for a Free Curved Bar using Finite Elements

Finite Element models are widely used in the modelling of guided waves to solve problems for which there is no analytical solution. The most common use of the method is to model the propagation of a wave along a structure using a time marching procedure, which allows the interaction of the wave with defects to be studied. For structures such as plates, these models can be two-dimensional, but the case of a curved bar would require the use of a three-dimensional model. The use of three dimensional models greatly increases the number of elements required to accurately model wave propagation, particularly if high frequency modes are studied, where a lot of elements are required through the thickness to accurately describe the complex mode shapes. The study of waves using this method also requires some knowledge of the dispersion curves to generate the correct modes and interpret the results [31,92], as it is difficult to use the method to obtain the modal properties of the structure. An alternative FE technique to find the modal properties of structures has been used by Gavric [106] and the implementation of the technique has been recently simplified and used by Wilcox [107] to determine the modal properties of beams with an arbitrary cross section.

6.9.1 Theory

The method used by Gavric [106] involves creating a two-dimensional finite element mesh representing the cross section of the structure to be examined. The natural frequencies of the system in a direction perpendicular to the mesh are then found using an Eigenvalue technique. By setting a stress-strain boundary condition corresponding to the cyclic variation in stress and strain generated by a propagating wave, the natural frequencies can be related to wavelengths. Varying the length of the cyclic stress-strain condition allows different sets of frequencies to be determined that each correspond to a different wavelength. For each wavelength, the frequencies are those at which guided waves with the specified wavelength can exist in the structure. The dispersion curves can therefore be constructed from different sets of wavelengths and frequencies, and the mode shapes can be found from the eigenvectors at each of the model nodes.

This method was modified by Wilcox [107], who used axial symmetry to remove the need for the specialised stress-strain conditions used by Gavric. Wilcox created the same two-dimensional mesh representing the cross section of the structure, hence creating a toroid about the axis of symmetry. Solution of such a model by using an eigenvalue technique will then yield a set of natural frequencies. The solutions actually represent standing wave patterns, equal to the sum of two similar propagating waves travelling in each direction around the toroid. By varying the harmonic order of the solution, the wavelength of propagating waves can be changed to give a different set of natural frequencies, allowing the dispersion curves to be constructed. For a harmonic order of 1, the wavelength is simply equal to the circumference of the toroid, and for a harmonic order of 2, the wavelength is equal to half of the circumference of the toroid. The relationship between harmonic order and wavelength is given in equation 6.9. The phase velocity can then be calculated from equation 6.10 once the frequency solution set is known.

$$\lambda = \frac{2\pi r_{curvature}}{n} \tag{6.9}$$

where n is the harmonic order and $r_{curvature}$ is the mean curvature radius.

$$V_{ph} = \lambda f \tag{6.10}$$

where Vph is the phase velocity, λ is the wavelength and f is the frequency.

There are two problems associated with this method of calculating dispersion curves. Firstly, the number of wavelengths for which a solution can be found is limited by the fact that the harmonic order must be a whole number. Each set of frequencies effectively lies along a line of constant wavelength, which equates to lines of constant gradient passing through the origin on the phase velocity dispersion curves. The longest wavelength, and the intervals of wavelength for which solutions can be found, are therefore limited by the radius of axial symmetry.

Secondly, this method only approximates the conditions in a straight beam, as the axial symmetry effectively creates a toroidal structure. However, using a large radius of axial symmetry approximates a straight beam very closely, and the use of a large radius also increases the range of harmonic orders can be used, and therefore the detail of the dispersion curves that can be found.

6.9.2 Curved Bar Geometry, Mesh and Validation

The method used by Wilcox [107] for determining the modal properties of guided waves in straight beams is very well suited to curved structures, as the radius of axial symmetry can be varied to obtain the dispersion curves for bars with different curvature radii. A large radius can also be used to validate the results against the straight bar case. Figure 6.25 shows the geometry and mesh that was used to produce the results obtained for a curved bar in the following sections. It is necessary to model the whole bar cross section, as although there is a plane of geometrical symmetry perpendicular to the rotational axis of symmetry, the mode shapes will not necessarily have displacement that is symmetrical about this plane.

The FE package FINEL [108], which incorporates an eigenvalue solution routine, was used for the curved bar analysis. The bar cross section was meshed using 60 square elements across the radius, to give a total number of 2700 elements. This high number of elements is not needed to obtain accurate results for low frequency modes, but is required for higher order modes where the mode shapes are more complex. The maximum variation in frequency was found to be less than 0.5% for the first 60 eigenvalues for 40, 60 and 80 elements across the diameter. This was found to be the case for a range of harmonic orders between 1 and 100. The dispersion curves calculated for a curved bar with a curvature ratio of 100 are shown in figure 6.26a, together with the dispersion curves for a straight plate, calculated using Disperse. The two sets of results show excellent agreement, which verifies that the FE model is working correctly and that the results are reliable.

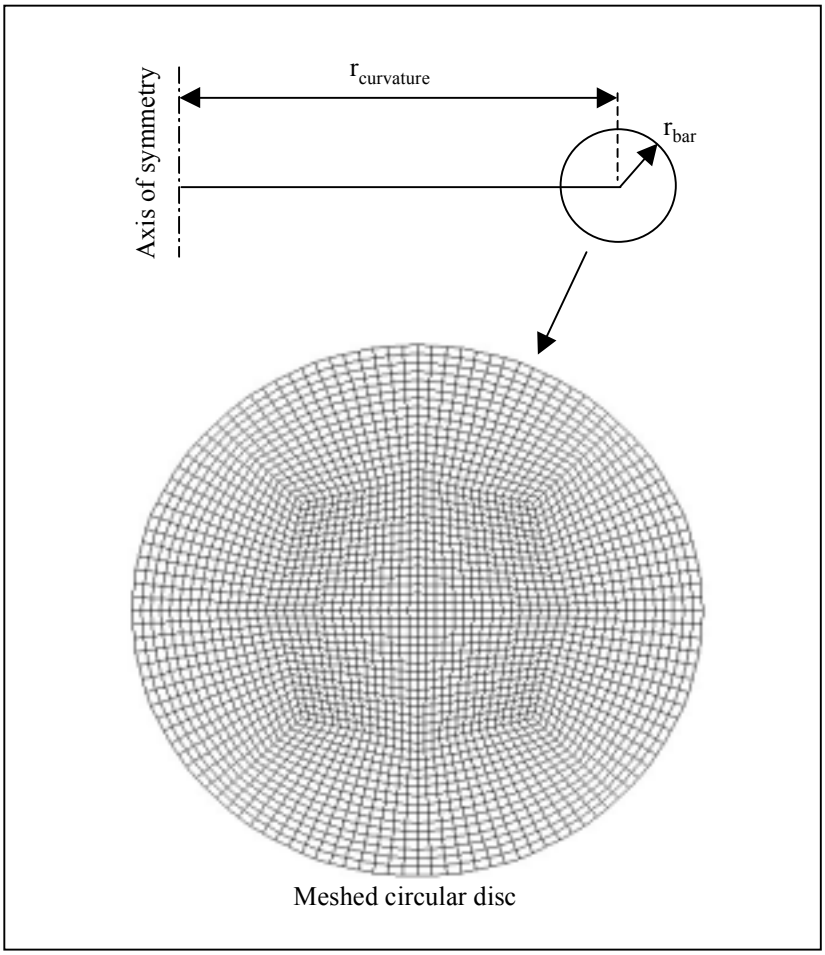

Figure 6.25: Finite element mesh and model geometry for calculating the dispersion curves for a curved bar using a finite element Eigenvalue technique.

6.9.3 Comparison of Straight and Curved Bar Phase Velocity Dispersion Curves

General Dispersion Relationships

Figures 6.26a-d show predicted points on the phase velocity dispersion curves for curved bars with curvature ratios of 100, 10, 5, and 2 respectively. The dispersion curves for a straight bar are also shown as solid lines for each case. The dispersion curves for a straight bar include the second and third order flexural modes, defined by the numbering system outlined in chapter 3. So far throughout this thesis, only longitudinal and first order flexural modes have been considered, and their inclusion in this chapter is simply to clarify the FE model results, as the FE model will predict all the mode types.

Figures 6.26a and 6.26b show that the curved bar dispersion curves for bars with a curvature ratio of 100 and 10 are almost identical to the straight bar case. If the curvature ratio is decreased below this, figures 6.26c and 6.26d show that the dispersion curves begin to change. This is consistent with the findings of Wilcox [100], who concluded that the dispersion curves

in curved plates were largely unchanged from the straight case unless the curvature radius was less than 10 times the plate thickness.

The flexural modes show an interesting phenomenon at low curvature radius, where two points are predicted for each corresponding point on the straight bar dispersion curve. This means that the flexural mode in a straight bar is split into two modes in a curved bar. This effect also occurs at higher curvature radii, but the two points may be closer in frequency than the tolerance of the FE model, which then predicts only 1 point. Examination of the mode shapes at the two points reveals that the displacements associated with the two modes are similar, but are rotated around the centreline of the toroid so that one mode is symmetric about the plane of symmetry of the toroid, and the other is asymmetric. In fact, both of the modes also exist in the straight case, but are identical due to the infinite number of symmetry planes in a straight bar. This effect has also been noticed for the flexural modes in curved pipes [96]. This effect does not occur for the points that overlay axially symmetric modes, and therefore does not particularly concern the low-leakage modes investigated for the testing of structures in this thesis. However, the splitting of the flexural modes may cause further phase differences between the straight bar modes formed from the A and B modes in a curved section of bar, which may increase the attenuation due to mode conversion at straight/curved boundaries over that expected for the plate case.

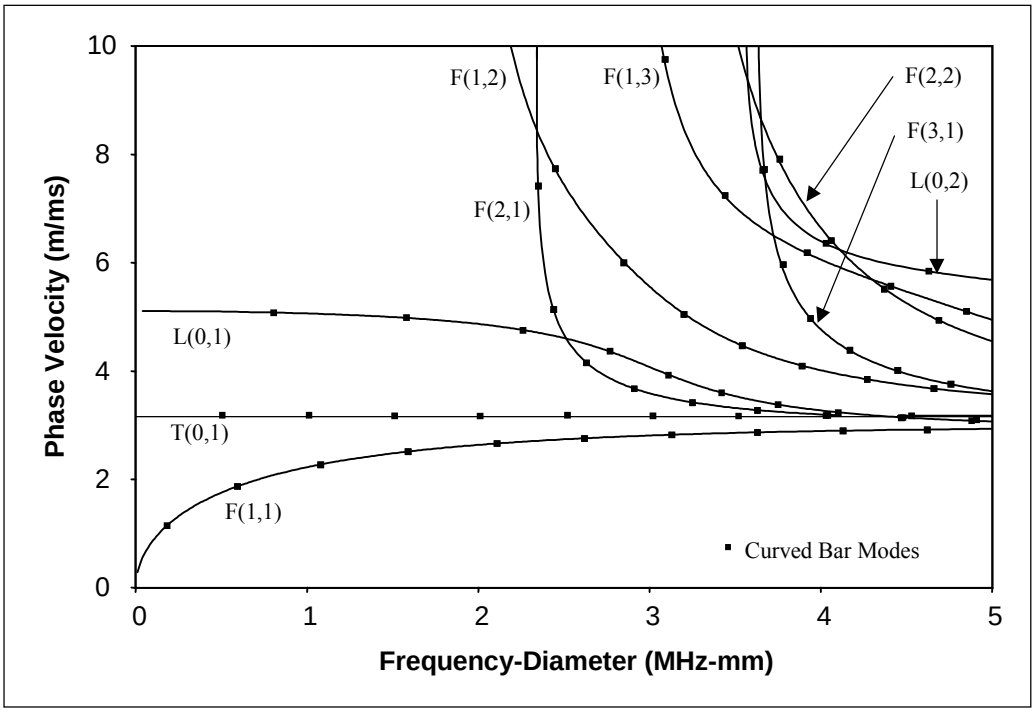

Figure 6.26(a): Dispersion curves for a straight steel bar, showing the points predicted for a similar curved bar with a curvature ratio of 100.

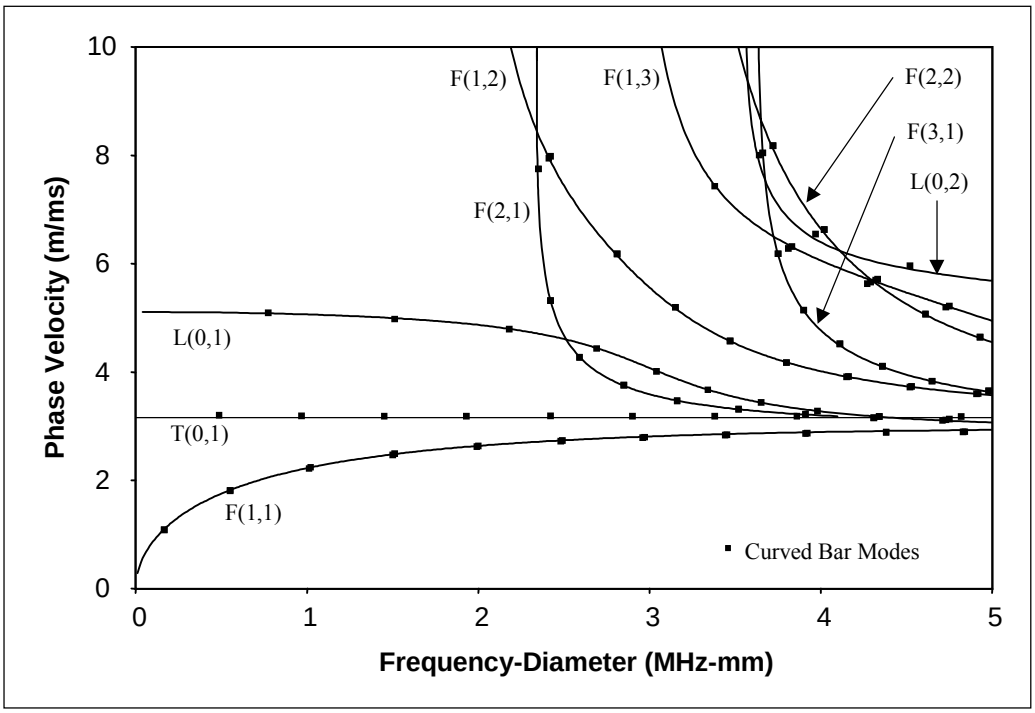

Figure 6.26(b): Dispersion curves for a straight steel bar, showing the points predicted for a similar curved bar with a curvature ratio of 10.

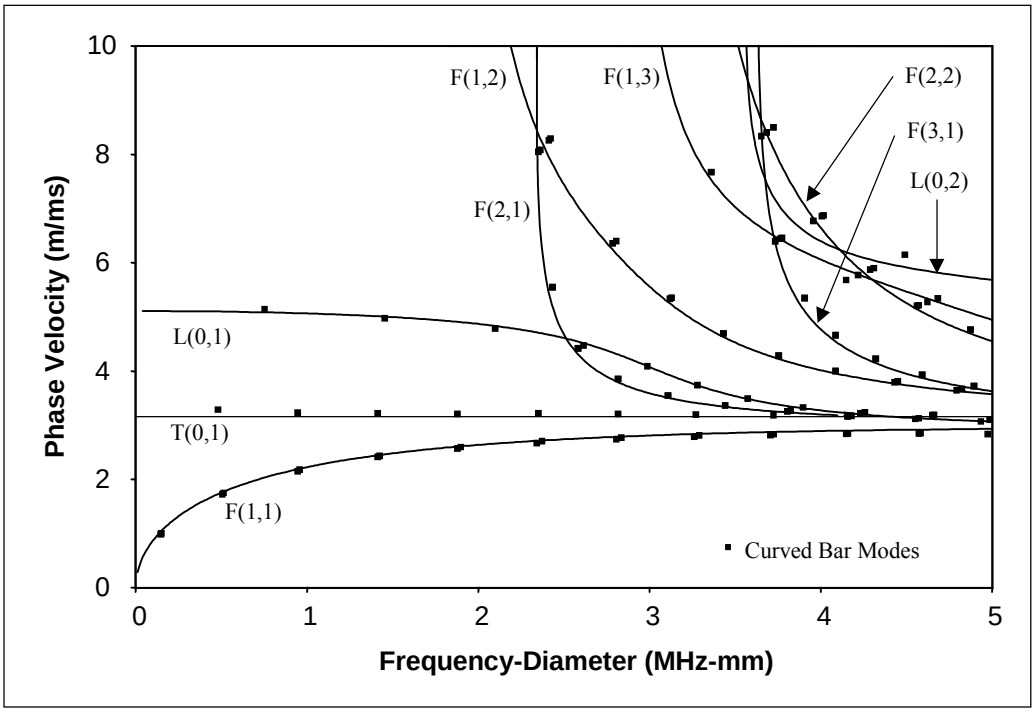

Figure 6.26(c): Dispersion curves for a straight steel bar, showing the points predicted for a similar curved bar with a curvature ratio of 5.

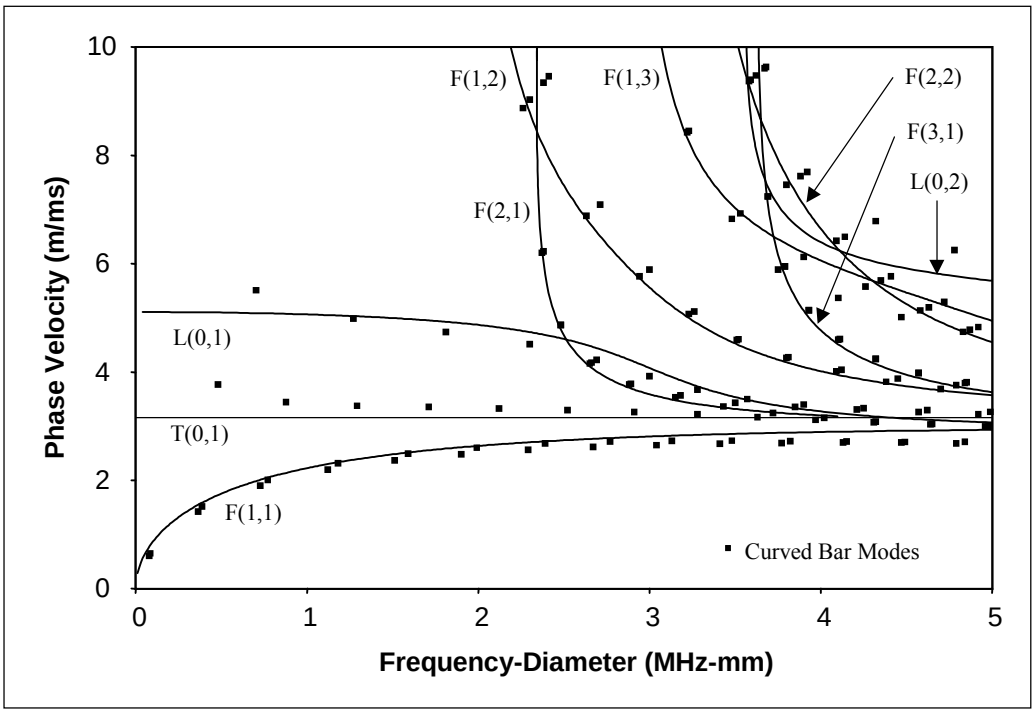

Figure 6.26(d): Dispersion curves for a straight steel bar, showing the points predicted for a similar curved bar with a curvature ratio of 2.

Mode Crossing Points

The investigation into straight and curved plates in this chapter has demonstrated that it is likely that the symmetric and asymmetric mode crossing points do not exist in curved plates. This effect has been used to explain attenuation of low-leakage guided modes in curved structures. The equivalent modes in a bar are the flexural and longitudinal modes, and it is important to see if the curved bar modes behave in the same way as the corresponding curved plate modes. Figure 6.27 shows the detail of the crossing point of the L(0,2) mode and the F(1,4) mode in a straight bar, and the corresponding points predicted by the FE method for a bar with a curvature ratio of 10. The likely curved plate dispersion curves are shown with a dotted line, although closer examination of the region with more FE points is not possible, due to the limitations of specifying a harmonic solution with whole number. A torsional mode also exists close to this point. The location of the points predicted by the FE model show that it is highly unlikely that the equivalent modes to F(1,4) and L(0,2) cross in a curved bar, and the same repelling effect can be observed as for the plate case. However, examination of the dispersion curves indicates that this repelling does not seem to affect other families of modes such as the higher order flexural and torsional modes. The fact that the repelling effect can be seen for first order flexural modes and longitudinal modes gives further confidence in the conclusions drawn from the examination of curved plates.

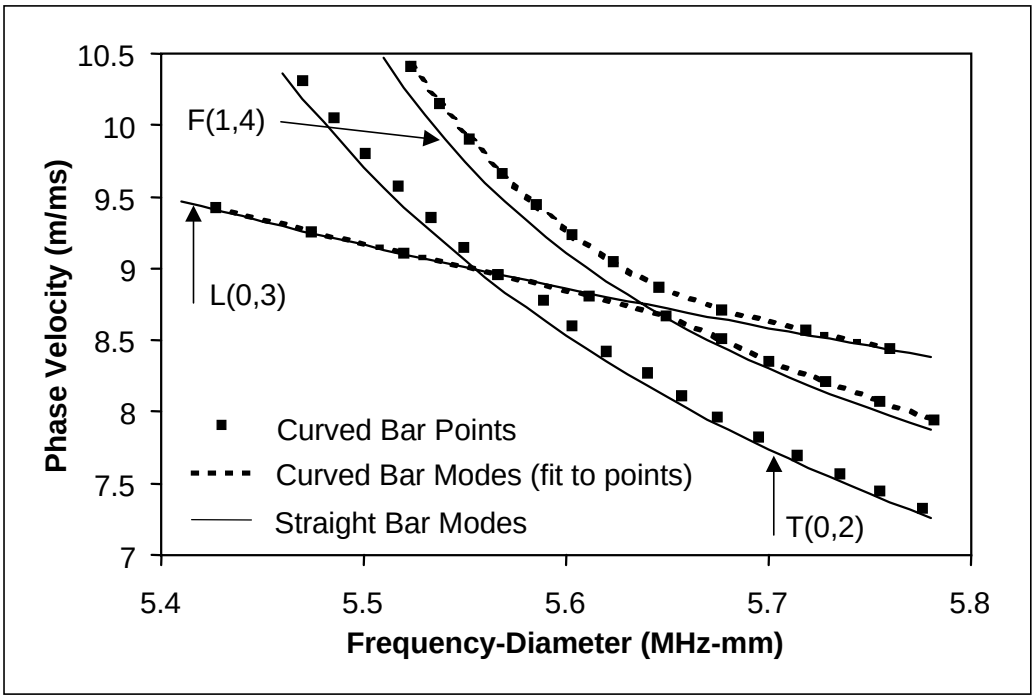

Figure 6.27: Phase velocity dispersion for a straight steel bar and a curved steel bar with a curvature ratio of 10, in the region of the straight bar L(0,2) and F(1,4) crossover point.

6.9.4 Comparison of Straight and Curved Bar Mode Shapes

The behaviour of the L(0,2) and F(1,4) modes examined in the previous section can be examined by looking at the displacement perpendicular to the FE mesh, i.e. along the centreline of the toroid. Figure 6.28 shows the mode shapes of the curved bar modes at frequencies before, after and at the crossover frequency of F(1,4) and L(0,2). Before the crossover point, the mode labelled 'B' is not axially symmetric, and is therefore flexural in nature. This is expected because the mode overlays the F(1,4) mode. After the crossing point, the 'B' mode overlays the axially symmetric L(0,2) mode and is predominantly symmetric in nature. The mode labelled 'A' is axially symmetric, and similar to the L(0,2) mode that it overlays before the crossover frequency. After the crossover frequency, this mode overlays, and is similar to the F(1,4) mode. No distinction is made here between the two 'split' flexural modes, as their mode shapes are in any case similar. At the crossing point, the modes show some symmetric and asymmetric properties, and are therefore not well matched to F(1,4) or L(0,2). This confirms that the axially symmetric low-leakage mode shapes are unlikely to exist in curved bars, in the same way as was shown for the plate case. This confirms that the attenuation mechanisms discussed for an embedded curved plate will also apply to an embedded curved bar.

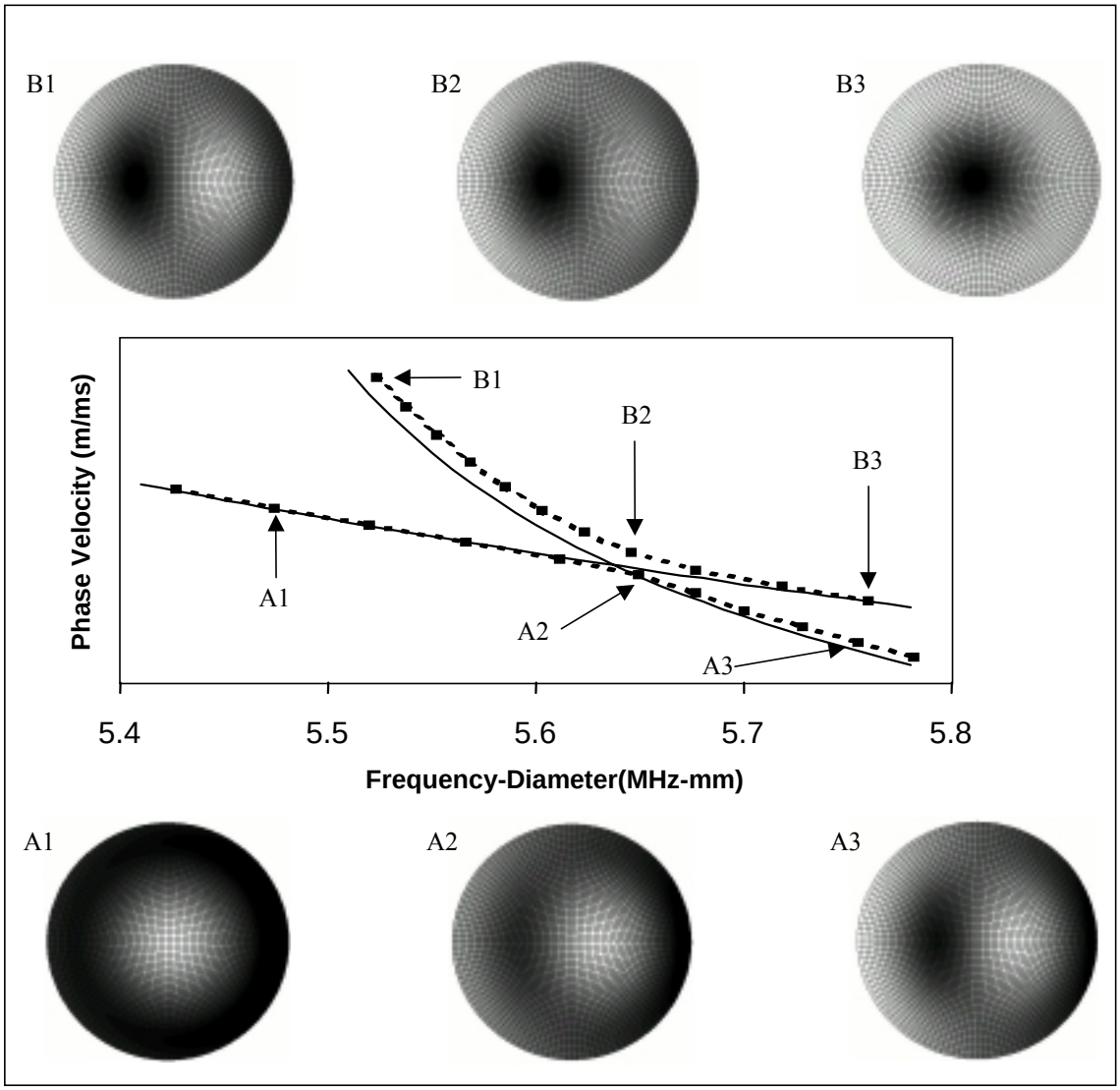

Figure 6.28: Phase velocity dispersion for the modes in a straight and curved bar around the frequency of the F(1,4) and L(0,2) mode crossing point. The axial displacements of the curved bar modes are shown before, after and at the crossover frequency as contour plots.

6.10 Conclusions

This chapter has examined the behaviour of guided waves in curved plates and bars in order to explain the high attenuation of low-leakage guided waves observed in embedded rock bolts and concrete reinforcing tendons. The high attenuation has been confirmed experimentally in both free and embedded bars. The cause of the high attenuation has been investigated by making comparisons with the mode shapes in free plates at low-leakage frequencies. It has been shown that the low-leakage frequencies occur at the crossing points of symmetric and asymmetric modes in embedded plates, and that the mode shapes in free plates show similar characteristics at these frequencies. The curved plate dispersion curves have been calculated for the representative low order L(0,4) mode, and also for the low-leakage region of the S10 mode, which is equivalent to L(0,11) in an embedded bar. The mode crossing points have been shown

not to exist in the curved case, as the modes repel away from each other, suggesting that the low-leakage mode shapes do not occur in curved structures. The mode shapes at these points have been calculated and compared with the straight case both visually, and by using a simple dot product method. It was found that the mode shapes at the low-leakage frequencies were not well matched, although the mode shapes of straight and curved plates were very similar in other regions of the dispersion curves. It is likely that this will result in the attenuation of the symmetric low-leakage mode by poor mode transmission through curved sections of plate.

The mode shapes of S10 and the corresponding curved plate modes were calculated at the low-leakage frequency of S10 in an embedded plate. The curved plate modes showed no evidence of the near zero axial displacement condition that is a characteristic of low attenuation due to leakage for these modes. It is therefore possible that the attenuation of the embedded curved plate modes could be an order of magnitude higher than that expected at the same frequency for a straight embedded plate.

The dispersion curves for a curved bar have also been calculated using a finite element eigenvalue technique, and the behaviour of the first order flexural and longitudinal modes has been shown to be similar to the plate case around the mode crossing points. This gives further confidence in the conclusions drawn from the examination of the low-leakage modes in plates.

It is therefore likely that the poor results obtained in the testing of embedded curved bars is caused by greatly increased attenuation due to leakage, and also attenuation through mode conversion at boundaries between straight and curved sections.

CHAPTER 7

CONCLUSIONS

7.1 Summary of Objectives and Achievements

The research presented in this thesis is motivated by the need to improve the inspection techniques available for the non-destructive testing of embedded cylindrical structures. Two industrial applications have been considered in detail; inspection of the post-tensioning tendons used for concrete reinforcement, and inspection of the rock bolts used for roof reinforcement in coal mines. In both cases, it is necessary to be able to detect complete breaks, and it is also desirable to be able to detect corrosion and defects. The proposed inspection method is a pulse-echo test using guided ultrasonic waves excited from the free end of the structure. Potential test modes and frequencies have been investigated using modelling techniques, and the results have been verified on a variety of site and laboratory specimens. Further research has been carried out in areas of a more general scientific interest to explain the observed test results.

Prior to this thesis, very little work on the inspection of rock bolts in coal mines had been published, and only a feasibility study had been completed on the potential use of guided waves, as a forerunner to this research. Previous authors have investigated the use of high frequency, low-leakage guided waves to inspect concrete reinforcing tendons, and the research reported in this thesis is aimed at establishing the maximum inspection range, and the ability to detect defects. This has been achieved through the measurement of attenuation in embedded tendon specimens and the determination of the high frequency mode reflection coefficients from angled defects experimentally. Research into both applications has shown that high frequency modes are affected by curvature at low-leakage points. This effect has been explained by making comparisons with the modes in a flat plate, which can be calculated using analytic methods, as well as through finite element modelling of a curved bar. Novel work in this area includes the comparison of mode shapes in flat and straight plates, and the calculation of the previously unreported dispersion curves for a curved bar. The progress made in each of these areas is summarised in the following sections.

7.2 Use of Guided Waves to Inspect Rock Bolts

The use of guided waves to inspect rock bolts has been thoroughly investigated through the modelling techniques described in chapter 3, as well as through the site and laboratory tests reported in chapter 4. Transducers and instrumentation requirements have been identified, and methods of coupling the transducer to the bolt have been devised. The project collaborators, RMT, have designed and produced a prototype tool to prepare the bolt end, which is necessary to ensure good ultrasonic coupling to the bolt. The use of a pulse-echo test configuration is ideal in this application, because an end reflection gives positive confirmation that the entire length of the bolt has been interrogated.

Considerable success has been achieved in using high frequency low-leakage modes to determine bolt length up to 3m. The low-leakage modes have several attenuation minima between 2MHz and 3MHz with predicted attenuation low enough to inspect a 3m bolt. The experimental results agree well with the modelling predictions. However, these modes are affected by curvature, and are not suitable for inspecting bolts that have become deformed. The mode properties mean that the high frequency test is not particularly sensitive to surface defects or changes in the epoxy or embedding rock properties. This is because most of the energy travels in the centre of the bolt, and the modes have very little displacement at the bolt edges. An advantage of this is that the high frequency test can be used to accurately determine the bolt length in most embedding conditions, and the end reflection is not easily obscured by reflections from changes in the resin properties or from geological features such as changes in the rock bed.

The reliability of the high frequency test could be improved significantly by incorporating a flat reflecting surface close to the embedded end of the rock bolt. It has been found that the reflection amplitude from angled bolt ends can be 40dB lower than that from flat ends, which limits the range that can be inspected. This could be achieved by manufacturing bolts with a flat end, fitted with a small plastic angled end cap, or by simply incorporating a flat saw cut through part of the bolt diameter. Currently, most bolts have an angled end to assist with the resin mixing and installation processes. In any case, it has still been possible to inspect 2.4m bolts with angled ends. The poor reflection of the high frequency modes from angled breaks also has implications for the detection of corrosion patches. Since such defects would not have flat reflecting surfaces, and also because they would most likely occur at the bolt surface, the reflection coefficient would be small. However, it is possible to detect defects such as necking using the high frequency test.

The fundamental L(0,1) mode has also been used successfully to inspect rock bolts, with the optimum excitation frequency being around 35kHz. This mode is more sensitive to surface

defects than the high frequency modes, as it has much more displacement at the bolt edges. This mode should also be largely unaffected by curvature, although further research is needed to demonstrate this on embedded bars. The low frequency test is very sensitive to the rock and epoxy conditions, and these factors must be considered when interpreting test results. This sensitivity means that the low frequency test can be used to detect defects such as loss of resin encapsulation, and should also be sensitive to large corrosion patches. The mode has been successfully used to detect the ends of bolts with a 2m embedded length in the laboratory, and to detect the start of resin encapsulation. End reflections were also obtained from rock bolts up to 2.4m long installed at Middleton mine, although the results were complicated by early reflections, thought to be from geological features. Further instrumentation developments, including the use of a time variable gain to prevent any early reflections from saturating the receiver amplifier should resolve this problem. The L(0,1) mode attenuation and optimum test frequency are lower than those predicted by a model based on the nominal material properties, but this can be explained by poor bond quality at the rock/epoxy interface and a lower than expected epoxy modulus, probably caused by poor mixing and the presence of contaminants. Good agreement between the model and experimental results was obtained when these factors were considered.

Overall, the behaviour of the high and low frequency modes is very different, and neither the high or low frequency test offers a complete testing solution on its own. The low frequency test is useful for identifying defects such as partial bolt encapsulation, and the high frequency test is useful for giving reliable confirmation of bolt length, even when surface corrosion or geological features complicate the low frequency test result. The fact that high frequency waves are attenuated by curvature also allows the possibility of determining whether or not bolts are deformed. A dual frequency test should therefore be able to successfully test for defects and residual length on most bolts. The results of the research have been shown to be very promising, and commercialisation of the technique will follow further developments in the instrumentation. This will include the ability to apply a time-variable gain to the received signals, and to incorporate high frequency circuitry within the instrument. In addition, the final product must be produced to meet the stringent mining safety regulations.

There are other applications where the inspection technique could be adapted to meet non-destructive testing needs. The high frequency test would be very suitable for inspecting the grouted rock bolts used in other civil engineering applications, where no deformation is expected to occur, and could also be used to inspect concrete re-bars.

7.3 Use of Guided Waves to Inspect Post-Tensioning Tendons

Previous authors have calculated the dispersion curves for grouted bars, and identified high frequency, low-leakage guided waves with the potential to inspect concrete post-tensioning tendons non-destructively. The initial experimental results were encouraging, but the maximum possible inspection range has never been identified. The research presented in chapter 5 of this thesis has added to this work to reach conclusions about the feasibility of using high frequency, low-leakage guided waves to inspect both single wire and multi-wire strand tendons. This has been achieved through the measurement of attenuation in short tendon specimens, and an experimental study into the reflection of the modes from angled breaks. Unlike the rock bolt case, it is not possible to use low frequency waves for tendon inspection, because the transducer would detect reflections of the leaked bulk waves from the grouting duct walls. At high frequency, the shorter wavelength leaked bulk waves are quickly attenuated in the embedding material.

The inspection range is determined by the total attenuation experienced by the guided wave as it propagates along the tendon. The main mechanisms of attenuation are through leakage into the grout material and through damping inherent in the material, but it is also necessary to consider how much ultrasonic energy will be reflected from defects, as this will contribute to the overall wave attenuation in a pulse-echo test. The attenuation in single wire grouted tendons was measured to be 27dB/m and 40dB/m for 7mm and 5mm diameter wires respectively. The attenuation was measured to be 20dB/m and 60dB/m respectively for the inner and outer wires of a 15.2mm diameter 7-wire strand. The large difference in attenuation between the inner and outer wires is primarily due to the curvature of the outer, spirally wrapped wire, although radiation into the grout will also have a small effect. The reflection coefficient of the low-leakage modes from a flat break normal to the tendon axis is almost unity, but if the break is at an angle of just 10° to the plane normal to the wire axis then the wave is poorly reflected, and the reflected signal amplitude can be reduced by as much as 40dB.

The measured attenuation suggests that the inspection range would be less than 2.5m for all of the tendons investigated, assuming perfectly flat breaks and that the testing instrument could compensate for 100dB of attenuation. Smaller diameter tendons would have higher attenuation, reducing the inspection range. However, the poor reflection of the waves from angled breaks means that in practice, it would not be possible to detect real breaks or defects at this range. It is unlikely that more than about 1m of a 7mm diameter wire could be inspected reliably, even for a complete break. In the case of stranded tendons, the inspection range is limited further by curvature of the outer wires, and the range would be only 0.5m. A further complication is that it is not possible to obtain positive confirmation of the inspection range, unless a defect is

detected. Partial depth defects would have even lower reflection coefficients, especially for the case of surface corrosion, as the rock bolt testing has shown that low-leakage modes are not sensitive to surface defects.

Overall, the high attenuation limits the usefulness of guided waves for the routine inspection of small diameter grouted tendons. However, the attenuation in larger diameter re-bars and grouted steel anchors would be much less, and the method may offer inspection opportunities for such structures, particularly if the length allowed an end reflection to be obtained, giving positive confirmation of the inspection range.

7.4 The Effect of Curvature on Low-Leakage Guided Waves

Chapter 6 of this thesis confirms experimentally that the high frequency low-leakage modes in bars are attenuated by curvature. This observation has been explained by making comparisons with the case of a free plate to draw conclusions about the behaviour of modes in curved, embedded bars. The low-leakage points on straight plate modes are shown to exist at mode crossing points close to the longitudinal bulk velocity line. These points do not exist if the plate is curved because the modes repel away from that point. The mode shapes in curved and straight plates have been compared visually, and by using a dot product method, to explain the additional attenuation. Comparison of the mode shapes has shown that the low-leakage mode shape characteristic found in straight plates does not exist in curved plates, which will lead to the attenuation being much higher. Additional attenuation is also expected at boundaries between straight and curved sections, due to mode conversion effects. Previous authors have published curved plate mode shapes and dispersion curves, but no comparison of the mode shapes had been made prior to this thesis.

Chapter 6 also presents the previously unreported dispersion curves for a curved bar, which have been calculated using a finite element eigenvalue method. The dispersion curves are shown to be generally similar to those of a straight bar when the radius of curvature is at least 10 times greater that the bar diameter. The examination of the crossover point of a first order flexural mode and a longitudinal mode shows that the curved bar modes repel away from the crossing point, in the same way as observed for the symmetric and anti-symmetric modes in a plate. This gives further confidence in the conclusions drawn about the low-leakage modes in bars from the study of plates. The curved bar dispersion curves will also provide a useful validation case for future analytical work in this area.

7.5 Recommendations for Further Scientific Research

This research presented in this thesis has highlighted several areas where further research would increase the general understanding of guided wave propagation. Specific recommendations for the industrial applications discussed in this thesis are included in the previous sections; this section discusses recommendations for further research that would have a wider scientific benefit.

The understanding of wave propagation through curved structures would be greatly improved if curved plate and bar geometry was incorporated into modelling software, such as Disperse. This is straightforward for the plate case as the equations have already been derived, and would allow multi-layer and embedded curved plate problems to be studied in detail. The curved bar dispersion curves have been obtained using a finite element method in this thesis, but the development of an analytic solution would be more convenient and more complete. It is unlikely that solution of the wave propagation equation for this geometry is possible using a standard mathematical approach, although the application of techniques such as ray-tracing may offer opportunities. Knowledge of guided wave behaviour in such systems would allow fast evaluation of the opportunities for NDT using guided waves, as well as better understanding of existing testing techniques.

The reflection of guided waves from angled defects that require three-dimensional finite element models is generally not well understood. The results in this thesis show that a small change in the end angle of a bar makes a large difference to the reflection coefficient of high frequency modes. Further development of finite element capability would allow larger models to be constructed to study this phenomenon, and it may also be possible to achieve results using an analytical approach. A related topic is the study of mode conversion at boundaries between straight and curved sections. It is possible that the development of techniques such as the S-Parameter method may allow the effect of mode conversion to be examined analytically.

The modelling work also showed that bonding between materials in multi-layer systems can dramatically affect mode properties such as attenuation due to leakage. Further research into the accurate modelling of bond conditions would allow better predictions of mode properties to be made. Accurate knowledge about wave behaviour under different bonding conditions may well offer new opportunities for guided wave inspection in industrial applications.

BIBLIOGRAPHY

1. B. Rowland, HM Inspector of Electrical Engineering in Mines, 'Research into the use of ultrasonic waves for rock bolting', *Letter to M.J.S. Lowe, Imperial College, in support of research proposal,* 17/6/97.
2. R. Woodward, F. Williams, 'Collapse of the Ynys-Y-Gwas bridge, West Glamorgan', *Proceedings of the Institution of Civil Engineers*, vol.84, pp.635-669, 1988.
3. D. Parker, 'Pacific bridge collapse throws doubt on repair method', *New Civil Engineer*, pp.3-4, 12/12/96 and 26/12/96.
4. D. Parker, 'Tropical Overload', *New Civil Engineer*, pp.18-21, 17/10/1996.
5. B.N. Pavlakovic, M.J.S. Lowe, and P. Cawley, 'Guided ultrasonic waves for the inspection of post-tensioned concrete bridges', in *Review of Progress in QNDE*, eds. D.O. Thompson and D.E. Chimenti, vol.17, pp.1557-1564, Plenum Press, New York, 1998.
6. B.N. Pavlakovic, M.J.S. Lowe, and P. Cawley, 'High frequency low loss ultrasonic modes in imbedded bars', *Journal of Applied Mechanics*, vol. 68, pp.67-75, 2001.
7. B.N. Pavlakovic, M.J.S. Lowe, D. Alleyne and P. Cawley, 'Disperse: a general purpose program for creating dispersion curves', in *Review of Progress in QNDE*, eds. D.O. Thompson and D.E. Chimenti, vol.16, pp.185-192, Plenum Press, New York, 1997.
8. The Highways Agency, SETRA, LCPC, 'Post-tensioned concrete bridges', Thomas Telford Publishing, London, 1999.
9. J.S. Popovics and J.L. Rose, 'A survey of developments in the ultrasonic NDE of concrete', *IEEE Transactions on Ultrasonics, Ferroelectrics and Frequency Control*, vol.41, pp.140-143, 1994.
10. R.A. Livingstone, 'Future directions in NDE research for highways', *Review of Progress in QNDE*, eds. D.O. Thompson and D.E. Chimenti, vol.13, pp.2099-2106, Plenum Press, New York, 1994.
11. A. Lewis, 'Moratorium lifted', *Concrete*, vol.30(6), pp. 25-27, 1996.
12. The Concrete Society, 'Durable bonded post-tensioned concrete bridges', *Technical Report 47*, The Concrete Society, Slough, Berkshire, UK, 1996.

13. D.W. Cullington, M.E. Hill, and R.J. Woodward, 'Special inspections on post-tensioned bridges in England: Report on progress', *Paper presented at a British Cement Association Seminar*, 11/4/97.

14. J.H. Bungey, 'Testing of concrete in structures', Surrey University Press, 1989.

15. H.T. Williams and M.E. Hulse, 'From theory to experience with inspection of post-tensioned bridges', in *Proceedings of the sixth international conference on structural faults and repair*, ed. M.C. Forde, vol.1, pp.199-202, Engineering Technics Press, 1995.

16. M.B. Leeming, J.S. Lane, and P.J. Wade, 'Post-tensioned bridge investigation - the way forward', in *Proceedings of the sixth international conference on structural faults and repair*, ed. M.C. Forde, vol.1, pp.193-197, Engineering Technics Press, 1995.

17. P. Kear and M. Leeming, 'Radiographic inspection of post-tensioned concrete bridges', *Insight*, vol.36(7), pp.507-510, 1994.

18. R. Guinez, 'SCORPION - Bilan de dix ans d'utilisation', *Bulletin de Liaison LPC*, pp.79-90, 1-2/1997.

19. PUNDIT 6, Operating manual, CNS Farnell, Manor Way, Borehamwood, Hertfordshire, UK.

20. J. Martin, M.S.A. Hardy, A.S. Usnami and M.C. Forde, 'Quantifying the defects in post-tensioned bridges using ultrasonics', in *Proceedings of the sixth international conference on structural faults and repair*, ed. M.C. Forde, vol.1, pp.199-202, Engineering Technics Press, 1995.

21. O. Kroggel, R. Jansohn, and M. Ratmann, 'Novel ultrasound system to detect voided ducts in post-tensioned bridges' in *Proceedings of the sixth international conference on structural faults and repair*, ed. M.C. Forde, vol.1, pp.203-208, Engineering Technics Press, 1995.

22. B.J. Jaeger, M.J. Sansalone, and R.W. Poston, 'Detecting voids in grouted tendon ducts using the impact-echo method', *ACI Structural Journal*, vol.93(4), pp.462-473, 1996.

23. P.J. Duncan, P.A. Gaydecki, and F.M. Burdekin, 'Ultrasonic NDT prototype for the inspection of ducted post stressing tendons in concrete beams' in *Review of Progress in QNDE*, eds. D.O. Thompson and D.E. Chimenti, vol.15, pp.1799-1806, Plenum Press, New York, 1995.

24. M. Sansalone, J.B. Jaeger, and W.P. Randall, 'Detecting voids in grouted tendons of post-tensioned concrete structures using the impact-echo method', *ACI Structural Journal*, vol.93(4), pp.462-472, 1996.

25. T. Watanabe, M. Ohtsu, and Y. Nakayama, 'Impact-echo NDT for grouting performance in post-tensioning tendon duct', in *Proceedings of the eighth international conference on structural faults and repair*, ed. M.C. Forde, Supplied on CD, Engineering Technics Press, 1999.

26. J. Martin, A. Giannopoulos, and M.C. Forde. Ultrasonic Tomography of grouted duct post-tensioned reinforced concrete bridge beams', in *Proceedings of the eighth international conference on structural faults and repair*, ed. M.C. Forde, Supplied on CD, Engineering Technics Press, 1999.

27. F.M. Burdekin, D.G. John, P.A. Payne, C. Locke, T.A. Smith, K. Simm, J.L. Dawson, 'Non-destructive methods for the field inspection of embedded or encased high strength steel rods and cables - Phase 1', *UMIST/CAPCIS Report*, 1986.

28. F.M. Burdekin, D.G. John, P.A. Payne, C. Locke, T.A. Smith, K. Simm, J.L. Dawson, 'Non-destructive methods for the field inspection of embedded or encased high strength steel rods and cables - Phase 2', *UMIST/CAPCIS Report*, 1991.

29. D. Alleyne, B.N. Pavlakovic, M.J.S. Lowe, P. Cawley, 'Rapid, long range inspection of chemical plant pipework using guided waves', *Insight*, vol.43(2), pp.93-96, 2001.

30. J. Weight, 'High frequency ultrasonics tests on grouted tendons', *Unpublished report supplied to the Transport Research Laboratory*, 1994.

31. B.N. Pavlakovic, 'Leaky guided ultrasonic waves in NDT', *PhD Thesis, Department of Mechanical Engineering, Imperial College of Science Technology and Medicine, London*, 1998.

32. J.L. Rebert, and M. Brachet-Rolland, 'Survey of Structures by using Acoustic Emission Monitoring', *Reports of the Working Commissions (International Association for Bridge and Structural Engineering)*, vol.39, p33-38, 1982.

33. D.W. Cullington, D. MacNeil, P. Paulson, J. Elliott, 'Continuos acoustic monitoring of grouted post-tensioned concrete bridges', *NDT&E International*, vol.34, pp.95-105, 2001.

34. E.I. Okanla, P.A. Gaydecki, S. Manaf, F.M Burdekin, 'Detecting faults in post-tensioned cables using time domain reflectometry', *Journal of Structural Engineering*, vol.123(5), pp.567-574, 1997.

35. M.D. Mitelli A. Santori, G. Nava, N. Tommasini, 'Prestressing cables inspection and assessment by means of the reflectometric method (RIMT), in *Bridge Management 3 - Inspection, maintenance, assessment and repair*, eds. J.E. Harding, G.E.R. Parke, and M.J. Ryall, pp.751-760, E. & F.N Spon, London, 1996.

36. T. Saarenketo, and M. Soderqvist, 'Ground penetration radar applications for bridge deck evaluations in Finland', *Insight*, vol.36(7), pp.496-501.1994.

37. K. Hurt, Rock Mechanics Technology Ltd., 'EPSRC Proposal Support' *Letter to M.J.S. Lowe, Imperial College, in support of research into rock bolt inspection*, 9/7/97.

38. F.L. Kent, J.S. Coggan, and P.F.R. Altounyan, 'Investigation into factors affecting roadway deformation in the Selby coalfield', *Geotechnical and Geological Engineering*, vol.16, pp.273-289, 1999.

39. F.S. Jeng, and T.H. Huang, 'The holding mechanism of under-reamed rock bolts in soft rock', *International Journal of Rock Mechanics and Mining Sciences*, vol.36, pp.761-775, 1999.

40. R. Schach, K. Garshol, and A.M. Heltzen, 'Rock bolting - A practical handbook', Revised Edition, Pergamon Press, Oxford, UK, 1979.

41. Geodynamik, 'Boltometer 011 - Users Manual', Geodynamik AB, Stockholm, Sweden.

42. J. Monaghan, and J. Willan, 'Final report on testing of grouted rockbolts using the Swedish Boltometer Model 002', *Ontario Ministry of Labour - Occupational Health and Safety Division - Mining Health and Safety Branch Report, Ontario,* 1983.

43. I. Vrkljan, A. Szavits-Nossan and M.S. Kovacevic, 'Non-destructive method for testing grouting quality of rockbolt anchors', in *International Congress on Rock Mechanics*, eds. G. Vouille and P. Berest, vol.9, pp.1475-1478, Balkema, 1999.

44. J. Pochhammer, 'Ueber die Fortpflanzungsgeschwindigkeiten kleiner Schwingungen in einem unbegrenzten isotropen Kreiszylinder'. *Journal fuer reine und angewandte Math*, vol.81, pp.324-336, 1876.

45. C. Chree, 'The equations of an isotropic elastic solid in polar and cylindrical co-ordinates, their solutions and applications', *Transactions of the Cambridge Philosophical Society*, vol.14, pp.250-369, 1889.

46. G.E. Hudson, 'Dispersion of elastic waves in solid circular cylinders', *Physics Review*, vol.63, pp.46-51, 1943.

47. R.M. Davies, 'A critical study of the Hopkinson pressure bar', *Phil. Transactions. Royal Society, London*, vol.240, pp.375-457, 1948.

48. M. Onoe, H.D. McNiven, and R.D. Mindlin, 'Dispersion of axially symmetric waves in elastic solids', *Journal of Applied Mechanics*, vol.29, pp.729-734, 1962.

49. Y.H. Pao, and R. Mindlin, 'Dispersion of Flexural Waves in an Elastic, Circular Cylinder', *Journal of Applied Mechanics*, vol.27, pp.513-520, 1960.

50. Y.H. Pao, 'The dispersion of waves in an elastic, circular cylinder - Part 2', *Journal of Applied Mechanics*, vol.29, pp.61-64, 1962.

51. T.R. Meeker, and A.H. Meitzler, 'Guided wave propagation in elongated cylinders and plates', in *Physical Acoustics, Principals and Methods*, eds. W.P. Mason and R.N. Thurston, pp.111-167, Academic Press, New York, 1972.

52. D.C. Gazis, 'Three dimensional investigation of the propagation of waves in hollow circular cylinders', *Journal of the Acoustical Society of America,* vol.31(5), pp.568-578, 1959.

53. A.H. Fitch, 'Observation of elastic-pulse propagation in axially symmetric and non-axially symmetric longitudinal modes of hollow cylinders', *Journal of the Acoustical Society of America,* vol.35(5), pp.706-708, 1963.

54. R. Kumar, 'Flexural vibrations of fluid-filled circular cylindrical shells', *Acoustica,* vol.24, pp.137-146, 1971.

55. R. Kumar, 'Dispersion of axially symmetric waves in empty and fluid-filled cylindrical shells', *Acoustica,* vol.27(6), pp.317-329, 1972.

56. R.W. Morse, 'Compressional waves along an anisotropic circular cylinder having hexagonal symmetry', *Journal of the Acoustical Society of America,* vol.26(6), pp.1018-1021, 1954.

57. I. Mirsky, 'Wave propagation in transversely isotropic cylinders, Part 1: Theory', *Journal of the Acoustical Society of America,* vol.26(6), pp.1018-1021, 1954.

58. P.C. Xu, and S.K. Datta, 'Characterisation of fibre-matrix interface by guided waves: axisymmetric case', *Journal of the Acoustical Society of America,* vol.89(6), pp.2573-2583, 1991.

59. V. Dayal, 'Longitudinal waves in homogeneous anisotropic cylindrical bars immersed in fluid', *Journal of the Acoustical Society of America,* vol.93(3), pp.1249-1255, 1993.

60. P.B. Nagy, 'Longitudinal guided wave propagation in a transversely isotropic rod immersed in fluid', *Journal of the Acoustical Society of America,* vol.98(1), pp.454-457, 1995.

61. M.J. Berliner and R. Solecki, 'Wave propagation in fluid-loaded, transversely isotropic cylinders - Part I: Analytical formulation', *Journal of the Acoustical Society of America,* vol.99(4), pp.1841-1847, 1996.

62. R. Thurston, 'Elastic waves in rods and clad rods', *Journal of the Acoustical Society of America,* vol.64(1), pp.1-37, 1978.

63. D.E. Amos, 'A remark on algorithm 644: a portable package for Bessel functions of a complex argument and non-negative order', *ACM Transactions on Mathematical Software*, vol.21(4), pp.388-393, 1995.

64. A. Safaai-Jazi, C.K. Jen, and G.W. Farnell, 'Cutoff conditions in an acoustic fiber with infinitely thick cladding', *IEEE Transactions on Ultrasonics, Ferroelectrics and Frequency Control*, vol.33(1), pp.69-73, 1986.

65. J.A. Simmons, E. Drescher-Krasicka, and H.N.G. Wadley, 'Leaky axisymmetric modes in infinite clad rods', *Journal of the Acoustical Society of America,* vol.92(2), pp.1061-1090, 1992.

66. M Viens, Y. Tshukahara, C.K. Jen, J.D.N. Cheeke, 'Leaky torsional modes in infinite clad rods', *Journal of the Acoustical Society of America,* vol.95(2), pp.701-707, 1994.

67. M.J.S. Lowe, 'Matrix techniques for modelling ultrasonic waves in multilayered media', *IEEE Transactions on Ultrasonics, Ferroelectrics and Frequency Control*, vol.42(4), pp.525-542, 1995.

68. B.N. Pavlakovic and M.J.S. Lowe, 'A general purpose approach to calculating the longitudinal and flexural modes of multi-layered, embedded, transversely isotropic cylinders' in *Review of Progress in QNDE*, eds. D.O. Thompson and D.E. Chimenti, vol.18, pp.239-246, Plenum Press, New York, 1999.

69. M.J.S. Lowe, 'Plate waves for the NDT of diffusion bonded titanium', *PhD Thesis, Department of Mechanical Engineering, Imperial College of Science Technology and Medicine, London*, 1993.

70. D.N. Alleyne, 'The non-destructive testing of plates using ultrasonic lamb waves', *PhD Thesis, Department of Mechanical Engineering, Imperial College of Science Technology and Medicine, London*, 1991.

71. B.A. Auld, 'Acoustic fields and waves in solids - vol.I', Stanford: Krieger Publishing Company, Florida, 1990.

72. M.G. Silk, and K.F. Bainton, 'The propagation in metal tubing of ultrasonic wave modes equivalent to Lamb waves', *Ultrasonics*, pp.11-19, 1979.

73. A. Bernard, M.J.S. Lowe, and M. Deschamps, 'Guided waves energy velocity in absorbing and non-absorbing plates', *Journal of the Acoustical Society of America,* vol.110, pp.186-196, 2000.

74. Engineering and Physical Sciences Research Council (EPSRC), 'Guided wave inspection of tendons in post-tensioned concrete and rock bolts in mines' *Research contract awarded to Imperial College*, 1998.

75. Transport Research Laboratory Limited (TRL), Old Wokingham Road, Crowthorne, Berkshire, UK.

76. Rock Mechanics Technology Limited (RMT), Bretby Business Park, Ashby Road, Stanhope Bretby, Burton-on-Trent, Staffordshire, DE15 0QD, UK.

77. B.N. Pavlakovic, 'Feasibility study into the use of guided waves to inspect rock bolts', *Unpublished report supplied to RMT Ltd.*, 1997.

78. B. Clifford, 'Ultrasonics for integrity testing of rock bolts in mines', *HSE Contract Report Number 3811BC20*, RMT Ltd., 2000.

79. G.W.C. Kaye and T.H. Laby, 'Tables of physical and chemical constants', 16thed., Harlow: Longman, 1995.

80. Exchem Mining and Construction, Venture Crescent, Motorway Link Estate, Alfreton, Derbyshire, UK.

81. T. Pialucha, M. Lowe, and P. Cawley, 'Validity of different models of interfaces in adhesion and diffusion bonded joints', in *Review of Progress in QNDE*, eds. D.O. Thompson and D.E. Chimenti, vol.12, pp.1547-1554, Plenum Press, New York, 1993.

82. A. Pilarski, J.L. Rose, J. Ditri, D. Jiao, and K. Rajana, 'Lamb wave mode selection for increased sensitivity to interfacial weaknesses of adhesive bonds', in *Review of Progress in QNDE*, eds. D.O. Thompson and D.E. Chimenti, vol.11, pp. 1579-1586, Plenum Press, New York, 1992.

83. A. Pilarski, 'Ultrasonic evaluation of the adhesion degree in layered joints', *Materials Evaluation*, vol.43, pp.765-770, 1985.

84. C. Pecorari, and P. Kelly, 'The quasi-static approximation for cracked interfaces in layered systems', in *Review of Progress in QNDE*, eds. D.O. Thompson and D.E. Chimenti, vol.18, pp.1471-1478, Plenum Press, New York, 1999.

85. L. Adler, M. Billy, and G. Quentin, 'Evaluation of friction-welded aluminium-steel bonds using dispersive guided modes of a layered substrate', *Journal of Applied Physics*, vol.68(12), pp.6072-6076, 1990.

86. A.H. Nayfeh, and P.B. Nagy, 'General study of axisymmetric waves in layered anisotropic fibers and their composites', *Journal of the Acoustical Society of America,* vol.99(2), pp.931-941, 1996.

87. M.J.S. Lowe, and P. Cawley, 'The applicability of plate wave techniques for the Inspection of Adhesive and Diffusion Bonded Joints' *Journal of Non-Destructive Evaluation*, vol.13, pp.185-200, 1994.

88. C.W. Chan, and P. Cawley, 'Lamb waves in highly attenuative plastic plates', *Journal of the Acoustical Society of America,* vol.104, pp.874-881, 1998.

89. Macro Design Ltd., 16 Palewell Park, East Sheen, London, SW14 8JG, UK.

90. D.N. Alleyne, and P. Cawley, 'The excitation of lamb waves in pipes using dry coupled piezoelectric transducers', *Journal of Non-Destructive Evaluation*, vol.15(1), pp.11-20, 1996.

91. Alltran Ltd., 565 Rayners Lane, Pinner, Middlesex, HA5 5HP, UK.

92. B.N. Pavlakovic, M.J.S. Lowe, and P. Cawley, 'Prediction of reflection coefficients from defects in embedded bars', in *Review of Progress in QNDE*, eds. D.O. Thompson and D.E. Chimenti, vol.18, pp.207-214, Plenum Press, New York, 1999.

93. T. Vogt, M.J.S. Lowe, and P. Cawley, 'Cure monitoring using guided ultrasonic waves in wires', in *Review of Progress in QNDE*, eds. D.O. Thompson and D.E. Chimenti, vol.20, pp.1642-1649, American Institute of Physics, New York, 2001.

94. Aerotech Ltd. UK Supplier: Krautkramer UK Limited, Millburn Hill Road, University of Warwick Science Park, Coventry, CV4 7HS, UK.

95. M.J.S. Lowe, and O. Diligent, 'Reflection of the fundamental lamb modes from the ends of plates', in *Review of Progress in QNDE*, eds. D.O. Thompson and D.E. Chimenti, vol.20, pp.89-96, American Institute of Physics, New York, 2001.

96. A. Demma, P. Cawley, and M. Lowe. 'Guided waves in curved pipes', in *Review of Progress in QNDE*, eds. D.O. Thompson and D.E. Chimenti, vol.21, American Institute of Physics, New York, in press 2002.

97 L. Rayleigh, 'On waves propagating along the plane of an elastic solid', *Proceedings of the London Mathematical Society*, vol.17, 1885.

98. H. Lamb, 'On waves in an elastic plate', in *Proceedings of the Royal Society*, vol.93, p114-128, London, 1917.

99. Q. Zhu, and G. Mayer, 'On the crossing points of Lamb wave velocity dispersion curves', *Journal of the Acoustical Society of America,* vol.93(4), pp.1893-1895, 1993.

100. P.D. Wilcox, 'Lamb wave inspection of large structures using permanently attached transducers', *PhD Thesis, Department of Mechanical Engineering, Imperial College of Science Technology and Medicine, London*, 1998.

101. G. Lui, and J. Qu, 'Guided circumferential waves in a circular annulus', *Journal of Applied Mechanics*, vol.65, pp.424-430, 1998.

102. P.B. Nagy, M. Blodgett, and M. Golis, 'Weep hole inspection by circumferential creeping wave', *NDT&E International*, vol.27(3), pp.131-142, 1994.

103. C. Valle, J. Qu and L.J. Jacobs, 'Guided circumferential waves in layered cylinders', *International Journal of Engineering Science*, vol.37, pp.1369-1387, 1999.

104. D.S. Drumheller, 'Coupled extensional and bending motion in elastic waveguides', *Wave Motion*, vol.17, pp.319-327, 1993.

105. B.A. Auld, 'Acoustic fields and waves in solids - vol.II', Stanford: Krieger Publishing Company, Florida, 2nd ed., 1990.

106. L. Gavric, 'Computation of propagative waves in free rail using a finite element technique', *Journal of Sound and Vibration*, vol.185(3), pp.531-543, 1994.

107. P. Wilcox, M. Evans, O. Diligent, M.J.S. Lowe, P. Cawley, 'Dispersion and excitability of guided acoustic waves in isotropic beams of arbitrary cross section', in *Review of Progress in QNDE*, eds. D.O. Thompson and D.E. Chimenti, vol.21, American Institute of Physics, New York, in press 2002.

108. D. Hitchings, 'FE77 User Manual', Imperial College of Science Technology and Medicine: London, 1987.